Newberry EGS
Enhanced Geothermal Systems
DEMONSTRATION

Phase 2.2 Report

DOE Award: DE-EE0002777

AltaRock Energy, Inc.

July 3, 2015

Contributing Authors

AltaRock Energy

Trenton T. Cladouhos, Susan Petty, Yini Nordin, Geoff Garrison,

Matt Uddenberg, Michael Swyer, Kyla Grasso

Consultants and Sub-recipients

Paul Stern (PLS Environmental)

Eric Sonnenthal (LBNL)

Pete Rose (EGI)

Gillian Foulger and Bruce Julian (Foulger Consulting)

Acknowledgment: This material is based upon work supported by the Department of Energy under Award Number DE-EE0002777.

Disclaimer: This report was prepared as an account of work sponsored by an agency of the United States Government. Neither the United States government nor any agency thereof, nor any of their employees, makes any warranty, express or implied, or assumes any legal liability or responsibility for the accuracy, completeness, or usefulness of any information, apparatus, product, or process disclosed, or represents that its use would not infringe privately owned rights. Reference herein to any specific commercial product, process, or service by trade name, trademark, manufacturer, or otherwise does not necessarily constitute or imply its endorsement, recommendation, or favoring by the United States government or any agency thereof. The views and opinions of authors expressed herein do not necessarily state or reflect those of the United States government or any agency thereof.

Table of Contents

TABLE OF FIGURES

TABLE OF TABLES

APPENDICES

1 INTRODUCTION

1.1 PROJECT DESCRIPTION

The Newberry Volcano EGS Demonstration is developing an Enhanced Geothermal System (EGS) in the high-temperature, low-permeability resource present in volcanic formations on the northwest flank of the Newberry Volcano. The Demonstration is being executed in multiple stage-gated phases, and this report summarizes the activities of Phase 2.2.

The project is located 37 km (23 mi) south of Bend, Oregon, with the nearest small community 11 km (7 mi) away at Newberry Estates, and the nearest town of La Pine 16 km (10 mi) away (Figure 1). The project site is on land leased from the Bureau of Land Management (BLM) with the surface controlled by both the BLM and the US Forest Service (USFS). The geothermal leases lie adjacent to the Newberry National Volcano Monument (NNVM), which was created in 1990 to preserve the scenic beauty and volcanic features inside the Newberry Volcano caldera while also providing for geothermal resource development and other uses on adjacent lands.

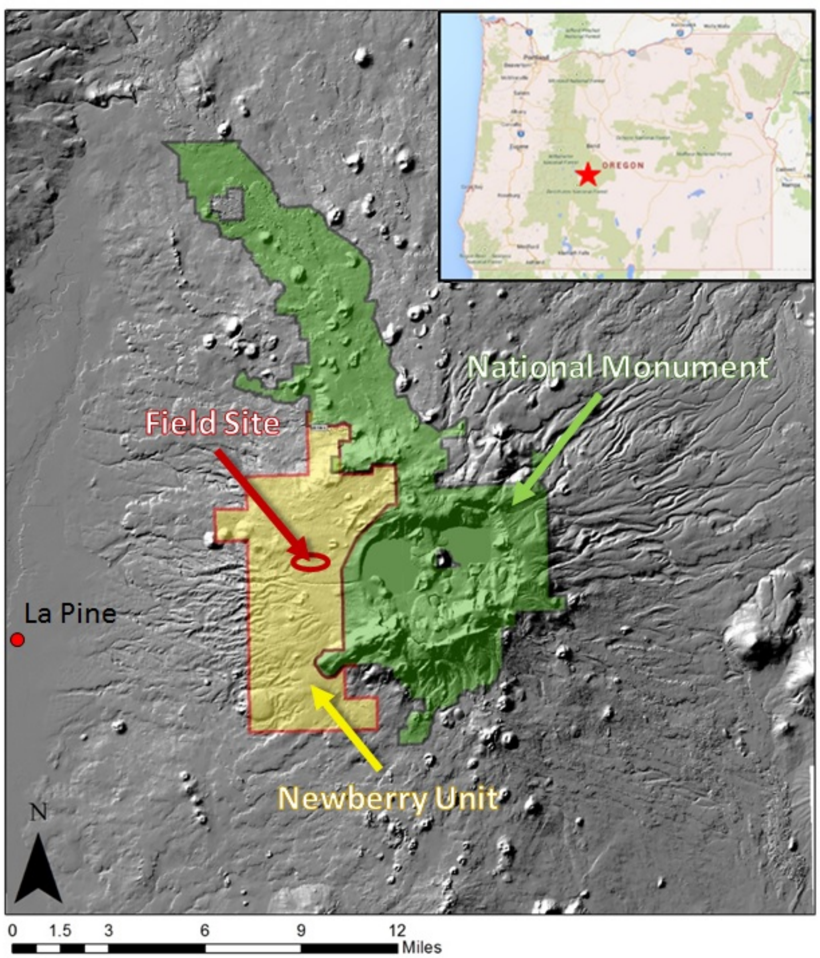

Figure 1. Location map for the EGS Demonstration at Newberry Volcano, showing Newberry National Volcanic Monument and surrounding geothermal leases within Newberry Geothermal Unit. Inset map of Oregon shows general location of Newberry Volcano.

1.2 SUMMARY OF PHASE 2.2 OBJECTIVES

Stimulation of well 55-29 first occurred during Phase 2.1, in the fall of 2012 (AltaRock, 2014). During this initial stimulation, 90% of the seismicity occurred at depths less than 1,830 m (6,000 ft). First, AltaRock and members of the seismology team investigated whether the shallow seismic events could have been due to systematic depth errors. After this possibility was eliminated, it was hypothesized that shallow seismicity was due to either high permeability pathways connecting the two depths, or holes in the casing which allowed water to escape and stimulate shallow zones. In the summer of 2013, caliper and video logs confirmed that there was both a horizontal crack in the casing at 683 m (2,240 ft) depth and a leak in the parasitic aeration string (PAS) (AltaRock, 2014).

Therefore, casing repair was determined to be necessary to further stimulation and create the deep EGS reservoir as originally intended. Repair and re-stimulation plans were made in the first quarter of 2014 to guide Phase 2.2 field operations. Casing repair commenced on August 11 and was completed on August 23. Upon completion of the casing repair the 55-29 pad was staged for a new round of stimulation which began on September 23.

1.3 SUMMARY OF PHASE 2.2 ACCOMPLISHMENTS

Phase 2.2 was successful in its goal to repair and re-stimulate NWG 55-29. Phase 2.2 accomplishments include:

- Casing was repaired by running 9⅝ in casing tie-back inside to the 13⅜ in casing and cementing up the PAS line to block off the hole.
- Set perforated liner to the bottom of the hole to prevent possibility of hole collapse;
- Successfully stimulated well 55-29, creating an EGS reservoir and target for a production well.
- Located 400 microseismic events with the highest density 150-200 m from the injection well
- Proved viability of new fibrous diverter material which blocked off existing zones and stimulated a new zones;
- Implemented lessons-learned from the 2012 stimulation to streamline stimulation operations. The Phase 2.2 stimulation effort had far less down-time than the 2012 stimulation;

In 2014, AltaRock was able to set up the stimulation system faster, run the pumps at higher pressures and run them for longer time periods with far less down-time than in the 2012 stimulation effort. Combined with the successful identification of the casing problem and subsequent repair, all the goals of Phase 2.2 were successfully achieved.

1.4 NEXT STEPS

The next phase of development, Phase 2.3, is scheduled to begin in the second or third quarter of 2015. Section 8 of this report details the scope and objectives of Phase 2.3, including:

- onsite maintenance;
- drilling a production well which targets the EGS reservoir created in 2014;
- stimulation of the production well, both individually and as part of the dual-well stimulation; and

- a short-term connectivity test between the injector and producer.

Phase 2.3 will validate the EGS concept in a volcanic setting. Drilling a production well and subsequent stimulation will expand the existing reservoir and provide higher resolution data of the resource. Circulation and tracer testing will allow for refined characterization of the developed EGS reservoir and will validate the economic and technical viability of using AltaRock Energy's technology to create an EGS. This will be the final phase of the Demonstration that includes American Recovery and Restoration Act (ARRA) funding. AltaRock will continue additional development that will lead to eventual commercialization of the project.

2 PHASE 2.2 PREPARATION AND PLANNING

2.1 SUMMARY OF ACTIVITIES

The Phase 2.2 build-out of the project site consisted of the following critical tasks:

Permitting

The permitting process for Phase 2.2 included BLM approval of two Geothermal Sundry Notices detailing the casing program and slotted liner installation for NWG 55-29. The Department of Geology and Mineral Industries (DOGAMI) also approved a Modification Application to perforate the NWG 55-29 Liner, and the Oregon Department of Environmental Quality (DEQ) approved the Water Quality Permit and maintains "rule authorization" for stimulation of NWG 55-29. The Oregon Water Resources Department (OWRD) approved changes to the existing water use license in November, 2014, amending the permit to include use of groundwater from NWG 55-29. The Special Use permit allowing seismic monitoring stations on USFS land remains in effect through 2015 with the Forest Service; in addition, USFS issued Industrial Fire Precaution Level Waivers for work during Phase 2.2. Further details of the permitting process can be found in section 2.2.1.

Public Outreach

Public outreach and education was an integral part of Phase 2.2, including public meetings, reports and publications, and outreach through online social media. Monthly public outreach meetings were held during stimulation and were conducted in Bend, La Pine, and Sunriver. All public outreach events include progress updates presented by AltaRock staff and question and answer time to address public inquiries.

Road and Pad Preparation

Roads required repair and grading from overuse. Watering for dust mitigation was needed during times of extreme dust and heat. Ruts, drainage damage and washboard conditions were repaired prior to delivery of the Paul Graham Drilling rig. Necessary road work was repeated after departure of the drill rig to repair normal wear and tear from site traffic. AltaRock worked with USFS to bring the road up to USFS specifications after rig departure.

Pad S-29 required no grading or maintenance prior to commencement of field activities. The cement pad installed in 2012 for pump anchoring was improved addition of small sections of concrete to better stabilize piping support structures.

2.2 PERMITTING

2.2.1 PHASE 2.2 PERMITS

The following permits were obtained during the 2014 field season to allow the well repair and stimulation to proceed:

BLM Geothermal Sundry Notice (GSN) to Repair NWG 55-29 Casing

We submitted a GSN detailing the work-over plans and procedures for repairing the casing in the well. BLM reviewed and approved this GSN on July 15, 2014.

DOGAMI Permit to Modify Geothermal well to Repair NWG 55-29 Casing

We submitted a detailed work-over plan and Geothermal Well Modification Permit to DOGAMI to repair the well. This modification permit was approved on June 7, 2014.

DOE and BLM approval of Proposed Amendments to Induced Seismicity Plan

Based on lessons learned during 2012 changes were proposed to the Induced Seismicity Mitigation Plan. Most significantly, the volume in sumps needed for flow back was reduced, eliminating the need for a pipeline connecting the 55-29 and 46-16 pad sumps. After review by the DOE and BLM the changes were approved. For the full text of ISMP Amendments as well as the DOE approval letter, see Appendix A.

Oregon Department of Environmental Quality (DEQ) Water Quality Permit

On September 8, 2014, OR DEQ issued a determination that the current underground injection control (UIC) permit and system in place had met the requirements for authorization by rule, and is "rule authorized" by the DEQ.

BLM Geothermal Sundry Notice (GSN) to Perforate NWG 55-29 Liner

We submitted a GSN detailing the plan to perforate the 7 in liner and notch the formation in the well at three depths. BLM reviewed and approved this GSN on November 5, 2014.

DOGAMI Modification Application to Perforate NWG 55-29 Liner

We submitted a geothermal well modification application detailing the plan to perforate the 7 inch liner and notch the formation in the well. DOGAMI reviewed this application and verbally approved it on November 5, 2014.

Other permitting activities included Forest Service Industrial Fire Precaution Level (IFPL) Waivers, and continued communication with regulators to keep them up to date on miscellaneous project activities.

2.2.2 PHASE 2.3 PERMITS

The following permits will be needed for the planned 2015 field season (Phase 2.3):

BLM Geothermal Drilling Permit (GDP)

BLM will require a GDP for the drilling of the new production well, NWG 55A-29, to be drilled on the S-29 well pad.

DOGAMI Geothermal Well Permit

DOGAMI will also require a Geothermal Well Permit for the new production well to be drilled on the S-29 well pad.

Oregon Department of Environmental Quality (DEQ) Water Quality Permit

In preparation for the stimulation activities in 2014, an application and injection plan was submitted to ORDEQ. Oregon DEQ determined the permit could be *rule authorized* as opposed to the *Special Letter Permit* process used in 2012. As a result, AltaRock is authorized to stimulate under the 2014 UIC permit and no new *Special Letter Permit* will be required for stimulation activities in 2015.

Oregon Department of Environmental Quality (DEQ) Air Control Discharge Permit (ACDP)

We currently have a Simple ACDP that we have put into suspension to cover the diesel generators needed to drill the production well. Depending on the size, type and duration of use of these generators, we may be exempt and can cancel the permit. Otherwise, we will modify this permit to allow the use of the specific generators needed to drill the production well. We will seek a determination from DEQ early in 2015 as to whether we should cancel or modify the permit.

Oregon Water Resources Department (OWRD) Water Permit

Up until now we have withdrawn groundwater from the water well at the S-29 well pad under a limited water use license (LL-1441). In August 2014 we filed an application to modify the existing water permit (G-17032) to include groundwater from the water well on pad S-29. On November 25, 2014 this change was approved by OWRD and a new permit was issued (G-17316) to reflect these changes. As a result of this approval, future water use will be under a water right permit not a limited water use license. The water permit allows withdrawal of up to 1,598 gallons per minute (3.56 cfs) and does not require the purchase of mitigation credits.

Forest Service Special Use Permit

Seven of the surface MSA stations and the Strong Motion Sensor (SMS) are located on National Forest system lands that are not on BLM geothermal leases. As a result, the Forest Service has jurisdiction and has issued a special use permit (BEN784, amended 5/28/13) permitting these stations. While the Special Use Permit is valid until the end of 2015, it is not renewable and we are required to submit an application for a new permit at least 6 months prior to the expiration of this permit. We plan on doing this in early 2015.

Forest Service Road Use Plan

We are currently authorized to use Forest Service roads under a Road Use Permit that is valid through 2019. As a condition of the Road Use Permit we are required to submit a road use plan describing the anticipated extent and duration of use. We plan on submitting this plan prior to the beginning the 2015 field season.

Forest Service Industrial Fire Precaution Level (IFPL) Waivers

Ordinary dry summer conditions will likely require that we file for IFPL waivers to allow continued operations on the NWG 55-29 well pad during USFS-issued IFPL notices. We have successfully been issued such waivers in 2012 and 2014 and see no reason they would not be granted in the future. In addition to these permits, we anticipate active continued communication with regulators to keep them up to date with the project.

2.3 PUBLIC OUTREACH

Public outreach and education during Phase 2.2 was accomplished through four primary mechanisms: public outreach meetings, reports and publications, outreach through online social media and networking at local business events. Reporting and publications completed in Phase 2.2 include quarterly and annual project updates to the DOE, publication and presentation of peer-reviewed reports to the geothermal industry, and this Phase 2.2 report.

Data collected and analyzed during Phase 2.2, as well as the overall project technical plan, will be published in various geothermal industry and scientific forums, as appropriate. Papers and presentations have already been written and given at the annual meetings of the American Geophysical Union (December, 2014) and the Stanford Geothermal Workshop (January, 2015).

Monthly public outreach meetings were held during stimulation and were conducted in Bend, La Pine, and Sunriver. Attendance at these meetings was between 20 and 100 people. Booths at the weekend-long Bend summer and fall festivals were also staffed to provide public outreach about the Newberry project. Presentations during Phase 2.2 were made to the La Pine Chamber of Commerce (two presentations), Bend Rotary Club, Mt. Bachelor Rotary Club, Sunriver Rotary Club, Economic Development for Central Oregon (EDCO), Bend City Council, La Pine City Council, Deschutes County Commission, Central Oregon Community College's power engineering class, University of Oregon Alumni group meeting, and

Newberry National Volcanic Monument Obsidian Series talks. The Geothermal Resource Council (GRC) Newberry and Central Oregon field trip visited the site in late October before the GRC annual meeting, bringing engineers, geologists, students and reporters to Newberry (Figure 2). Excellent reports on this field trip were published in the November/December 2014 GRC Bulletin and on RenewableEnergyWorld.com in December, 2014.

Figure 2. Geothermal Resource Council annual meeting attendees visit the Newberry site.

Outreach via online social media during Phase 2.2 included regular updates to the Newberry EGS blog, Facebook™ and Twitter™ webpages, and the AltaRock Energy website. An informational hotline number was also maintained for public comments and questions and published on all the webpages. Articles published to these webpages during Phase 2.2 include updates on the stimulation, seismicity, environmental monitoring, site tours for various groups, and photos from the field. Links to published academic work are provided on the AltaRock website for those interested in greater detail.

Local and national media sources published articles about the Newberry EGS Demonstration during Phase 2.2. In addition, the Bend Bulletin and BLM each shot and produced short videos on the project which have been published to their websites. Articles about the project published in Phase 2.2 include:

- *Using Engineered Geothermal Systems to Meet our Energy Demand*. January 29, 2014. RenewableEnergyWorld.com.
- *The long, hard slog to unlock the potential of geothermal energy.* August 7, 2014. www.GigaOm.com
- *Northwest Researchers Work to Boost Geothermal Power.* August 24, 2014. Courtney Flatt, Oregon Public Broadcasting EarthFix.
- *Why The Northwest Is the New Frontier in Geothermal Energy.* September 29, 2014. Cassandra Profita, Oregon Public Broadcasting.
- *Newberry Geothermal Project.* October 10, 2014. Institute for Ethics & Emerging Technology.
- *Geothermal Project Continues on Newberry Volcano.* October 16, 2014. Bend Bulletin.

- *The Dream Becomes Real: Touring the Newberry Enhanced Geothermal Site.* December 15, 2014. Meg Cichon, www.RenewableEnergyWorld.com.
- *Can new drill tech unleash the potential of geothermal energy?* December 17, 2014. Katie Fehrenbacher, www.GigaOm.com.
- *Lava Amps: Tapping into Volcano Power.* January 29, 2015. Don Willmott, www.huffingtonpost.com.

2.4 ROAD REPAIR AND CONSTRUCTION

During Phase 2.2 the planned and actual project work occurred only on the 55-29 Pad.

Before the Paul Graham Drilling rig arrived on the site, FS road 9735 was graded the entire length from US Highway 97 to the project gate and mile marker 7.5 and then from the gate to the 55-29 pad. Due to heavy road use during operations in 2012 and 2013 and winter run-off, repairs of road ruts, side drainages and lead-outs (drains) were necessary at the beginning of the 2014 field season. Taylor NW was commissioned to perform the pre-mobilization grading which was completed in a week, just prior to rig arrival. Extensive road use by medium- and heavy-weight vehicles wore the road surface during the six weeks the drill rig was on site. Minor grading and watering was employed to remediate the road 9735 to the project site.

Upon completion of the drilling and demobilization of the bulk of drill rig structure and equipment, AltaRock and the USFS collaborated to further repair and condition the road to USFS specifications. That work was undertaken both during and after the setup of the stimulation equipment at the site. Before the onset of winter, the road had received a full and complete restoration from the Highway 97 turnoff up to the gate to the project area. Within the project area, additional selected grading was performed, to restore section of the road where grade was steep and traction needed to be insured.

Additional road repair work is anticipated at the start of Phase 2.3 in spring, 2015. This will be done according to USFS guidance.

3 PHASE 2.2: 55-29 WELL REPAIR

Table 1. Schematic of well repair work schedule during 2014 field season.

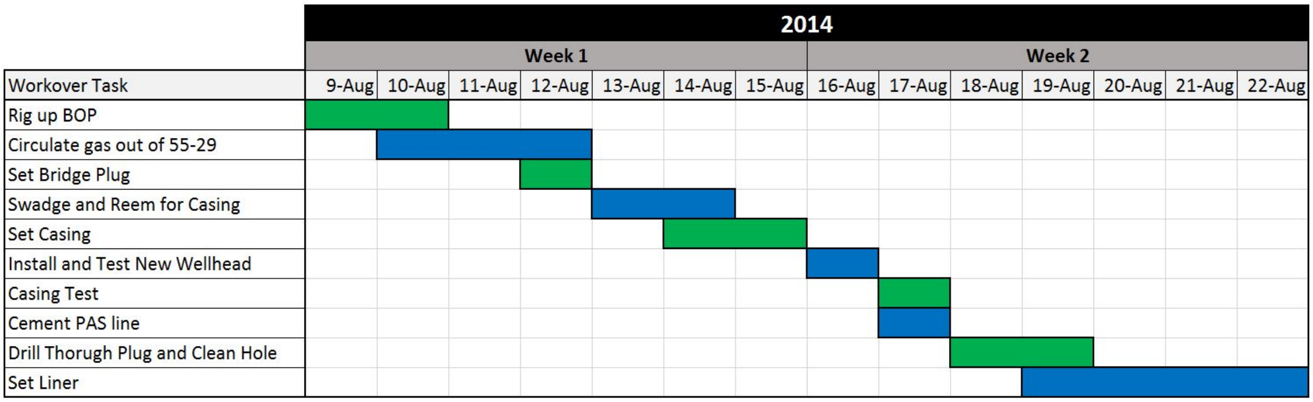

The repair of well 55-29 began August 9 with the installation of the blow-out preventer (BOP) stack on to the well head. Once the rig was completely assembled the master valve was opened the rig began to trip a bit and drill-string down hole. The bit tagged a minor obstruction at 2,006 m (6,580 ft) and upon drilling through this zone over-pressured gas was encountered, which caused the well to unexpectedly flow. The rig spent more than a day circulating out the gas in order to proceed downhole safely. After the gas was circulated out of the hole and the bit tripped to the top of fill at 3,037 m (9,964 ft), the well and rig were ready for installation of 9⅝ in casing (Table 1).

3.1 CASING REPAIR

Casing for the repair came from surplus casing stored in the Davenport storage yard since 2008. Inspection performed December 9-13, 2013, determined that of the 139 pieces of 9⅝ in, 53.5#/ft, L-80 casing stored in the yard, 116 had no apparent defects. The length of acceptable casing contained in the storage yard was 1,473 m (4,834 ft), which was more than the 1,277 m (4,189 ft) needed to complete the tie-back.

Starting on August 12 a bridge plug was installed at 1,348 m (4,424 ft) inside the existing 9⅝ in casing with 15 barrels of cement placed on top of the plug. This depth for the top of cement was confirmed at 1,312 m (4,305 ft) below the top of the existing 9⅝ in liner at 1,279 m (4,199 ft). On August 14, the tie-back string and casing shoe were installed from surface to the top of the original 9⅝ in casing at 1,279 m (4,199 ft) (Figure 3). The casing was cemented with 317 barrels of cement using a reverse-circulation method.

Figure 3. Picture of the casing shoe just before installation in NWG 55-29.

3.2 CASING INTEGRITY TEST

On August 16 after the installation of casing was complete, a refurbished 10 inch Series 1500 wellhead was installed and pressure tested to 20.6 MPa (3,000 psi). The results of the test showed that the wellhead was completely sealed and installed correctly. The casing was subsequently tested on August 17. Cement inside the 9⅝ in casing was cleaned out from 1,063 m (3,488 ft) to 1,312 m (4,305 ft) and the casing pressure tested to 17.2 MPa (2,500 psi) to confirm mechanical integrity. The test results showed that the casing held pressure and that there were no apparent leaks.

3.3 LINER INSTALL

The process of installing 23#/ft, K-55 7 in liner began with drilling out the bridge plug and cleaning out the wellbore to a total depth of 3,044 m (9,990 ft). First, an attempt to hang the liner from 1,918 m (6,294 ft) was made in order to keep the lower 390 m (1,280 ft) of the well open for future open-hole logging such as the borehole tele viewer (BHTV). Unfortunately, the liner slips failed to fully engage and allow the liner to be hung as planned. An attempt to pull the liner out also failed, indicating that the slips has at least partially engaged, just not enough to allow the liner to be set and unscrewed. After some deliberation on the available options the technical and drilling team decided that the safest option would be to lower the liner to the bottom of the wellbore and set it there. After releasing the drill string, this left the liner sitting on the bottom from 2,289 m (7,512 ft) to 3,044 m (9,990 ft), with 320 m (1,050 ft) of open hole above the liner. Thus installation of the second 7 in liner became necessary to complete the well properly. The second liner was run in the hole and 389 m (1,277 ft) of additional 7 in, 23#/ft, K-55 liner was set on top of lower liner. The top of this second piece of liner was set at 1,896 m (6,222 ft). The original plan was to hang the 7 in liner with a 201 m (661 ft) of blank section to overlap with the 9⅝ in casing and cover unstable formation to approximately 2,133 m (7,000 ft) depth. A consequence of having this first piece of liner set at the bottom is that there is now a blank piece of liner in the middle of the open hole between

2,288 m (7,509 ft) and 2,492 m (8,177 ft) depth. Table 1 details the casing repair schedule and Figure 4 shows the completed design after casing repair and slotted liner installation at NWG 55-29.

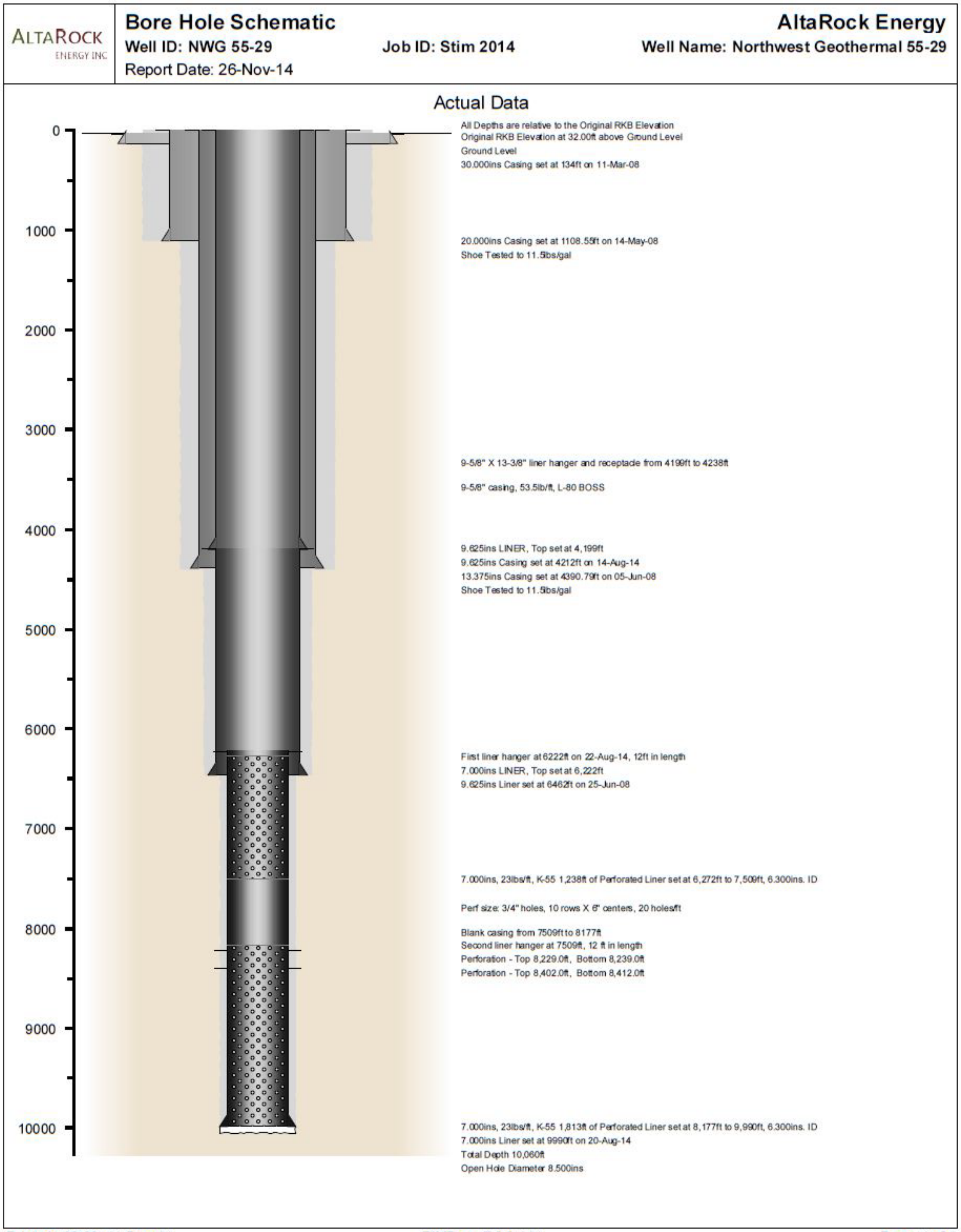

Figure 4. New wellbore schematic for NWG 55-29 after completion of repairs made in 2014.

4 STIMULATION SET-UP

4.1 PAD 29 WATER STORAGE AND SUMP PUMPS

Significant changes were made to the water storage and pumping system from the Phase 2.1stimulation effort. In the 2012 stimulation, Rain-For-Rent water tanks in combination with Victaulic piping and booster pumps were used to supply water to the stimulation pumps. This configuration encountered numerous problems, which led to pump failures and shut downs. The problem was that there was not enough water head in the tanks to allow the booster pumps to operate smoothly. The solution to this problem was that a sump pump was placed in the northern sump to supply water to the booster pumps and from there to the stimulation pumps. For more detailed information on this please see the Phase 2.1 Report.

In 2014, no booster pumps were used. In place of the water tanks and booster pumps, the northern sump was filled with water and two sump pumps were installed to supply sufficient water and pressure directly to the stimulation pumps. Two sump pumps were used for the reason of redundancy and for the potential need to supply of water at a higher rate.

Figure 5. Picture shows the exposed sump pumps in the northern sump at the conclusion of stimulation.

These two sump pumps were designed specifically for the work at Newberry by Cascade Pump and Irrigation. Cascade used two submersible turbine pumps, model 700ST8 created by Franklin Electric, and housed them in two pieces of casing, connected by a cross piece of casing connecting the two pumps (Figure 5, Figure 6). This cross piece of casing was then connected a long high capacity hose which fed the stimulation pumps. In line with the hose, a bypass valve and a filter system were installed. The bypass valve ensured that the pumps operated within the pump curve set by the manufacturer and the filtration system prevented any harmful materials entering the stimulation pumps. Both pumps could be independently controlled by operators at an electric control interface located near the stimulation pumps or by the Human Machine Interface (HMI) in the office.

Figure 6. Picture of the sump pumps on the support skid used to keep pumps away from direct contact with the sump liner.

4.2 UPDATE TO STIMULATION PIPING INFRASTRUCTURE

There were three principal modifications made to the stimulation pump infrastructure between Phase 2.1 in 2012 and Phase 2.2 in 2014.

a. Modification to the Pump Support Concrete Pad

b. Modification of Pad Piping between Pumps and Wellhead

4.2.1 MODIFICATION TO THE PUMP SUPPORT CONCRETE PAD

In 2012, a concrete support pad was poured before the arrival of the stimulation pumps. Late changes to the piping design required the distance between the pumps to be widened – leaving some piping supports off of the concrete pad. Inadequate support resulted in the pumps becoming temporarily mis-aligned, which hampered pump restarts on multiple occasions. To solve this problem, the concrete pad was enlarged in 2014 as shown in Figure 7 to provide additional stable support for the piping supports.

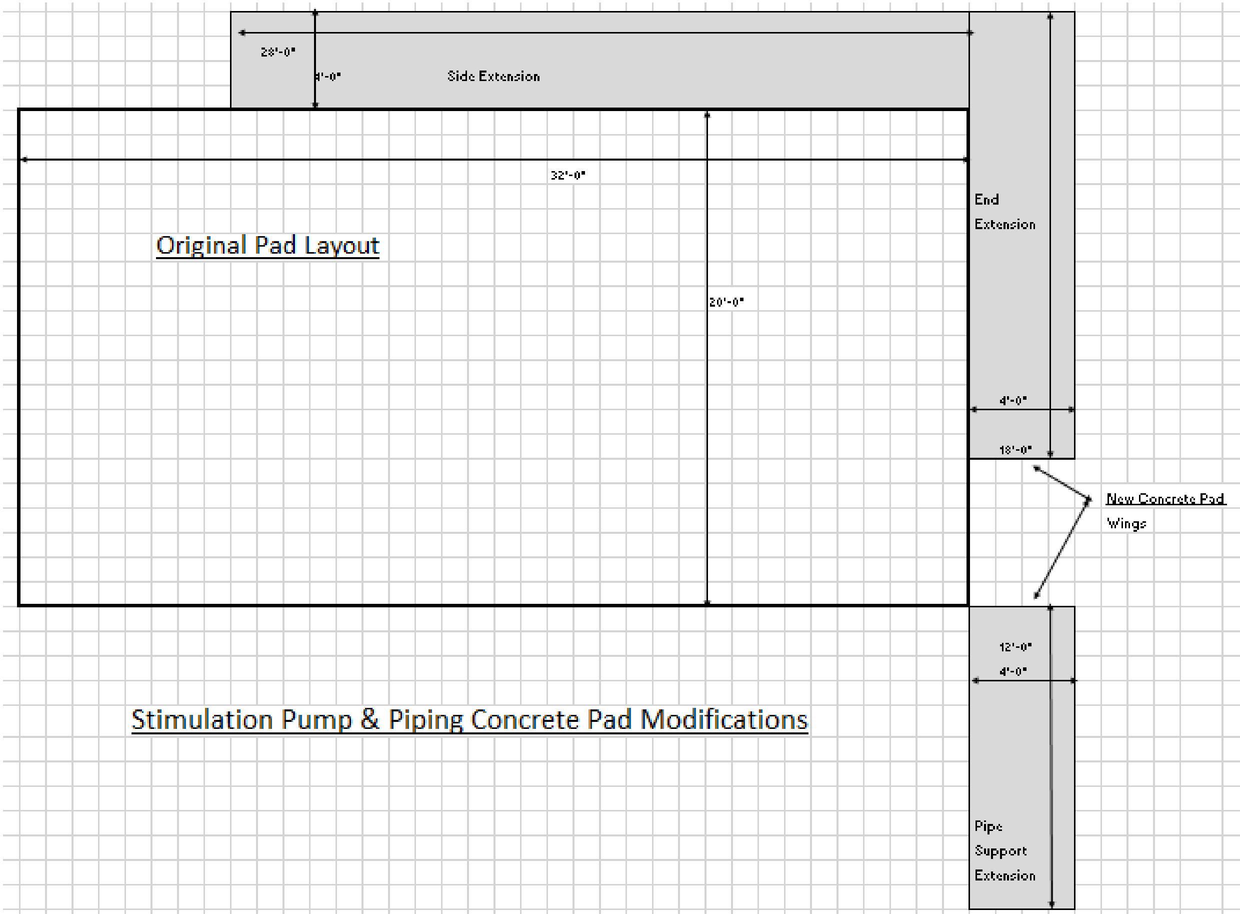

Figure 7. New Concrete pad layout for stimulation pumps.

4.2.2 FABRICATION OF PAD PIPING BETWEEN PUMPS AND WELL HEAD

After the completion of the well work-over and the installation of the new wellhead valve the new wellhead outlet flange was elevated approximately 50 cm (20 in) above the 2012 well head placement. This new elevation, along with the installation of the new concrete pads necessitated a field fit of piping between the pump outlet and wellhead. In addition to a field fit on the pump skid outlet piping, the inlet piping to the wellhead and the outlet piping connecting the well to the separator needed to be "re-fit". This was a field cut-and-fit operation that requires cutting, beveling and adjusting large-bore, thick wall piping to the final fit. Figure 8 through Figure 10 detail the fabrication and installation of piping infrastructure during Phase 2.2.

Figure 8a-b. Hudson Crew making final weld in flow line; (b) Inlet line piping bevel for welding.

Figure 9a-b. Flow line fit from stimulation pumps to wellhead; (b) complete inlet line fit up.

Figure 10. Complete Flow line fit up from well head to Line leading to separator (elevated).

4.3 ELECTRICAL AND CONTROLS

4.3.1 ELECTRICAL

Significant improvements were made to the electrical and control systems for the Phase 2.2 stimulation. The goal for this stimulation was to have a system that was reliable, simple and less susceptible to uncontrolled shut-downs. This was accomplished by obtaining two generators that could handle the entire load of the pad, wiring all of the equipment on the pad to both these generators and having a switching system that would make switching from one generator to the other an efficient and simple process. Changing the stimulation infrastructure in this way allowed for better maintenance, easier fueling and a system less prone to errors.

Medium- and Low-Voltage Electrical

The Newberry EGS demonstration site on Pad S-29 is 12 km (7.5 mi) from highway US-97 and an equal distance from the nearest electrical transmission or distribution line. As such, Pad S-29 does not have utility electrical services or connectivity to the local grid; all electrical power requirements must be provided by portable diesel generator sets. The full operational load of the injection pumps and accessories was approximately 1,400 kW. Electrical generation equipment used during the stimulation project is shown in Figure 11.

Table 2. Electrical generator parameters

Requirement	Qty	Output (kW)	Voltage	Phase
Stimulation Pump Generator(s)	2	1,825	480	3
Site Office/Control Room	1	60	480/230	3

To keep the generators well serviced and eliminate unnecessary risk of generator failure, AltaRock planned to have pump shut downs occur at opportune scheduled times. During shut down the primary generator would be shut off and the secondary generator would be turned on. This allowed for more reliable service and less maintenance needs as each generator would have an overall smaller run time.

The two 1825 kW generators were connected to a breaker box (cubicle) which in turn was connected to two other cubicles. Each cubicle provided electrical service to the dedicated stimulation pump and booster pump, at 480 V. Finally, a step-down transformer and distribution panel provided power to the remaining 208/120 V loads including the control PLC, the ultrasonic flow meter, and electrical bypass control valves.

Figure 11. Photo of the stimulation pump electrical system.

Figure 12 is a diagram of the stimulation pump electrical system. In this diagram we see two 2 MW generators connected to one cabinet or ATS box located right in front of the generator. This ATS box is called ATS Comb., and from this cabinet both generators are connected to two more cabinets located just in front of ATS Comb. These cabinets are called ATS box 1, located on the right, and ATS box 2, located on the left. Connected to ATS box 1 are a VFD (Variable Frequency Drive), the white box in front of the pumps, components of the programmable logic controller (PLC), the water well and one of the submersible pumps. Connected to ATS box 2 are: another VFD, more components of the PLC, one of the sump pumps and the separator drain pump.

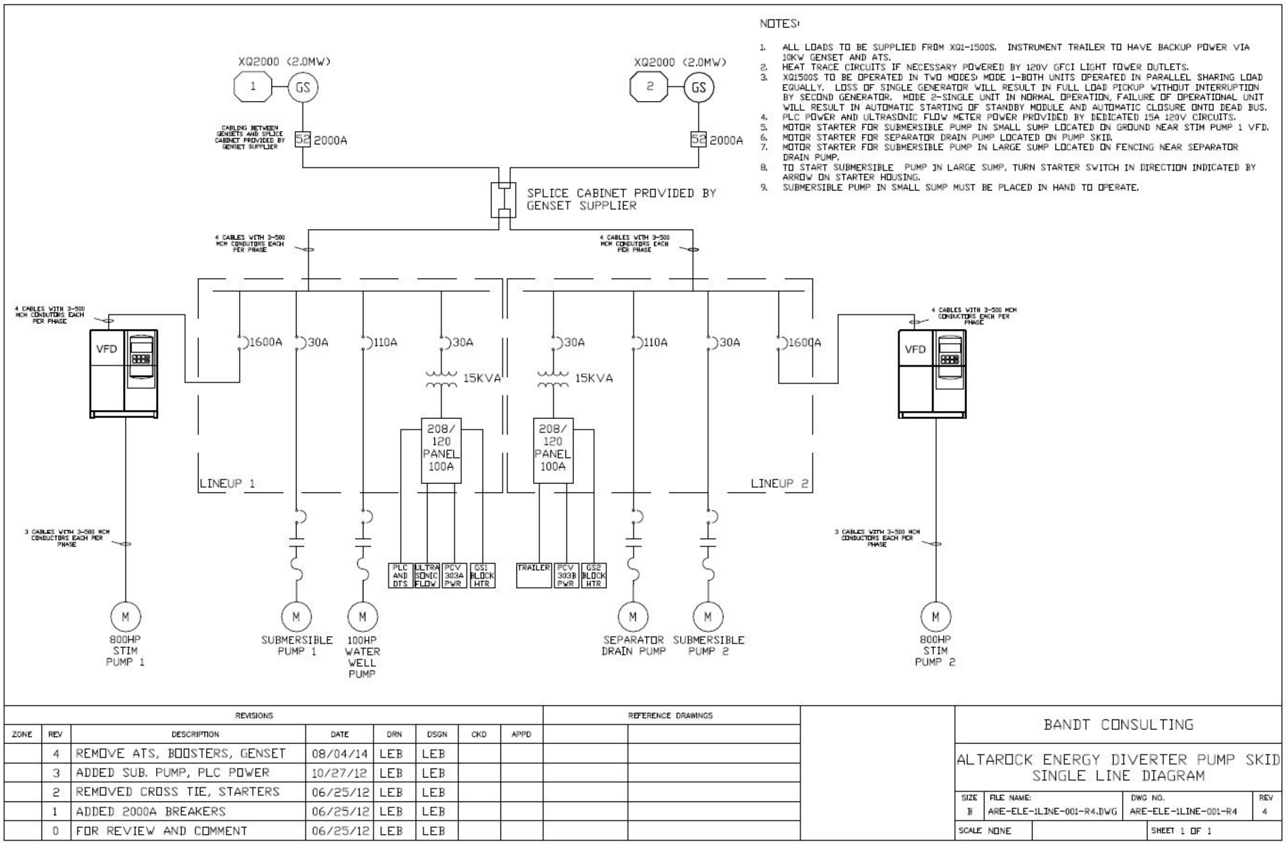

Figure 12. P&ID of electrical set-up for the Phase 2.2 stimulation.

All equipment and power cabling was installed on grade. The equipment was rated for outdoor use and therefore sealed from weather and elements. The power cabling was designated as special outdoor, armored, and surface-installed cable and was selected to mitigate the need for construction of buried or conduit-encased wiring runs.

Grounding of the entire electrical system was required. A single ground point for the entire system was created utilizing the NWG 55-29 wellbore and its 1,981 m (6,500 ft) steel casing as a ground rod. The electrical system design, specification, and configuration were provided by Bandt Consulting of Reno, NV.

4.3.2 INSTRUMENTATION AND CONTROLS

4.3.2.1 CONTROL SYSTEM AND INFRASTRUCTURE

The control system for the stimulation project was a combination of instrumentation, for automatic monitoring, and limited automatic control of devices. Active field monitoring and manual adjustment of control valves was also required to change operating settings.

The PLC Controller is the principal device that allowed for the automation and control of the stimulation system. All sensors, as well as control panels for different equipment, were connected to the PLC. Signal inputs into the PLC came from the sensors located on or within pieces of equipment; outputs went to the different equipment control panels. The PLC uses programmed imbedded logic to take incoming information from the sensors on site and to make decisions about trips and alarms for the different pieces of equipment under its control. Choices have to be made about what should be automated and what should be controlled by the operator. Typically, automated decisions consist of sending trip commands to different pieces of equipment when a known operational threshold is crossed. When there is not a clear need to turn off a piece of equipment, but there may be operational concerns about running a certain piece of equipment at a specific state for too long, an alarm is sent to the operator. This alarm is sent to a human machine interface (HMI) unit located in the control trailers where an operator can see different streams of information in real time and make changes to equipment settings when needed.

At Newberry, the HMI used during operations was an Allen-Bradley PanelView Plus 1000. The PanelView is a programmable touch screen that allows an operator to set up controls and access live streaming data in a way that is in accordance with the method of operations. For this first phase at Newberry, there were six control and data screens programmed for the HMI. These screens included: pump diagnostics, live data from various sensors, a pump control panel, and a stimulation control panel (Figure 13).

From the panel shown in Figure 13, staff could control the speed of each stimulation pump and the amount each bypass valve was open. The gray square, upper right, displays the current well head pressure over an hour-long increment. The green squares underneath numerically display the current well head pressure, flow into the stimulation pumps, and flow into the well. The blue squares on the bottom of the image are links to the other panels programmed into the touch screen. The red box to the right of these is the alarm display panel, where active alarms and trips are displayed.

This stimulation system provided a means to reasonably influence induced seismicity. Pressure and injection rates during stimulation could flexibly be controlled by changing pump speed or by throttling the bypass valve.

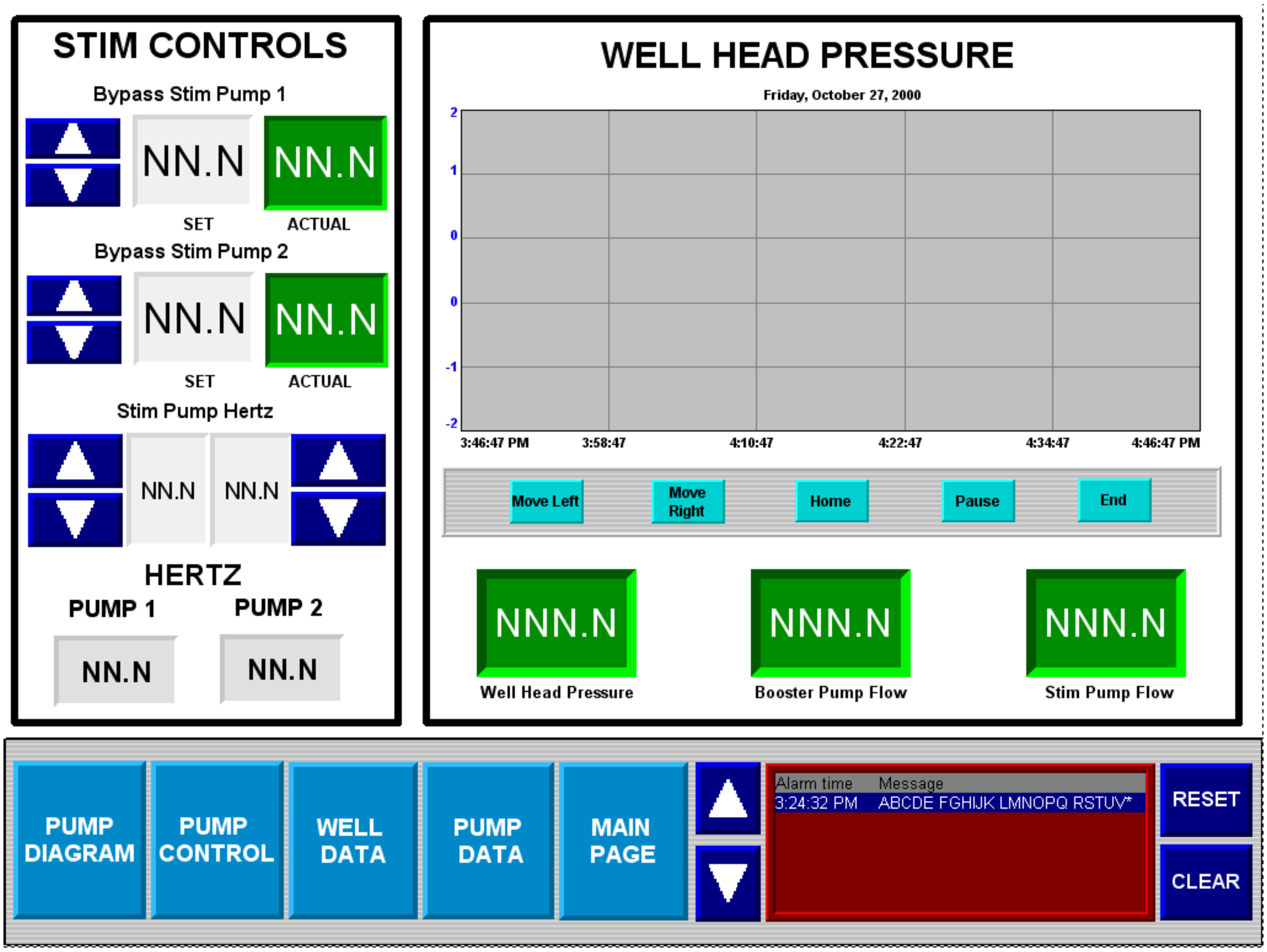

Figure 13. Picture of the stimulation control panel.

4.3.2.2 INSTRUMENTATION

The Stimulation in Phase 2.1 used lab grade instrumentation to monitor pump parameters. Using this grade of sensor lead to problems with data capture and stimulation pump operations. During the Phase 2.2 Stimulation heavy duty industrial grade instrumentation was used instead. All instrumentation for temperature and pressure monitoring of the stimulation system was upgraded to Rosemount Transmitters. These transmitters are more reliable than what was previously installed and are rated for outdoor industrial settings. This was done because during the previous stimulation the less robust sensors were adversely affected by the cold weather and tough operating conditions. There were two types of sensors bought: the Rosemount 644 Temperature Sensors and the Rosemount 2088 Pressure Transducers. Both pressure sensors and temperature transducers are shown in Figure 14.

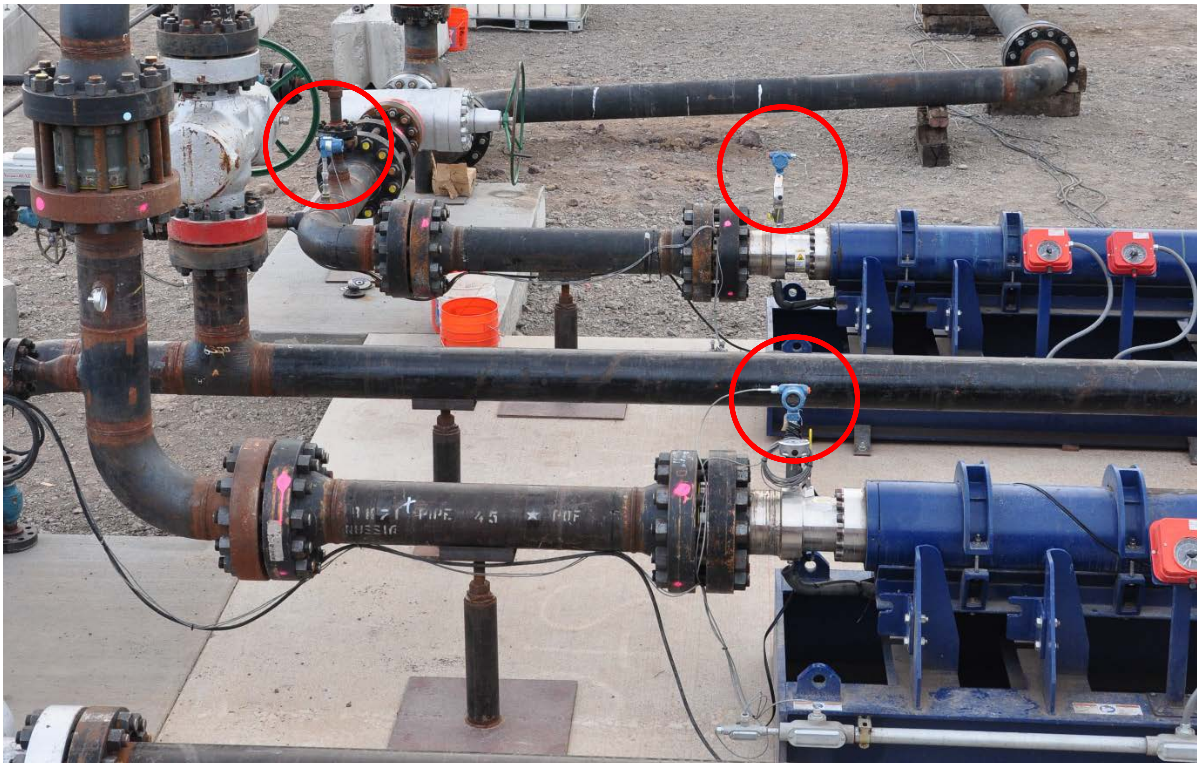

Figure 14. Picture of installation of new Rosemount sensors.

Another element in the instrumentation infrastructure was that each sensor was insulated and wrapped in heat tape programmed to supply heat once the ambient temperature went below 0 °C (32 °F). This guaranteed that no ice would build up in the pressure transducer or temperature sensors and potentially destroy the instrument. During the 2012 stimulation the intake pressure transducer for stimulation pump 1 malfunctioned in this way and subsequently led to extensive damage to that pump. The Phase 2.2 Stimulation had no significant delays or damages caused by instrument error.

4.4 UPDATE TO DIVERTER AND DIVERTER INFRASTRUCTURE

The diverter injection system used during Phase 2.1 stimulation at Newberry proved inefficient and time consuming. During the 2012 stimulation the diverter was added on the intake side of the stimulation pumps and this lead to considerable problems with pump operations. Based on lessons learned during 2012 at Newberry and at other project sites, AltaRock engineered and used a much more effective system for diverter injection during Phase 2.2 work. The design, layout and effectiveness of the new system as well as the new fibrous diverter are outlined in the following sections.

4.4.1 DIVERTER INJECTION VESSEL ASSEMBLY (DIVA)

The largest change made to the diverter infrastructure was the addition of the Diverter Injection Vessel Assembly (DIVA). The DIVA was designed and built by AltaRock to efficiently and cheaply inject thermal zonal isolation material (TZIM) and tracer material into the well under pressure. The DIVA consists of 25.4 cm (10 in) heavy-wall steel pipe and inlet valves from pumps and diverter mixing bowl, and outlet valve to the well. This DIVA system allowed the operators to fill a 570 L (150 gal) high pressure vessel with TZIM or tracer, pressurize the vessel, and then inject the pressurized slug into the well. The DIVA eliminated the need to pump TZIM through the stimulation pumps, eliminating the risk of pump damage from TZIM accumulation (Figure 15). The reason diverter needs to be injected under high pressure is to keep previously injected diverter in place. If well bore pressure is allowed to quickly decrease, pressure in blocked fractures will exceed the pressure in the wellbore, causing water to flow out from the fractures, and flushing the diverter away.

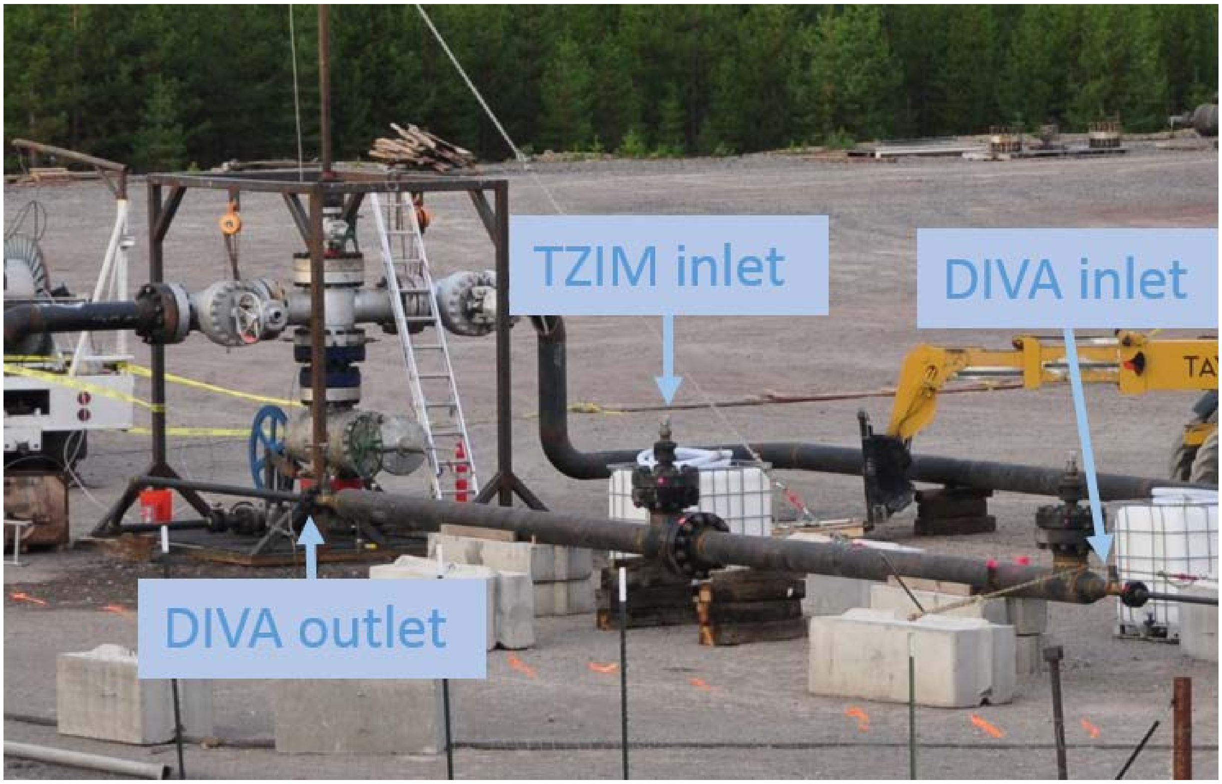

Figure 15. Diverter Injection Valve Assembly (DIVA) used for TZIM injection.

4.4.2 DIVERTER

New and more effective diverters were used during 2014 stimulation. During the Phase 2.1 Stimulation the primary diverter used was AltaVert 151. Laboratory testing in 2014 found that AltaVert 151 degraded at lower temperatures than anticipated. These laboratory results highlighted the need to find a better suited diverter. A series of tests on other diverter candidates found the most suitable diverter material for the high temperatures in NWG 55-29 was AltaVert 251. This work was conducted at the Earth & Geoscience Institute at the University of Utah under direction of Pete Rose.

The experiment designed for testing of the AltaVert 251 involved the use of a flow-through reactor developed by EGI. This reactor allows for the flow of hot water under large pressures through a porous medium, in this case sand, to mimic fluid flow in the subsurface. For this specific test the AltaVert 251 was emplaced on the intake side of the device, and the resulting differential pressure, from one side of the porous media to the other, was recorded. The final temperature reached during the test was 204°C (400°F). The back pressure on the flow through reactor was 6.89 MPa (1,000 psi). The stable differential pressure shown in Figure 16 indicates that the diverter continued to hold after 2 hours at 204°C (400°F). When the diverter was taken out of the flow through reactor degradation had initiated, indicating that diverter would block fractures efficiently and degrade with time.

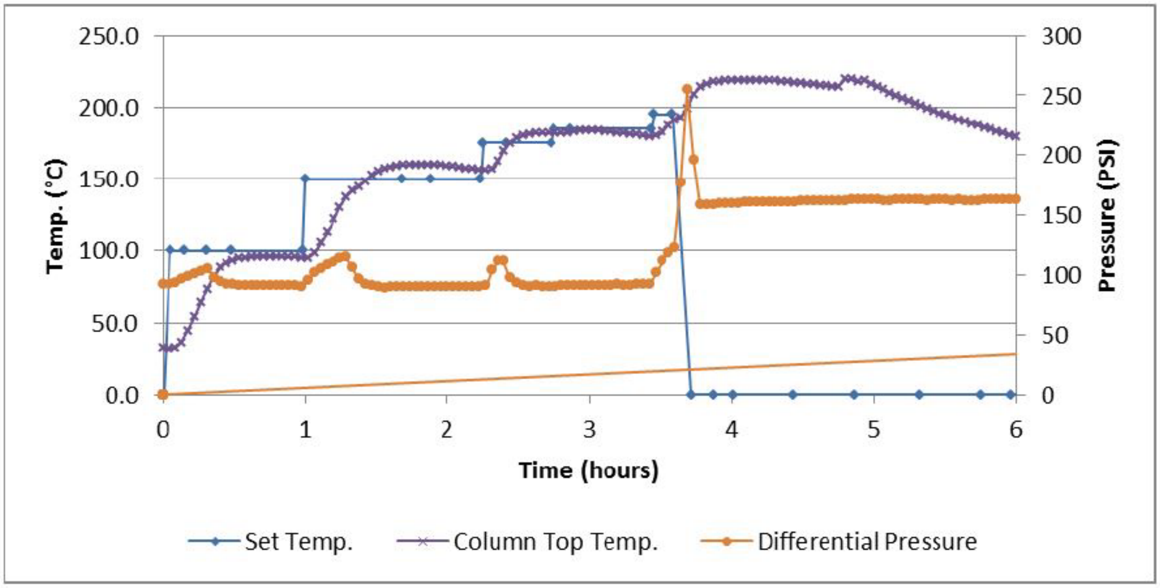

Figure 16. Graph showing the resultant differential pressure of the flow through reactor after the Twaron was injected into the flow stream in the laboratory. The stable differential pressure indicates that the material is not degrading at a significant rate.

Two forms of AltaVert 251 were used during the Newberry 2014 stimulation. A granular form of three different size fractions, leftover from 2012, was used again. Testing at EGI in 2014 indicated that in the laboratory setting, fibrous materials are more effective at reducing permeability Therefore, a fibrous form, AltaVert 251F, was procured in the form of short fibers approximate 1.5 cm (0.6 in) long.

4.5 REAL TIME ANALYSIS TOOLS

A suite of tools was developed for acquiring and analyzing data in real time so that informed decisions could be made during the stimulation process. The first necessary component of these tools are acquisition of the data coming from each sensor. The primary sensors used for real time analysis were pressure and temperature transducers, flow meters, and the Distributed Temperature Sensor (DTS). Pressure, temperature and flow sensors were recorded into a Red Lion data logger. The Red Lion retrieved data from the Programmable Logic Controller (PLC), which acts as the control system for the pumps and stimulation infrastructure, and automatically uploaded data to the AltaRock server with a pre-set file convention. A more detailed explanation of the PLC is given in section 4.

The data from the DTS was automatically uploaded to a workstation on-site. Programs were written in Matlab to visualize the data as it came in so that decision about how to conduct the stimulation could be responsive to resource. These data visualization and analysis tools proved to be invaluable for assessing the state of the resource and general success of the different phases of the stimulation.

4.5.1 DTS DATA VIEWER

The Distributed Temperature Sensor (DTS) data viewer is a program which allows a user to specify an interval of time as well as a specific length of the wellbore and create a contour plot of temperature or temperature gradient for that time and depth (see Figure in section 5.3.2 for DTS image). The DTS takes measurements once per second of temperature every meter along the length of the cable, enabling easy and accurate interpretation of temperature data. This tool allows operators to quickly see the wellbore heat up and cool down as a function of flow as well as identifying fluid exits points in the well. Fluid exit points in the well are located by identifying zones with high temperature gradients. Unfortunately, during the installation of the DTS, the optical fiber within the DTS cable broke and preventing any readings below a depth of 2,434 m (7,985 ft) to be made; this was above the depth of all known exit points within the open hole.

4.5.2 WELLBORE MODEL

A wellbore model written by graduate student Morgan Ames, during his time as an intern at AltaRock, was developed to accurately predict the flow of water into each identified exit zone in the wellbore using DTS data. This wellbore model used a new mathematical approach for calculating flow into the exit zones of a wellbore experiencing variable flow rates over time. This new approach was developed by Manish Nandanwar at the University of West Virginia and was incorporated into the tools code. This tool is useful because it can give an estimate of the volume for each stimulated zone in the wellbore as well as allow one to predict the placement of tracers in order to get optimal information about the fracture geometry. Furthermore, one could use this tool to have fine-tuned control over the development of each stimulated zone. However, this tool could not be used because of the broken fiber within the DTS cable.

4.5.3 SEISMIC DATA ACQUISTION AND VISUALIZATION

The Microseismic Data Visualization tool developed by AltaRock plots processed seismic data in a three dimensional interactive format to allow for quick analysis during stimulation (Figure 17). Seismic data for the tool was gathered from the Micro-Seismic Array and then processed and analyzed by different entities to determine the location and in some cases the magnitude of events right after they occurred. This information was then visualized as soon as it was received to determine whether there was any significant risk of going outside the spatial bounds set by the Induced Seismicity Mitigation Program (ISMP). The tool was useful for both better determining potential seismic risk, with regards to location, as well as correlating actions taken during the stimulation to groupings of seismic events. The tool plots the seismic data in three dimensions and shows the 1,000 m (3,280 ft) horizontal boundary set by the ISMP as well as a three dimensional representation of the wellbore. The tool also shows the time of the events by color and the magnitude of the events by size. The three principal entities which AltaRock used to determine seismic location are LBNL, Foulger Consulting and ISTI. Locations from all three entities are plotted on separate plots and interpreted individually. A screen shot of the tool is shown in Figure 17.

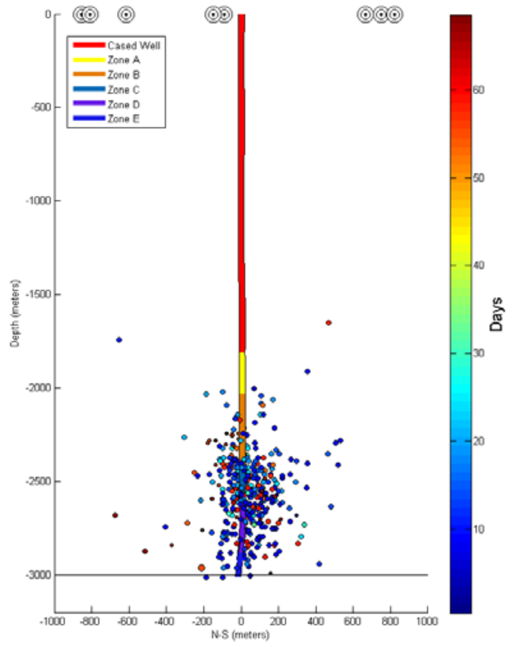

Figure 17. Screen shot of the seismic data visualization tool. Circles at the top of the graph represent the MSA stations. Different colors of the wellbore represent different rock lithologies. The horizontal extent of the graph is 1,000 m (3,281 ft), which is the threshold set by the ISMP.

4.5.4 RED LION

All sensors used in the stimulation infrastructure were wired to the PLC to allow for automation of pump controls, easier interface with the equipment, through a human machine interface (HMI), and to assemble and format all the data coming from these sensors. The memory of the PLC is limited, therefore the data being processed by the PLC was uploaded to a red lion data logger for storage and third party viewing. The red lion data logger that AltaRock used was a ***red lion data station plus.*** This data logger set up an IP address located within AltaRock's intranet and stored the data on a virtual server. This allowed AltaRock staff to see the data in real time as well as download any time interval of data regardless of their location. This allowed all personnel to make informed comments about activities as they happened. The ability for everyone working on the project to see data in real time was invaluable.

5 STIMULATION

5.1 STIMULATION TIMELINE AND SUMMARY

Stimulation at the Newberry EGS Demonstration site began on September 22 (Table 3). Daily summary reports were prepared at the close of each day of stimulation activities and are included as Appendix B.

Table 3. Stimulation procedure timeline at the Newberry EGS Demonstration site.

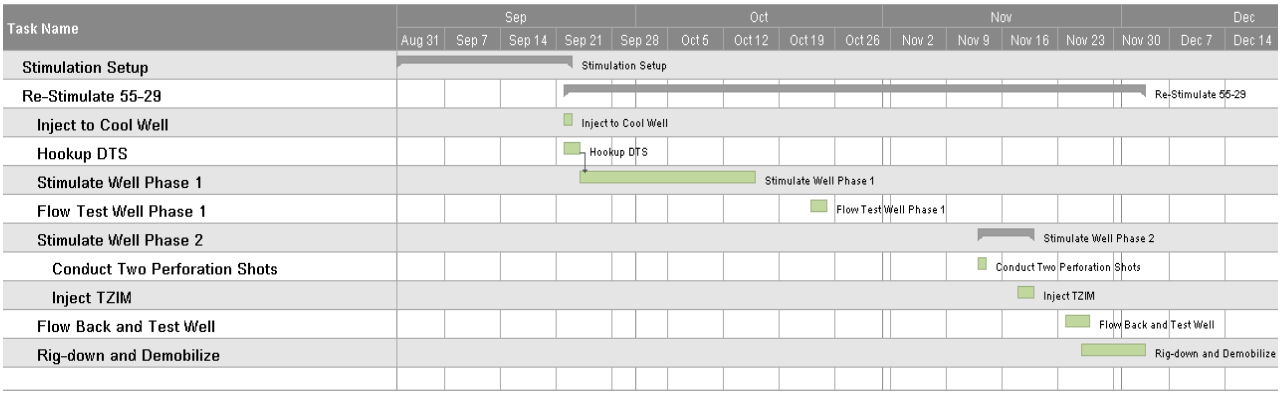

Injection into NWG 55-29 began on 9/22/14. One stimulation pump was started and ran at 46.8 Hz in order to begin the inject-to-cool process and prepare the wellbore for the DTS installation. On 9/23/14, rig up and testing of the stimulation system were completed. An initial step-rate test was conducted from September 23 to 24 (described in section 5.4.1). Conducting a step-rate test allows post-work-over well injectivity to be ascertained and identified critical pressures for different stimulation zones within the well. Stimulation pressure increased to above 17.2 MPa (2,500 psi) on 9/25/14. The increase in wellhead pressure resulted in several leaks in the lubricator connections, which required a welder to be on site on 9/26/14 for repairs. Consequently the pumps where shut down and another step-rate test was conducted on 9/26/14 while ramping up pumps to stimulate the first zone. Once the step-rate test was completed, stimulation of the first zone began. The stimulation of this zone took place over a three week period, where two TZIM treatment were injected on 10/13/14 and 10/14/14 before shutting the pumps in on 10/15/14. After the first round stimulation, the well was allowed to heat up and a flow test was conducted on 10/24/14. During the period of 10/24/14 and 11/10/14, the first round stimulation data was assessed and used to finalize Round 2 stimulation plans.

On 11/11/14, the stimulation pumps were restarted and a step-rate injectivity test followed by constant pumping at 15.2 MPa (2,200 psi) wellhead pressure was used to cool the wellbore down in preparation for the perforation shot. On 11/13/14, Cogco wireline performed two perforation shots from 2,509-2,512 m (8,229-8,239 ft) and 2,562-2,565 m (8,402-8,412 ft). Following the perforation shots, the well was allowed to flow back to clean out debris created by the shots before restarting stimulation on 11/14/14. Then Round 2 of stimulation began on 11/14/14 and lasted for one week. The TZIM injection process was repeated on 11/18/14 and 11/19/14 to block the first zone and allow stimulation to open a second and third zone. Stimulation ended on 11/20/14. Upon conclusion of the stimulation, the pad was cleared of essential equipment, and the well was shut in and allowed to thermally equilibrate with the formation. From 11/24/14 to 11/26/14 a flow test was conducted to determine different characteristics of the reservoir.

5.2 STIMULATION INFRASTRUCTURE PERFORMANCE

The following details the pump operation parameters, distributed temperature sensing cable deployment, background and stimulation microseismicity data collected over the course of Phase 2.2.

5.2.1 PUMP CURVES/OPERATIONS

The stimulation pumps were operated in such a way that flow rates and wellhead pressures were maintained within the pumps' optimum performance parameters (i.e., the pump performance curve). Pump operations were guided by the pump curves provided by Baker Hughes (Figure 18). To safely reach the pressures needed to stimulate the well, the outlet flow from the pumps had to be higher than could be injected into the well to keep the pumps cool. This design challenge was overcome by installing a flow bypass manifold, which allowed the extra flow needed to run the pumps within the optimal conditions. When flow down the well was not high enough, water was discharged through the bypass line to the sumps for recycling.

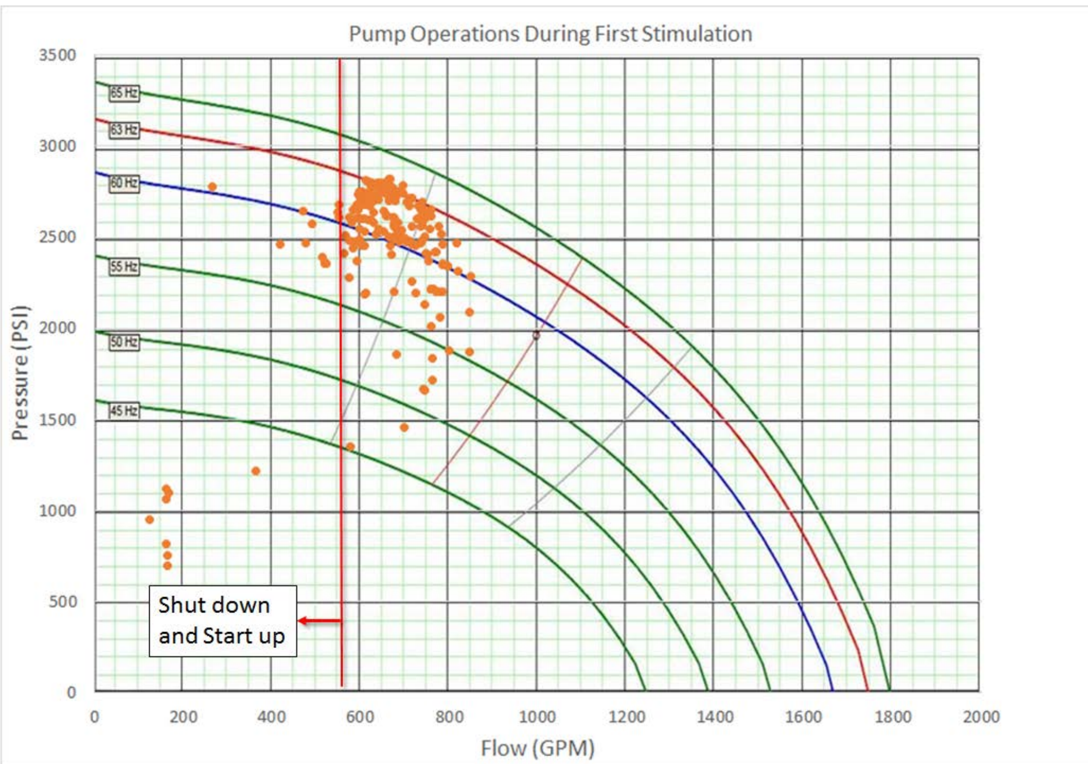

Figure 18. Pump operating points during stimulation Round 1 (orange dots).

LESSONS APPLIED

Based on lessons learned in 2012, the pumping and monitoring equipment were protected from freezing conditions to prevent operational down time. To ensure foreign materials do not enter the pump intake, the sump pump/booster pump design was also reconfigured to prevent debris and low stimulation pump inlet pressure shut-downs. Overall, the entire pumping operation was successful during the 2014 stimulation.

5.3 DISTRIBUTED TEMPERATURE SENSING

5.3.1 DISTRIBUTED TEMPERATURE SENSING CABLE

Distributed Temperature Sensing (DTS) cable provides essential information about the depth of fracture initiation and the efficacy of the TZIM in sealing fractures. AltaRock obtained a high-temperature DTS system in 2012 from BMP Enterprises. This DTS contains one single-mode and two multi-mode fibers with carbon polyimide coating. The 3,658 m (12,000 ft) DTS fiber is enclosed in 825 Incoloy tubing that has been temperature hardened and gel filled. This cable was first deployed in 55-29 during Phase 2.1 work in 2012.

The DTS was shipped to BMP in July for calibration and testing. During the optical time domain reflectometry (OTDR) shots, the DTS displayed only 3,280 m (10,760 ft) of signal, and the fiber was difficult to splice due to brittleness. The cable was likely degraded during the 2012 deployment. Therefore, the bad portion of the DTS was cut off and the DTS shipped back to Newberry for use.

In October, a back-up DTS cable with two single mode and two multi-mode fibers was ordered from Draka Cableteq, a subsidiary of the Prysmian Group. The plan was to install fiber optic strands developed as part of a DOE project awarded to Draka Cableteq into capillary tubing. However, during installation of the Prysmian DTS cable, the cable developed a hole at 1,098 m (3,600 ft). As a result the back-up DTS cable was not completed.

5.3.2 DEPLOYMENT AND RESULTS OF FIRST DTS

The BMP cable was deployed into NWG 55-29 on 9/23/14. While running the DTS fiber into the well, the cable was weight tested every 305 m (1,000 ft) and signal tested periodically to ensure good signal return to surface. When the cable reached 2,913 m (9,556 ft), the signal test with power meter showed no signal returns. After connecting the fiber to the signal box, it was determined that a fiber break occurred at approximately 2,377-2,392 m (7,800-7,850 ft) downhole in both channels. The decision was made to reconfigure the DTS box for single channel use and monitor depth to approximately 2,043 m (6,700 ft) downhole. The DTS contour visualizations of stimulation Round 1 is shown in Figure 19 This DTS cable was pulled from the well on 10/15/14 at the end of stimulation Round 1.

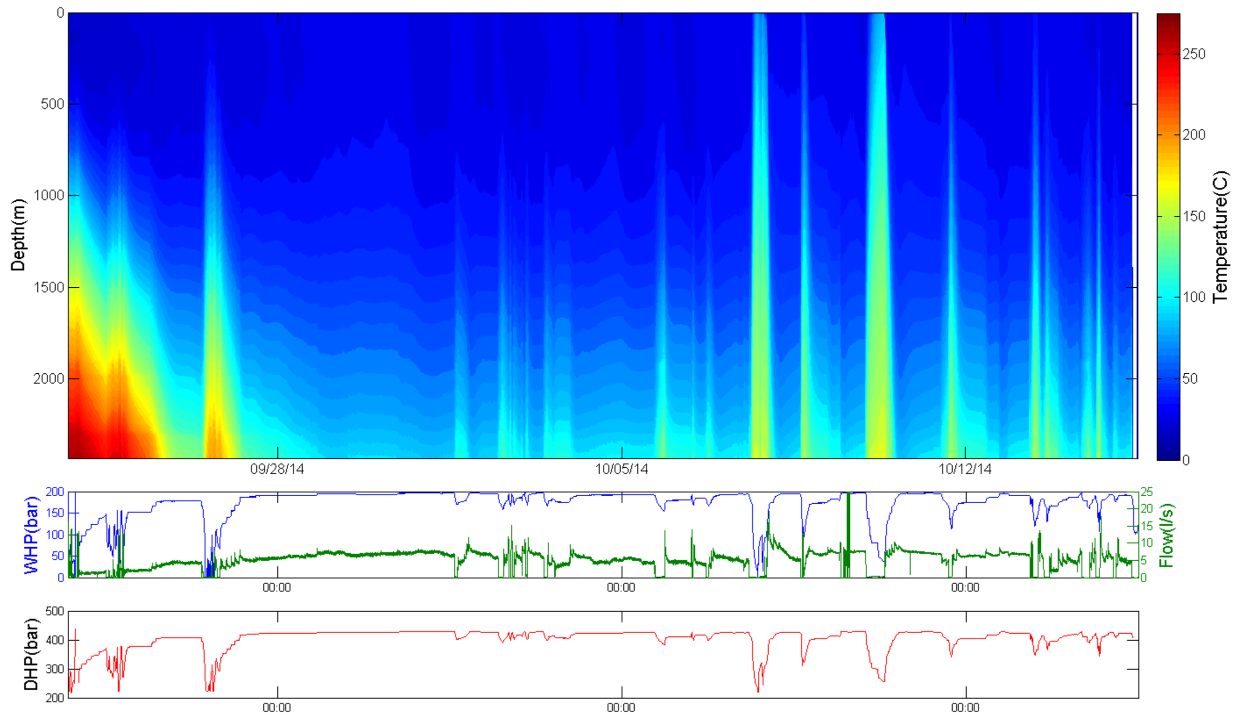

Figure 19. DTS temperature vs depth over time. Bottom graph displays wellhead pressure (WHP), injection flow, and calculated downhole pressure (DHP) over time.

Figure 20 contours the temperature gradient in the well during the stimulation. There are two temperature gradient anomalies near the casing shoe at 1,970 m (6,462 ft) and where the blank section of liner begins 2,290 m (7,509 ft), which may be due to turbulence created locally from changes in diameter. However, the temperature gradients above and below these features are about the same, so there are no significant gradient changes in the in this section of the well, which indicates that there were no leaks in the casing.

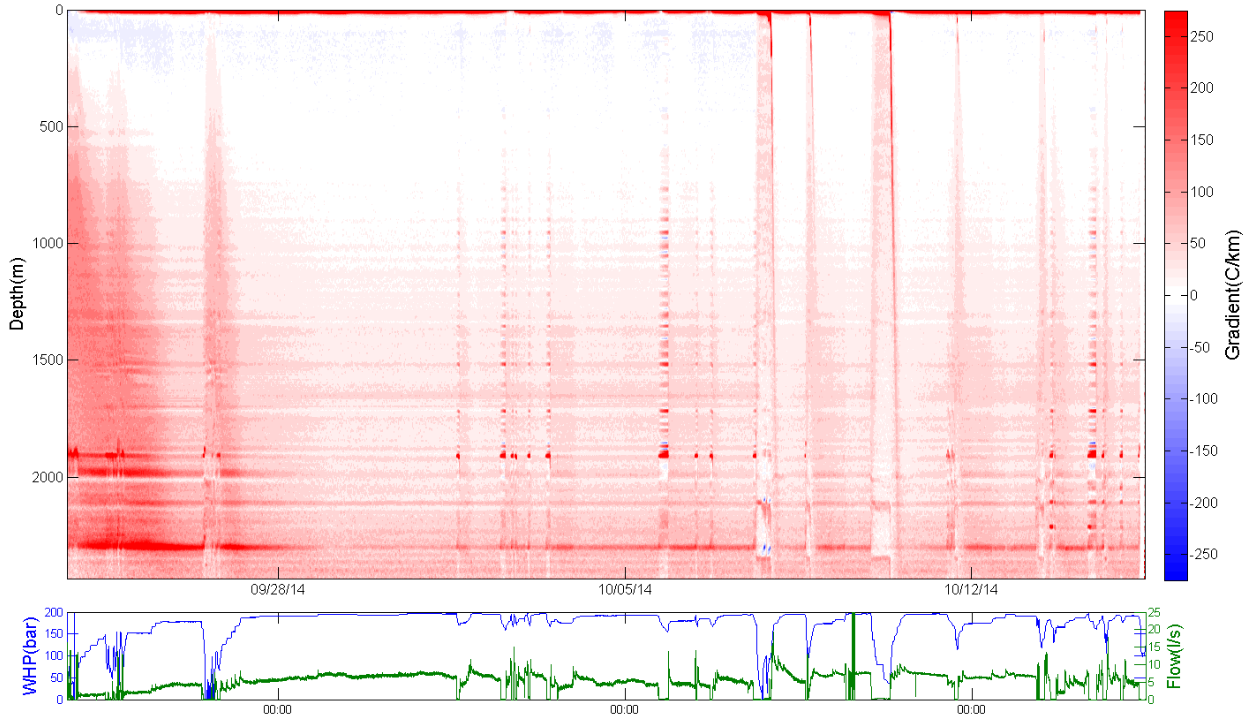

Figure 20: Temperature gradient over time with WHP and injection flow.

Figure 21 shows how fast the well was heating up and cooling down during the stimulation. The initial rate of cooling in the well from the step rate test was about 2 °C/hr (3.5 °F/hr). During a WHP release on 9/26/14, the well heated up at over 30 °C/hr (55 °F/hr), and cooled at a rate similar to the initial cool down after injection resumed. Later during the stimulation, cool down rates were over 30 °C/hr (55 °F/hr) in the casing and 15° C/hr (27 °F/hr) in the open hole, which indicates that the formation just away from the well was much cooler but it is still able to recover its temperature rapidly.

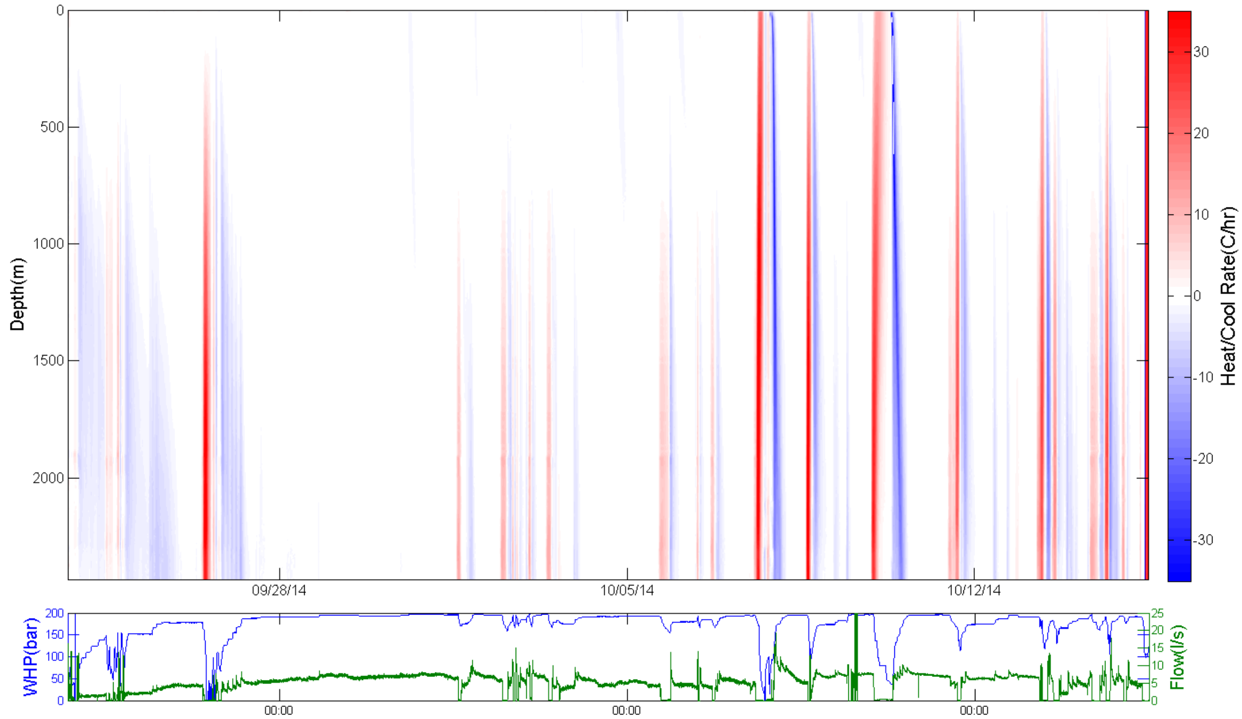

Figure 21: Heat up and cool down rate of the well over time with WHP and injection flow.

5.4 WELLHEAD PRESSURE, FLOW, DIVERTER INJECTION, AND MULTI-STAGE STIMULATION

5.4.1 STEP-RATE TEST

The stimulation started with a step-rate injection test to assess the pre-stimulation parameters and determine hydroshearing initiation pressure (Figure 22). Injectivity calculated during the step-rate test averaged 0.012 L/s/bar (0.013 gpm/psi), which was equivalent to the injectivity and flow testing values measured after drilling in 2008. The highest well head pressure (WHP) obtained during the injectivity test on 9/24/14 was 140 bars (2,030 psi) with 2 L/s (25 gpm) injected down hole. Shortly after this, the pumps were shut down to repair leaks in the lubricator. After the leaks were repaired, the pumps were started again and another step rate injectivity was conducted before increasing the WHP to 190 bars (2,765 psi) and 6 L/s (90 gpm) injection rate for the Round 1 of stimulation.

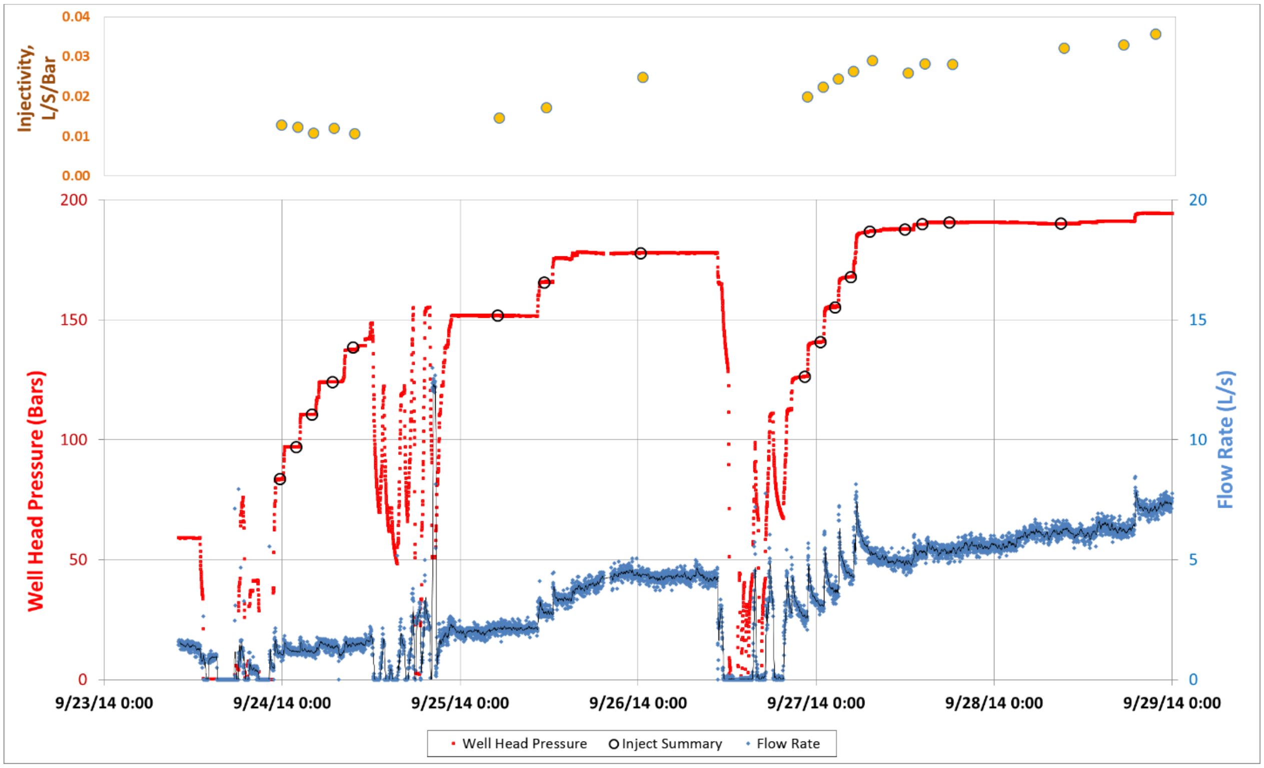

Figure 22. Wellhead pressure (red), injection flow rate (blue) and calculated injectivity (orange) observed during the initial step-rate test carried out in Phase 2.2.

5.4.2 STIMULATION ROUND 1

Stimulation Round 1 began after the step-rate test and calibration of the stimulation pumping system on September 28. Injectivity improved when injection pressure exceeded 19 MPa (189 bar; 2,755 psi) and the corresponding flow rate reached 6.5 L/s (100 gpm). The improved injectivity rate remained stable with moderate pressure injection until October 1. Until October 1, flow was increasing while maintaining constant injecting pressures. Between October 1 and October 13, WHP mostly remained around 19.3 MPa (193 bar; 2,800 psi) with few brief periods of lower pressure due to pump trip or surface equipment repairs. On October 7, the WHP was reduced to test the DIVA with a low temperature TZIM material. On October 13 and 14, the WHP was reduced briefly for two TZIM injections. By October 15, the pumps were shut off and a 12 hour pressure fall off test was conducted while monitoring surface and downhole pressure fall-off. The improvement in injectivity during stimulation Round 1 was approximately 2 L/s/MPa (0.21 gpm/psi). Round 1 data was used to assess the improvement achieved to date and plan out stimulation Round 2. Figure 23 chronicles the well head pressure, flow rate and injectivity during the step-rate test prior to stimulation.

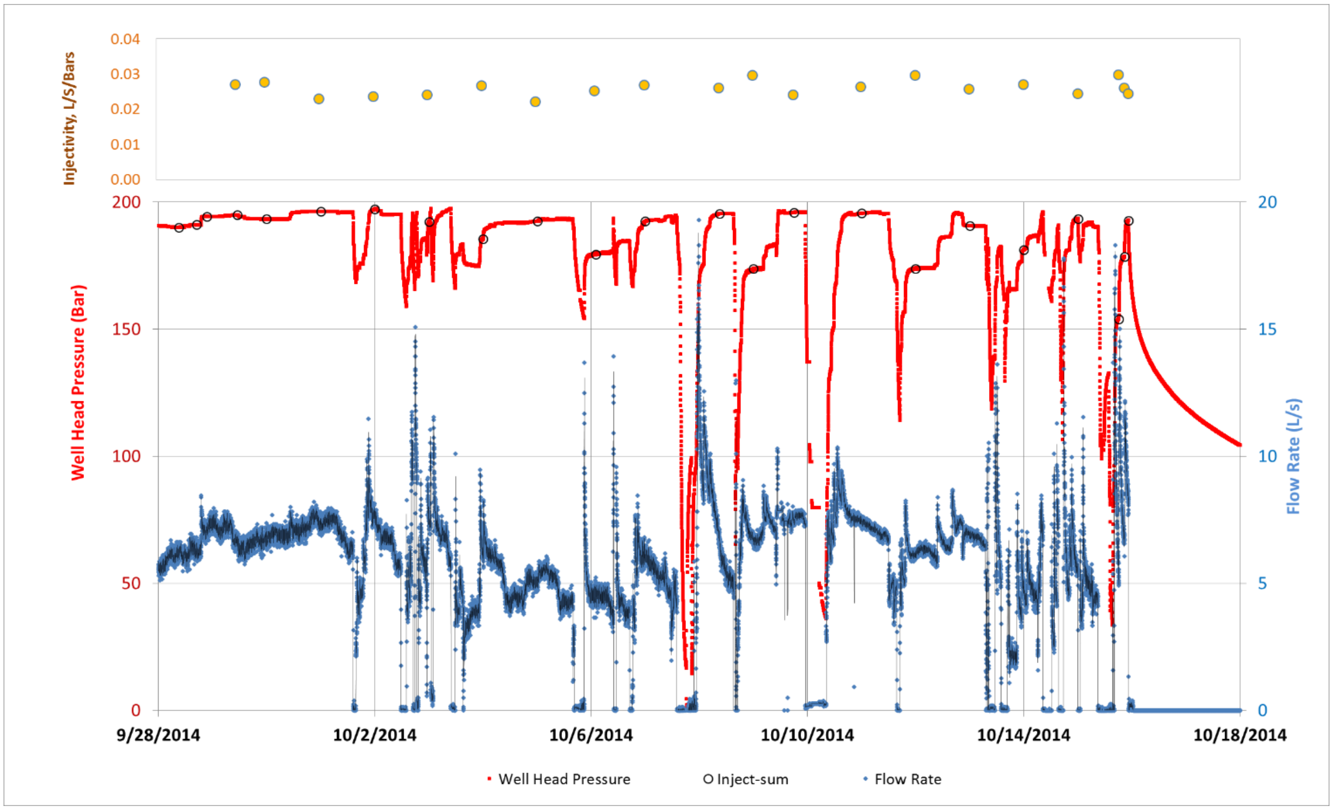

Figure 23. Wellhead pressure (red), injection flow rate (blue) and calculated injectivity (orange) during beginning of stimulation Round 1.

5.4.3 STIMULATION ROUND 2: TZIM TREATMENT

After the three weeks of stimulation in Round 1 the injectivity of NWG 55-29 increased by ~3-4; however, the well's permeability was still considered too low to become an economic injector in an EGS well pair. Therefore between stimulation rounds, AltaRock investigated methods of further improving the well injectivity. Two methods to augment hydraulic stimulation were initially proposed; first perforation shots and chemical leaching of silicate minerals using a strongly basic NaOH solution. After further research and modeling, the chemical stimulation was dropped from the program.

Three depths were chosen for perforation shots. The criteria for choosing the depths for perforations were 1) a relatively brittle rock type, 2) in a portion of the hole that already has fractures and breakouts, 3) in a portion of the hole that already shows evidence of fluid exit, and 4) at a depth that could be cooled to 200 °C (400 °F) at a flow rate of 40 gpm. A November 10 memo to the DOE technical monitoring team (Appendix C) describes the planning and decision process for the perforation shots. Section 5.7 reviews the results of the perforation shot.

Round 2 of the stimulation started on November 12 with injection to cool the wellbore in preparation for the perforation shots. The WHP during the inject-to-cool operation was kept at approximately 148 bar (2,150 psi) due to surface valve pressure constraints (Figure 25). On November 13, Cogco performed two perforation shots, the first one at 2,562-2,565 m (8,402-8,412 ft) depth and the second one from 2,508-2,512 m (8,229-8,239 ft) depth. After perforation, the equipment and wellhead valves were rigged down and re-injection restarted on November 14. During the second round of the stimulation, Pump 2 discharge pressure was recorded instead of WHP, as the WHP instrumentation malfunctioned. Stimulation Pump 2 discharge pressure was kept at approximately 185 bar (2,680 psi) from November 14 to November 18.

On November 18, TZIM treatment occurred. Each pill of diverter consisted of 90 lbs (41 kg) of granular AltaVert 251 mixed in 150 gallons. A total of 5 pills were injected over 74 minutes (Table 4). Pumping pressures were reduced to approximately 140 bar (2,000 psi) in order to boost the TZIM downhole with the DIVA.

On November 19, fibrous TZIM treatment were injected. Each pill of fibrous diverter consisted of 10 lbs (4.5 kg) of AltaVert 251 mixed in 150 gallons. A total of 5 pills were injected over 128 minutes (Table 4). After the fiber TZIM was injected, the rate of water injection decreased, while WHP remained relatively constant at 190 bar (2,750 psi). The decrease in injectivity as a result of TZIM injection indicated that the fracture zones enhanced in Round 1 had been blocked (Figure 25). Prior to both TZIM treatments, tracers were injected to characterize changes in flow paths due to TZIM. See Section 5.9 on tracer injection details and results.

Table 4: Shows the time and pressure at which each pill of TZIM was injected.

	11/18/2014		11/19/2014	
Pill	Time	Pressure (psi)	Time	Pressure (psi)
1	11:24	1923	11:07	2010
2	11:45	2000	12:07	2150
3	12:02	2118	12:25	2150
4	12:20	2198	12:55	2216
5	12:38	2212	13:15	2257

Note: Each pill is 150 gallons in volume

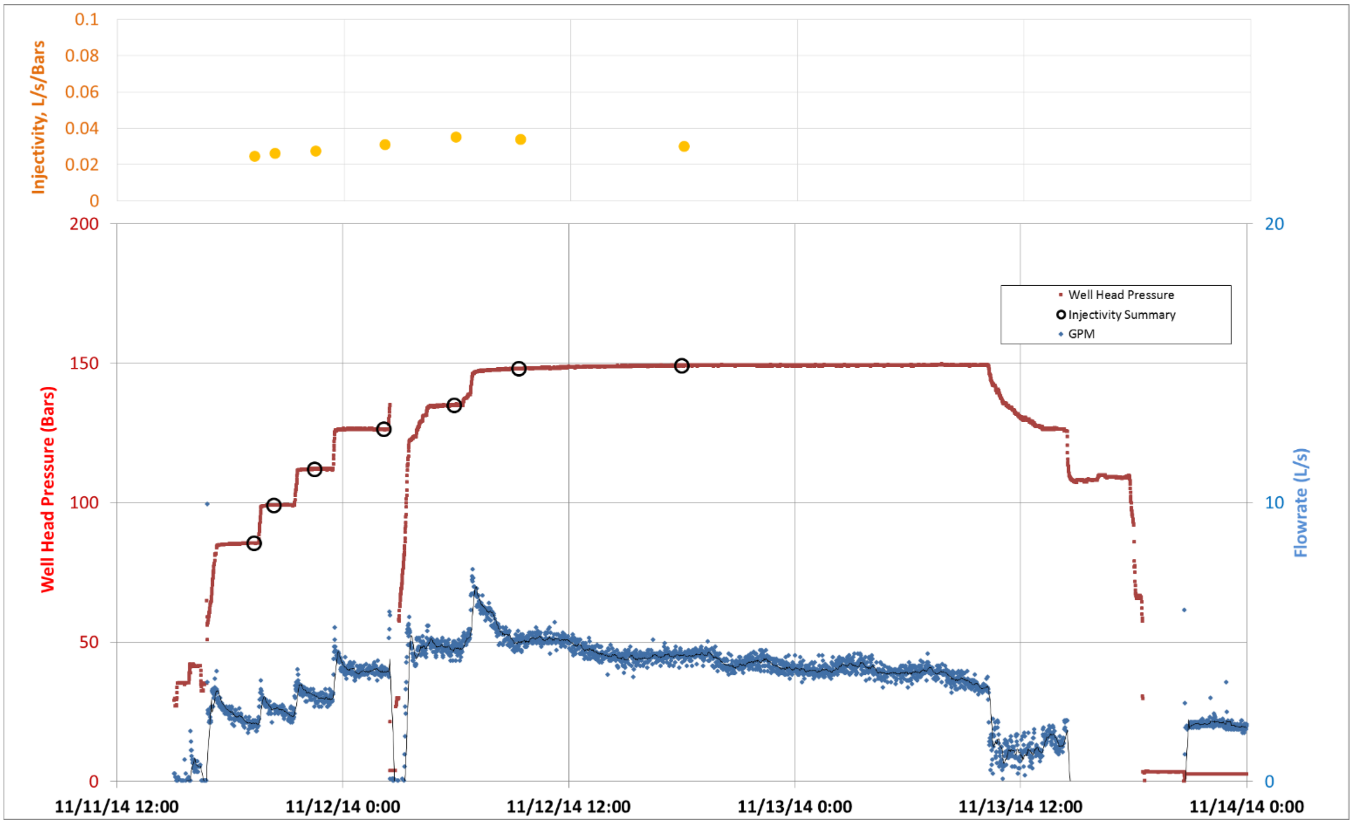

Figure 24. Wellhead pressure (red), injection rate (blue) and calculated injectivity (orange) during stimulation Round 2.

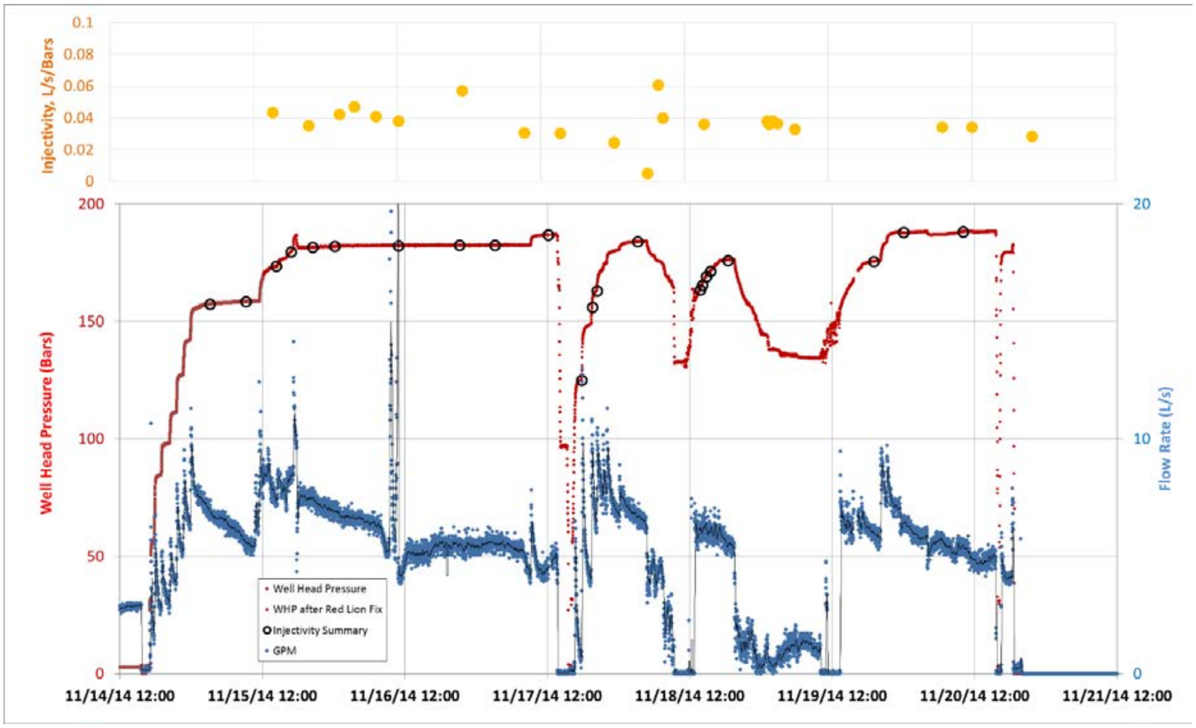

Figure 25. Wellhead pressure (red), injection rate (blue) and calculated injectivity (orange) during stimulation Round 2.

5.5 PTS SURVEYS

5.5.1 Round 1

The DTS cable was retrieved from NWG 55-29 on 10/15/14. During the DTS removal process, a cut in the tubing was discovered at 258 m (847 ft) below ground surface. After retrieving the DTS cable, a memory pressure, temperature, and spinner PTS tool was used to log to 2,988 m (9,800 ft) while the well was put on flow back (Figure 26). After the first survey run, the well was then put on injection and the PTS tool was again lowered to 2,988 m (9,800 ft) in order to observe permeable zones (Figure 27). At the end of the injection survey, the PTS tool was pulled up to 1,220 m (4,000 ft) and used to monitor downhole pressure while a step-rate injectivity test was performed. Then the well was shut-in and the PTS tool sat at 1,220 m (4,000 ft) for 11 hours while monitoring downhole pressure fall-off.

Both flowing and injecting surveys conducted on October 15 showed the most permeable zone during round 1 stimulation was around 2895 m (9500 ft). The flowing survey also showed several zones below the blank liner to exhibit permeability, such as 2500-2512 m (8200-8240 ft), 2558-2565 m (8393-8415 ft) and 2680-2693 m (8790-8835 ft).

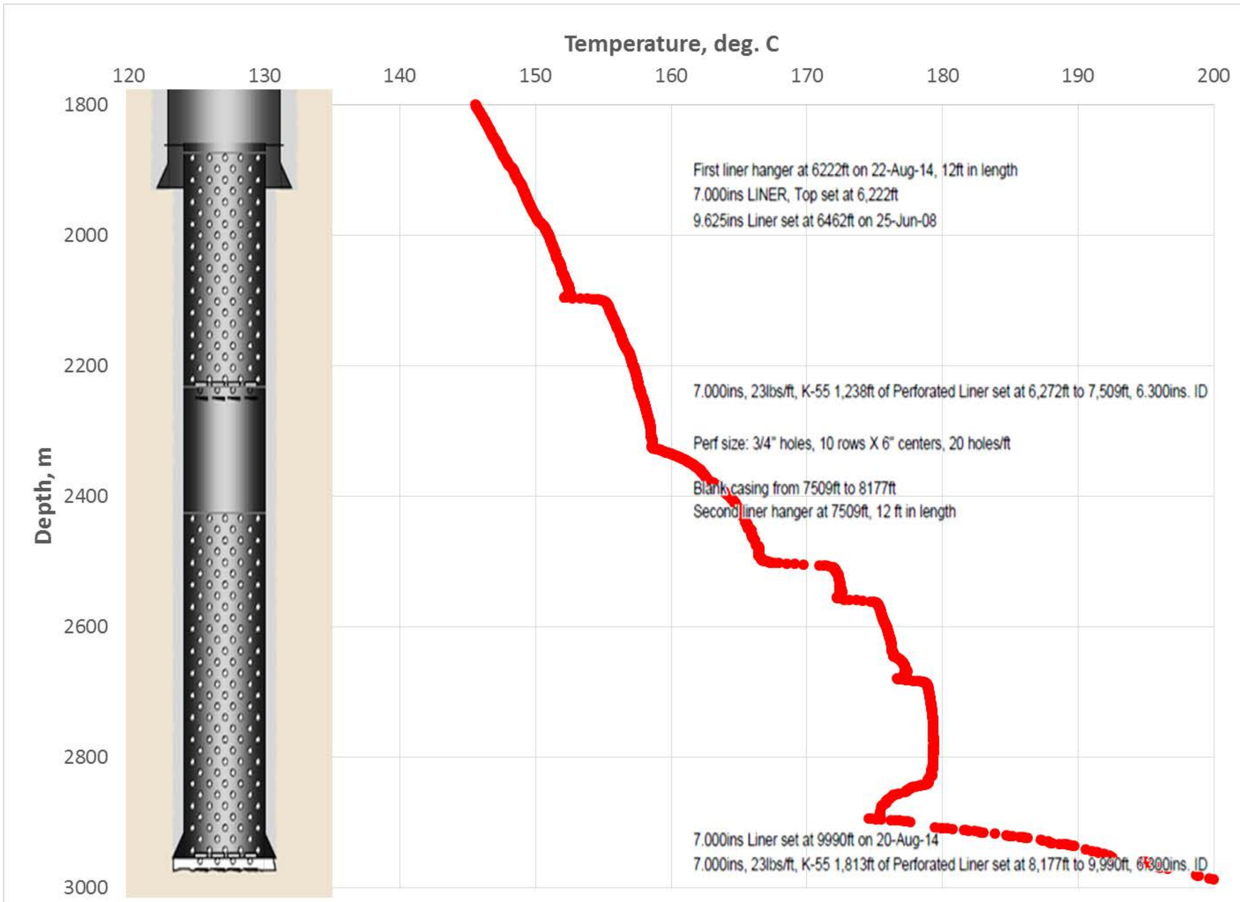

Figure 26. Flowing temperature survey on 10/15/2014.

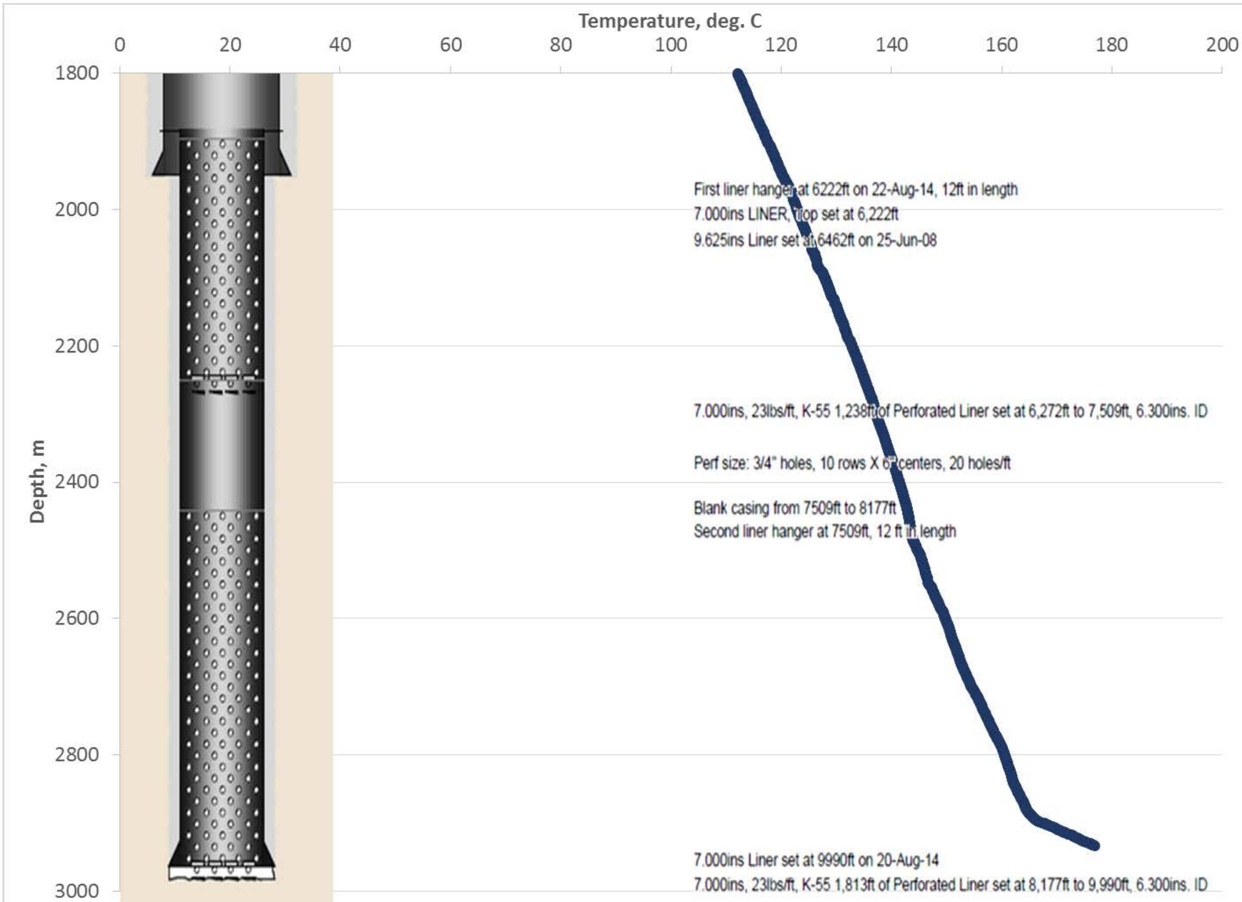

Figure 27. Injecting temperature survey on 10/15/2014.

5.5.2 Round 2 PTS Logging and TZIM treatment

To complete Round 2 stimulation with downhole temperature monitoring, a surface readout PTS tool provided by Well Analysis Corp was deployed to monitor diversion in real time. Four PTS surveys were completed from 11/17/14-11/20/14.

The first injecting temperature survey was taken on November 17, prior to any TZIM injection in this round. This temperature profile showed pronounced inflections in the temperature gradient at approximately 2515 m (8250 ft) and 2927 m (9600ft), indicating fluid exiting the well bore at those two depths (Figure 28). The remaining fluid exited below the depth of the logging run at 2,910 m (9,950 ft), as indicated by the relatively cool 175 °C (348 °F) temperature at the bottom of the log compared to the static temperature of 620 °F.

After the injection of the granular TZIM, a temperature survey was run on November 18. This survey showed a similar profile to the November 17 log, with two zones at approximately 2,515 m (8250 ft) and 2,926 m (9,600 ft) taking fluid and the remaining fluid exiting below 3,032 m (9,950 ft). This indicates that the granular TZIM did not appear to cause significant diversion at the well bore.

After the injection of the fibrous TZIM, two more PTS surveys were performed. The November 19 survey showed that the 2,926 m (9,600 ft) zone was taking less fluid (a less pronounced temperature inflection), and that an interval between 9720-9800 ft began to take fluid as indicated by a 40 °F increase in temperature across this depth interval. In addition, the temperature at the bottom of the log at 3,032 m (9,950 ft) increased to 210 °C (411 °F) while under continuous injection, indicating that the bottom 15 m

(50 ft) of the hole was no longer being significantly cooled, due to plugging of exit zones in that interval by fibrous TZIM.

A final survey was conducted on November 20 to confirm the observed downhole diversion. The November 20 temperature survey continued to show a reduced flow into the 2,926 m (9,600 ft) zone (Figure 29). The cooling observed in a 24 m (80 ft) interval 12 hours before became more pronounced and localized to 2,976 m (9,766 ft) in the November 20 survey, showing cooling at this depth to 150 °C (302 °F) lower than the previous three surveys. In addition, the temperature at 3,032 m (9,950 ft) reached 226 °C (440 °F), an temperature increase of almost 37 °C (100 °F) when compared to the pre-TZIM injecting survey. This indicates that little or no fluid was exiting out of the bottom section of the wellbore and that the bottom of the hole was rapidly heating back up to the native, static temperature of 326 °C (620 °F) (Figure 29).

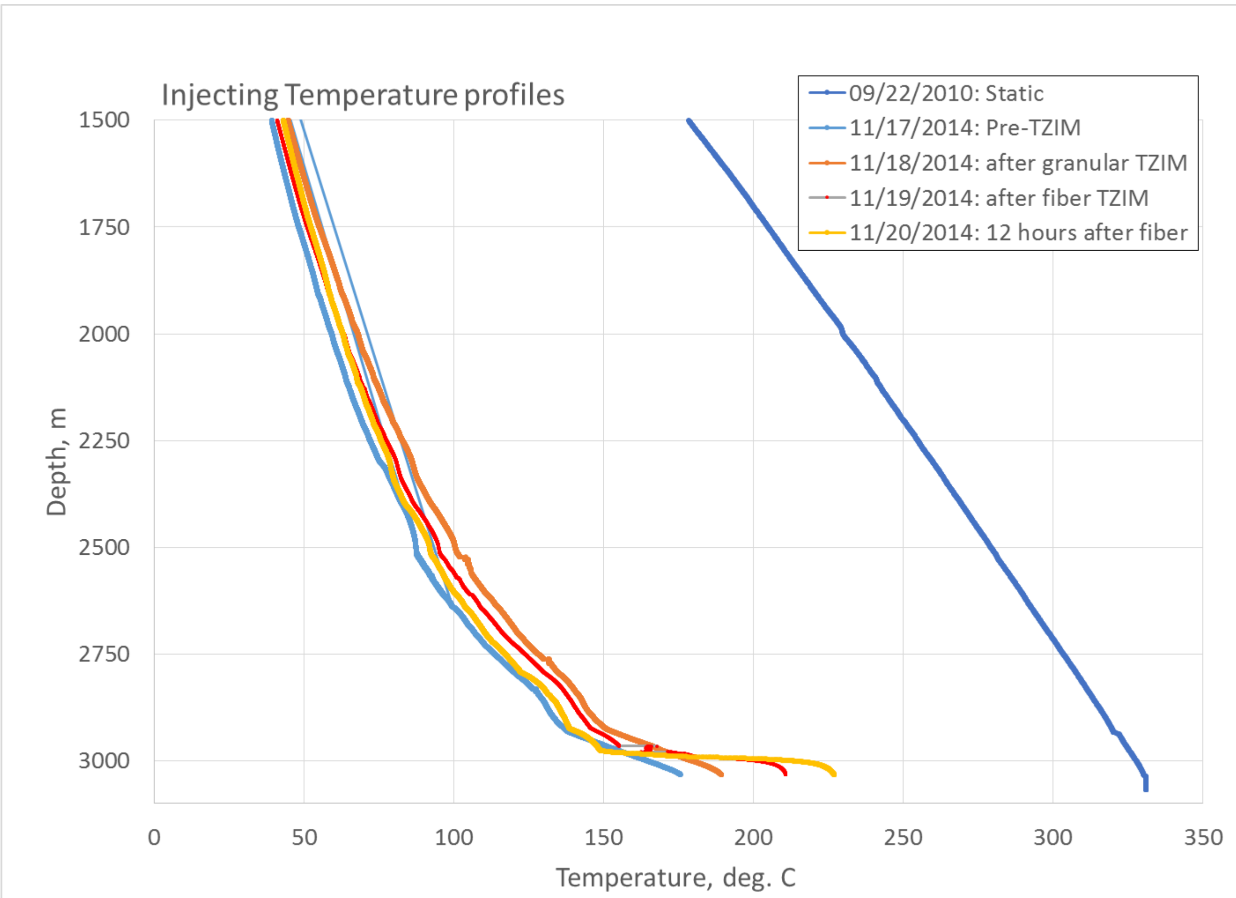

Figure 28. Injecting temperature profiles from November 17-20 relative to static temperature measured in 2010.

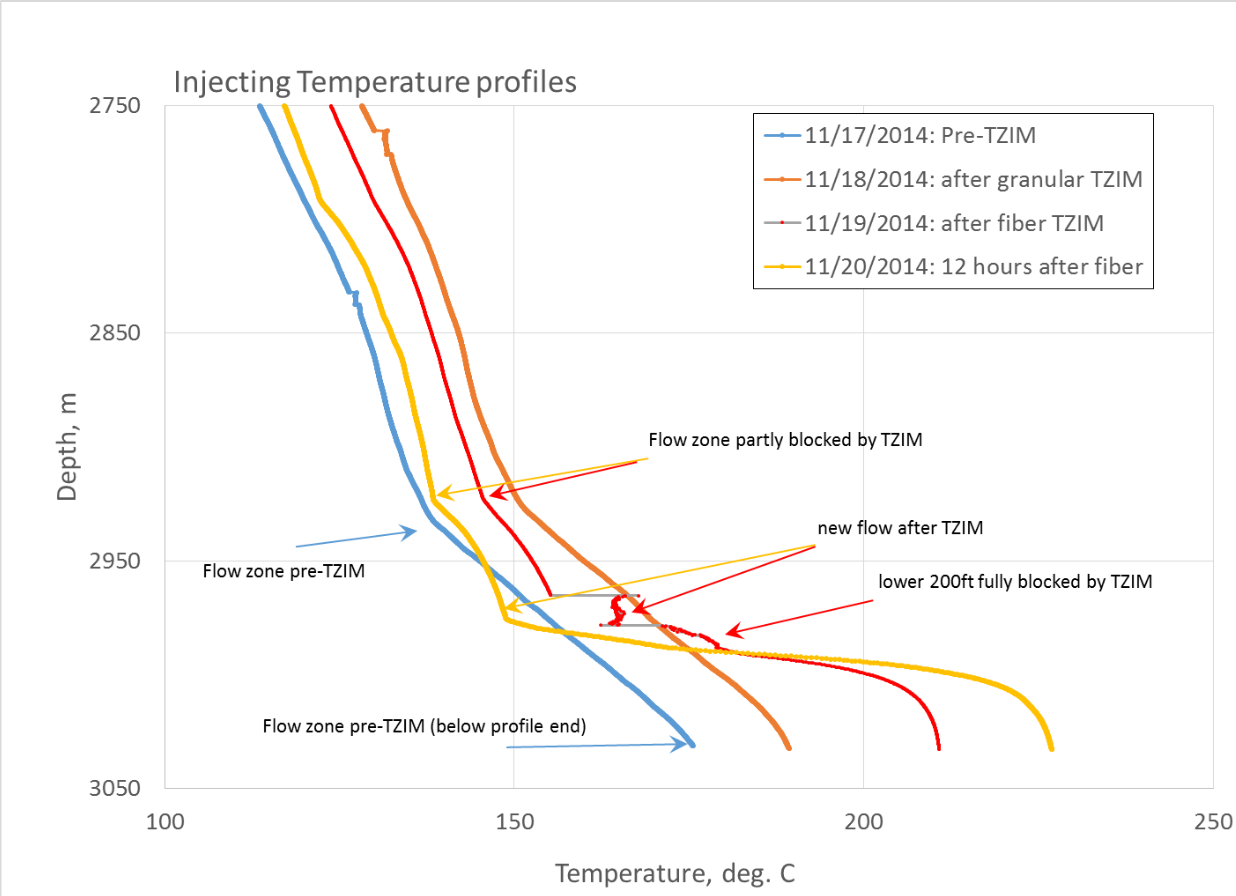

Figure 29. Detail of wellbore lower section during injecting surveys carried out in 2014.

Spinner results were also evaluated in order to assess downhole flow profiles. The spinner tool is not able to calculate quantitative flow results, but comparing the spinner profiles at various depth did give indication of flow and validated the temperature profile behaviors.

Figure 30 displays the spinner results in the interval from 2,440 m (8,005 ft) to 2,740 m (8,989 ft) compared to its corresponding temperature surveys. The temperature survey shows a clear kink at 2,515 m (8,250 ft) on November 17, indicating a permeable zone taking fluid. The temperature survey on the following two days show a reduced slope change above and below 2,515 m (8,250 ft), which could indicate a reduction in the zone taking fluid after TZIM injection. The three spinner responses, however did not show any strong evidence of fluid exiting and blocking off. The noise observed on the spinner log could be related to low fluid speed or debris or TZIM clogging the tool.

The spinner results (Figure 31) in the interval from 2,740 m (8990 ft) to TD showed on 11/19/14, post injection of the fibrous TZIM, spinner RPM approaching zero below 2950 m (9670 ft). Indicating low or no flow below that depth, which correlated with the increase in temperature shown in the adjacent temperature profile. This spinner response was repeatable, meaning the tool was moved up and down the interval in order to shake lose any debris that might have clogged the spinner tool. This behavior matches the temperature survey profiles and is a good indication that TZIM altered the flow profile downhole in 55-29.

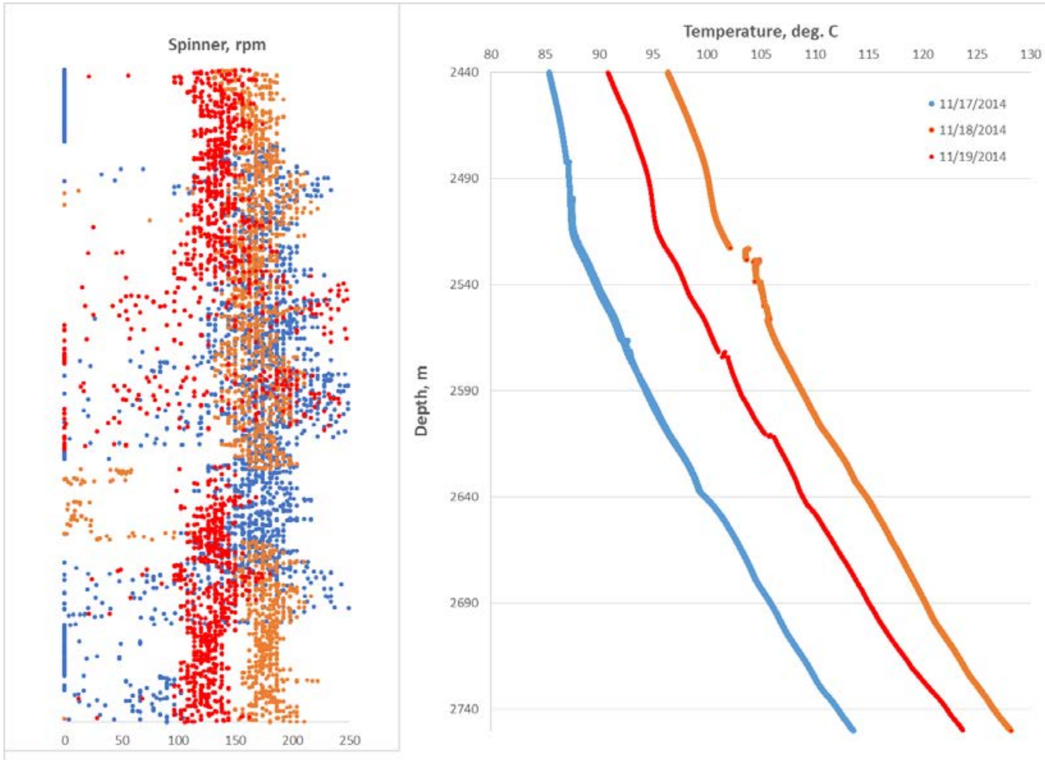

Figure 30. Spinner and temperature log comparison from 2,440 m (8,005 ft) to 2,740 m (8,989 ft). Note change in flow at approximately 2,515 m (8,251 ft).

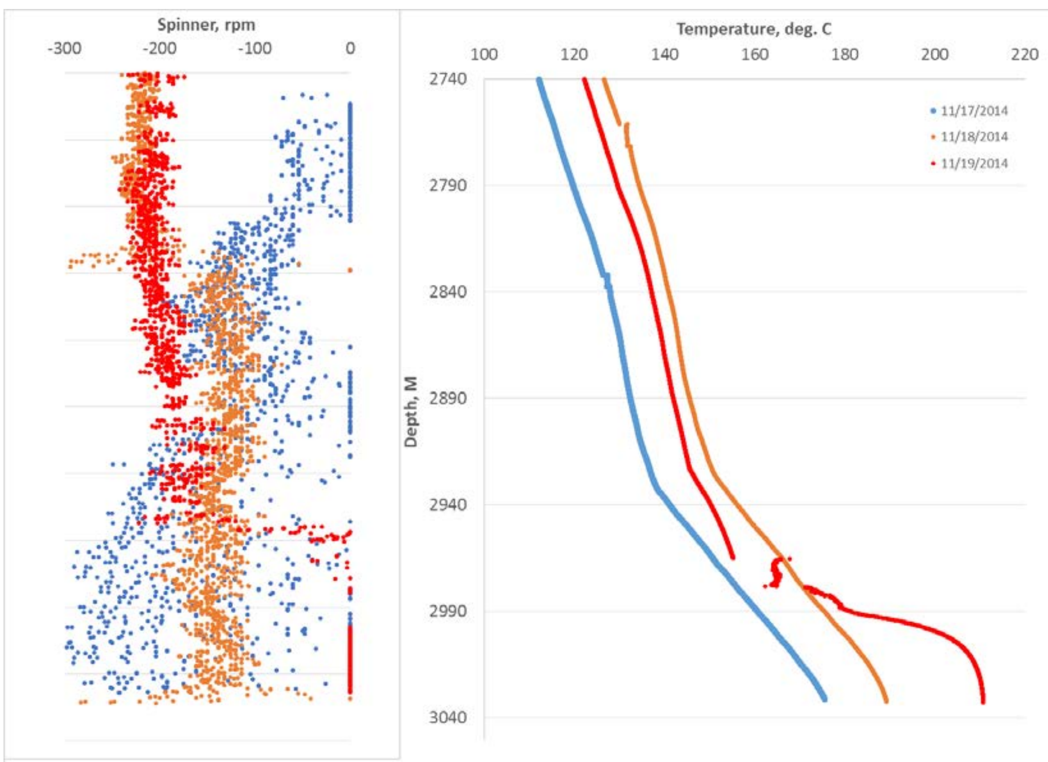

Figure 31. Spinner and temperature survey comparison from 2,740-3,040 m (8,990-9,974ft).

5.6 MICRO-SEISMICITY

A microseismic array (MSA) was installed in August 2012 as part of Phase 2.1. Two-Hz 3 component geophones were installed at seven surface sites and eight borehole sites (Figure 32). The 15 stations stream continuous data via cell phone modem to a server running acquisition software at AltaRock's office in Seattle where the continuous data are saved and archived. Triggered waveforms were sent to Lawrence Berkeley National Lab (LBNL) for locating and publishing to their public website (LBNL, 2015). Microseismic events were also analyzed by the Pacific Northwest Seismic Network (PNSN, 2015) and Foulger Consulting, who focused on deriving moment tensor solutions (Julian and Foulger, 2004).

The regional seismic network at Newberry Volcano has improved greatly in the past two years. In 2009, the only station was NCO, a single-component, short-period seismometer on the east flank and only four microearthquakes (M 1.3-2.2) were detected on Newberry in the prior 25 years (PNSN, 2015). In 2011, the USGS installed six three-component broadband seismometers and one three-component short-period sensor (PNSN, 2015). Four of the borehole stations in the AltaRock Newberry MSA (NN32, NN19, NN17, and NN21) were also added to the PNSN network. The seismic coverage on Newberry Volcano is now comprehensive, with events smaller than M 0.0 being locatable. During the 2012 stimulation, about 175 events were located in the stimulation zone with magnitude between M 0.0 and M 2.3 (Cladouhos et al., 2013a, 2013b). Between 3/1/2013 and 9/20/2014 there were about 60 natural seismic events located on the Newberry edifice (PNSN, 2015). This apparent increase in Newberry Volcano seismicity since 2012 is due to a much improved seismic monitoring network with better detection abilities, and not EGS activities.

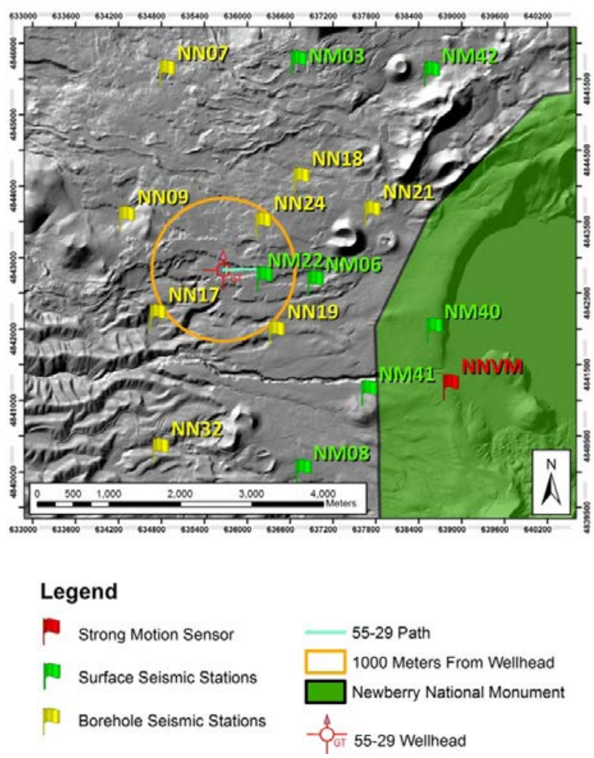

Figure 32: MSA monitoring locations, EGS well 55-29, and Newberry National Volcanic Monument (green shading).

5.6.1 WELLHEAD PRESSURE AND SEISMIC EVIDENCE OF HYDROSHEARING

During the two rounds of stimulation, the MSA located 400 events, ranging in magnitude from M 0 to M 2.26. The first micro-seismic event occurred after two and a half days of injection when the WHP exceeded

180 bar (2,600 psi). After two more days of injection the second event occurred when the WHP exceeded 193 bar (2,800 psi) and continued at higher rates of over 30 events per day from September 30 – October 2, with a peak of 42 events/day on October 1 (Figure 33). After five days of increasing seismicity and improving injectivity, the seismicity rate dropped by more than 50% by October 6.

At the beginning of Round 2, while injecting to cool for 44 hours in preparation for the perforation shots below 155 bar (2,250 psi) no microseismic events were detected. After the perforation shots, injection continued for 17 hours and the first event of the 2nd round was created at WHP of 162 bar (2,355 psi), and seven more events were detected over the next six hours while the WHP was below 180 bar (2,600 psi). After increasing the WHP to 187 bar (2,700 psi) there was a 17.5 hour seismic gap followed by a six event swarm over 23 minutes. The rate of seismicity that day (November 16) reached 19 events/day, with a peak rate of 22 events/day at a WHP of 193 bar (2,800 psi) on the final day of stimulation (November 20). Thus, we can conclude that the hydroshearing pressure is around 180 bar (2,600 psi). This is significantly higher than determined in 2012, even before leaks developed in the casing.

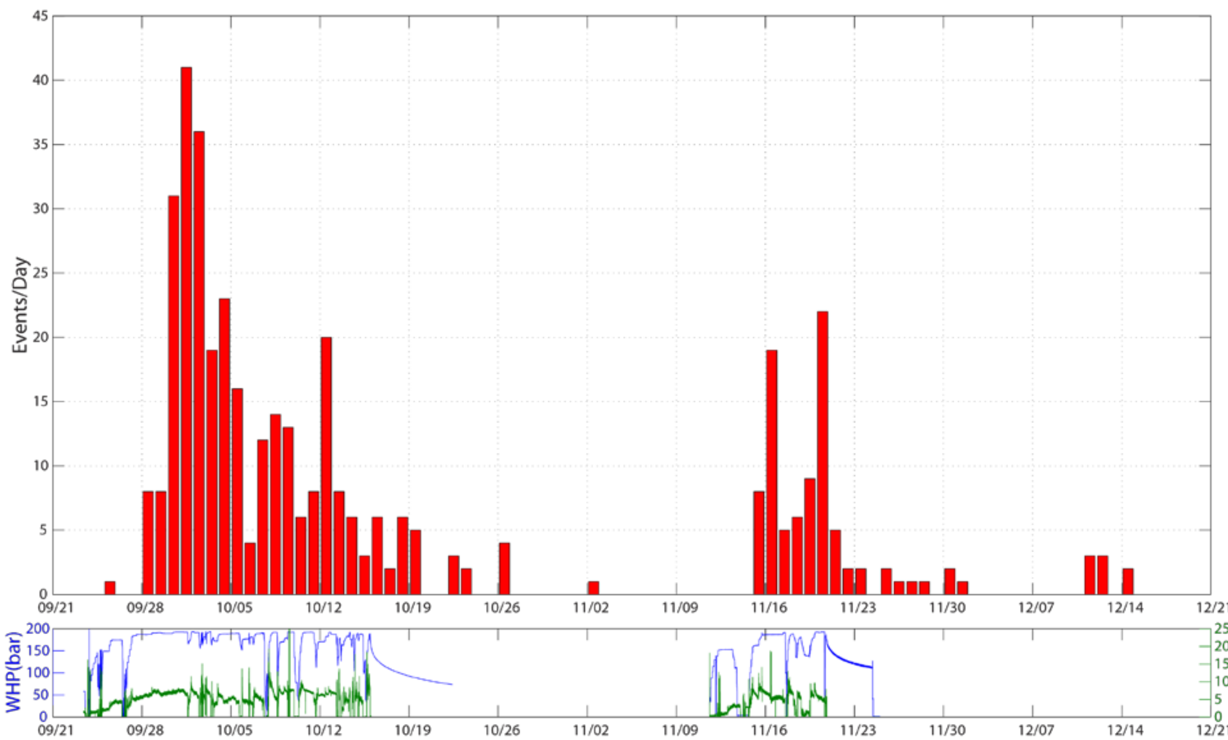

Figure 33: Daily rate of seismicity detected during stimulation with WHP and flowrate plotted below.

5.6.2 LOCATIONS

Triggered waveforms were analyzed by multiple means. First, the seismic acquisition software automatically identified events, generating preliminary P- and S-wave picks and locations. The software sent an alert email to project scientists and seismologists including a map of the preliminary location. In addition, waveforms were sent to LBNL and Foulger Consulting. The P&S picks for all triggered events were reviewed by a seismologist within a day, resulting in location catalog of 400 hand-picked events. The locations of the 400 microseismic events are diffuse likely due to location errors and plot up to 500 m (1,640 ft) from the injection well (Figure 34).

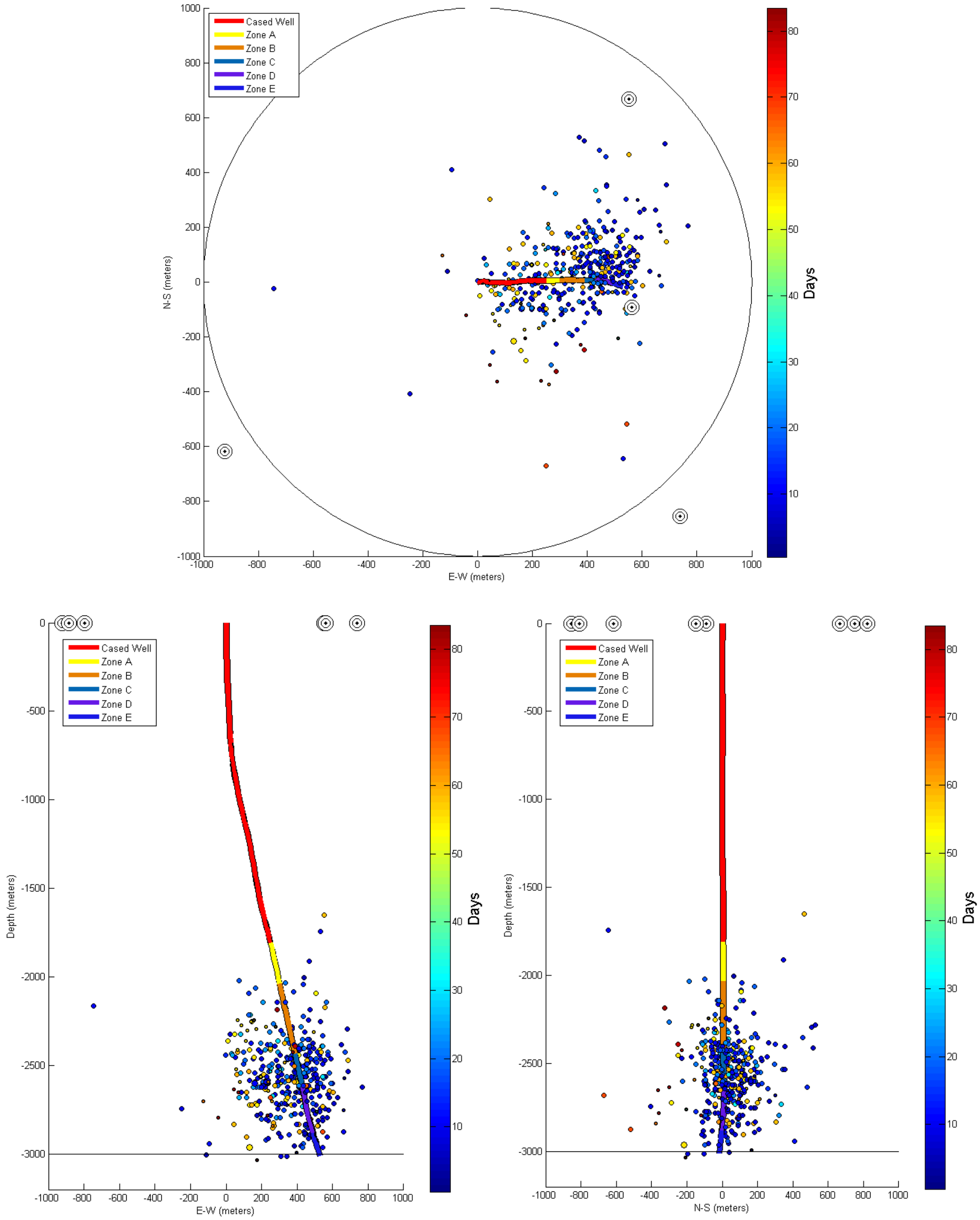

Figure 34: Location map (top) and cross sections (bottom left looking north; bottom right looking west) of all located events from initial seismic catalog.

5.6.2.1 STIMULATION ROUND 1

The majority of all the seismic events (266) detected during both rounds occurred before the first TZIM injection on October 13 (Figure 35Figure 35). These events also occupy the total seismic volume of all the events with almost all subsequent seismicity being located within 500 meters of the wellbore. Eleven additional seismic events were created during the TZIM treatments before the well was shut in (Figure 36). Twenty-two events were created after the well was shut in on 10/15 (Figure 37), and seven more were created after flow back on 10/23 (Figure 38). A total of 306 events were created during the first round of stimulation that initially reached mostly to the west and to the northeast of the wellbore. The events created during the TZIM treatments reached more to the south than any other stage during Round 1. Events detected in the stages after the first one (Figure 35) were located more shallow than the initial events of the stimulation.

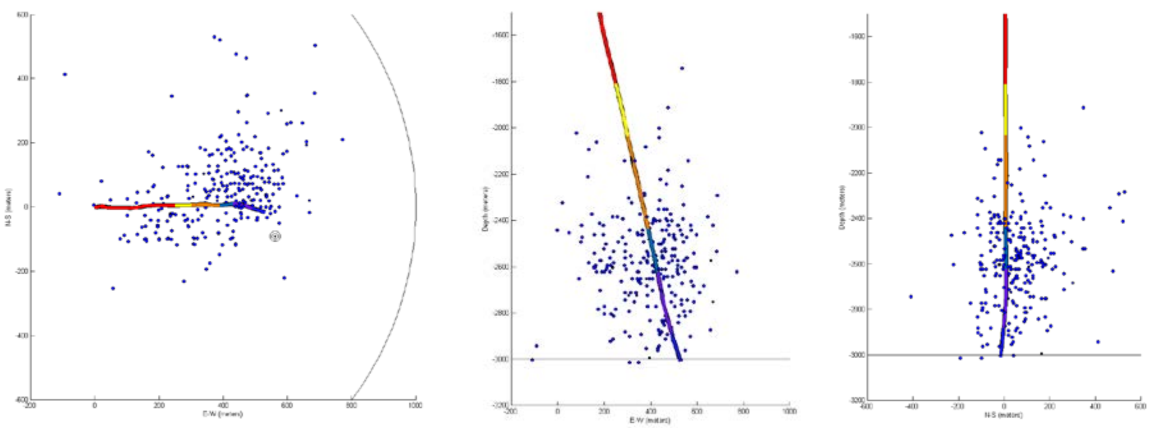

Figure 35: Microseismicity detected before 1st TZIM injection on 10/13

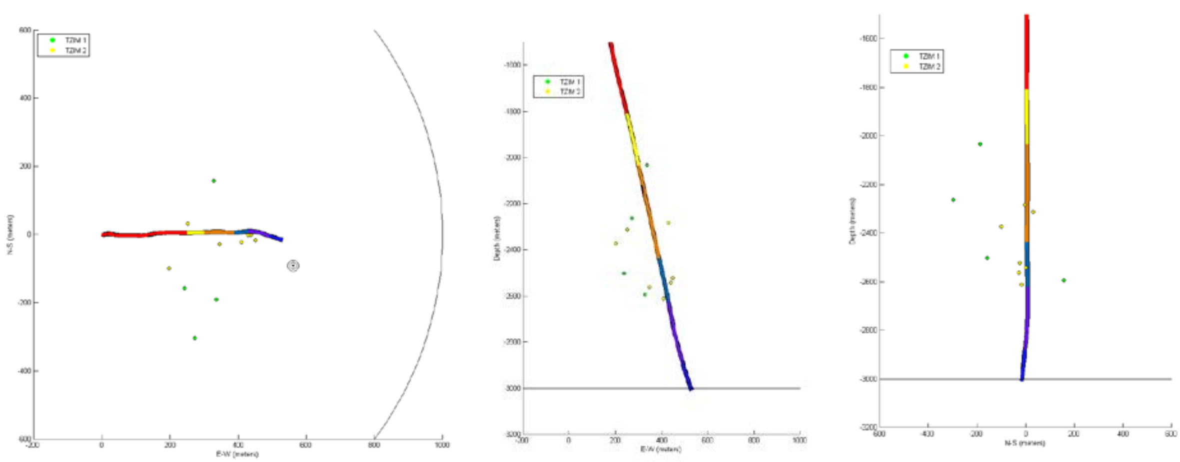

Figure 36: Microseismicity detected during 1st and 2nd TZIM treatments before shut-in.

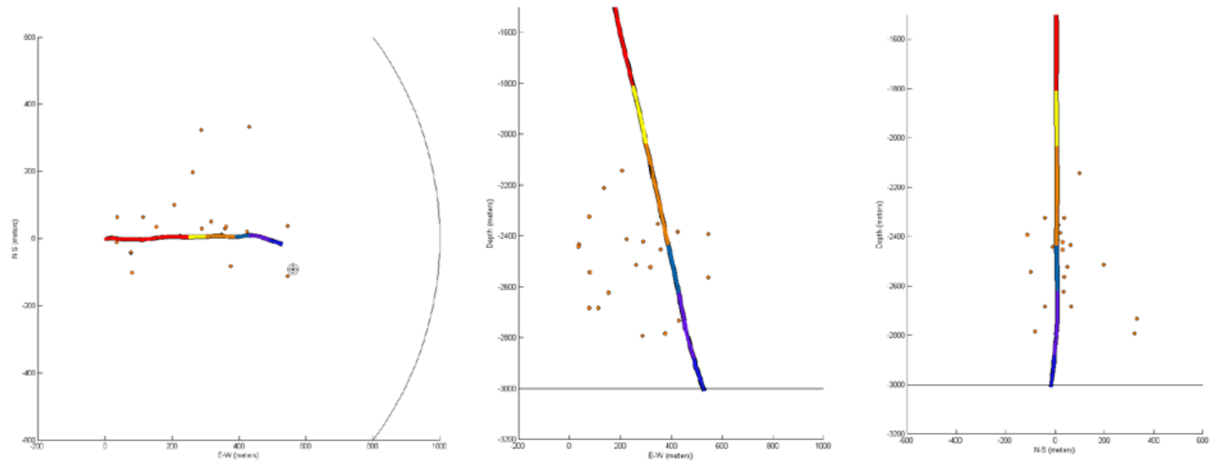

Figure 37: Microseismicity detected after shut-in on 10/15.

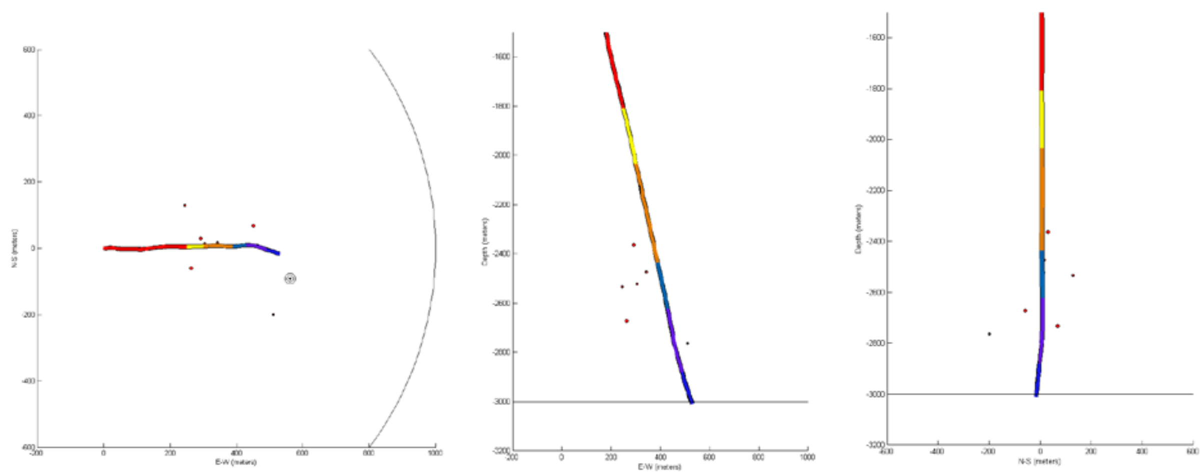

Figure 38: Microseismicity detected after flow back on 10/23.

5.6.2.2 STIMULATION ROUND 2

At the start of Round 2, two perforation shots were performed in order to provide additional fracture initiation points in the well bore wall. In addition it was hoped that the perforation shots would be detected in the seismic network and used to provide a better seismic velocity model. Unfortunately, while the shots were detected, the signals were not sharp enough to significantly improve the velocity model. See Appendix C and Section 5.7 for further discussion of the perforation shots.

The eight first events of round 2 are shown in Figure 39 and they form a WSW striking sub-vertical plane that intersects the wellbore. The events following the 17.5 hour gap are shown in Figure 40. The six event swarm that happened on the morning of November 16 are marked with stars and they are part of a NW striking plane that is approximately 100 m (330 ft) from the wellbore and dips steeply to the SW. The events during the TZIM treatment are shown in Figure 41. There were far more events detected during this round of TZIM treatments, and there was a shift from where they were being created in the south to the north of the wellbore. The events detected after shut-in (Figure 42) were all within 200 m (656 ft) to the north and south of the wellbore but reached 400 m (1,312 ft) to the west, and the events after flow back (Figure 43) reached over 500 m (1,640 ft) to the west and to the south.

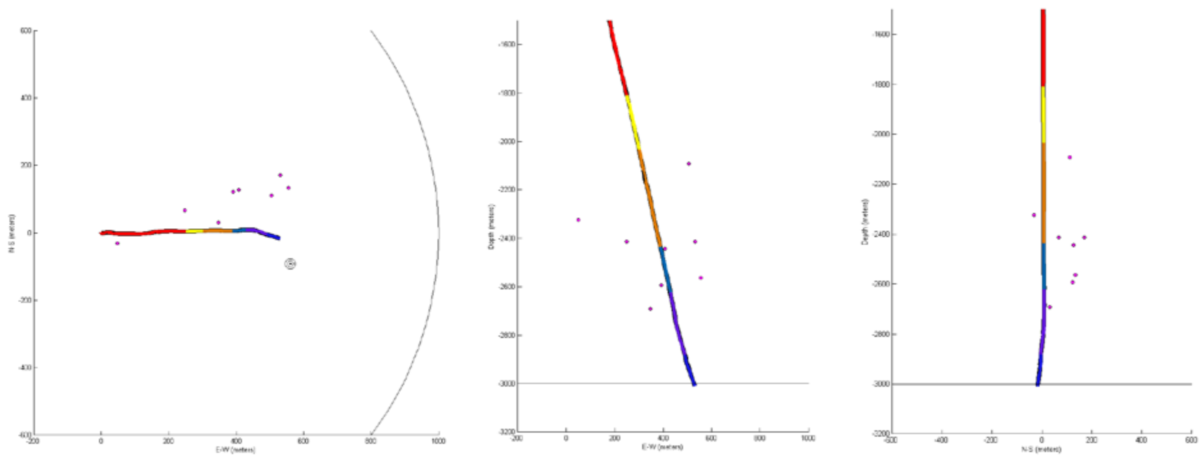

Figure 39: First eight events of round two detected while injecting at lower pressure (>180 bar).

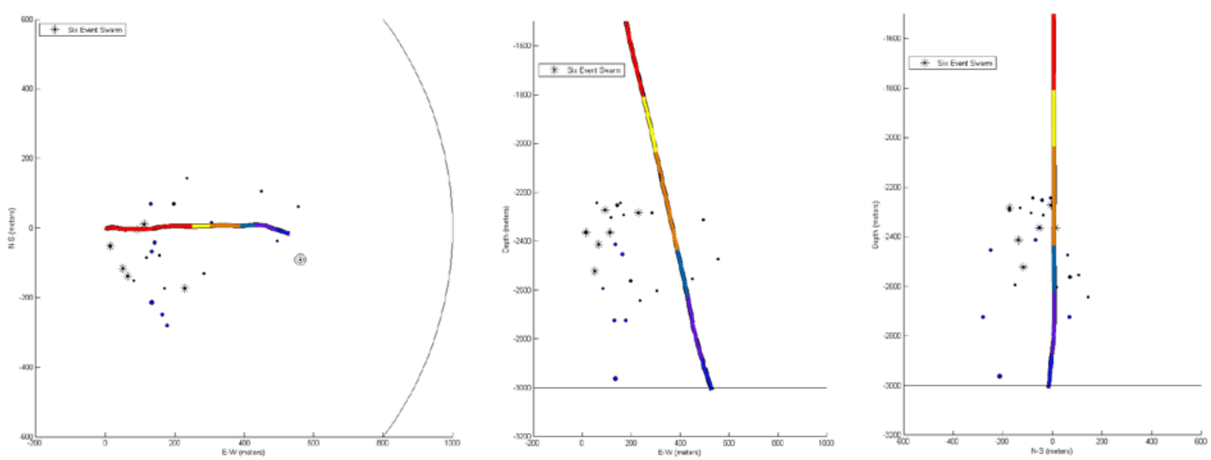

Figure 40: Microseismicity created following 17.5 hour gap and before diverter injection and 6-event swarm marked with stars.

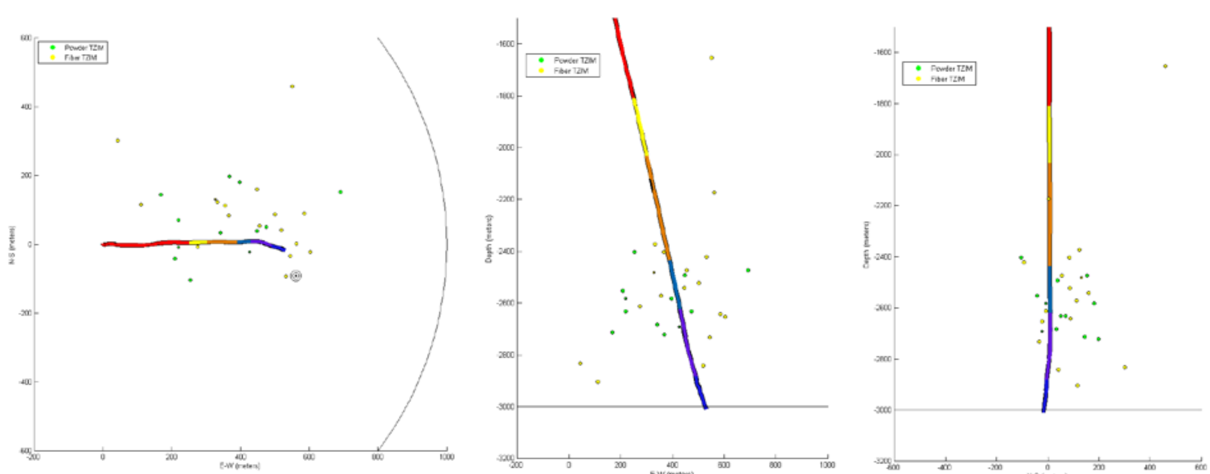

Figure 41: Microseismicity created during TZIM treatments.

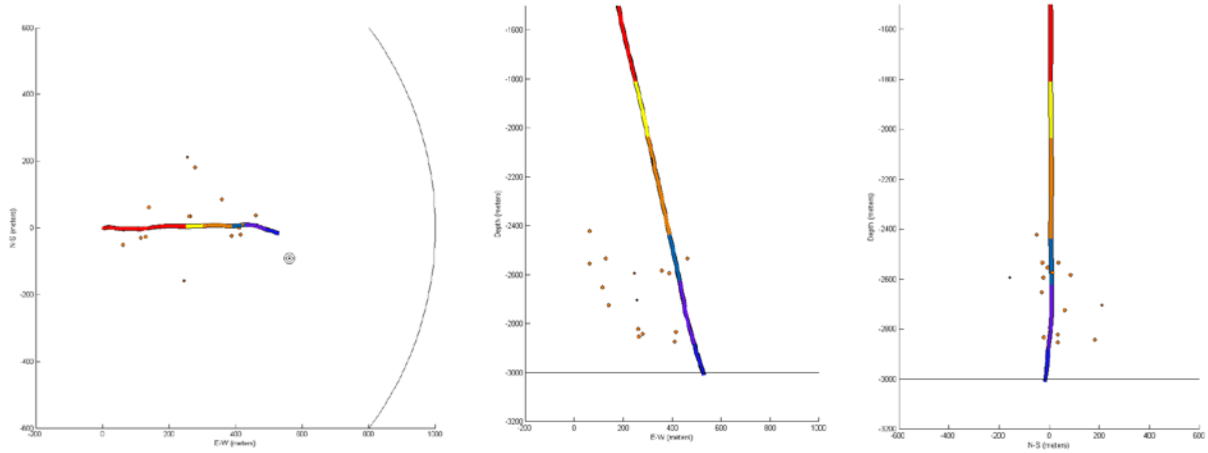

Figure 42: Microseismicity detected after shut-in.

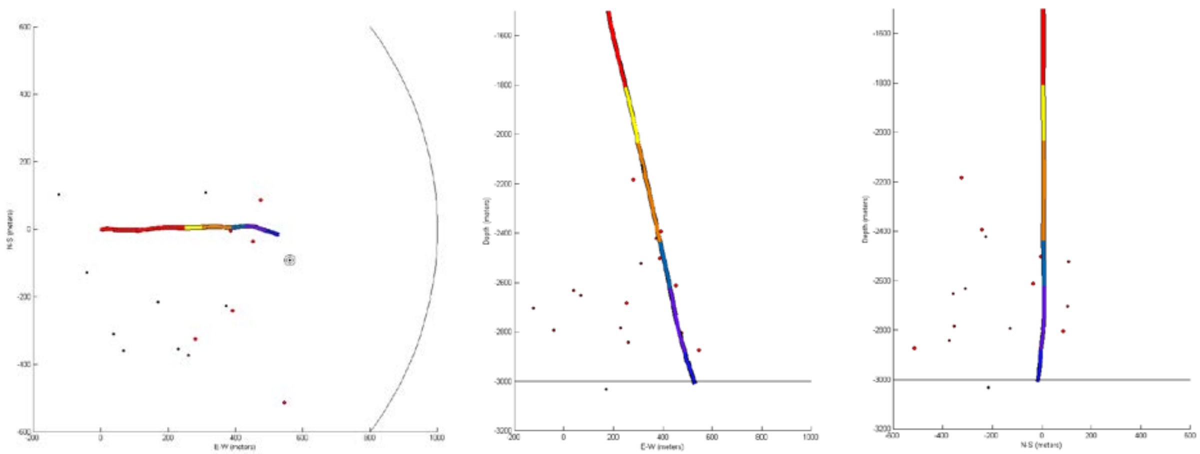

Figure 43: Microseismicity detected after flow back.

5.6.3 INDUCED SEISMICITY MONITORING

As required by the ISMP (AltaRock, 2011), we tracked b-value and cumulative seismic moment to quantify seismic risk. The most reliable moment magnitudes for the induced microseismic events were determined by LBNL. The 350 LBNL magnitudes were used to determine the Gutenberg-Richter Law b-value of 1.0 (Figure 44). The only two events above M 2.0 during the stimulation were an M 2.1 on October 4 and M 2.3 on November 17. There were 23 events between M 1.0 and 2.0. The rollover of the size distribution below M 0.0 (Figure 44) indicates that the seismic system's lower sensitivity threshold was near M 0.0.

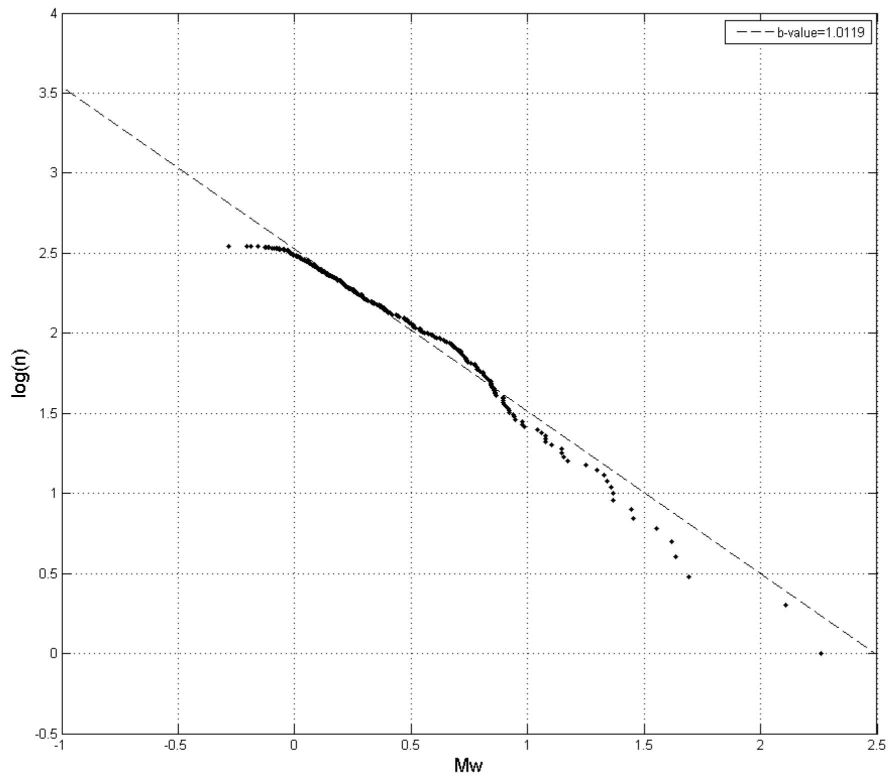

Figure 44. Log-log plot of size distribution of MEQs. Slope of line is b-value in the Gutenberg-Richter Law.

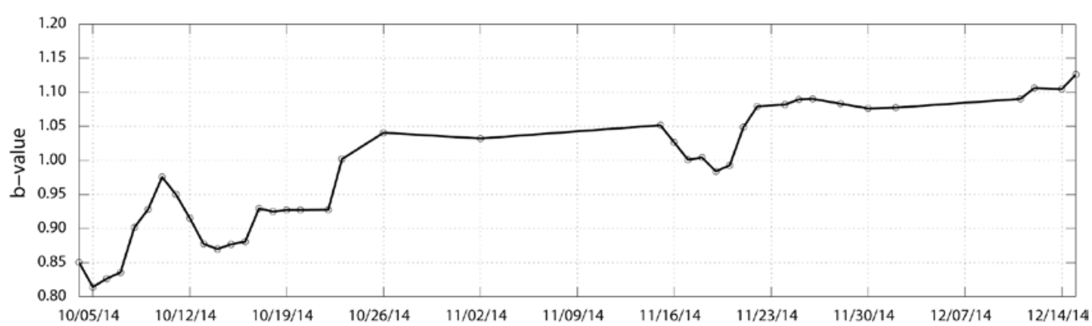

Figure 45. Evolution of b-value during stimulations. Calculated from last 100 events including the date shown.

In addition, we tracked the evolution of the b-value during the stimulation as part of the ISMP. At the end of each day the size distribution of the previous 100 events was plotted and the b-value calculated (Figure 45). This figure shows that although the overall b-value was 1.0, the sliding window of 100 events started low (0.85) and trended upward (1.1). Dips in the trend were associated with events with M> 1.3 on 10/5, 10/12, 10/13, 11/16, and 11/17.

McGarr (2014) proposed a simple relationship between the maximum moment of induced seismicity and volume change due to extraction or injection of fluid:

$$M_{o(max)} = G\ V_{inj} \qquad \text{(Equation 1)}$$

where $M_{o(max)}$ is the moment of the largest *possible* induced event, G is the modulus of rigidity of the rock mass and V_{inj} is the injected volume of fluid in cubic meters (we only need consider injection here). McGarr (2014) compiled data from injection projects worldwide to compare to the theoretical limit on induced seismicity magnitudes. In order to track seismic risk at Newberry, we plotted cumulative injected volume, cumulative moment magnitude, and maximum moment magnitude and overlaid them on the McGarr (2014) data compilation (Figure 46). For Newberry data points, the values were plotted daily, and cumulative moment magnitude included as well as the maximum moment. The ratio of seismic energy to volume of injected water at Newberry was significantly lower than at other sites that have experienced seismicity due to fluid injection. Thus, the Newberry site appears to have a much lower seismogenic index (i.e. Shapiro et al., 2010) than other sites. The Newberry data points fall far below the line plotted from the empirical formula developed by McGarr (2014) on a plot of maximum seismic moment to injected volume.

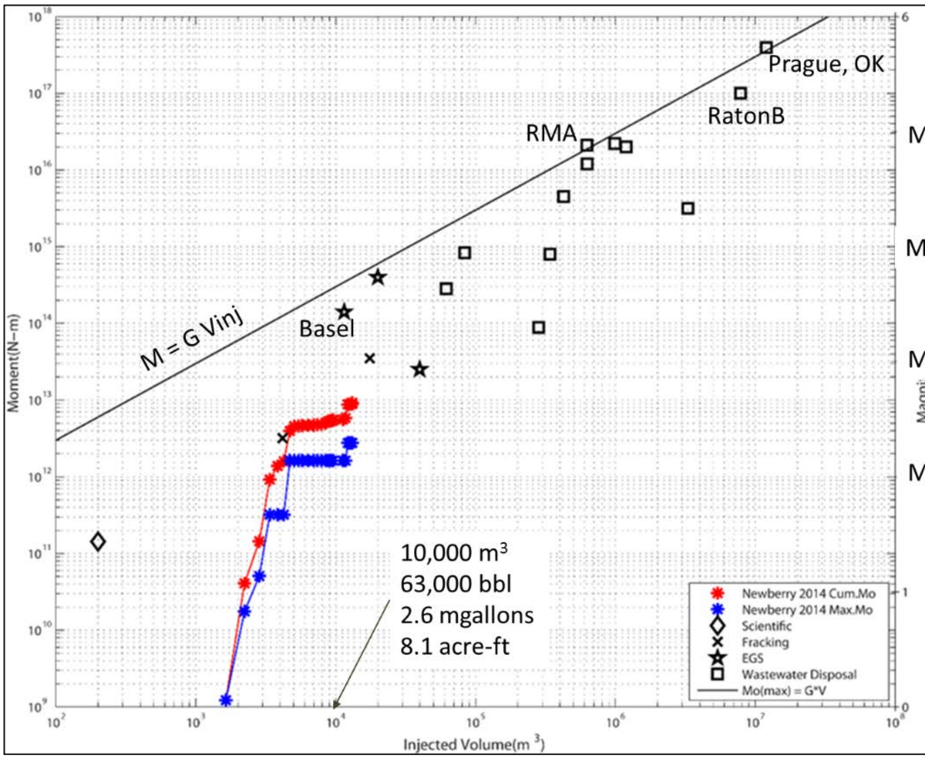

Figure 46. Maximum seismic moment and magnitude as functions of total volume of injected fluid. Data compiled by McGarr (2014).

Another aspect of the ISMP is the requirement that events be located within a defined stimulation volume. This volume was within 1 km of the well and at a depth below the casing shoe, approximately at sea level. These requirements were met (Figure 34).

5.7 PERFORATION SHOTS

Options for increasing wellbore-to-reservoir connectivity discussed after the first flow test and PTS surveys included chemical stimulation with a strong acid or base and perforation shots (see Appendix C for details). Chemical stimulation techniques typically work by dissolution of precipitate minerals from existing fractures. Well logs from NWG 55-29 show low concentration of precipitated minerals, and therefore chemical stimulation was deemed inappropriate. The challenge of permitting a chemical stimulation may also have led to further time delay late in the field season. Shaped perforation charges result in directed blasts approximately 0.5 in in diameter through the well liner and up to several feet into the surrounding formation under test conditions.

The 7 in slotted liner installed in NWG 55-29 was set on bottom after failing to attach to the liner hanger during installation and the liner is under compression. Additional perforation of the entire liner was not advised, and three 10 ft depth intervals were chosen for perforation: run #1 (8,390-8,410 ft), run #2 (8,230-8,240 ft) and run #3 (7,685-7,695 ft), all within 7 in, 23 lb, K-55 casing. These intervals were chosen based on liner condition, PTS survey results and microseismic data. Cogco Wireline Services, Inc., Woodland, CA, was chosen to perform the perforation shots at Newberry. Cogco's equipment is capable of deploying 39 g shaped charges using a 10 ft by 4.5 in perforation gun with two shots per foot resulting in 20 perforations per gun length (total charge = 780 g) (Figure 47). The gun produces 0.40 in diameter perforations with up to 72 in penetration inside 7 in casing and is rated to 400 ^{o}F for one hour. The total calculated explosive force of all shots, assuming detonation at the same time, was expected to be at the lower threshold of detectability by the microseismic array.

Figure 47. Picture showing the perforation guns before they were ran in the hole.

On November 13, Cogco installed the lubricator assembly and rigged up to survey and confirm an appropriate temperature profile for perforation gun deployment. After four failed attempts to run in hole with temperature survey equipment the flow back valve was opened, reducing wellhead pressure and facilitating the temperature survey. After completing the survey the stimulation pumps were ramped up to initiate flow into the well, and the perforation gun was deployed down hole. Perforation run 1 was completed at 8,402-8,412 ft and the shot was fired at 17:09:15. After run 1 pumps were shut down and the flow back valve was opened to lower WHP and stop a leak in the crown valve. Perforation run 2 was completed at 8,229-8,239 ft and the shot was fired at 19:33:30. Perforation run 3 was cancelled due to concerns over the functionality of the master valve in a cold environment and ability to continue support of the wireline lubricator during perforation gun changes. Removal of the perforation gun from the wellbore showed all shots were successfully detonated at depth for both run 1 and 2.

In order to use the 780 g perforation shot to calibrate the seismic velocity model, LBNL provided a geophone (OYO Geospace, 8 Hz, 3 component,) and digitizer (Reftek 130, 24 bit). The geophone was banded to top of casing, just below the master valve. The digitizer was set to record 1000 samples per second.

The timing of the 2 calibration shots was recorded and the waveforms on the AltaRock MSA examined shortly afterwards (Figure 48). The shot was evident on three to five stations, as well as the LBNL recording. However, the seismologists associated with the project (Ernie Majer at LBNL, Bruce Julian at Foulger Consulting, or Paul Friberg at ISTI), felt that the arrivals were of insufficient quality to improve the velocity model. At a depth of about 2.5 km, the P wave travel time would be about half a second (500 milliseconds) assuming an average velocity of 5 km/s, or 510 milliseconds at 4.9 km/s. Picking the first arrivals from the perforation shots with less than 100 milliseconds of accuracy was not considered possible.

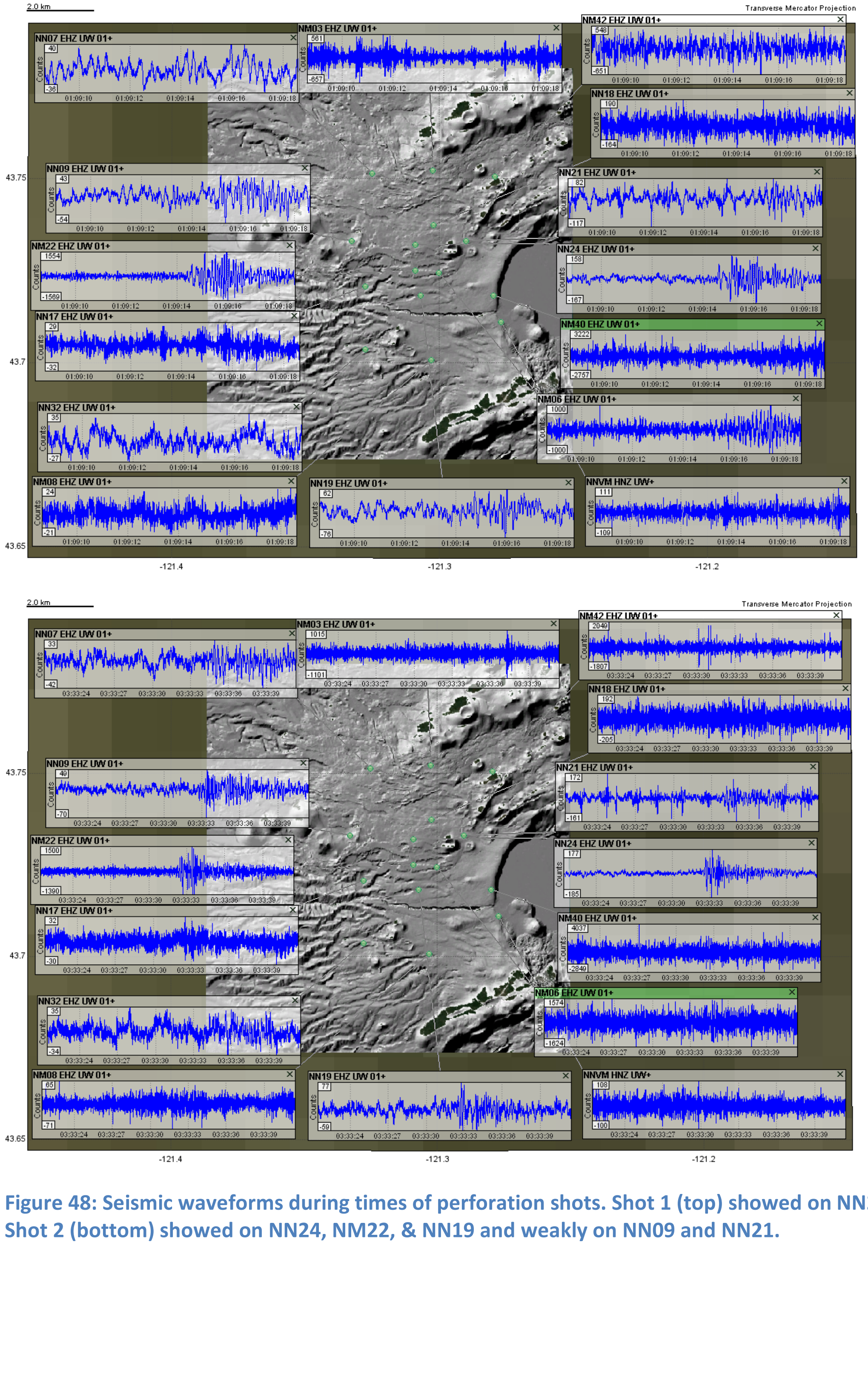

Figure 48: Seismic waveforms during times of perforation shots. Shot 1 (top) showed on NN24, NM22, & NN19. Shot 2 (bottom) showed on NN24, NM22, & NN19 and weakly on NN09 and NN21.

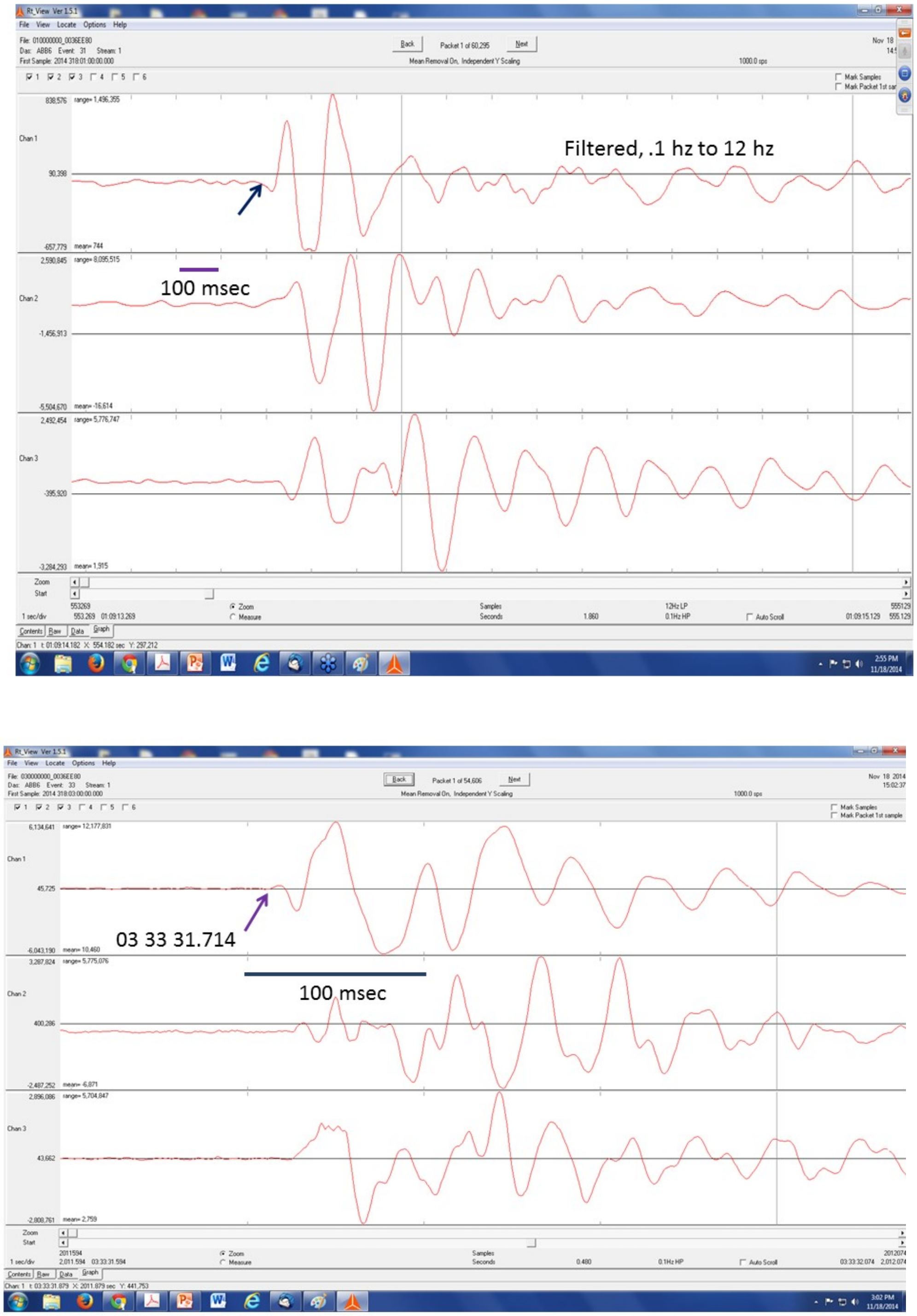

Figure 49: Perforation shots are recorded on LBNL seismometer attached to casing. CH 1 = Vertical, CH =2 N-S, CH 3 E-W. Figure courtesy of LBNL.

5.8 FLOW TEST

5.8.1 FIRST FLOW TEST

The first flow test of well 55-29 started at 9:00 am on Oct 23. The well began flowing on its own at 150 gpm (data derived from weir box measurements). This initial flow rate soon declined to about 80 gpm and then gradually stabilized to 50 gpm over a two-day period. The total flow was approximately 363 m^3 (96,000 gal). The initial pressure was 70 bar (1,037 psi) and quickly dropped to 0.24 bar (3.5 psi), approximately the amount of head required to transport the water to the separator. Temperature of the fluid started at 14 °C (57 °F) and quickly rose to 65 °C (150 °F) from which it gradually stabilized to approximately 93 °C (200 °F), the boiling temperature for the elevation of the wellhead. The temperature was measured on the line connecting the well to the separator. Geysering likely caused the recorded temperature value to be lower than the temperature of the water at the wellhead. When the temperature of the flow back fluid approached boiling within the well, the pressure reading on the well began to exhibit peculiar behavior; as one can see by the pressure shown in Figure 50. At roughly 20:00 on October 23 the WHP pressure begins to oscillate significantly. At the well head there was a clear sound of surging water through the pipeline followed by silence. This pattern repeated along with oscillating flow through the weir box. It was then determined by review of temperature, pressure and flow data that the well was geysering.

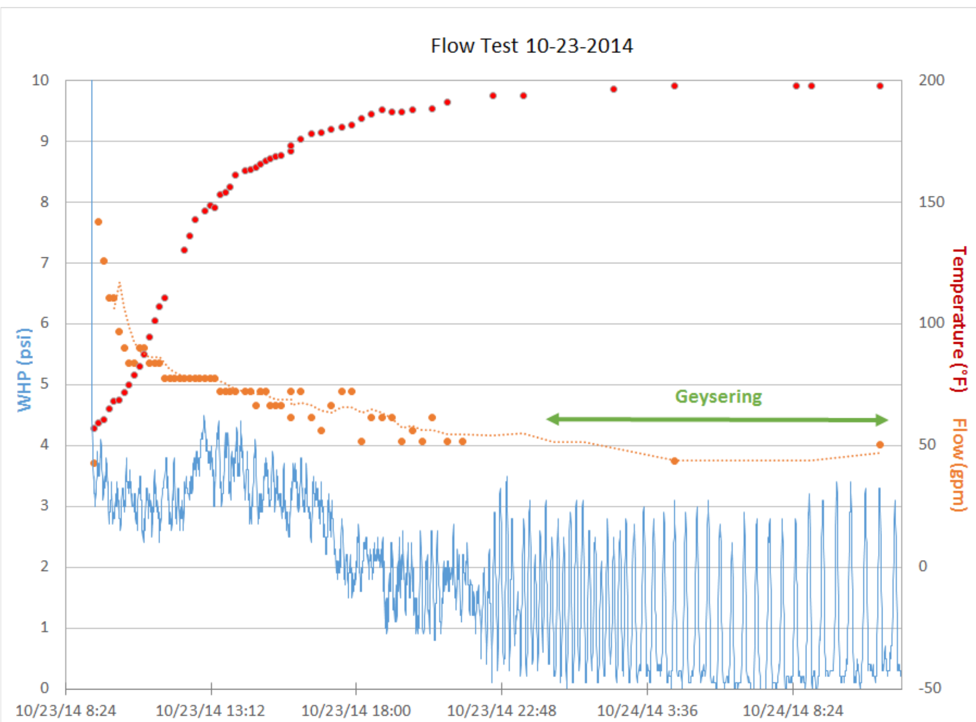

Figure 50. Pressure, temperature and flow for the first flow test.

5.8.2 SECOND FLOW TEST

The second flow test started approximately 10:00 am on November 24. The well began flowing on its own at approximately 12 l/s (200 gpm). The flow quickly reduced to about 3 l/s (50 gpm) in seven hours and then slowly decline to approximately 1.5 l/s (25 gpm) over 39 hours. The temperature of the flow back water started at 23 °C (72.8 °F) and quickly reached approximately 93 °C (200° F) within 13-14 hours (Figure 51). No pressure was recorded during the second flow-test as there was trouble with communications between the sensor and the data logger. However, the same geysering characteristics experienced in the first flow back test were seen when the temperature of the flow back water approached 93 °C (200 °F). The total flow from the well during the second flow back test was approximately 272 m^3 (72,000 gal). Flow was measured using both the weir box and the separator. Flow was calculated using the separator by measuring the change in height of the water column over a specific increment of time.

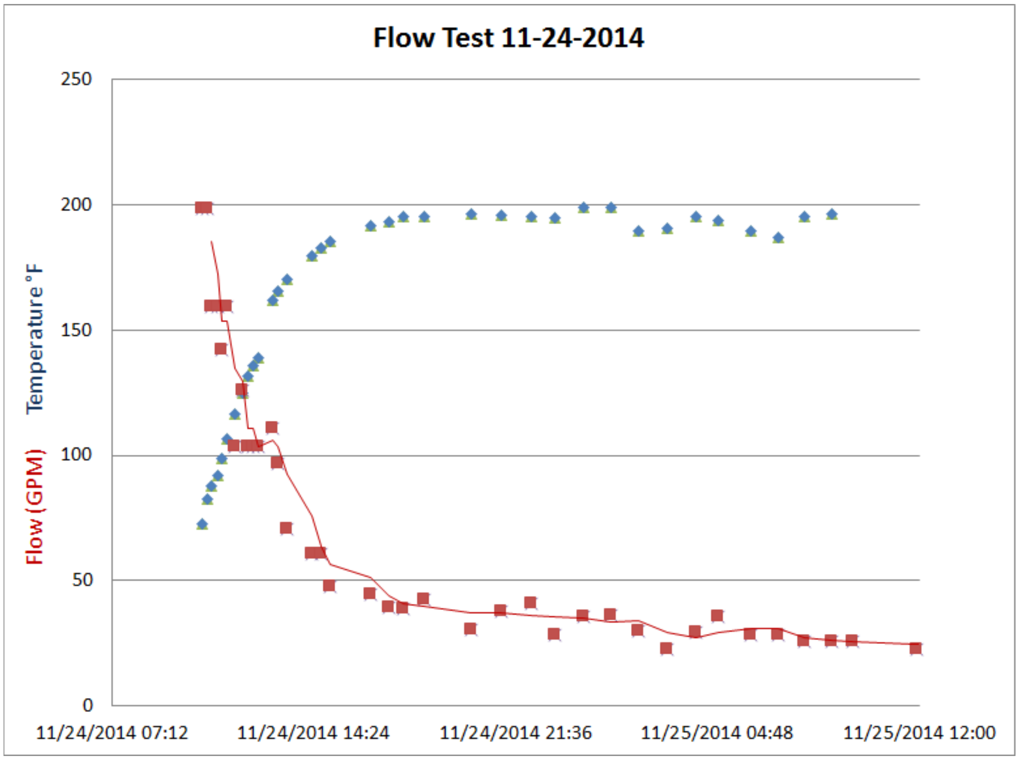

Figure 51. Pressure, temperature and flow for the second flow test.

5.8.3 FLOW BACK WATER SAMPLING

Flow back samples were collected downstream of the wellhead-T at a 2 cm (¾ in) ball valve controlled sampling port and pipe elbow (Figure 52). The port was opened and flushed for 5-10 seconds prior to sample collection. Samples were collected and processed in the same manner as water well samples. An YSI 556 MPS field meter was used to measure field parameters. Field parameters include temperature, conductivity, total dissolved solids, salinity, dissolved oxygen, pH, oxidation-reduction potential, and turbidity. Temperature was recorded at collection and the remaining field parameters were recorded Samples were vacuum filtered through 0.45 µm acetate, bottled and cooled on ice after collection. Filter papers from most samples were dried, labelled and saved for x-ray diffraction analysis. A true steam phase was not reached during the flow back, and no steam samples were collected.

Samples were collected every 1-2 hours or when a noticeable change in flow back water occurred (color, temperature or increased steam surge frequency) during the October 7 flow test. Samples were collected every hour for the first nine hours and every 2-9 hours during the October 23-24 flow test. Samples were collected every two hours during the final November flow test, which for the first time included tracers which had been injected at the end of Round 2. Flow back water chemistry data is presented in Section 7. Tracer sampling and returns is presented in the next Section.

Figure 52. Picture showing flow line and location of ball valve where samples were taken (red arrow).

5.9 SINGLE-WELL TRACER STUDY

In geothermal fields heat-tolerant tracers can be used to estimate fracture pore volume. Dr. Peter Rose of the Energy and Geosciences Institute at the University of Utah (EGI) provides consultation, planning and analysis for tracer use at the Newberry EGS Demonstration. Two tracers were used during Phase 2.2: 1,3,6-naphthalene trisulfonate and 2,7-naphthalene disulfonate.

During stimulation Round 1, no clear benefit was seen to injecting TZIM into the wellbore; therefore, no tracers were injected either.

5.9.1 TRACER INJECTION

Two tracer injections took place during stimulation Round 2. Each of these were followed by injection of a TZIM pill. On November 18, 25 kg (55 lbs) of 1,3,6-naphthele trisulfonate was mixed with approximately 570 l (150 gal) of water and injected as a slug into 55-29. Granular AltaVert 251 injection followed shortly thereafter. On November 19, 25 kg (55 lbs) of a second tracer, 2,7-naphthalene disulfonate, was mixed with approximately 570 l (150 gal) of water and injected as a slug into 55-29. This was followed by injection of fibrous AltaVert 251. Each of the two tracer injections were followed by 5 TZIM pills, each mixed with approximately 570 l (150 gal) of water.

5.9.2 TRACER SAMPLING

Nineteen samples of flow back water were collected during the November flow test of 55-29. The sampling procedure is detailed in the Flow back section of this report (section 5.8.3). Results from the final flow test in November are presented below.

5.9.3 TRACER RETURNS

The 19 samples collected during the November flow test were analyzed to determine the concentrations of the two naphthalene sulfonate tracers using Ultra Performance Liquid Chromatography (UPLC) with fluorescence detection. This method provides a detection limit not to exceed 0.100 parts-per-billion (ppb). Figure 53 shows the measured concentrations of tracers in the flow-back samples.

Tracer was detected in the first samples collected 3 hours after the flow test began. This corresponds to the time needed to flow back the volume contained by the cased part of the hole. The cased part of the hole is roughly 92 m^3 (24400 gallons), which given the recorded flow values would have taken three hours and six minutes to flow back. Peak tracer returns occurred five hours after the well began to flow, which roughly corresponds to the time water from fractures in the well would begin flowing to the surface. Summing the concentrations and flow rates, 9.1% of the injected 1,3,6 NTS tracer was recovered and 18.1% of the 2,7-NDS tracer was recovered.

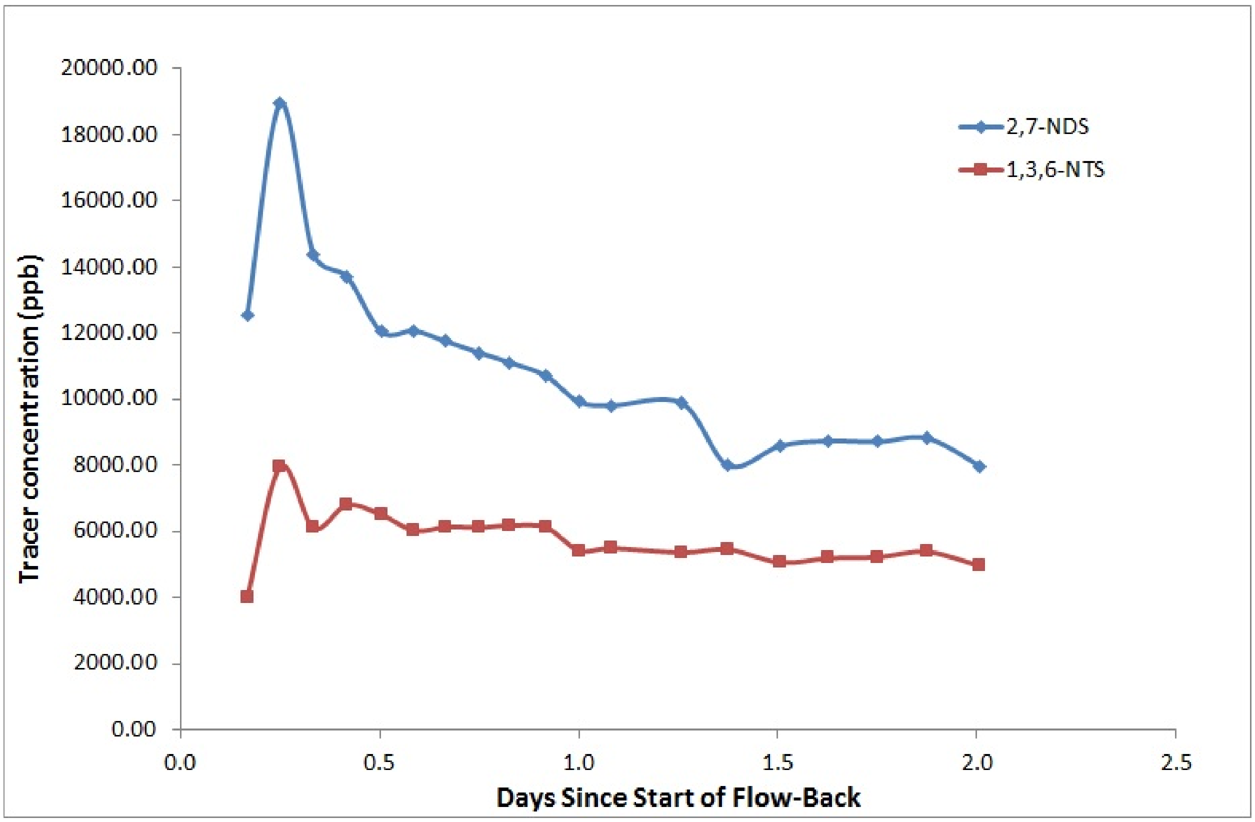

Figure 53. Tracer returns during the second flow back test (November) after stimulation was complete.

The concentration of 1,3,6-NTS becomes relatively constant at about 5,200 ppb after about 1.3 days of flow back, indicating that it has mixed evenly throughout the volume of water filling the fractures created pre-diverter application. If the assumption of even mixing is correct, then the concentration between about 1.3 days and 1.8 days can be used to provide a rough estimate of the mass (M) of water filling the fracture-pore volume created during the stimulation up until the application of the first diverter:

$$M = \frac{mass\ of\ tracer\ injected}{final\ tracer\ concentration} = \frac{25\ kg_{tr}}{5{,}200\ kg_{tr}/10^9\ kg_w} = 4.8\ x\ 10^6\ kg_w \qquad \text{(Equation 2)}$$

Likewise, the concentration of 2,7-NDS over the same time period can be used to estimate the mass of fluid filling the fractures resulting from stimulation after the application of diverter. If it is assumed that the concentration has leveled off at about 8,700 ppb, then the mass of water filling the accessible fractures after the first application of diverter is:

$$M = \frac{25\ kg_{tr}}{8{,}700\ kg_{tr}/10^9\ kg_w} = 2.9\ x\ 10^6\ kg_w \qquad \text{(Equation 3)}$$

The mass of water filling the fractures can be directly related to the fracture pore volumes resulting from the stimulation.

5.9.4 TZIM Breakdown Products

A method based on UPLC with UV detection was used to analyze the flow back water for para-phthalic acid, which is breakdown product from the thermal degradation of the AltaVert 251 diverter. Shown in Figure 54 is the concentration of para-phthalic acid as a function of flow back time. It is evident that the para-phthalate was measured at much lower concentrations than the naphthalene sulfonate tracers. The detection limit for para-phthalate is about 500 ppb, which makes it is about 5,000 times less detectable than the naphthalene sulfonates. Therefore, even though the first production of para-phthalate was observed almost one day after the initiation of flow-back, it likely was produced but in concentrations less than 500 ppb at very early flow-back times. Roughly an hour before para-phthalate was observed partly degraded TZIM was encountered on the screens of the weir box, however it was in fairly low concentrations and quickly disappeared as the flow back continued. Water samples containing TZIM break down products were found to change color quickly after being exposed at the surface. It was later discovered that AltaVert 251 breakdown products contained photo reactants, and were responsible for this unusual behavior.

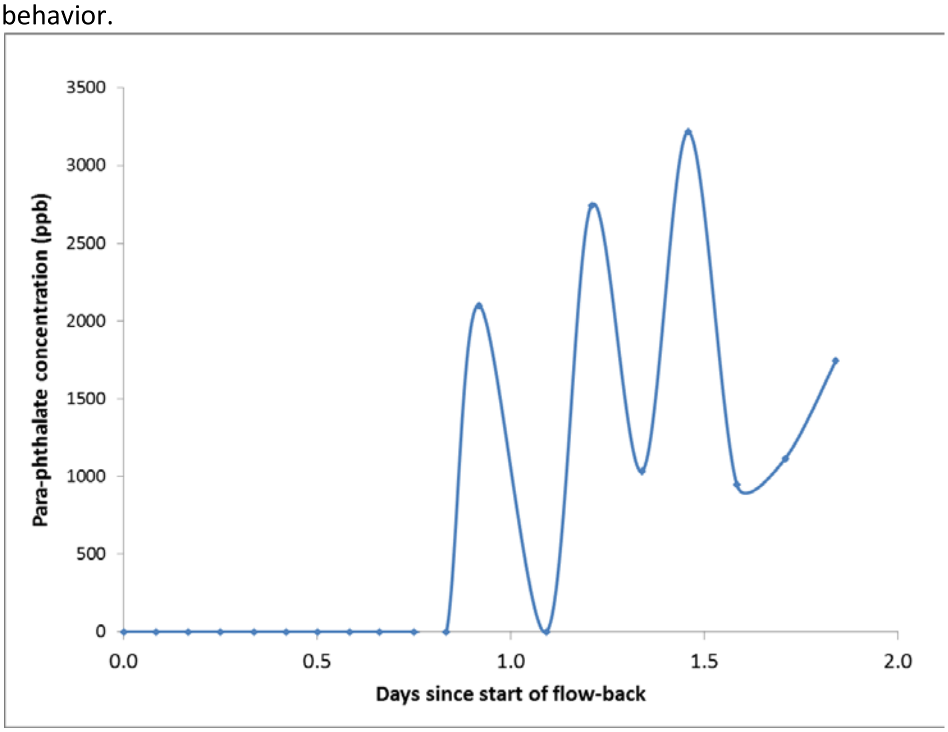

Figure 54. The concentration of para-phthalate in water samples taken during the flow back.

5.10 ENVIRONMENTAL MONITORING

Seven sites were selected for groundwater monitoring in Phase 2.2. These include the water well on Pad 55-29 (55-29WW), seismic monitoring well NN-17, two drinking water wells located within NNVM at Prairie Campground (PCG) and the Visitor Center (VCWW), one hot seep along the southeastern shore of East Lake (ELHS) and one hot seep along the eastern shore of Paulina Lake (PLHS), and one private water well located in the Newberry Estates area east of La Pine (NEWW1). Depth to water measurements are recorded at NN-17 down gradient from NWG 55-29 and at seismic monitoring well NN-18 up gradient of NWG 55-29. Depth to water data for NN-18 and the water well on Pad 46-16 (46-16WW) is reported annually to Oregon Water Resources Department. In addition, OWRD maintains a continuously recording depth transducer in water well NN-18. Sites NN-18 and 46-16WW were removed from the groundwater monitoring program in Phase 2.2. The low-flow pump at NN-18 was removed in 2013 due to malfunction; the cost of mobilizing and wiring a large generator to power the pump in 46-16WW is significant, and the well was dropped from the monitoring plan as a result.

The Phase 2.1 report outlines the sampling methodology. Field parameters (temperature, pH, conductivity, oxidation-reduction potential and turbidity) are recorded at sampling time and prior to filtering samples. Samples are filtered to remove sediment and bottled in the field prior to shipment on ice for analysis. As with samples previously collected at Newberry, Sierra Environmental Monitoring, Reno, NV continues to provide geochemical suite analyses. Tracer test samples are processed at the University of Utah. Isotope samples are processed at the University of California, Davis.

Background groundwater samples were collected at all seven monitoring sites in September. Site NN-17 was sampled once in October and 55-29WW was sampled twice. Third and fourth rounds of groundwater sampling occurred in late January and mid-March, 2015. Sites 55-29WW, VCWW and PCG are winterized and inaccessible until late spring. No significant changes in groundwater quality were detected at any of the monitored sites during Phase 2.2. Tracer returns at groundwater monitoring sites were insignificant. Results from this phase of monitoring as well as average historic and average Phase 2.1 data are presented in Appendix D.

6 EGS RESERVOIR CHARACTERIZATION

This section characterizes the EGS reservoir using micro-seismic data, well test analysis, and stress analysis.

6.1 INDUCED SEISMICITY

Microseismic data provide information about the locations of presumed permeability-enhancing seismic events and the failure mechanisms generated during hydraulic stimulation. The complete microseismic data set provides the best estimate of the shape and size of the EGS reservoir and the nature of the stimulated fracture system.

After the stimulation, two teams -- LBNL (headed by Ernie Majer), and Foulger Consulting (headed by Gillian Foulger) -- used different software packages to perform relative relocations. They found that generally the seismic cloud extends 150-200 meters (492-656 ft) around the wellbore from below the shoe at 1940 meters TVD (6370 ft) and to the bottom of the hole at 3009 meters TVD (9,870 ft). However, details of two catalogs are different, which required development of a method to combine the results to arrive at consensus seismic density plots that are then used for production well targeting.

6.1.1 LBNL RELATIVE EVENT RELOCATIONS

LBNL was one of three groups responsible for collecting and analyzing micro-seismic data. Initial locations were analyzed using an automated arrival time software which showed the results on the LBNL Induced Seismicity website. However, these initial results were scattered and were determined to have significant location error.

After the stimulation, all the events were reviewed and arrival times for each event were handpicked by seismologists at LBNL. In addition the Vp/Vs ratio, the P-wave velocity over the S-wave velocity was refined. This parameter primarily affects the seismic event depths and can be poorly constrained. This uncertainty was reconciled by calculating locations and depths using different Vp/Vs ratios and then determining which depth ranges best explained the data gathered in the wellbore.

A Vp/Vs ratio of 1.7 was chosen because the events most closely matched locations as one would expect from well logging and geological data. It has been confirmed on multiple PTS surveys that one of the major flowing zones in the well was at the bottom of the well. Zones of outflow from the well are some of the best constrained data gathered during the stimulation. The Vp/Vs ratio which put the deepest seismicity near the outflow zone at the bottom of the well is 1.7. The choice of Vp/Vs of 1.7 is further corroborated by the fact that the shallowest seismicity is located just under the casing shoe and that the largest density of seismicity is located at the other known major outflow zone at approximately 2,520 meters (8,265 ft) TVD, which translates to a measured depth of approximately 2560 meters (8,400 ft).

This hand-picked catalog of locations with a Vp/Vs ratio of 1.7 is one of the four catalogs considered in siting the production well below.

Locations were then relatively relocated using a software package called tomoDD, a program developed by Haijiang Zhang and Clifford Thurber of the University of Wisconsin. This program, a double difference tomography model, uses absolute and differential arrival time data to determine event locations and velocity structures. Using tomoDD and refining the parameters of the velocity model, LBNL arrived at what they determined to be their best set of data. Comparison of the original hand-picked locations and the relocated dataset shows a systemic shift of the seismic events. The average event was relocated at an azimuth of 213° at a radius of 189 meters away and 72 meters deeper than the original auto-picked events (Figure 55).

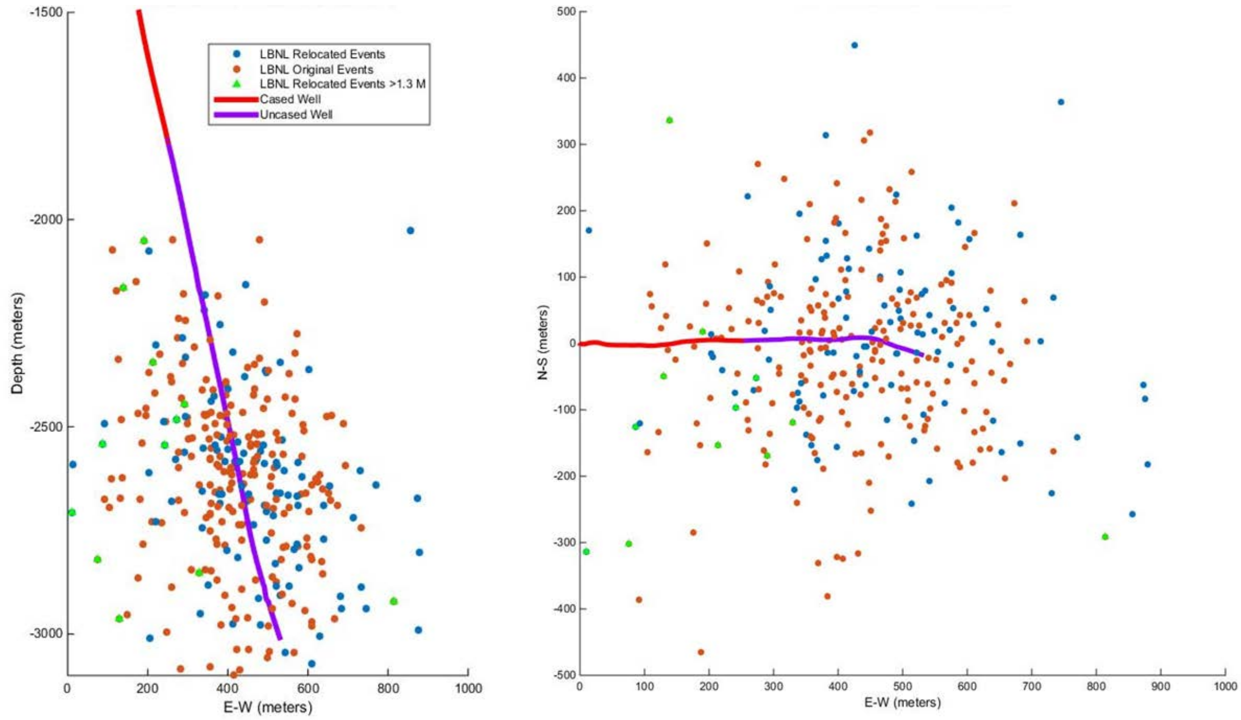

Figure 55. North-looking cross section (left) and map view (right) showing original LBNL locations and final relative relocations. Catalog is for events recorded on 8 or more components.

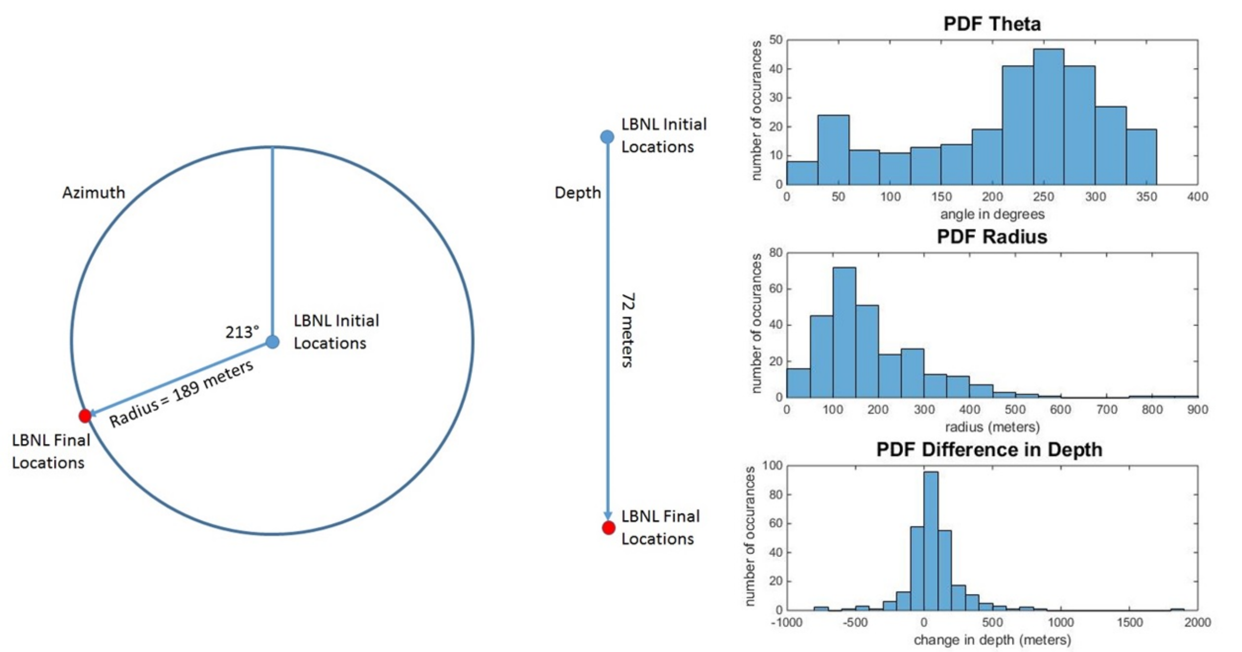

Figure 56. Statistics of event relocations. Left: average change in direction for all relocations. Right: histograms for the direction of change, horizontal distance change, and depth change.

The relocations performed by LBNL suggest that the events are likely to be located near the wellbore elongated east-to-west. As compared to the original location, the relocated events are located generally more south and east, as well as deeper.

6.1.2 MOMENT TENSORS

Microseismicity in geothermal reservoirs can involve several different physical processes (Julian et al., 1998; Miller et al., 1998a), including:

1. Simple shear slip on planar faults
2. Tensile cracking
3. Rapid fluid motion

Understanding these processes is critical to understanding hydroshearing mechanics in EGS projects. Traditional "fault-plane solutions" assume only simple shear slip occurs, which ignores both processes associated with opening and closing cracks and fluid flow. For this reason, a moment-tensor approach should be used, which requires more information than just P-wave polarities. The most effective and readily obtained information is P- and S-phase amplitudes (Julian and Foulger, 1996). Moment tensor solutions and precise locations (Figure 57) were calculated for 100 events, two of which were for the same event (10/12/2014 21:10:23). Appendix E provide six weekly reports prepared during the stimulation and a final report summarizing the entire results. Here, we summarize the most salient aspects of the Foulger Consulting results.

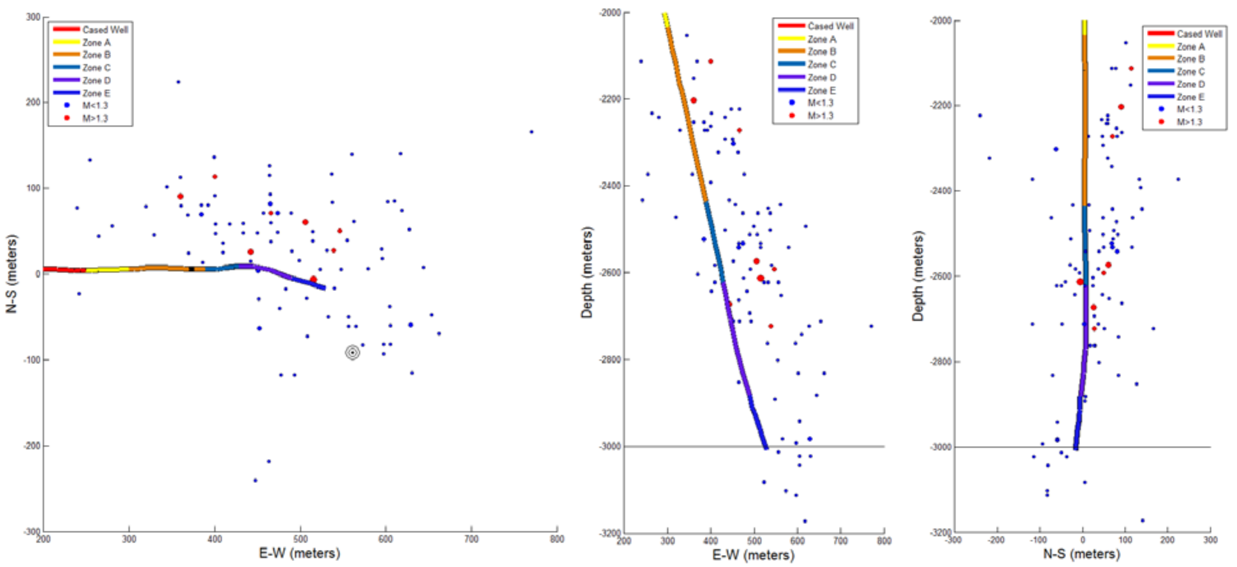

Figure 57: 100 locations for moment tensor solutions. Largest events (M>1.3) are red and smaller events (M<1.3) are blue.

Moment tensors are displayed graphically using source-type diagrams (Hudson et al., 1989). This has been applied to many natural and industrially induced micro-earthquake sequences, including geothermal and hydrocarbon reservoirs and EGS stimulations (Julian and Foulger, 1996; Julian et al., 1997; Julian et al., 2010a; Miller et al., 1998). A source-type diagram (Figure 58) illustrates the deviation from a pure earthquake double-couple (DC) source at the center in terms of a volumetric component, explosion on top and left or implosion on bottom and right. Tectonic earthquakes typically fall near the center point of the plot (labeled DC). Injection-induced seismicity, which involves an underground change in volume, may require non-DC source-types.

The source-type plot for the 2014 stimulation at Newberry (Figure 58) indicates a wide variety of source mechanisms ranging from double couple to opening cracks (+Crack) to closing cracks (-Crack). This variety may be due to a relatively low differential stress and stimulation of variable volcanic features (e.g., dikes, flow boundaries, ring fractures). The corresponding P, I, and T axes (Figure 59) are approximate indicators of the principal stresses. The T-axis average, which approximates the minimum principal stress direction, has a N12°E trend and plunges 57° to the north. The P-axes, which approximates the maximum principal stress direction, are mainly horizontal but are highly varied directionally with a 270° range.

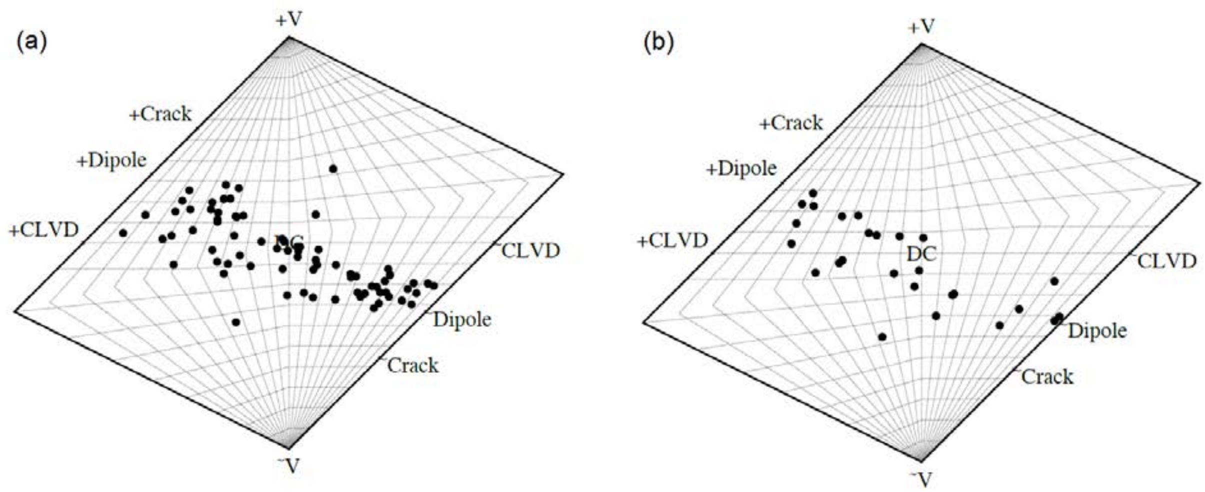

Figure 58: Source-type plots of 100 moment tensors. (a) 74 events for round 1 and (b) 26 events for round 2.

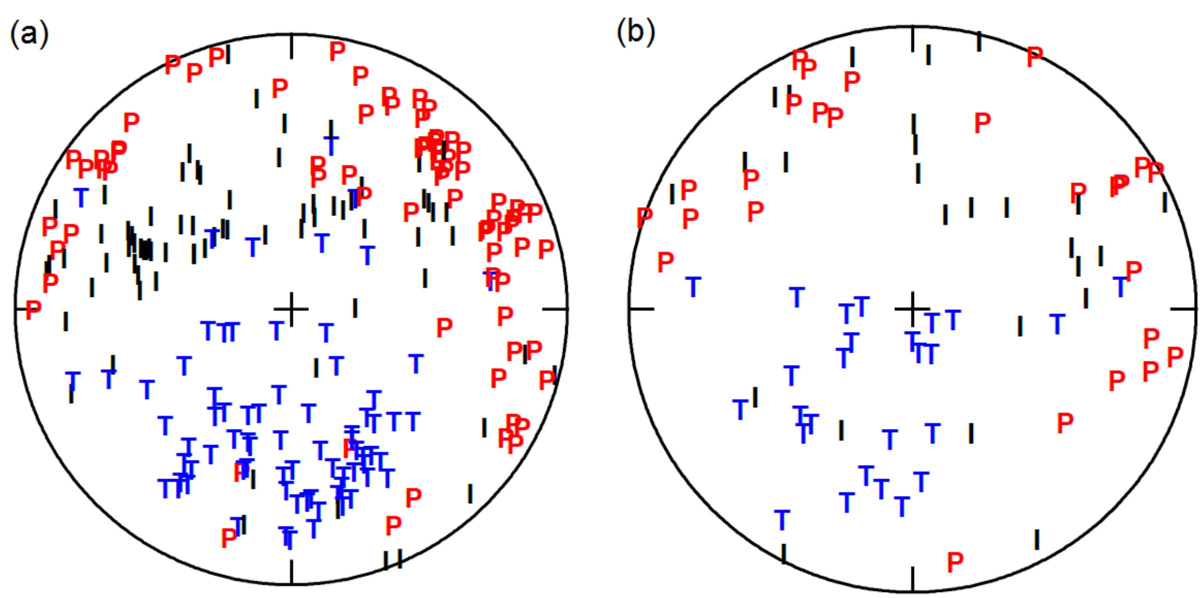

Figure 59: Upper-hemisphere stereonets of principal axis for (a) 74 moment tensors for round 1 and (b) 26 moment tensors for round 2.

The spatial distribution of the P and T axis is plotted in Figure 60 along with volume loss/gain by plotting the k-values for the source types, which represent the isotropic component of the moment tensor and are also the vertical axis on the source type plot. Positive values indicate a relative volume gain, and negative values indicate a relative volume loss. The vertical distribution of the source types further reveals where similar source types are grouped at depth, which may indicate individual structural features. The small grouping of positive k source types just to the southeast of the bottom of the well exhibits a northwest striking sub-vertical planar feature, which has a strong right-lateral component.

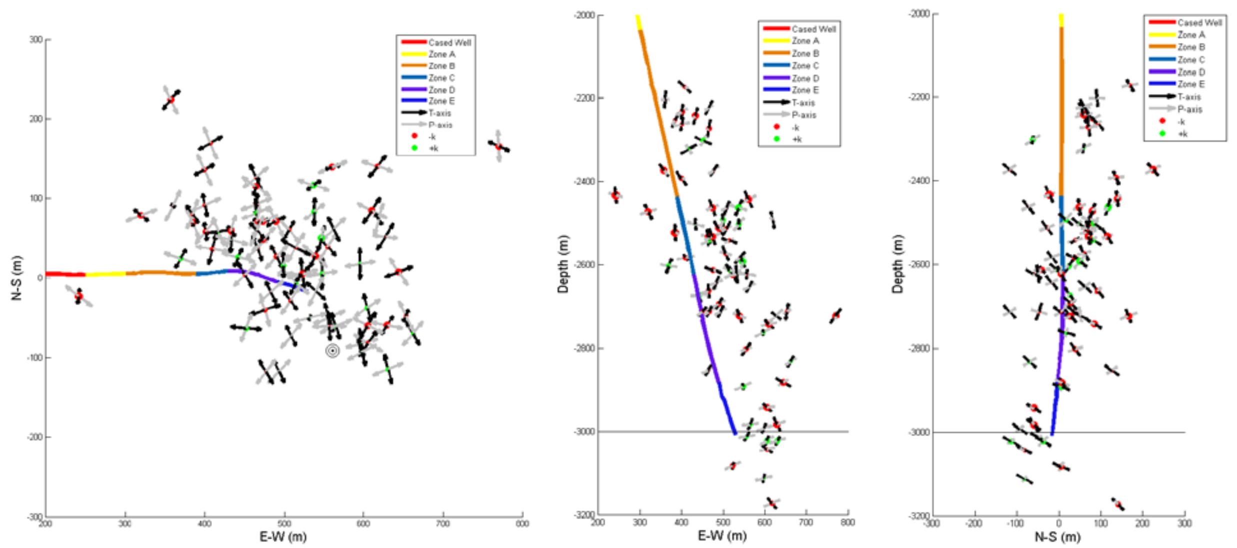

Figure 60: Spatial distribution of P and T axis around well with volume gain (k+) and volume loss (k-).

Locations of volume gain and loss can be used as an indicator of the extent of the reservoir created during stimulation. Figure 61 shows an iso-surface between positive and negative volume gain. There are three main groupings of volume gain, two near the depth of the casing shoe and one near the bottom of the well. The deeper volume gain occurred early during well stimulation, whereas the shallow grouping to the northeast occurred later during the stimulation, and the shallow volume gain to the south of the well occurred after injection stopped.

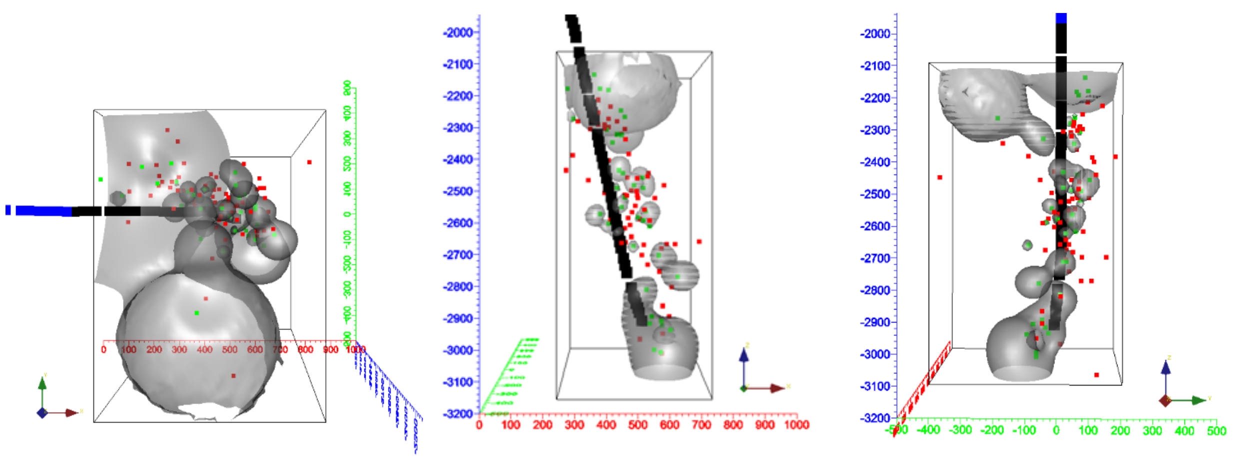

Figure 61: Iso-surface between positive and negative volume gains from a 3D linearly fit grid. Green events have volume gain and red events have volume loss. Distances in meters.

6.1.3 COMBINED CATALOG SEISMIC DENSITY PLOTS

The prior two subsections plus the ISTI catalog (Section 5.62) provides four different catalogs of seismic event locations based on different assumptions and calculated with different software packages. Even the "best" two catalogs show some systematic differences. In the LBNL relocation catalog the events are generally west and south of the well while in the Foulger Consulting catalog the events are generally east and north of the well. As of now there is not a clear explanation for the discrepancy between the results from the two different groups. However, as Foulger has outlined in her report:

> *The art of locating earthquakes is imprecise. Calculated absolute locations depend on many details of the workings of individual location programs, including how the issues of starting-guesses, non-uniform station elevations, ray-tracing and outlier rejection are handled. By far the largest source of error in locations is error in the crustal model used. Errors in arrival-time measurements and station locations are typically much smaller in the case of reasonably well-processed data.*

To reconcile the differences in seismic event locations between different teams of seismologists AltaRock decided to summarize the seismic data sets from a different perspective. Rather than debate the relative accuracy of each methodology in an attempt to arrive at the "best" data set, we have instead decided to determine the probability that an event has occurred within a defined grid cell volume. There is a range of error associated with each method of analysis; this is largely because of assumptions made about the velocity model and the software used to help locate events. To reduce noise due to error, we combine the four catalogs to create seismic density plots. This is done by assigning relative weights to the individual datasets based on perceived location quality (Table 5). For example, the dataset "Foulger MT Locations" has the highest weight (40%) because the events in this catalog were carefully hand-picked on seismograms rotated to ray path coordinates (up, radial, transverse). The dataset labeled "ISTI Original Locations" is the least constrained, so these events are given the lowest weight (10%). A side-effect of this weighting scheme is that the largest (M>0.7), and presumably best located, 99 events (Table 5) are represented in all four catalogs, thus will be counted four times. Meanwhile, the smallest 38 events (M<0.0) will only be counted once. Weighting events in this way gives far more weight to the larger events than the smaller events. This is beneficial because larger events are highlight areas where significant stimulation has occurred.

Table 5. Table showing relative weights for each dataset shown in the seismic density plots.

Catalog	Number of Events	Weight
ISTI Original Locations	400	10%
LBNL Hand-picked Locations	362	20%
LBNL Relative Relocations	278	30%
Foulger MT Locations	99	40%

The stimulated volume is defined by grid cells that are sized 50 m (164 ft) along the x-axis, 50 m (164 ft) along the y axis and 100 m (328 ft) along the z-axis. The grid cells are asymmetrical with respect to depth because the location error is known to be more pronounced with respect to depth as well. The scale of the grid cell with respect to x and y was chosen for two reasons. It roughly correlates with the error associated with the best located events (LBNL relocs) which has a precision of 44 m (144 ft), and because it is not so small as to show only a uniform distribution of events but not so large as it doesn't capture the structure of the seismic cloud. After assigning a weight to each dataset (Table 5) all points contained within a single grid cell, or bin, are summed to create a specific value for that cell. This creates a 3D histogram, which clearly outlines which rock volumes are the most likely to have had an event or multiple events occur during stimulation.

The zones with highest seismic density are located near the well at 2,500-2,600 m (8,200– 8,528 ft). This is associated with a known outflow zone at 2,560 m MD (8,400 ft). The seismicity from this exit point seems to extend approximately 150 m to 200 m (490-660 ft). The combined catalog seismic cloud is elongated and denser in the East-West direction. Generally, events tend to get deeper as one goes from West to East (Figure 62). In the North-South direction the seismic cloud is less coherent than in the East-West direction and events become deeper as one goes from North to South. While the trend of events getting deeper in the North-South direction are likely the result of structural elements down hole, the trend of events getter deeper in the West-East direction is the result of the angle of the well. Another interesting result from these seismic plots are that there is clearly a continuous seismically stimulated area, where events are located close to each other and clumped around the well, and a discontinuous seismically active stimulated area, where there are isolated patches of seismicity which appear to be unrelated to the denser seismic cloud near the wellbore. These isolated patches of seismicity are likely caused by one of two reasons. Either there are elongated permeable elements, such as fractures, where the seismicity is occurring along the terminus of these elements, or pressure increases in the reservoir are causing failure of fractures in the far field without being infiltrated by water.

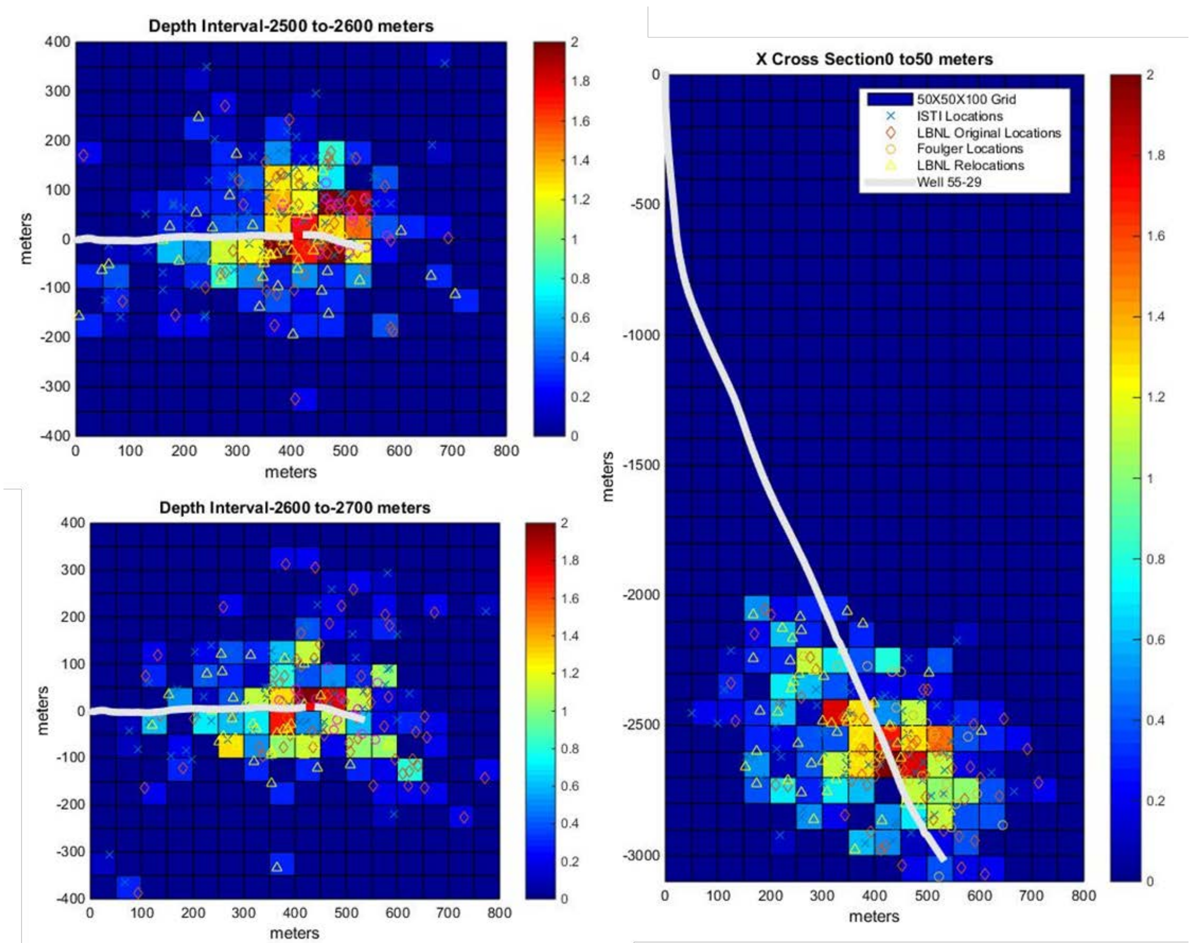

Figure 62. Example of seismic density plots for well 55-29.

While increasing clarity about the characteristics of the stimulated volume of rock, the seismic density plots also raise significant questions. What is most curious about these seismic density plots is that they show a small amount of seismicity at depth, near where one of the large exit zones is known to be. During the 2012 stimulation and the most recent stimulation, DTS data and PTS logs showed strong evidence for a large exit zone, if not the largest, at 2,927 m (9,600 ft). Further corroborating the hypothesis that 2,927 m (9,600 ft) is a major exit zone for the well is that this depth was the location of the largest mud-loss zone recorded in the mud log. If the majority, or near majority, of the fluid is exiting from this zone then why is there so little seismicity? This discrepancy between known permeable structures and lack of seismicity suggest that frequency and density of seismicity may not be directly analogous to permeability enhancement. Combined catalog seismic density plots for all depth and cross sectional slices are provided in Appendix G.

6.1.4 RESERVOIR DIFFUSIVITY

To hydraulically characterize the seismically active stimulated region around the well, an underlying mechanism of pore-pressure diffusion is applied to the temporal distribution of events around the point of injection. This is done by assuming a point source of pressure from the bottom of the well and measuring the distance of each event from the point source for the length of the stimulation. The spatial distribution of the events over time has a triggering front with a parabolic signature (Parotidis, et al., 2004):

$$r = \sqrt{4\pi D t} \qquad \text{(Equation 4)}$$

Where *r* is the distance of the triggering front, *t* is time, and *D* is the hydraulic diffusivity of the surrounding rock. After pumping of the well has ceased, and the well is shut-in, seismicity continues to spread from the point source of pressure but develops a parabolic back front from the point source:

$$r = \sqrt{6Dt\left(\frac{t}{t_0} - 1\right) ln\left(\frac{t}{t - t_0}\right)} \qquad \text{(Equation 5)}$$

Where t_0 is the shut-in time. The LBNL relocated event distances with time were fit to parabolic triggering and back fronts for both round 1 and 2 stimulations using a hydraulic diffusivity value of 0.006 m^2/s with the wellhead pressure and flow (Figure 63). Assuming a porosity (ϕ) of 0.03, dynamic viscosity (μ) of $8.5x10^{-5}$ Pa-s for 150°C water, and total system compressibility (c_t) of $9.4x10^{-10}$ Pa^{-1}, this equates to a permeability (k) of $1.44x10^{-17}$ m^2 using:

$$k = D\phi\mu c_t \qquad \text{(Equation 6)}$$

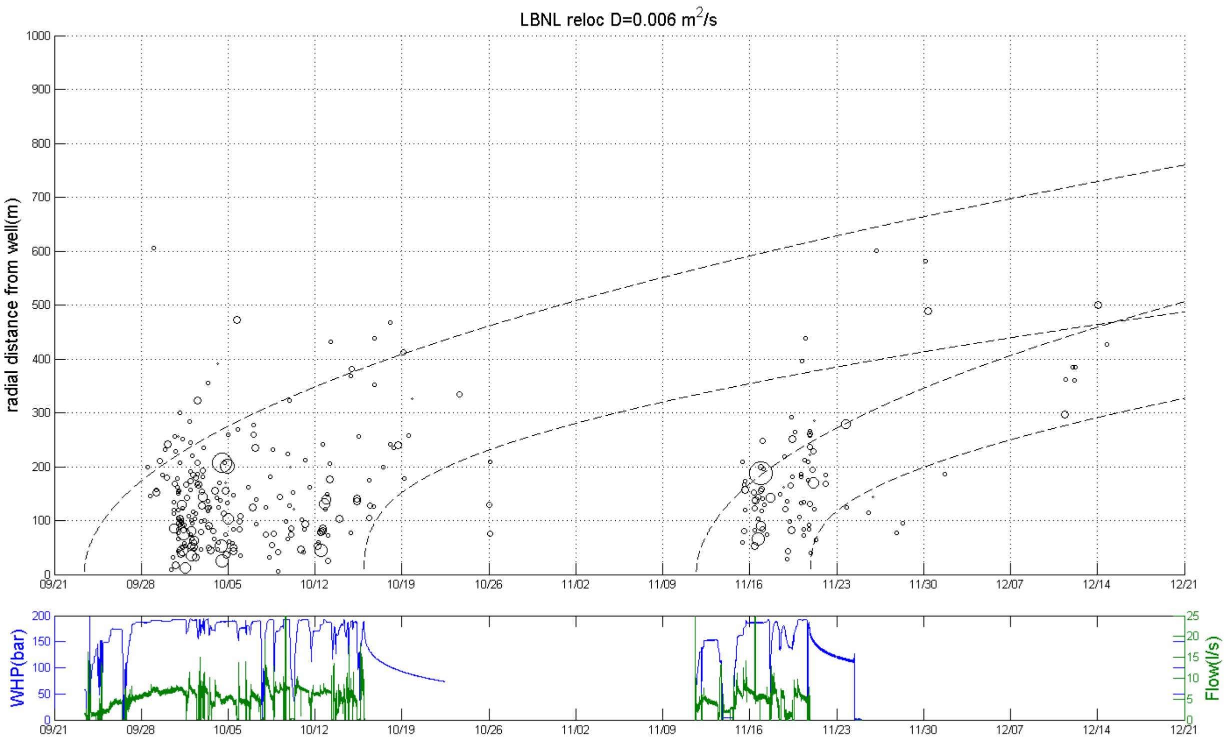

Figure 63: Radius vs time for events (sized by magnitude) for both rounds of stimulation with wellhead pressure and injection rate.

The hydraulic diffusivity value can be used to predict pore-pressure diffusion from the injection well during a stimulation using:

$$P_p(r,t) = \frac{q}{4\pi Dr} erfc\left(\frac{r}{\sqrt{4Dt}}\right) \qquad \text{(Equation 7)}$$

Where P_p is the pore pressure as a function of radius and time, q is the point-source pressure, or down-hole pressure in the well above hydrostatic pressure using a water table depth of 180 m and *erfc* is the complementary error function. Using an average WHP of 193 bar (2,800 psi) or 211 bar (3,060 psi) downhole pressure during the stimulation, the pore-pressure above hydrostatic for round 1 is shown in Figure 64a, which approaches zero 250m away from the well, and is also the extent of the seismic cloud from the well. Figure 64b shows the pore-pressure distribution with a second well 200m away, which is the anticipated distance between the bottom of the well and the 2nd well to be drilled. Both wells in this scenario are stimulated with a WHP of 241 bar (3,500 psi) or 259 bar (3,756 psi) downhole pressure for the same amount of time as round 1 (22.5 days). Although the pore-pressure near the well is unchanged, the pore-pressure directly in between the wells is twice as high as a result of a dual stimulation. Further investigations into the parameter sensitivity of WHP and injection time are presented in section 8 of this report.

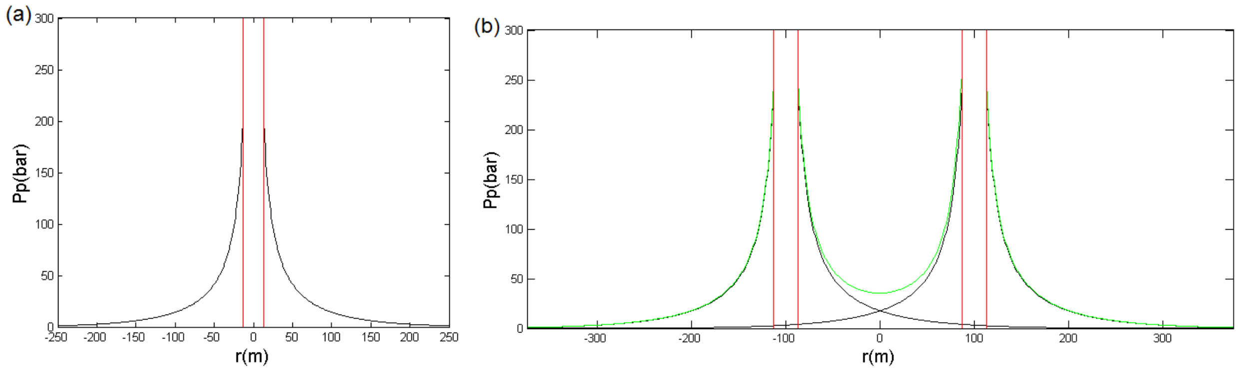

Figure 64: Pore-pressure away from exit point at 2,895 m (9,498 ft) MD in black for (a) single well and (b) well doublet, showing the sum of both wells in green.

6.2 PRESSURE FALL-OFF ANALYSIS

On October 15, a pressure fall off (PFO) test was conducted with the PTS tool set down hole at 1,219 m (4,000 ft) for 10 hours (Figure 65). The log-log analysis of pressure difference (dP) and elapsed time (blue) and its derivative (grey) begins with a ½ slope, and then deviates after approximately 1.5 hours (Figure 66). The ½ slope indicates an "infinite conductivity" fracture behavior near the wellbore. Deviation from the ½ slope is a sign that the well has reached radial flow. The lack of negative slope in the derivative plot indicates that there is no evidence of clear fracture closure observed during the fall-off test period. The log-log analysis and derivative plot is completely different when compared to the same analysis of the 2013 fall-off data (Figure 67). The 2013 PFO data derivative displayed a minimum value between two distinct curves. This behavior resembles a dual porosity reservoir, which could indicate the deep fracture stimulated and shallow casing leak observed.

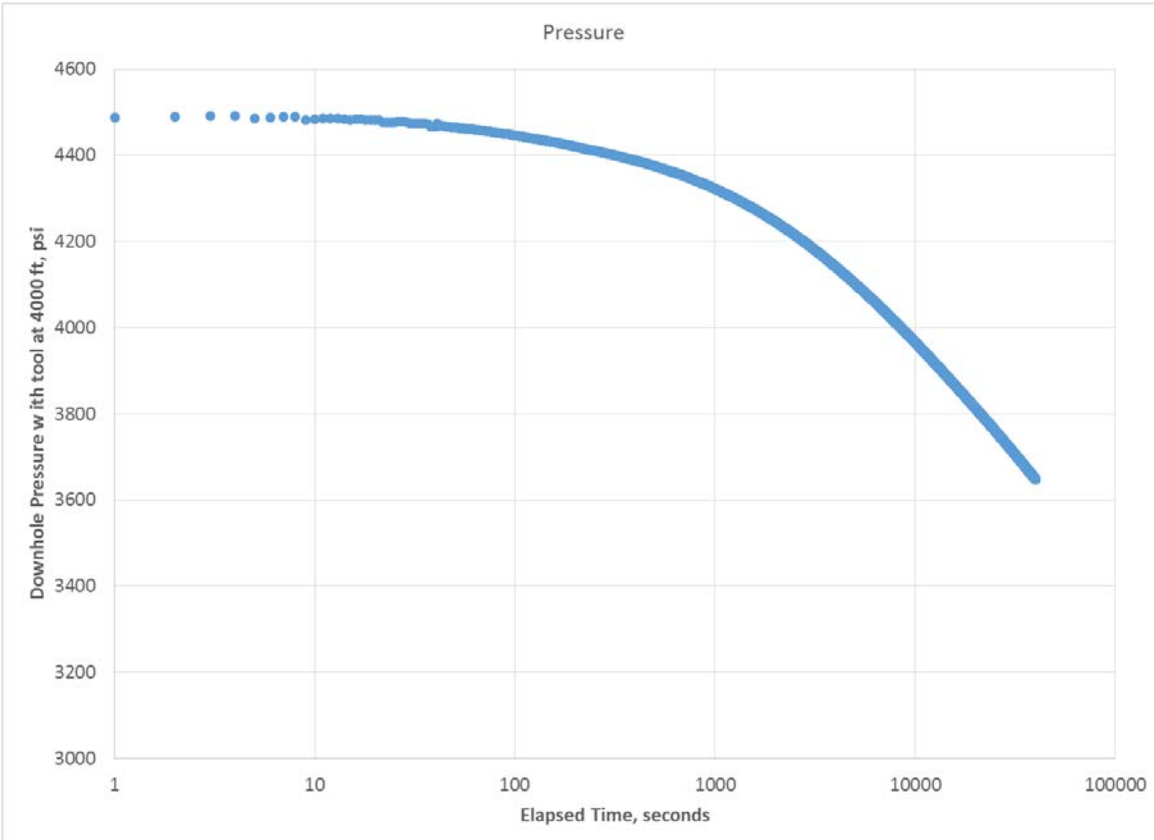

Figure 65. Pressure fall off test conducted on 10/15/14.

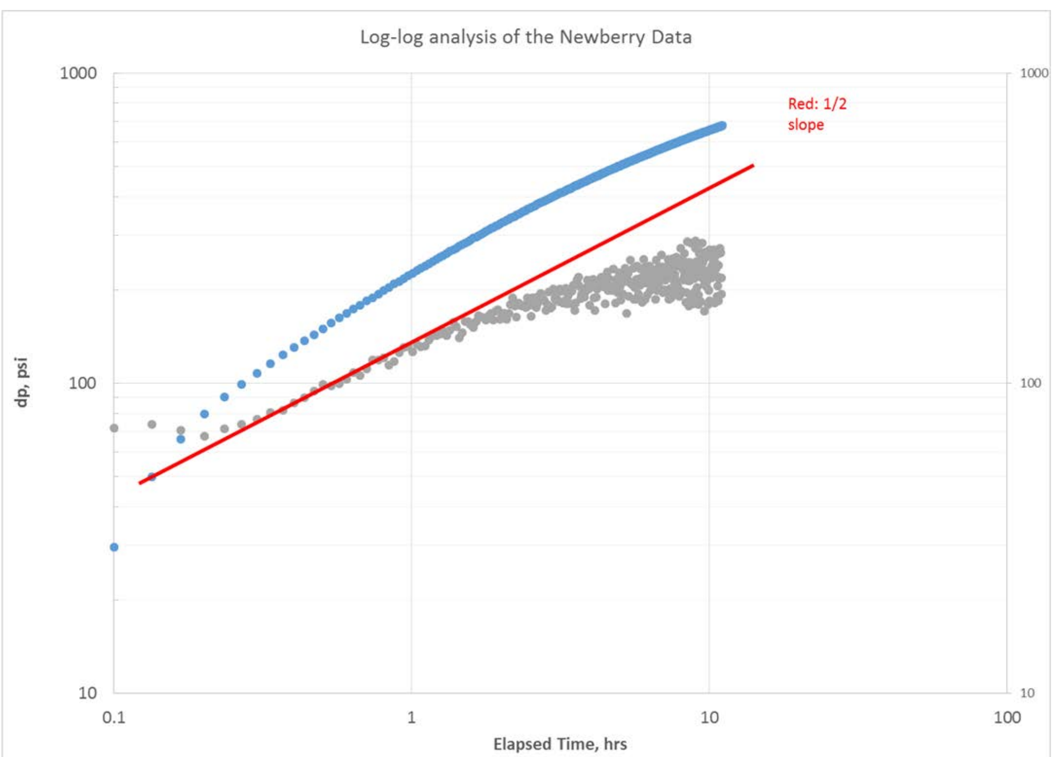

Figure 66. Derivative plot of the 2014 fall off test. dP shown in blue, and derivative shown in grey.

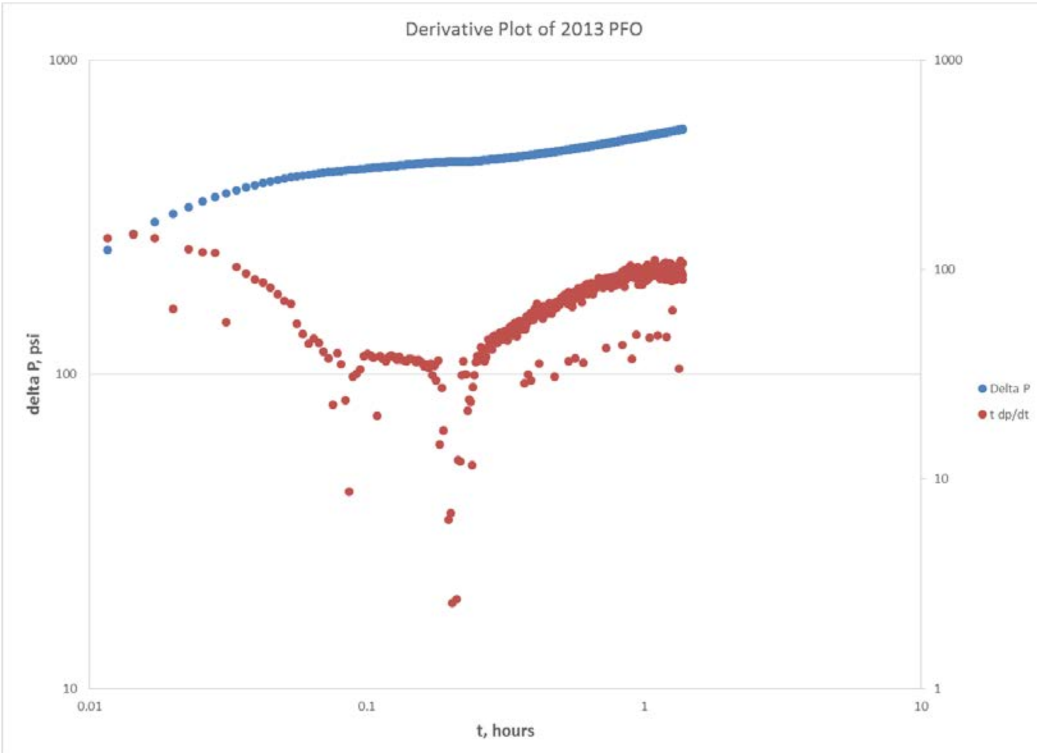

Figure 67. Derivative plot of the 2013 fall off test. dP shown in blue, and derivative shown in red. Two distinctive curve shown in the derivative plot suggest a dual porosity reservoir, potentially due to leak in the casing shallow.

A Horner analysis of the transient period for the 2014 fall-off test produced a semi-log slope of 5.52 MPa/log (800 psi/log) cycle (Figure 68). Using the Horner equation, the calculated transmissivity (kh) is 957 md-ft. And the permeability (k), assuming a reservoir height of 200 m (656 ft), is 1.46 mD. This permeability leads to a calculated skin factor of -6.19, indicating fractured reservoir, and a radius of investigation of 150 m (494 ft).

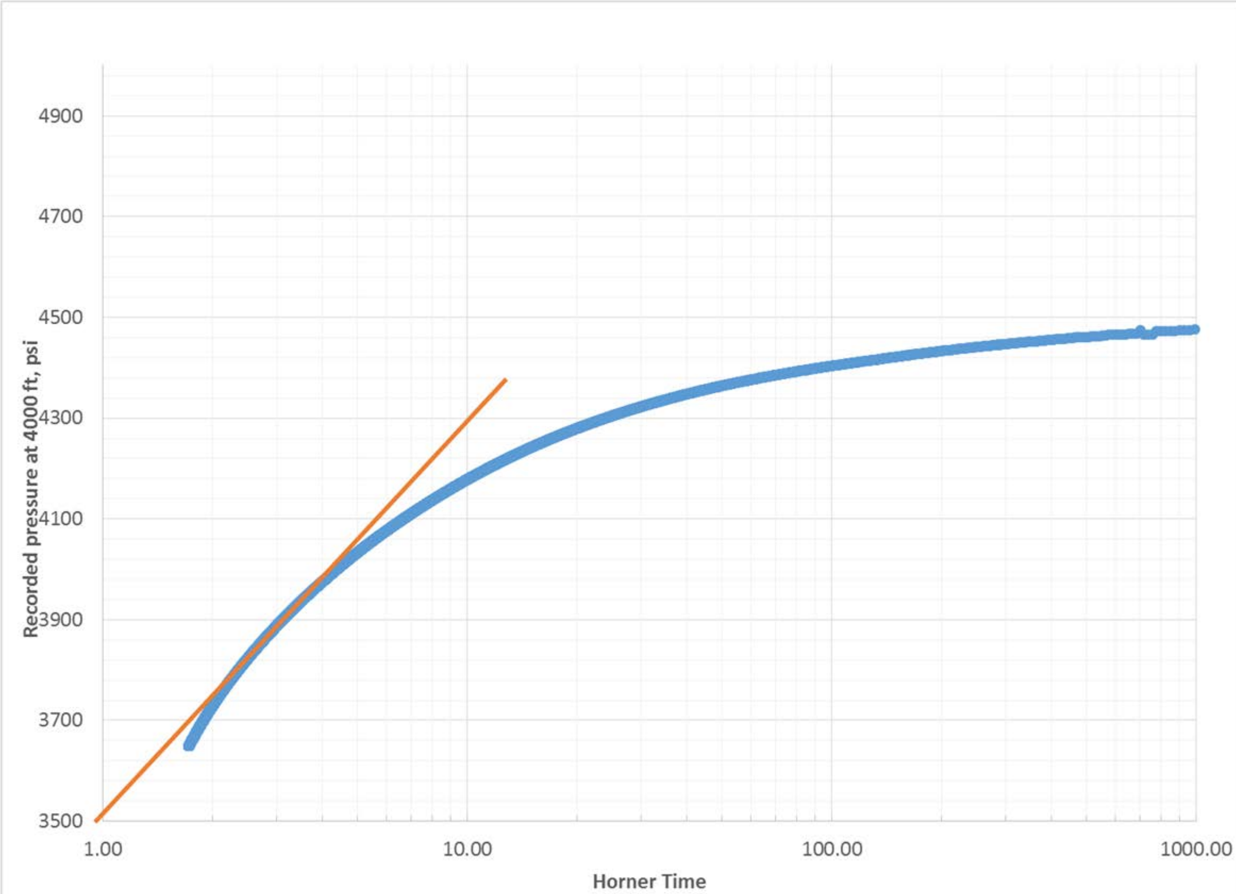

Figure 68. Horner plot of the fall-off test data.

Using the pressure vs square root of time method, the ½ slope period from the log-log plot in Figure 69 can be used to estimate the surface area of the hydraulic fracture (Equation 8). The calculated fracture surface area is approximately 25,500 m^2 (274,100 ft^2) and the fracture half-length is 127 m (417 ft) [assuming 200 m (656 ft) of reservoir height].

$$\Delta p = \frac{4.06qB}{hL_f} \cdot \sqrt{\frac{\mu \cdot t}{k\phi c_t}}$$

(Equation 8)

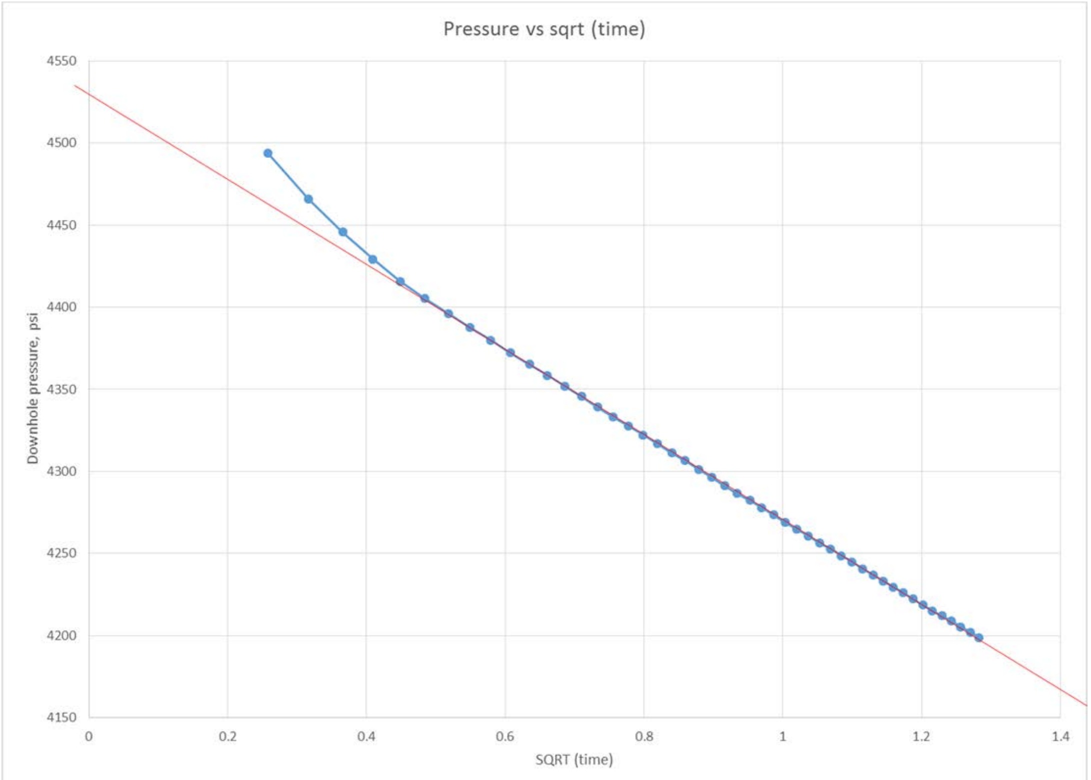

Figure 69. Pressure vs square root of time of the 2014 fall-off test data. Graph showing data from ½ slope period based on derivative plot.

Another method for observing injectivity change and calculating reservoir permeability is through the use of a Hall Plot. The Hall plot method uses continuously monitored injection data to create a cumulative pressure time product vs. the cumulative volume of water injected. A change in injectivity appears as a change in the slope on a hall plot. This cumulative summing method reduces fluctuations in the injectivity index, caused by either inaccurate measurements or transient effects caused by reservoir changes. Figure 70 is the Hall plot of Round 1 of stimulation. The injection pressure potential {[$(Pbh - Pe)\Delta t$, is plotted against the cumulative injection, Wi. Using the injection pressure potential instead of the wellhead pressure reduces error caused by reservoir pressure changes or WHP fluctuations due to pump shut downs. The Round 1 Hall plot shows a steeper slope in the beginning of the stimulation, and a shift in slope after September 28, when an increase in MEQs was observed. The change of slope is an indication of improved injectivity. Using the Hall plot slope from the period 9/28/14-10/15/14 the permeability of the reservoir can be calculated based on Equation 9.

$$m_H = \frac{141.2\mu_w B_w \left(\ln \frac{r_e}{r_w} + s \right)}{k_w h_i} \qquad \text{(Equation 9)}$$

The Hall plot method resulted in a permeability thickness (kh) of 877 mD-ft. Using the same assumption of 200 m (656 ft) reservoir height, the permeability calculated is 1.34 mD or 1 x10^{-17} m^2, comparable to results from the Horner analysis (Table 6).

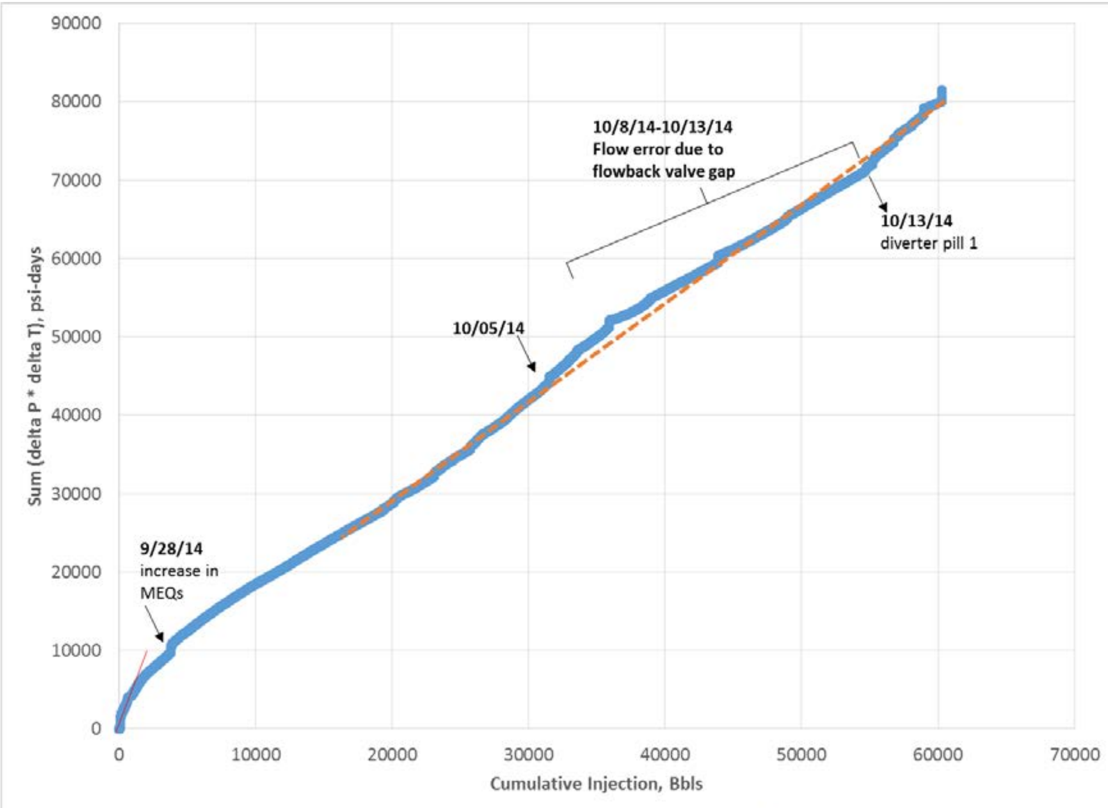

Figure 70 . Hall Plot for round 1 of stimulation at NWG 55-29.

Table 6. Summary of permeability from variety of techniques

Method	Measure	Initial Value	Final Value	Units	Final/ Initial
Pressure vs Flow	Injectivity	0.01	0.05	psi/gpm	5
Horner Analysis (200m high res)	Transmissivity Permeability	$2x10^{-15}$ $1x10^{-17}$	$2.9x10^{-13}$ $1.44x10^{-15}$	m^3 m^2	145
Horner Analysis	Fracture size		25,500	m^2	
Hall Plot	Permeability	$1x10^{-17}$	$1.34x10^{-15}$	m^2	134
R vs time plot	Hydraulic diffusivity		0.006	m^2/s	
THM Model	Permeability (elements <50 m from well)	$1x10^{-17}$	10^{-13} to 10^{-16}	m^2	10-10,000
THM Model (*a priori*)	Bulk Permeability	$1x10^{-17}$	$7x10^{-17}$	m^2	7

6.3 STRESS MODEL

The results of the stimulation with respect to the stress magnitudes and orientations were unexpected; therefore we start with a review of the expected stress regime based on pre-stimulation data.

In October 2010, NWG 55-29 was logged using a high temperature Borehole Tele Viewer (BHTV) manufactured by Advanced Logic Technology (ALT). The borehole breakouts showed a consistent azimuth indicating that the minimum horizontal stress, S_{hmin} is oriented at 092 ±16.6° relative to true north (Davatzes and Hickman, 2011). This azimuth of S_{hmin}, in combination with the attitude of the majority of natural fractures revealed in the image log, are consistent with normal faulting indicated by the regional tectonic setting.

Determining the magnitudes of the three principal stresses is more difficult. In a normal faulting regime, the maximum principal stress is vertical (S_v) with a magnitude related to the weight of the lithostatic overburden. The minimum horizontal stress (S_{hmin}) at a given depth is best determined from an *in situ* stress test, a well test in which S_{hmin} is determined from the fluid pressure at which tensile failure occurs. An accurate stress test requires a short (15 m) section of relatively unfractured well bore to be isolated. Isolation allows for sufficient pressure build-up to cause tensile failure, provides a narrow depth range over which to calculate S_{hmin}, and ensures that the measured pressure response is due to a tensile failure and not hydroshearing. Because NWG 55-29 has over 1000 m of open hole and isolating a short section would require a drilling rig, it was not feasible to conduct a stress test to determine S_{hmin} in advance of stimulation. Instead, S_{hmin} and the rest of the stress model was constrained based on reasonable geomechanical assumptions derived from injection tests and material properties (Davatzes and Hickman, 2011; Cladouhos et al., 2011).

Table 7. Stress model from stimulation planning.

Component	Gradient (MPa/km)	Gradient (psi/ft)	Direction
S_v	24.1	1.07	vertical
S_{Hmax}	23.5	1.04	2° (N-S)
S_{hmin}	14-9 - 15.8	0.66-0.70	92° (E-W)
Ph	8.8	0.39	Fluid pressure

Based on this stress model (Table 7) and numerical modelling (Cladouhos et al., 2011) it was predicted that microseismicity and injectivity improvement would initiate at a WHP of 9 MPa (1350 psi) and that 13-15 MPa (1950–2200psi) would be sufficient to reach the required reservoir volume goal. The 2012 stimulation (Cladouhos et al., 2013a, 2013b) seemed to confirm this prediction with injectivity improvements and deep seismicity (>8000 ft, >2.4 km) initiating at a WHP of 9.3 MPa (1360 psi) and four additional deep seismic events occurring at a WHP of 13.2 MPa (1910 psi). Thus, the need to exceed 16 MPa (2400 psi) WHP to promote stimulation in 2014 (Figure 23) was unexpected. The practical effect is that the stimulation pumps reached their maximum pressure of 20 MPa (2900 psi) on September 29, the sixth day of the stimulation. Surface equipment, shoe depth and regulatory agreements also specified that the stimulation pressures be kept below 20.7 MPa (3000psi), so the pump performance was not the only limit preventing significantly higher pressures.

Figure 71 shows the assumed stress and measured fluid pressure profiles in 55-29. This figure shows that if tensile failure did NOT occur in the formation below the cemented shoe, as the stimulation history and analysis in Section 6.3 indicates, then the minimum principal stress gradient during the stimulation must have been greater than 0.86 psi/ft. This is a much higher rock fracturing gradient, 0.7 psi/ft, than modelled during Phase 1 (Table 7) and also higher than normally assumed during geothermal well drilling and testing, 0.6-0.65 psi/ft (Lou Capuano, Jr., personal comm.).

The high minimum principal stress gradient and thus high fluid pressures needed to initiate hydroshearing and enhance permeability are also reflected in the results of the seismic moment tensors (section 6.2). The moment tensors are consistent with horizontal compression over a wide azimuthal range, and relatively weaker vertical stress. Though this strain and apparent stress configuration derived from the micro-earthquakes is internally consistent, it is inconsistent with the local and regional strain field. Thus AltaRock contracted with Earth Analysis to further investigate the stress field at the Newberry EGS site by modeling other possible sources of stress that could explain the discrepancy between stress models. The paragraphs below are adapted from the executive summary of the report from Earth Analysis. The full report can be found in Appendix F.

Earth Analysis built first-order, quantitative models of four likely source of native stress in the region, to evaluate their contributions to the total stress field and to test whether they can explain the observations from the stimulation seismicity;

1) Tectonic stress, through a regional stress inversion;

2) Local topographic stress;

3) Magmatic stress; and

4) Subduction zone stress.

They found that

1) Regional tectonic stress has a maximum compressive stress trending at 15° and increases with depth at about 0.15 * gz (i.e. about 3 MPa/km). The minimum horizontal compressive stress is tensile and has a most likely value near zero, but may be more strongly tensile.

2) Topographic stresses at the bottom of the injection well have a steeply west-plunging 1 of about 12 MPa, and are consistent with normal faulting on steep, north-striking faults.

3) Magmatic stress, calculated using locations from previous studies and estimated magma production rates since the last eruption (1300 years ago), can feasibly contribute up to 30 MPa of EW compression at the bottom of the well, and other stress components (which may be tensile) in the tens of MPa. The location and size (or, equivalently, pressure) of any magma chambers are poorly resolved at this point, so changes to these parameters can surely reproduce the stress state inferred from the induced seismicity, though this would not necessarily be independently validated.

4) Stresses from the Cascadia subduction zone, modeled as 15 m of slip accumulating below the locked zone of the megathrust, are insignificant at Newberry.

The combined stresses as modeled from comparisons with external data are on the whole inconsistent with the local stress field inferred from the induced seismicity, though it is possible that particular configurations of a magma pressurized magma chamber could increase consistency.

Earth Analysis also analyzed the moment tensors and locations of the induced earthquakes, in order to discern any patterns or correlations that may yield insight into the stress discrepancy. There are few apparent correlations with moment tensor properties and time or location. The most elucidating relationship is that near the center of the cloud, the P-axes of the events point towards the center, while farther away they do not. This suggests that *the fluid injection, with a wellhead pressure of about 20 MPa, is significantly modifying the stress field in addition to simply raising pore fluid pressures* (emphasis by AltaRock). Without additional, careful modeling of this phenomenon, it is not clear whether this could cause the stress field inferred from the seismicity.

Thus AltaRock tentatively concludes that the most likely explanation for the discrepancy between expected (pre-stimulation) stress magnitudes and orientations those derived during the stimulation, is that the fluid injection itself significantly modified the stress field adjacent to the well in addition to simply raising pore fluid pressures. If that is the case, then a production-injection well pair with a low pressure production well and a high pressure injection well, will also modify the stress field in a complex way. Future modelling by LBNL (See section 7) should provide further insight into the potential stress regime during different stimulation and production scenarios.

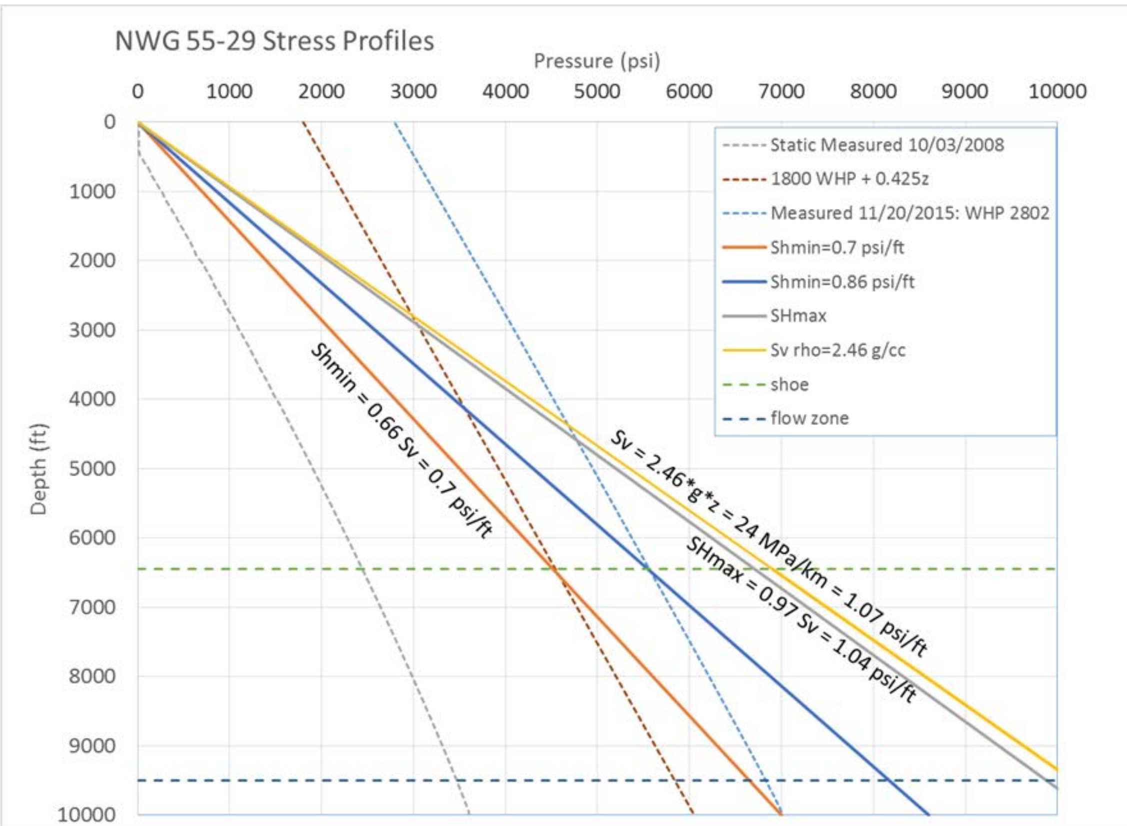

Figure 71. Shows two values for the frac gradient, the pre-stimulation predicted gradient shown in orange and the gradient indicated by the stimulation results shown in the dashed blue.

7 THERMO-HYDROLOGICAL-MECHANICAL & -CHEMICAL MODELING

Measured changes in stimulation injection flow rate, injection pressure, and reservoir fluid geochemistry are used to recalibrate the computational native state model built during Phase 1 of the Demonstration Project (AltaRock, 2011a).

7.1 THM MODELING DETAILS

A 3-D Thermal-Hydrological-Mechanical (THM) computational model of the reservoir conductivity around well NWG 55-29 was developed and calibrated using data from low-pressure injection tests in 2010 and 2013 and the 2012 stimulation. This is a first application of this model's new computational code called TOUGHREACT-ROCMECH, the details of which are described in Smith et al. (2015). The model area shown in Figure 72 is approximately 3,700 m x 2,160 m x 3,360 m (2.29 x 1.34 x 2.09 mi) in size with a 66 x 14 x 93 grid of nearly rectangular elements and is based on Sonnenthal, et al. (2012; 2015). Geology is approximated two-dimensionally around the well, with a north-south strike (Figure 72 ordinate). The modelled volcano surface slopes 160 m upward over 3700 m in the E-W direction (Figure 72 abscissa). Flow, displacement and stress are modelled in three dimensions (3-D) for injection from a 3,028 m (10,050 ft) well with a 1,088 m (3,569 ft) open section situated near the center of the model, in the y=0 plane. Part of the open section (236 m; 774 ft) was treated as cased due to the presence of an unperforated liner. With initial conditions uniform in the strike direction, and appropriate boundary conditions placed at y=0 (no flow, no normal displacement), symmetry allows half the domain to be eliminated. Wellbore and uniform reservoir rock characteristics used in the model are listed in Table 8 and described in Sonnenthal, et al. (2012; 2015). Initial bulk porosities and permeabilities in the reservoir unit were estimated to be 0.03, 5×10^{-18} m^2 (5×10^{-14} in^2) in the E-W direction, and 10^{-17} m^2 (1.55×10^{-14} in^2) in the N-S and vertical (z) directions respectively, with about an order of magnitude higher permeabilities in known fracture zones. Mechanical properties were approximated as isotropic and initially uniform, with a Young's modulus of 45 GPa (6,530,000 psi), a shear modulus of 18.75 GPa (2,719,000 psi) (Poisson's ratio 0.2), which are middling values measured in basalts. Initial temperatures and pressures were steady state values with temperature at the surface held at 12°C (54°F) and at depth held at 365°C (689°F). Initial vertical stresses were vertically integrated gravity forces and smoothed slightly in the horizontal directions. Initial horizontal N-S stresses were 0.975 of the vertical stress, and initial E-W stresses were 0.625 of the vertical stress (as suggested by Cladouhos, et al. 2011), and these were allowed to relax in solution to the stress force balance equation – where the sum of gravity force density and the divergence of stress vanishes. The model uses a 30° friction angle in the Mohr-Coulomb shear failure criteria, and a 2° dilation angle (3.5% aperture/shear) in the failure strain potential. Most cases assume a Mohr-Coulomb material strength of 2 MPa (290 psi). If a failure criterion indicates material failure at a Gauss point then the MC cohesion is assumed to be zero.

Table 8. Hydrological properties for the rock units and wellbore.

Model Area	Model Unit	Porosity	k_x (m^2)	k_y (m^2)	k_z (m^2)
Wellbore	Cased interval	0.95	0.0	0.0	1.5×10^{-3}
Wellbore	Uncased (lined) interval	0.98	1.0×10^{-6}	0.0	7.9×10^{-4}
Reservoir rock	Newberry-Deschutes (upper 300 m)	0.20	1.5×10^{-12}	1.5×10^{-12}	1.5×10^{-12}
Reservoir rock	Newberry-Deschutes	0.04	2.0×10^{-15}	4.0×10^{-15}	4.0×10^{-15}
Reservoir rock	John Day	0.05	5.0×10^{-18}	1.0×10^{-17}	1.0×10^{-17}
Reservoir rock	Intruded John Day	0.03	5.0×10^{-18}	1.0×10^{-17}	1.0×10^{-17}
Reservoir rock	Intruded John Day (lowest 100m)	0.01	1.0×10^{-18}	1.0×10^{-18}	1.0×10^{-18}

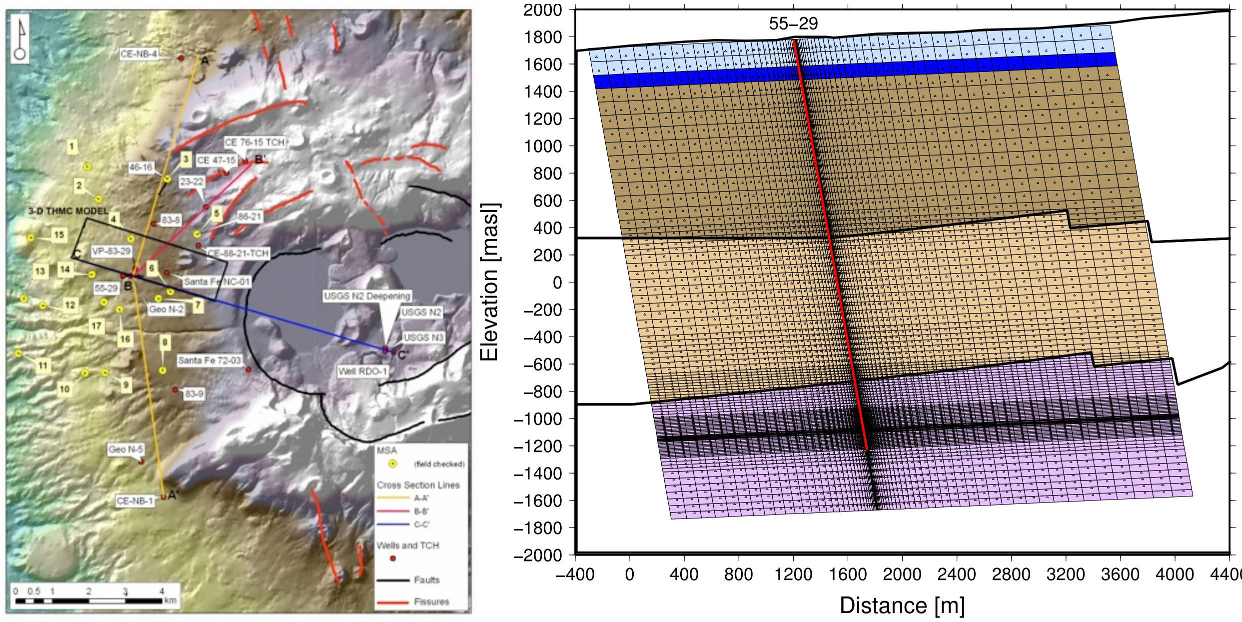

Figure 72. Left: THM modeling domain shown on the west flank of Newberry Volcano (black rectangle). Right: THM model numerical mesh with major rock units and 55-29 well projection at depth.

Heat flow, fluid flow, and stress are modelled using sequential coupling (Kim, et al. 2012). At each modelled time step, flow is controlled by the current porosity and permeability model, and stress is controlled by the most recent changes in pressure from flow. Changes in stress result in coupling terms resulting in changes in porosity. In the current implementation, changes in pressure also result in changes in effective stress, which are tested against Mohr-Coulomb (MC) criteria for shear failure, and against a criteria for tensile failure. Positive criteria indicate material failure. When material fails the return mapping algorithm (Borja, et al. 2003) is used to find the failure strains needed to return the stresses to stresses admissible under the failure criteria. In the return mapping algorithm, changes in failure strains are proportional to the gradient(s) of failure strain potential(s). Each failure criterion has a corresponding failure strain potential - with Mohr-Coulomb friction angle ϕ, replaced by dilation angle ψ. The failure strains proportional to the gradient of the failure strain potential corresponding to the most stringent failure criterion (largest) are used to reduce that criterion to zero. If, after mitigation of the most stringent failure criterion, other failure criteria remain positive, multiple failure occurs, and failure strains associated with remaining largest criterion are also needed. Simultaneous equations are solved for the scales (Lagrange multipliers) of the two failure strains proportional to the gradients of the two relevant failure strain potentials (Borja, et al. 2003). If after doing so, other failure criteria indicate additional failure, triple failure occurs. In the case of triple failure, simultaneous equations are solved for the scales of failure strains needed to return the stresses to stresses admissible under the three successive largest criteria. Criteria held to zero through addition of scaled failure strain potential gradients are considered active. With isotropic mechanical moduli, changes in effective stress due to failure strain have the same principal directions (eigenvectors) as the effective stress, so failure strains in three principal directions are sufficient to return effective stresses to the admissible region of all failure criteria. With isotropic elastic properties, for isotropic changes in effective stress due to an increase in pore pressure from a previously isotropic effective stress, the corresponding failure strain is an isotropic expansion.

If tensile failure occurs, the resultant failure strain is assumed to be normal to the fracture(s) involved. If triple failure occurs the resultant failure strain is presumed to be primarily isotropic with fractures opening normal to their planes. In both of these cases, on the reduction of fluid pressure one would expect fractures to close with decreasing fluid pressure. The return mapping algorithm as sketched above (and in reference [Borja, et al. 2003]) was originally developed for deformation of plastic material, and does not, as such, allow for fracture deflation on fluid pressure reduction. A fairly simple modification to the return mapping algorithm allows reversible opening of tensile failure and triple failure fractures. When tensile failure or triple failure has previously occurred at a point in an element where stresses are computed (a Gauss point), before evaluating failure criteria there, an estimate is made of the previous failure strain due to tensile failure and triple failure. The estimate is removed from the previous failure strain used in computing effective stresses in material failure computations. That is, Gauss points that have had previous tensile opening or triple failure volume expansion are treated as if they had not yet had it, and the tensile or triple failure expansion is computed anew at each time step. If at any time step, a Gauss point that has had previous tensile opening or triple failure volume expansion no longer requires it, then the tensile opening or triple volume expansion is considered closed there, and special treatment is no longer needed until tensile failure or triple failure again occurs there.

After failure criteria have been tested at each point of the model and mitigated as needed through changes in failure strains, the resulting total stress fields may no longer satisfy the force balance equation. So, the stress force balance equation is solved for a new set of node displacements, and the implied strains and stresses recomputed. In re-forming the force balance equation tangential elastic moduli are used in place of the original moduli (Borja, et al. 2003). The process is iterated to convergence or until a maximum number of iterations is reached. Noting that inner products of the gradients of the active failure criteria (3x3 tensors) with the tangential modulus tensor (a 3x3x3x3 tensor) must vanish, tangential moduli are computed by removing the projections of the gradients of the active failure criteria from the range space of the elastic modulus tensor.

Mechanics calculations interact with flow calculations in three ways: changes in volumetric stress (stress trace) which change porosity through a coupling porosity correction term (Kim, et al. 2012), changes in failure volumetric strain which result directly in changes in porosity, and changes in porosity due to failure strain which are considered to increase (connected) fracture porosity and thus increase permeability. Initial conditions were set as follows to model changes in porosity due to failure:

- some portion of the initial porosity is considered to be due to connected fracture porosity (e.g., 0.001);
- a portion of initial permeability is due to fracture permeability (e.g., 0.887);
- model permeability is initially set as the sum of matrix (non-fracture) permeability; and
- the initial fracture permeability is the product of the initial fracture permeability times the cube of the ratio of fracture porosity to initial fracture porosity .

7.2 THM MODELING RESULTS

The model was used to simulate the initial fluid injection into well NWG 55-29. Ten minute averages of measured and modeled injection pressure and flow rate for multiple scenarios based on 21.5 days of stimulation are show in the Figures below.

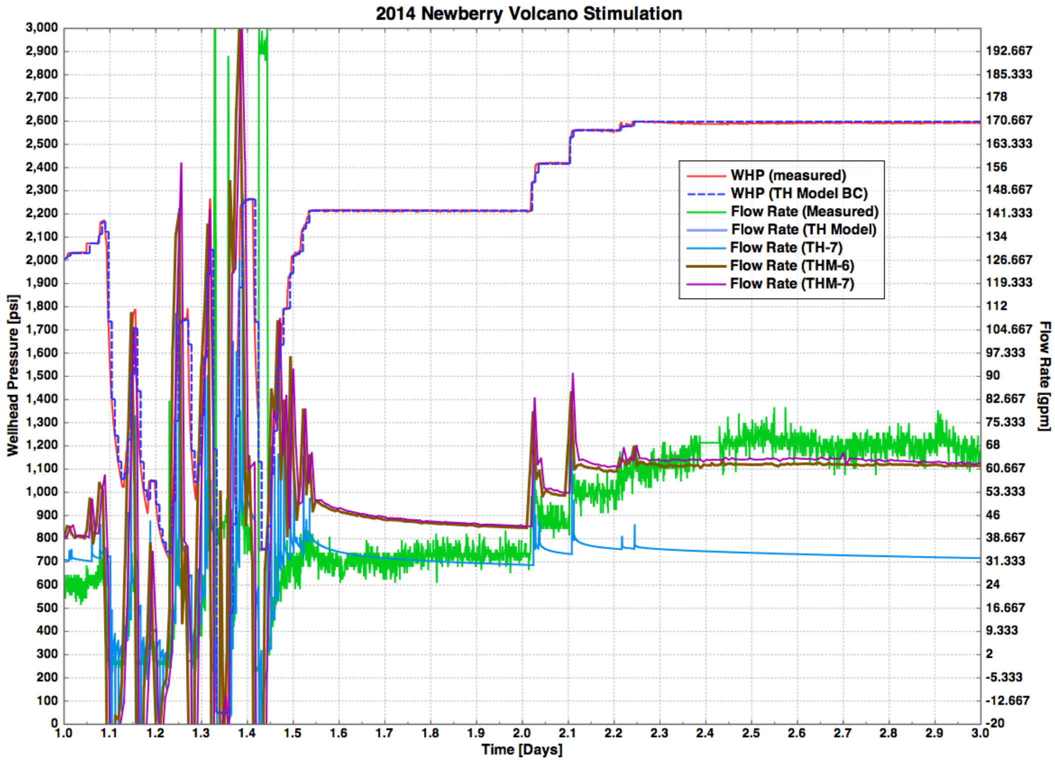

Figure 73. Measured and modeled WHP and flow rate during stimulation days 1-3.

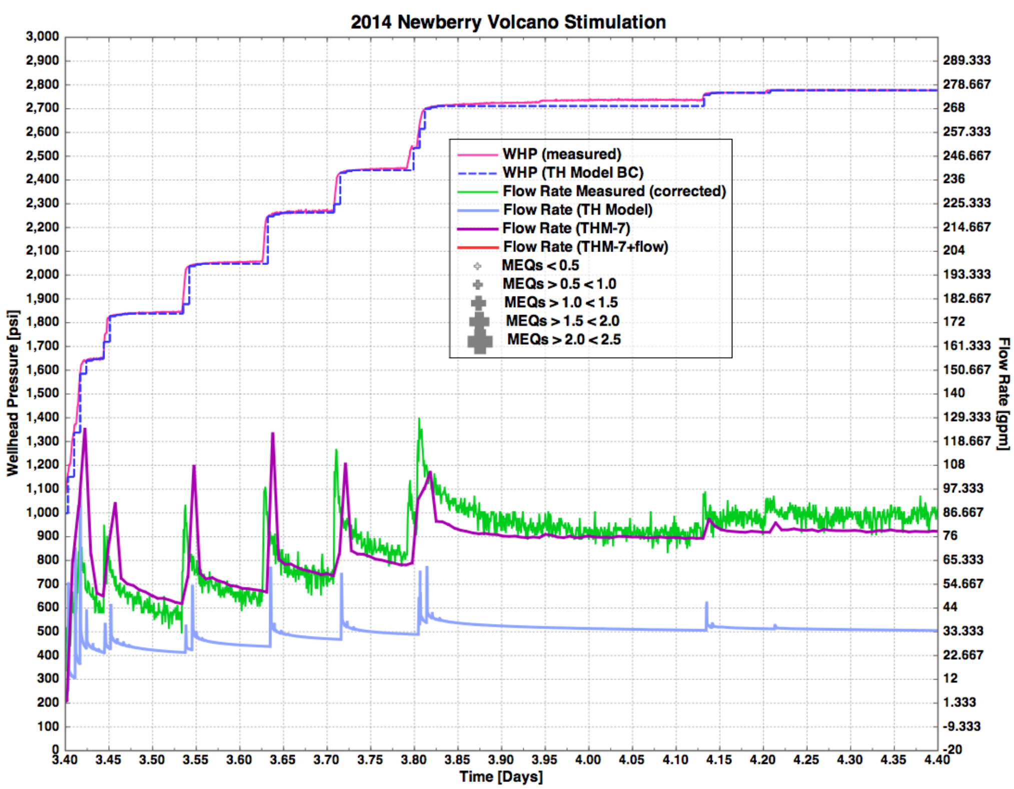

Figure 74. Measured and modeled WHP and flow rate during stimulation days 3.4-4.4.

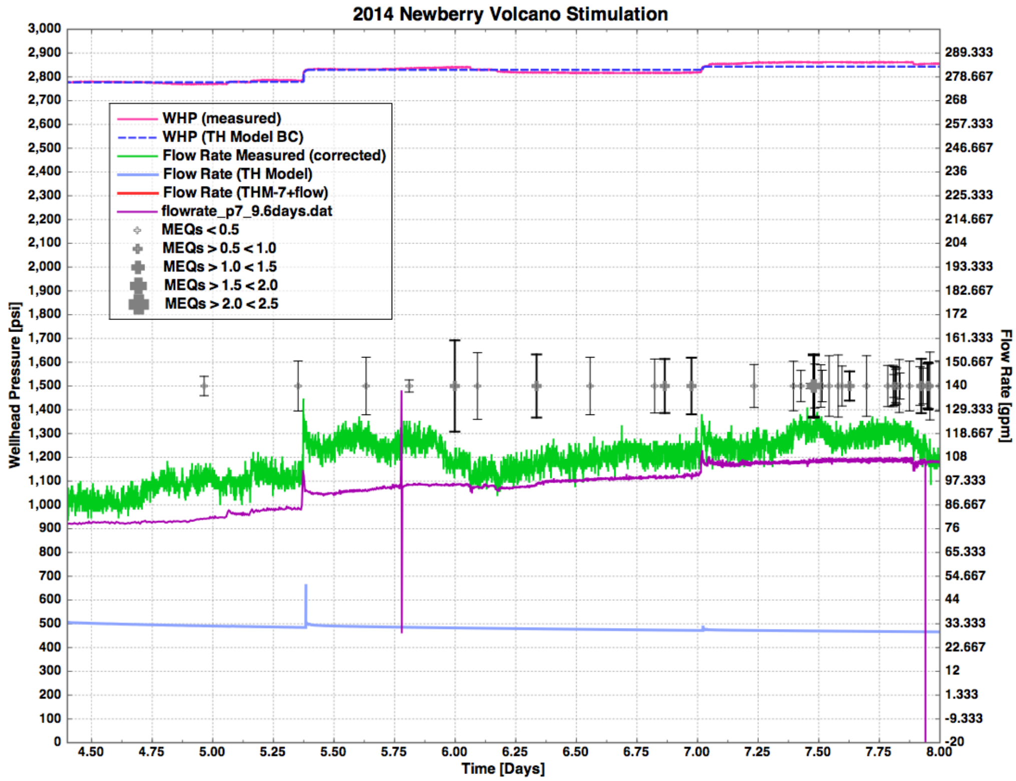

Figure 75. Measured and modeled WHP and flow rate during stimulation days 4.5-8.0.

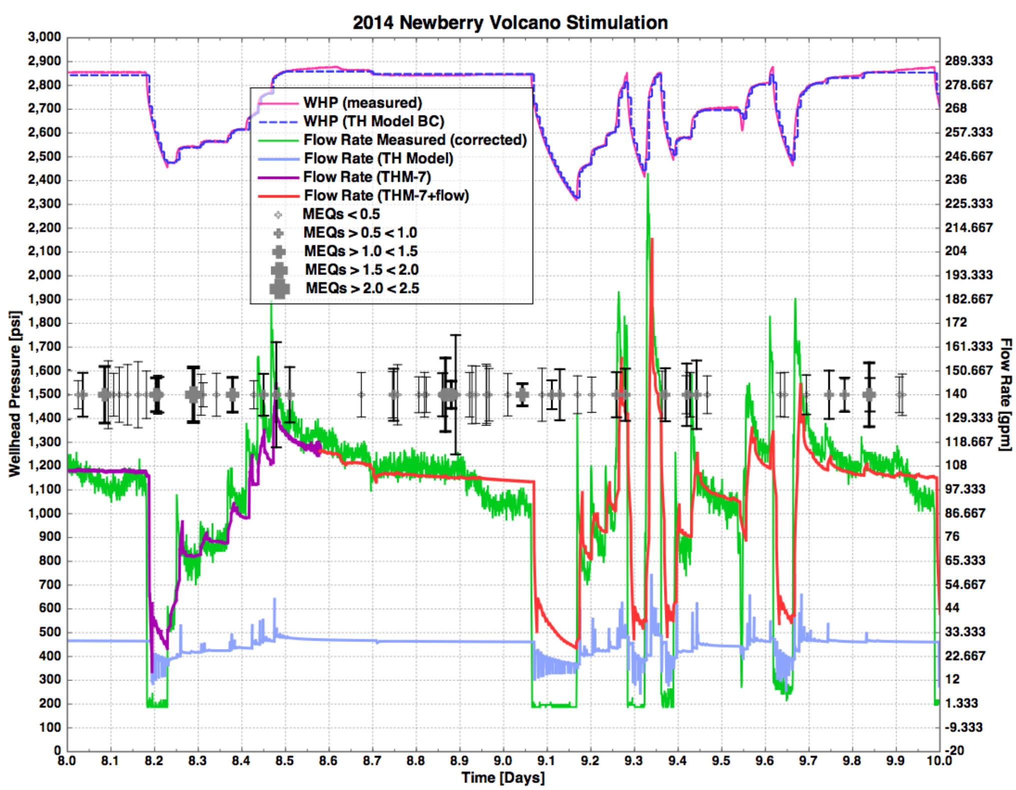

Figure 76. Measured and modeled WHP and flow rate during stimulation days 8-10.

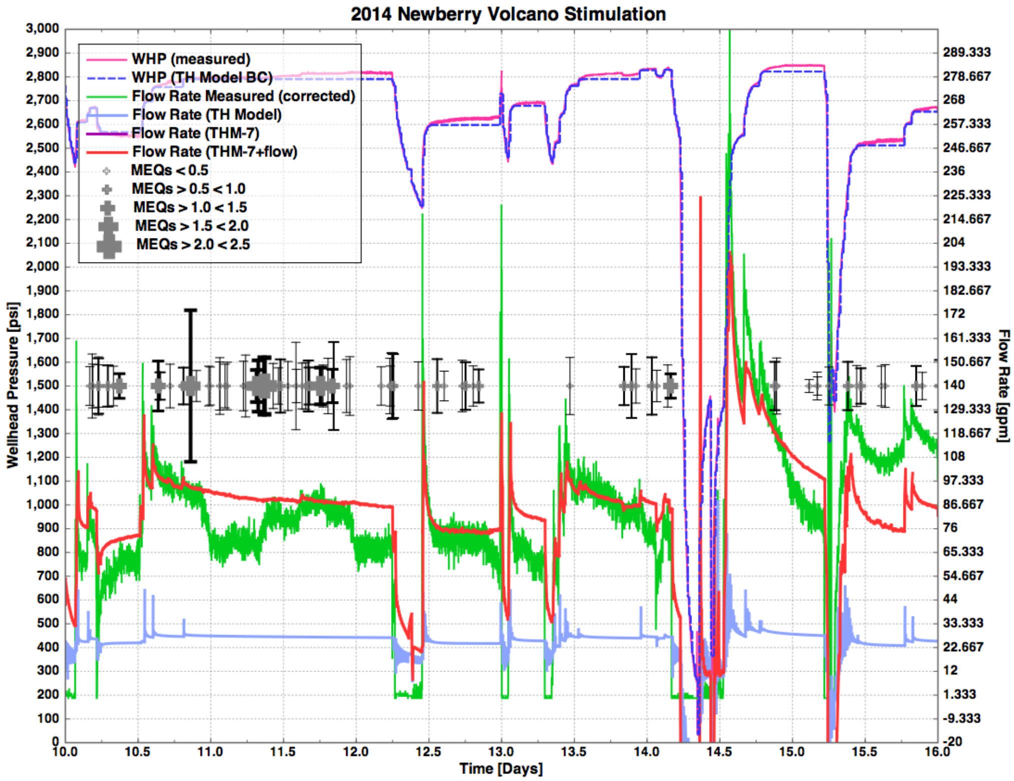

Figure 77. Measured and modeled WHP and flow rate during stimulation days 10-16.

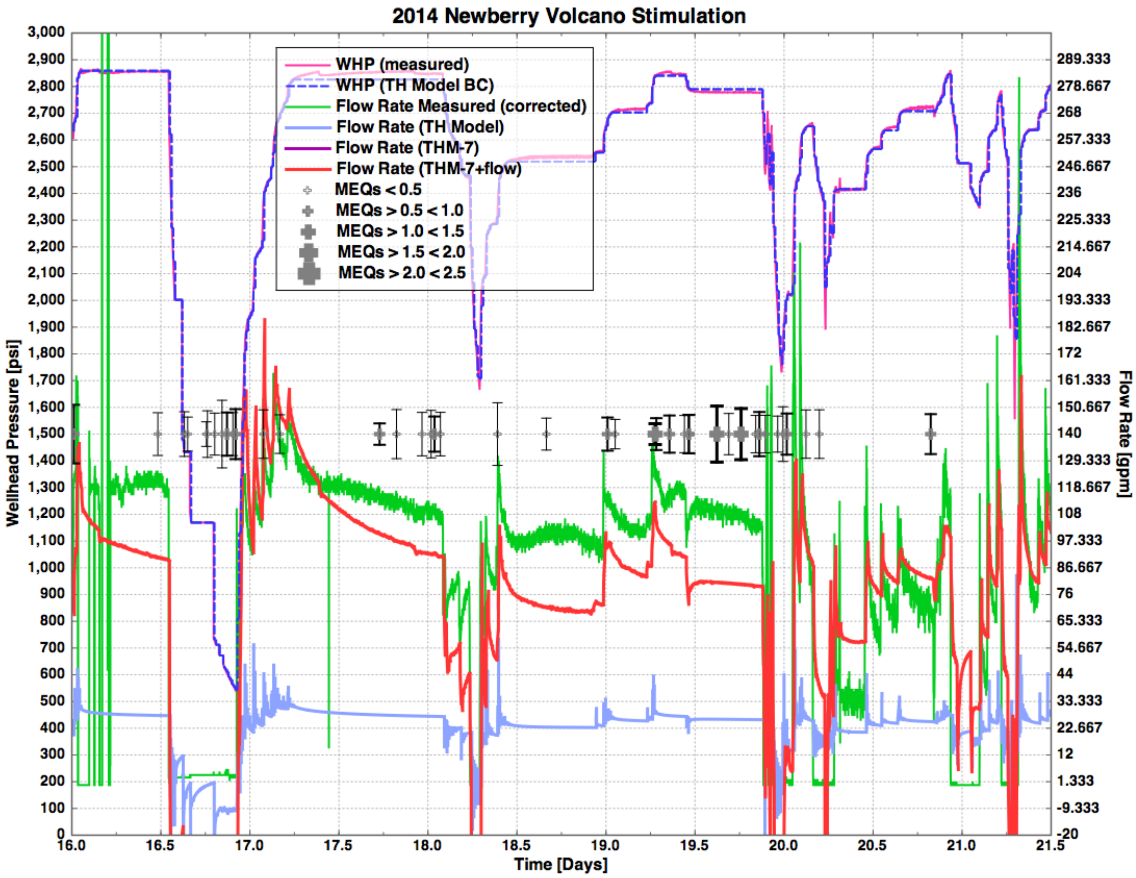

Figure 78. Measured and modeled WHP and flow rate during stimulation days 16-21.5.

Initially, we very roughly approximated the injection pressures as a series of steps from 0 MPa (0 psi) to 17.2 MPa (2,494 psi). We modeled the site considering 0.0004 of porosity to be fracture porosity, and 0.887 of permeability to be fracture permeability, with negligible material strength (MC cohesion), supposing a fracture density of 1/m and a fracture aperture of 11 microns. Using rough approximations for WHP, simulating the initial 206,900 seconds of stimulation results in the injection rates plotted in Figure 79. Simulated flow spikes briefly with stepped injection pressure increases. Simulated flow stabilizes to about 1.04 kg/s after the first simulated pressure increase, and to about 4.45 kg/s (9.81 lbs/s) after the sixth simulated pressure increase. The initial flow rates are a bit above the 1.7 kg/s (3.75 lbs/s) injection rate observed in the first 10^4 s, and quite a bit above the 2.0 kg/s (4.40 lbs/s) rate observed between $1.3x10^5$ s and $1.8x10^5$ s. The number of model elements that have experienced MC failure increases to 100 by $2x10^5$ s. A few elements at the western edge of the grid shear on the first time step, due to a minor error in elements at the boundary there (this has been subsequently corrected). Elements containing the open section of the well, and elements next to it begin to shear after about 1,100 s. Shearing increases greatly after injection pressures step to 8 MPa (1,160 psi). Since the model permeabilities had been previously adjusted to fit flow tests at lower pressures, we considered that shearing was occurring too easily in the model and affecting flow too much. Therefore, a 2 MPa (290 psi) cohesion term was introduced in the MC failure (and in tensile failure) criteria, modelling (perhaps) light cementation in pre-existing fractures. Enhanced modelling capability allowed use of the measured injection pressure history (Figure 79). Resulting simulation injection rates through 217,800 s are plotted in Figure 79, and simulated flow rates match measured flow rates tolerably for the first 10,000 s. The number of model elements that experienced MC failure reaches over 100 by $2x10^5$ s. Shearing is negligible until 8 MPa (1,160 psi) is reached at 48,200 s, and increases sharply once 14.9 MPa (2,161 psi) pressure is reached at 135,400 s.

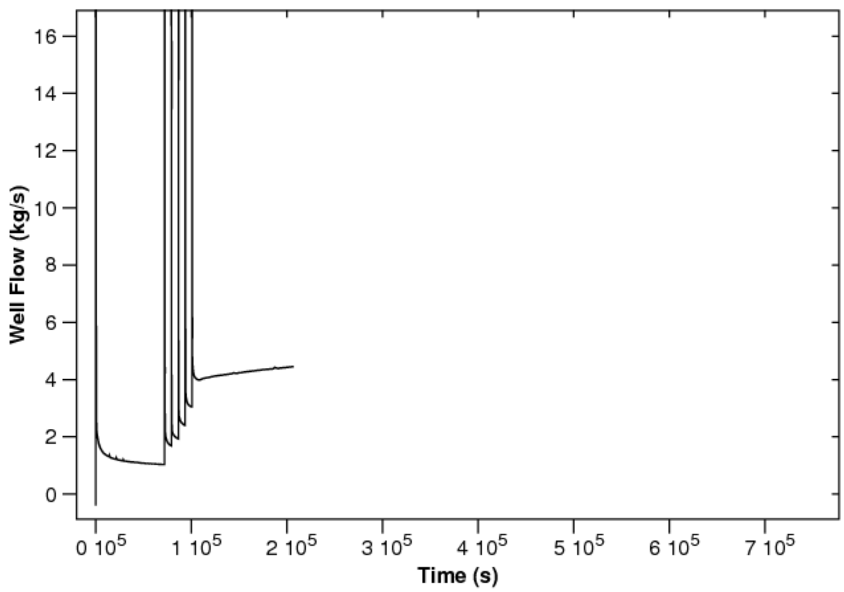

Figure 79. Simulated injection rate, initial 206,900s, for model with 0.0004 initial fracture porosity/porosity ratio, 0.887 initial fracture permeability/ permeability ratio, and negligible cohesion, with stepped injection pressures.

Between 132,000 and 174,400 seconds simulated injection rates are about 6 kg/s (13.22 lb/s), significantly above measured injection rates, and when shearing greatly increases after 135,400 s, simulated injection rates increase much more than measured rates. This suggests that the modeled effect of shearing on permeability should be reduced.

Increasing the presumed initial fracture porosity decreases the effect of failure dilation on permeability because: 1) fracture porosity is the sum of initial fracture porosity and MC failure (e.g., shear) dilation; and 2) fracture permeability is the product of the initial fracture permeability and the cube of the ratio of fracture porosity to initial fracture porosity. As long as the ratio of initial fracture permeability to total permeability is near one, its value has much less effect on changes in permeability due to MC failure. Thus, the model ratio of initial fracture porosity to total porosity was increased to 0.03333 (and the ratio of initial fracture permeability to initial total permeability increased to 0.999), while keeping all other model parameters constant (including 2 MPa [290 psi] MC cohesion).

Computed injection rates are plotted in (Figure 80) again using the 10 minute averaged well head pressures as a boundary condition at the well head. The effects of MC failure on porosity are very slight in this model, and it does not match the increased measured injection rates seen after 174,600 s. The number of elements experiencing MC shearing in this model surpasses 100 by $2x10^5$ s. Decreasing the initial ratio of fracture permeability to total permeability to 0.001 and assuming an initial ratio of 0.995 fracture porosity to total porosity, results in injection rates plotted in Figure 80. This captures much of the rise to injection rates near 6 kg/s seen in the measured injection rates (Figure 73). The numbers of elements experiencing MC failure in this model increase to over 1000 by $7x10^5$ s. The greatest rates of increase in the number of elements with MC failure occurs when well head pressure is above 1.78 MPa (258 psi) from 192,600 s to 261,600 s and again after 329,400 s. Most of these have failed in either single or double MC failure, although 30 elements along the open well and 5 elements adjacent to it undergo general expansion from triple MC failure. The integrated amount of volume expansion during material failure is plotted in Figure 81a, divided into portions occurring during single MC failure in elements, double MC failure in elements, and triple failure in elements (resulting in direct expansion). Single MC (shear) failure contributes about half of the total volume of fractures opening, and double MC failure contributes about one third. Centers of elements undergoing failure are plotted in Figure 81b, with vertical coordinate relative to the well head. The spacing between symbols gives an indication of the distances between grid element centers. Affected elements are clustered around the well, with a hiatus between the upper section of open well and the lower section of open well. Lack of a similar hiatus in observed seismicity may indicate that significant flow is occurring alongside of the liner there.

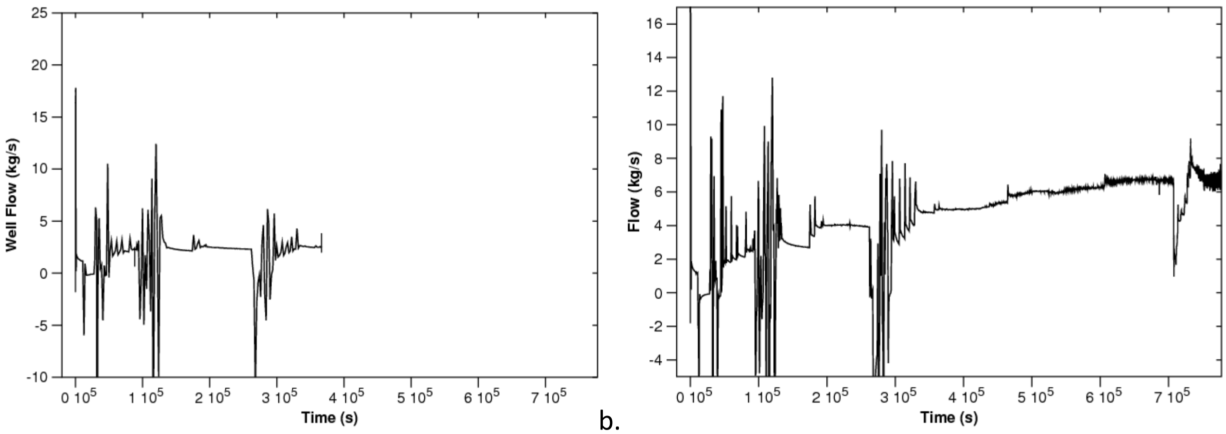

Figure 80. (a) Simulated injection rate, initial 366600s, for model with 0.0333 initial fracture porosity/porosity, 0.999 initial fracture permeability/permeability, and 2 MPa material cohesion, and using measured injection pressures. (b) Simulated injection rate, initial 777600 s, for model with 0.001 initial fracture porosity/porosity, 0.995 initial fracture permeability / permeability, and 2 MPa material cohesion, using the measured injection pressures.

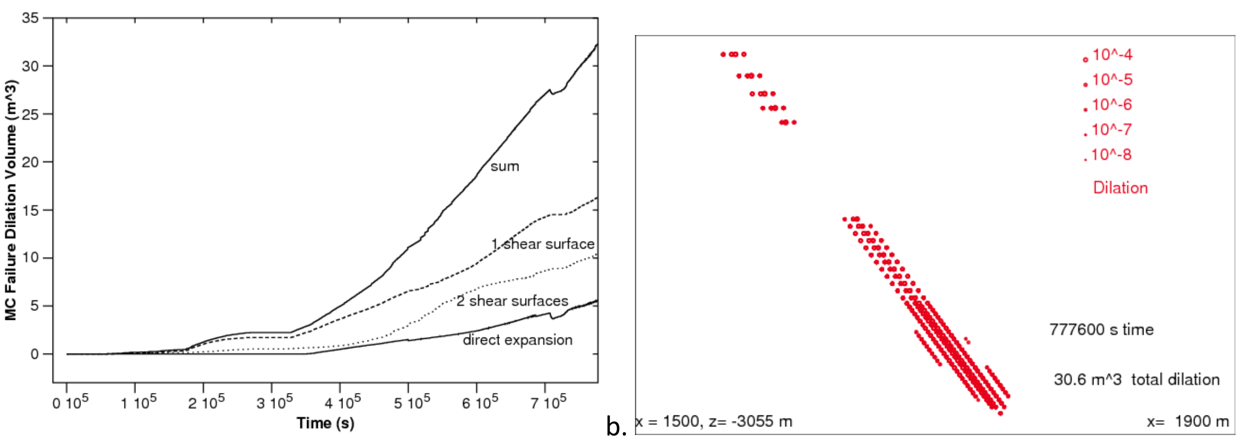

Figure 81. (a) Integrated volume expansion (crack opening) from Mohr-Coulomb failure, divided into parts occurring during shearing on a single surface, shearing on a pair of surfaces, and on triple failure (general volume expansion). (b) Location of model elements undergoing MC failure in first 777,600 s of injection; vertical coordinate is relative to well head.

Finally, the model was also run with a smaller Mohr-Coulomb dilation angle of 0.6° in place of 2°. One would expect to have 0.3 as much dilation per shearing as in the previous model. The assumed initial ratio of fracture porosity to porosity was dropped to 0.0007, although 0.0003 would have made for a case more directly comparable with the previous model, as then the change in permeability per amount shear would be identical. Calculated injection rate is plotted in Figure 82. The modeled injection rates are very similar to those measured. The effects of MC failure on porosity are very slight in this model, and it does not match the increased measured injection rates seen after 174600 s. This is not surprising as the ratio of fracture porosity ratio to dilation angle differs here by only about 30% from that of the model giving the results.

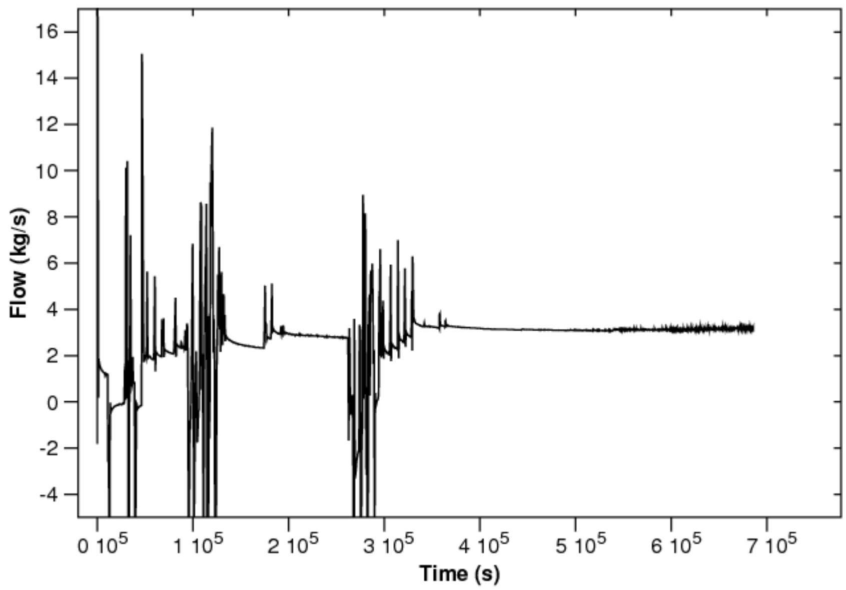

Figure 82. Simulated injection rate, initial 685800s, for model with 0.0007 initial fracture porosity/porosity, 0.995 initial fracture permeability/permeability, 2 MPa cohesion, and 0.6 degrees MC dilation angle, and measured injection pressures.

Another important constraint on the results of TOUGHREACT-ROCMECH model is the temperature distribution in the wellbore as a function of injection rate and time. Thermal stimulation is a well-known aspect of stress drop and fracture propagation in geothermal systems (Tarasovs and Ghassemi, 2012). The model was tested and calibrated starting with the 2010 static profile and flow tests, the 2012 Stimulation, and the 2013 flow test. TOUGHREACT-ROCMECH showed excellent matches to temperatures measured throughout the 2012 stimulation despite many changes in wellhead pressures and flow rates (Figure 83). The excellent agreement over the full time of the stimulation, indicated that there had been very limited permeability changes in the open hole section. During the first two days of the 2014 Stimulation, the TH Model was close or over-predicted the temperature decline in the wellbore, also indicating that there had been little or no permeability increase in 2012, and possibly even some permeability decline owing to mineral precipitation. By October 1, 2014, temperatures in the wellbore were at their lowest values through the stimulation and were as much as 70°C lower than the TH Model prediction, which captured all prior temperature profiles. The THM simulations that matched the flow rates so well had a modified wellbore for the FEM Model that is re-gridded from the TOUGHREACT MESH. Although they matched the pressures and flow rates exceedingly well, these models averaged the temperatures over the wellbore, casing, and about a radius of one meter of rock. Therefore these averaged temperatures over short time periods of the stimulation were too high.

TOUGHREACT-ROCMECH was further improved and was able to run the exact MESH that matches temperatures quite well. The fine gridding around the well though tends to induce more localized shear failure and thus leading to higher permeabilities and higher flow rates given the assumed proportion of total porosity that is existing fracture porosity (0.002), and the estimated drained bulk modulus (10.4 GPa). The Poisson's ratio was modified from 0.2 to 0.235, based on the LBNL MEQ relocations. This led to slightly larger early permeability changes (up to a maximum of 4 orders of magnitude, but typically less than 3 orders of magnitude) in the new simulations relative to the results shown earlier in this section. They are still running so it is not clear if over longer time periods the permeability changes will not increase faster than those observed. From these results it is clear that the significant permeability increases around the well are necessary to increase the flow rates over the initial permeabilities. Many sensitivity studies are underway to evaluate different mechanical properties based of seismic data, lab experiments, fracture measurements and relationships between undrained and drained moduli.

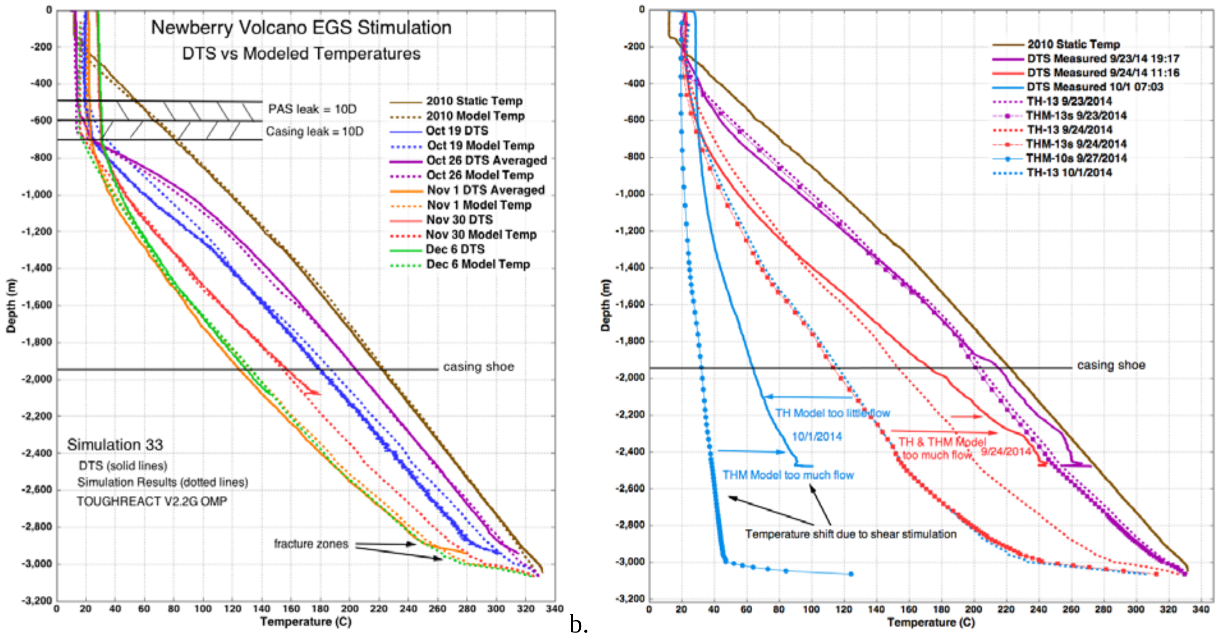

Figure 83. (a) Temperature profiles (solid-measured and dotted-modeled) for 2012 Stimulation using TH Model with no permeability increases owing to failure (only modification to model was the addition of a shallow casing leak after 5 days of stimulation. (b) Temperature profiles (solid-measured and modeled) for 2014 Stimulation. Dotted lines are TH model results. Dashed with symbols are preliminary THM Model results.

7.3 THM CONCLUSIONS

Preliminary simulations of the EGS Demonstration Site at Newberry Volcano were made using a 3-D THM model, and simulated with the recently developed TOUGHREACT-ROCMECH code. We find that the first 9 days of the September/October hydraulic stimulation can be modeled fairly well using a permeability and porosity model based on references (Sonnenthal, et al. 2012, 2015) using a Mohr-Coulomb model for shear failure with a 30° friction angle and a 2° dilation angle, assuming that 0.001 of initial porosity is fracture porosity, and most initial (e.g., 0.995) permeability is due to flow in connected fractures (fracture permeability). Limited simulation runs suggest that fairly similar results are obtained if the ratio of the ratio of initial fracture permeability to (the sine of) the Mohr-Coulomb dilation angle is held constant while varying the two parameters together. In the simulations, the ability to model double Mohr-Coulomb failure (simultaneous failure on two non-parallel sets of surfaces) is important as roughly one third of the total volume of fracture opening is seen to occur in double failures. Similarly, the ability to model triple MC failure is may be important as 1/6 of the total volume of fracture opening occurs in this way. However, that is limited to elements containing the open well bore or immediately adjacent to them and may have less consequence on permeability changes at distance from the well bore.

In addition to full multiphase reactive-transport capabilities, TOUGHREACT-ROCMECH also couples thermohydromechanical rock deformation (poroelasticity), shear and tensile failure, with coupling to porosity and permeability changes. The THM model has captured the approximately 4-fold increase in injection rates quite closely, as well as the spatial distribution of permeability increases and pressure changes. The overall spatial distribution of microseismicity can be captured with an approximately 0.1 MPa increase over the hydrostatic pressure. New geochemical data is being incorporated into a full THMC analysis of the test to further constrain fracture properties such as surface area, porosity, and permeability.

7.4 FLOWBACK GEOCHEMISTRY ANALYSIS

Water and gas samples were collected during flow back to evaluate the spatial extent of permeability changes associated with shear/tensile failure, fracture porosity, surface area, and aperture, combined with thermal-hydrological-chemical-mechanical (THMC) modelling using TOUGHREACT-ROCMECH (Kim et al., 2012; 2015). Samples were analysed for aqueous and gas geochemistry and stable isotopes (Ca, Sr, O, H, and He). Despite widespread use of isotopes in evaluating processes in geothermal systems, few have been integrated rigorously into coupled THMC models. The GeoT software program was used to assess reservoir geothermometry based on geochemical speciation and the multicomponent geothermometry method originally developed by Reed and Spycher (1984), and using thermodynamic data primarily from Reed and Palandri (2006). Reservoir temperatures are estimated from statistical analyses of mineral saturation indices computed as a function of temperature. The program allows unknown or poorly constrained input parameters to be estimated by numerical optimization using known parameter estimation. This integrated geothermometry approach presents advantages over classical geothermometers for fluids that have not fully equilibrated with reservoir minerals as was expected at Newberry given the short residence time of the injected water. Combined with THMC models of the stimulation and flow back it will allow for much more constrained estimates of fracture surface area and permeability as done by Wanner et al. (2014) for up flow along faults in the Dixie Valley geothermal system. Some predictive THC simulations were also performed to assess the mineral-reactions around the injection zone using the newly parallel code TOUGHREACT V3-OMP (Sonnenthal et al., 2014; Xu et al., 2011, 2006).

Three sets of flow back waters were collected during the 2014 Stimulation:

1. 10/7/14: the five hour flow back
2. 10/23/14 - 10/24/14: Flow back after first stimulation
3. 11/24/14 – 11/26/14: Flow back after second stimulation

Cation and anion sample analyses for the first and second flow backs are mostly complete, and isotopic analyses on the second flow back are 75% complete, and samples from the final flow back are still being analyzed. Most of the data shown in this section are from the second flow back, for which multiple water and gas samples were collected and prepared for different measurements.

7.5 FLOWBACK GEOCHEMISTRY RESULTS

Geochemical data from the 2014 flow back water show a systematic trend from heated groundwater to waters showing significant water-rock reaction (Figure 84). The first four samples, collected every hour and starting approximately 45 minutes after the well was reopened after the one week shut-in, show similar trends with respect to most cations and anions (Figure 84 & 85). Although these samples should be identical to groundwater, significant deviations occur for a few elements.

Based on Sr isotopic data (see Section 7.6), and elemental data, the latest injection waters had included water from the October 7 flow back that was mixed with the later injected groundwater in the sump pond. These mainly affected elements that were much higher in the flow back water than in the groundwater, since the amount of admixed water was likely only 10% or less. Strong decreases in Mg in the first four samples and those coming from the open well interval are likely a result of amorphous Mg-silicate precipitation during groundwater heating in the casing, precipitation of chlorite in rock, followed by mineral re-dissolution in the casing during flow back (Figure 84). Increases in Ca, followed by a sharp decline reflect calcite dissolution and precipitation at higher temperatures (Figure 84). In addition to significant water-rock interaction, conservative species such as Cl show sharp increases in the flow back waters indicates mixing of injected groundwater with a small amount of more saline *in-situ* geothermal/magmatic fluid (Figure 84).

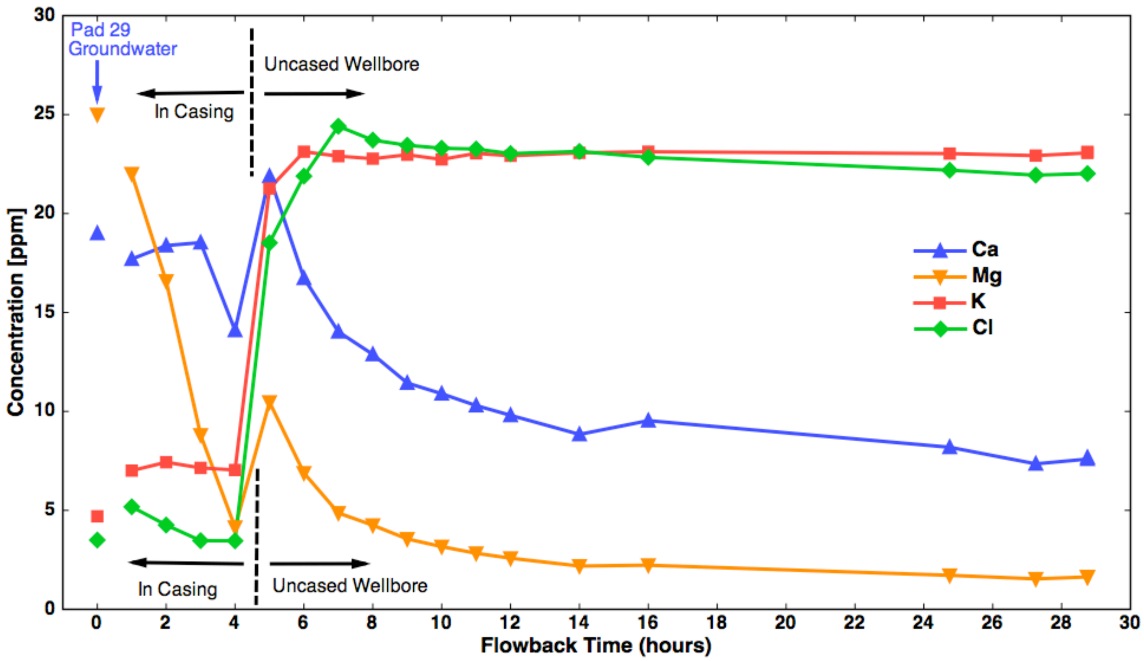

Figure 84. Geochemistry of produced flow back water with time.

The silica vs. sulfur plot (Figure 85) also shows unreacted groundwater at the lower left with nearly identical compositions, followed by increasing silica over time and temperature. Total sulfur (sulfate and sulfide) increases early on through reaction with sulfides (e.g., pyrite) but then declines likely as a result of boiling and degassing H_2S. The sharp transition in concentrations with only a one hour period separating the two groups of samples, indicates plug-flow and little mixing in the wellbore during flow back. Declines in total sulfur may also be a result of fluids coming from deeper zones with less abundant pyrite, as evidenced in the mineralogical descriptions and XRD analyses from the chip samples.

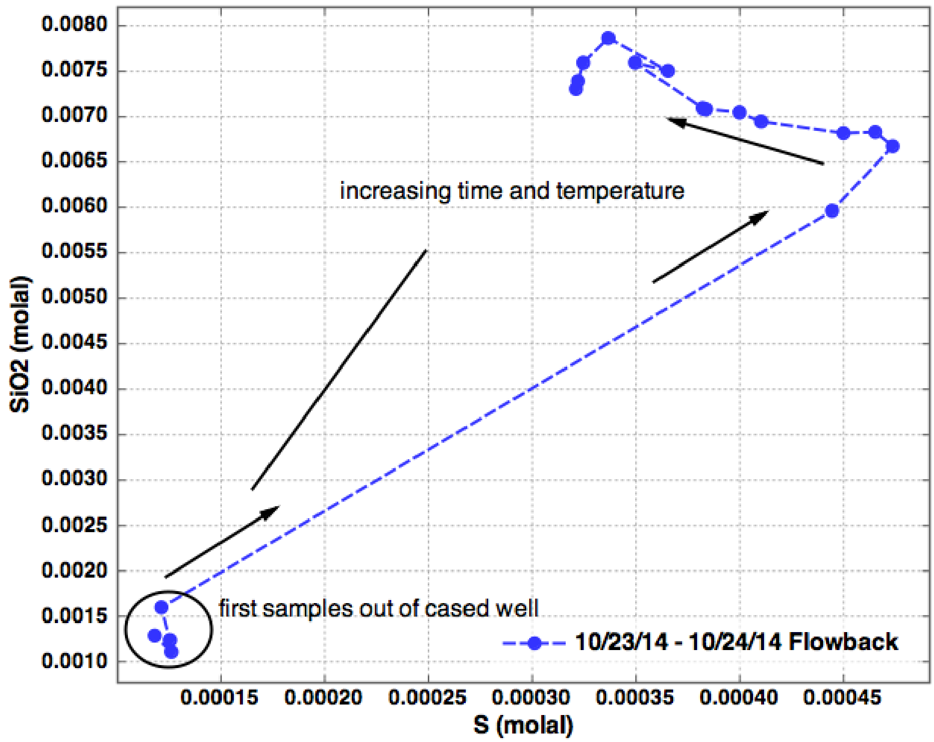

Figure 85. The relationship between silica and sulfur in the waters produced from well NWG55-29 during the 2015 flow back period

The plot of Ca:Sr versus Na:K (Figure 86) shows fairly uniform Na:K ratios in the first four samples during flow back (with low Na:K of approximately 9.5), followed by all other samples showed significant water-rock reaction (higher Na:K of about 13). Ca:Sr continuously declines primarily due to Sr increases in the first 4 samples and Ca decreases in the open interval. One sample collected during the partial flow back on October 7 (red symbol) shows a nearly a 50% mixture between unreacted groundwater and water that had contacted hot reservoir rock. More samples from this first flow back are currently being analyzed since they were collected prior to any admixing with the injection water.

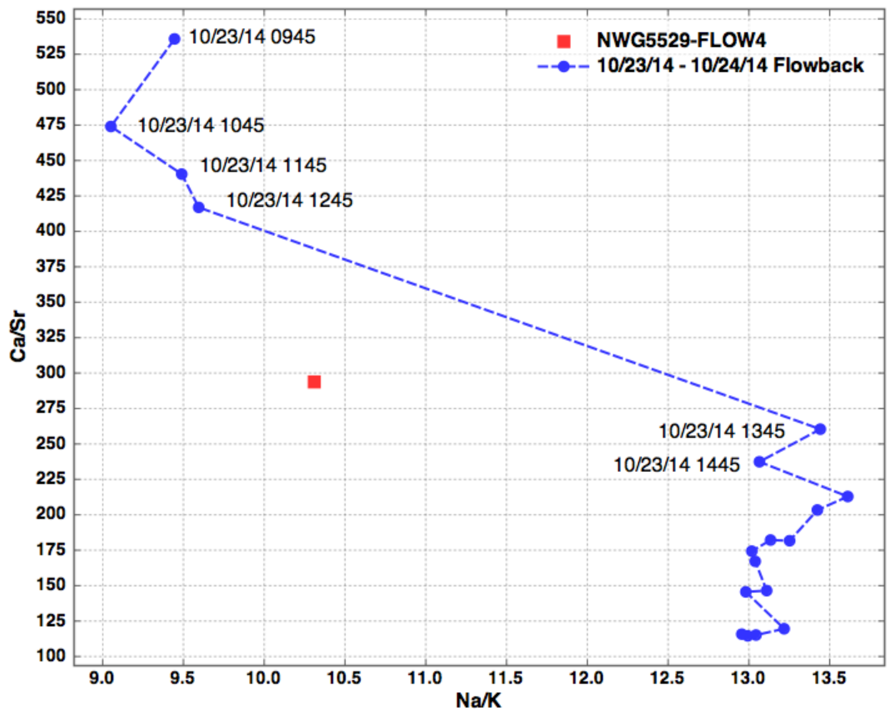

Figure 86. The relationship between the calicum:strontium and sodium:potassium ratios in the waters produced from well NWG55-29 during the 2015 flow back period

The Piper diagram (Figure 87) shows the trends in water chemistry over time, with samples labeled according to the order of collection. Total Na+K shows the clearest trend to higher concentrations.

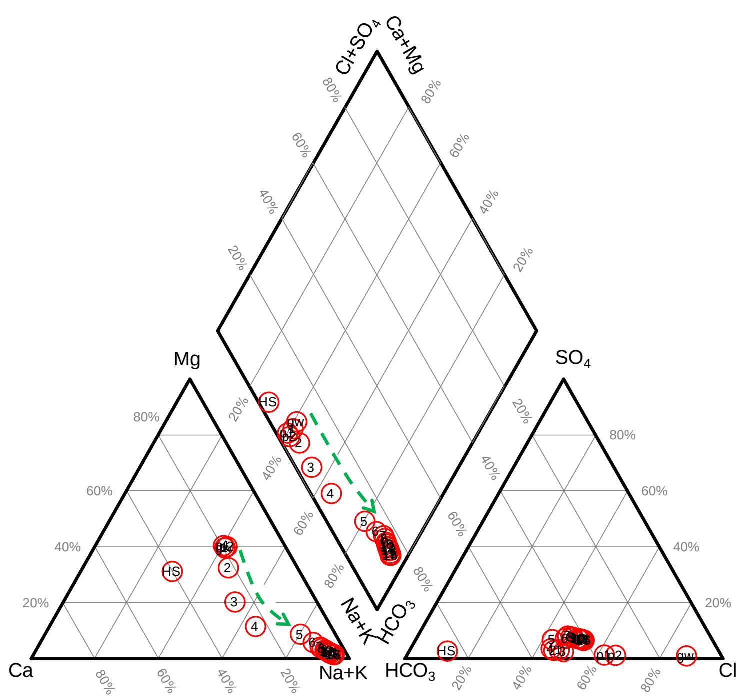

Figure 87. Piper diagram of the flow back geochemistry showing geofluid chemical evolution

Figure 88 shows the trends in Na and Cl, K and Cl, and K and Na over time (molal). Late Na/K ratios correspond to temperature approximately 250°C, based on the Fournier and Truesdell Na-K geothermometer (1973).

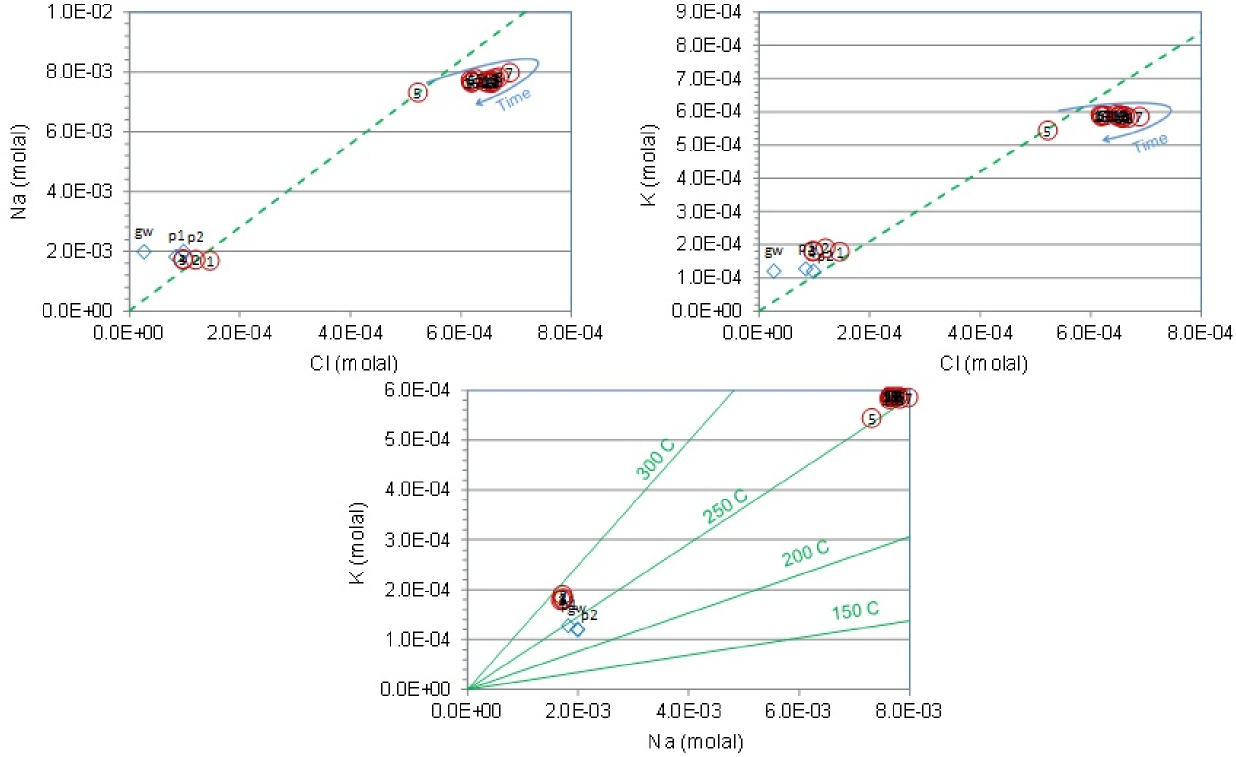

Figure 88. Alkali and alkaline earth element flow back geofluid chemical evolution

Figure 89 shows total S including SO_4 and HS that has oxidized. Fe-S, As-S correlations indicate interaction with pyrite and/or other sulfides. Concentrations reverse (decrease) with time after initial increase. This may be due to sampling waters from deeper intervals with fewer sulfides and/or boiling and precipitation in the wellbore.

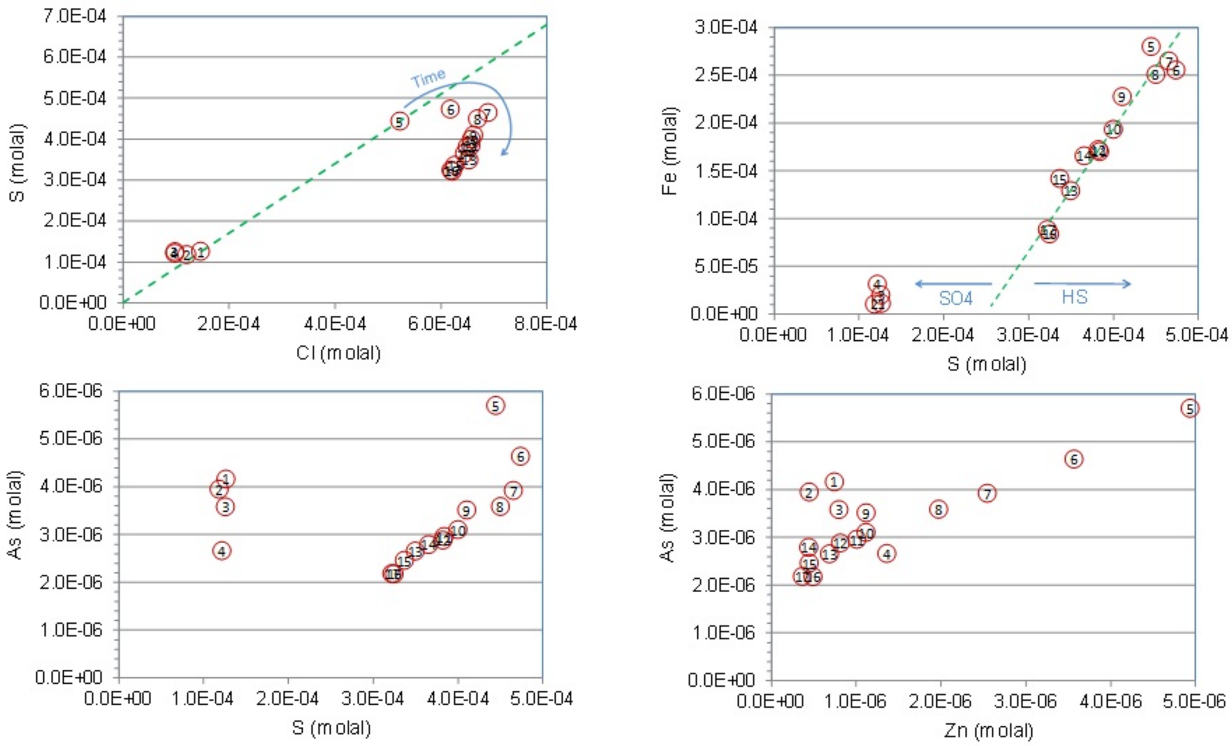

Figure 89. Geochemical evolution flow back fluids

7.6 FLOWBACK ISOTOPE GEOCHEMISTRY

Ca, Sr, O, H isotopes were measured on flow back waters and He isotopes on gas samples. Figure 90 illustrates $\delta^{18}O$ and δD on flow back water samples (red) compared to groundwater samples (blue). Red data point furthest to the left is the early sample (before return of water from below the casing). Other samples are all shifted to the right, away from the meteoric water line, likely indicating some vapor loss due to boiling or a shift due to water-rock interaction, but shift in δD suggests vapor loss.

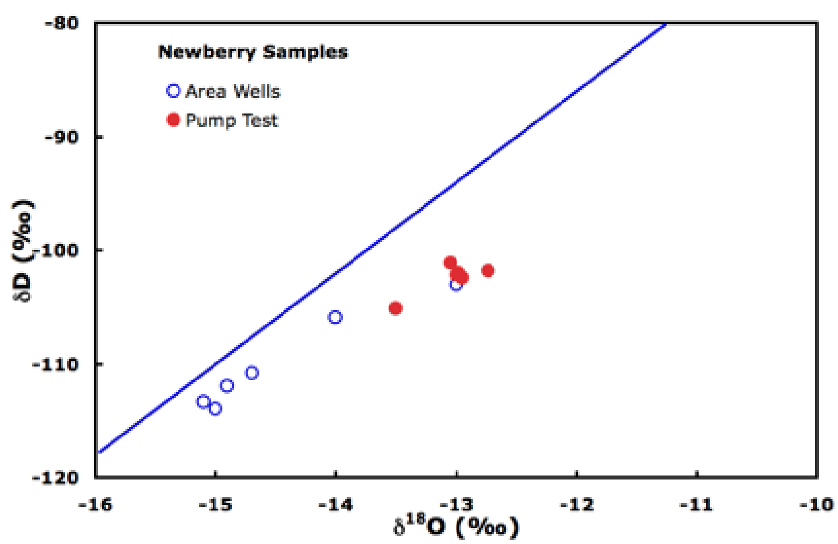

Figure 90. $\delta^{18}O$ and δD on flow back water samples (red) compared to groundwater samples (blue) in plot at upper right

Figure 91 shows calculated sulfate-water oxygen isotope temperatures for a limited set of samples. Calculated temperatures starts from the sample out of the cased interval showing an expected low temperature, followed by a sharp increase approximately 220°C, dropping down to <150°C then increasing up to 230°C in the last sample. The applicability of the sulfate-water oxygen isotope geothermometer to the Newberry stimulation is likely ideal because oxygenated groundwater having a very low sulfate concentration resulted in pyrite oxidation and formation of nearly all sulfate from reaction of pyrite in the rock mass. The high temperature of last sample is consistent with multicomponent and Na-K geothermometers (240-250°C), as discussed in the following section.

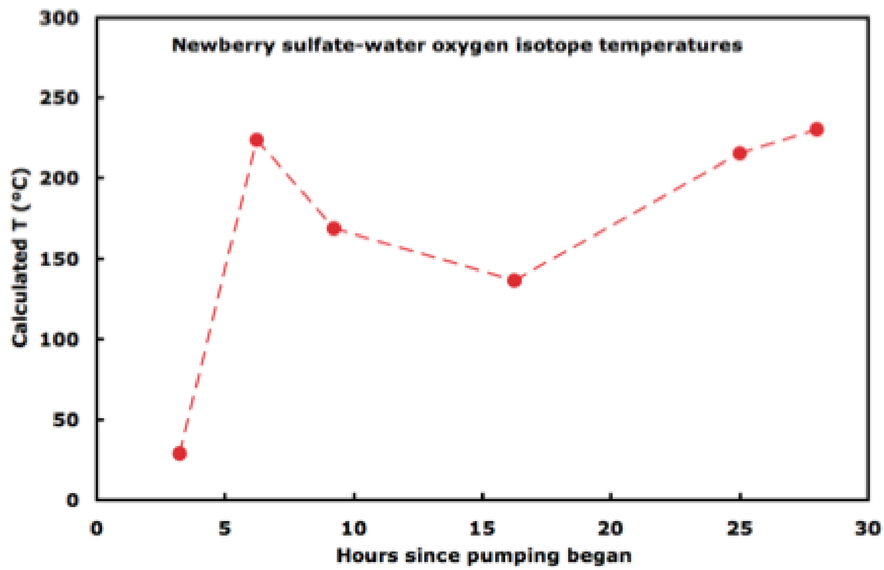

Figure 91. Calculated sulfate-water oxygen isotope temperatures plotted versus time.

The flow back $^{87}Sr/^{86}Sr$ ratio is a sensitive indicator of the reservoir rock type and identity of fracture-filling minerals of different ages and isotopic compositions which the geofluids were in contact with. Injected groundwater has $^{87}Sr/^{86}Sr$ ratio very close to mean of all surface Newberry basalts (Figure 92), as indicated by the blue crosses from Goles (1990). This range of isotopic ratios is much lower than the much more radiogenic Oligocene-Pliocene age silicic volcanics (rhyolitic tuffs, dacites, rhyolites) characterizing rocks outside Newberry Volcano, such as at Smith Rocks, Oregon (Goles, 1990), and likely similar to those rocks pre-dating and underlying Newberry Volcano. All the samples collected during flow back show ratios of about 0.7046-0.7048, highly elevated from any Newberry volcanics, indicating reactions with a mixture of pre-Newberry and Newberry volcanics. It is likely that the tuffs and rhyolites in the rocks considered to be the John Day formation have elevated Sr isotopic ratios and the intruded granodiorites are similar to the recent obsidian flows and rhyolitic rocks that have compositions in the upper range of the Newbery basalts. However, the isotopic compositions of specific rocks and hydrothermal minerals (particularly calcite which is usually high in Sr) in the open interval are not known and will have to be measured to fully interpret these data. The elevated $^{87}Sr/^{86}Sr$ ratio in the sample from the cased interval (first elevated ratio) is clear evidence that the waters in the casing were not pristine groundwater and may have had some re-injected fluid from the brief October 7 flow back. Luckily this contamination only affected some species and isotopic ratios having very high concentrations in the reservoir relative to the groundwater. Ca isotopes have also been measured on these samples, however, owing to the contamination in the injected water from earlier flow back water, groundwater samples, and likely some rock samples, need to be analyzed to interpret the results. Preliminary He R/Ra values in gas exceed 8, and Cl increased in flow back water, indicating mixture of injected groundwater with small amounts of magmatic-geothermal fluid.

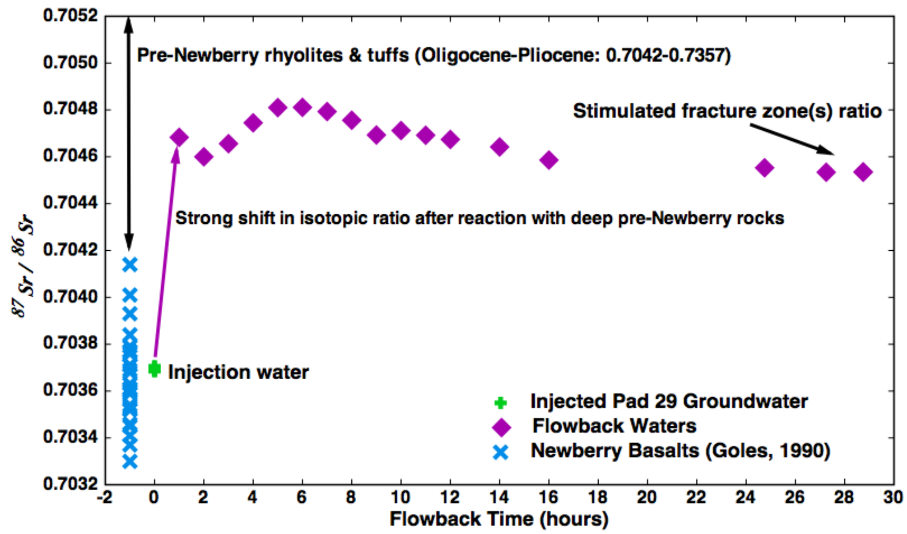

Figure 92. $^{87}Sr/^{86}Sr$ ratios of injected water, flow back waters, and Newberry and pre-Newberry volcanics.

7.7 FLOWBACK GEOTHERMOMETRY

This section discusses some of the empirical and multicomponent geothermometry performed on the October 23-24, 2014 flow back waters. Figure 93 shows the flow back water concentrations plotted on the silica polymorph saturation curves and calculated Na/K temperatures. Later samples show consistent Na/K and quartz equilibration temperatures around 250°C. The first samples from the cased interval waters are far from equilibrium, as expected, and plot at the far right in an unrealistic temperature range. Data plotted on the Na - 10K - $1000Mg^{0.5}$ ternary diagram (Figure 94) show a clear progression to an equilibration temperature of 250°C. These waters also are in the Giggenbach "immature" field which would be expected given the short time the groundwater was in the reservoir.

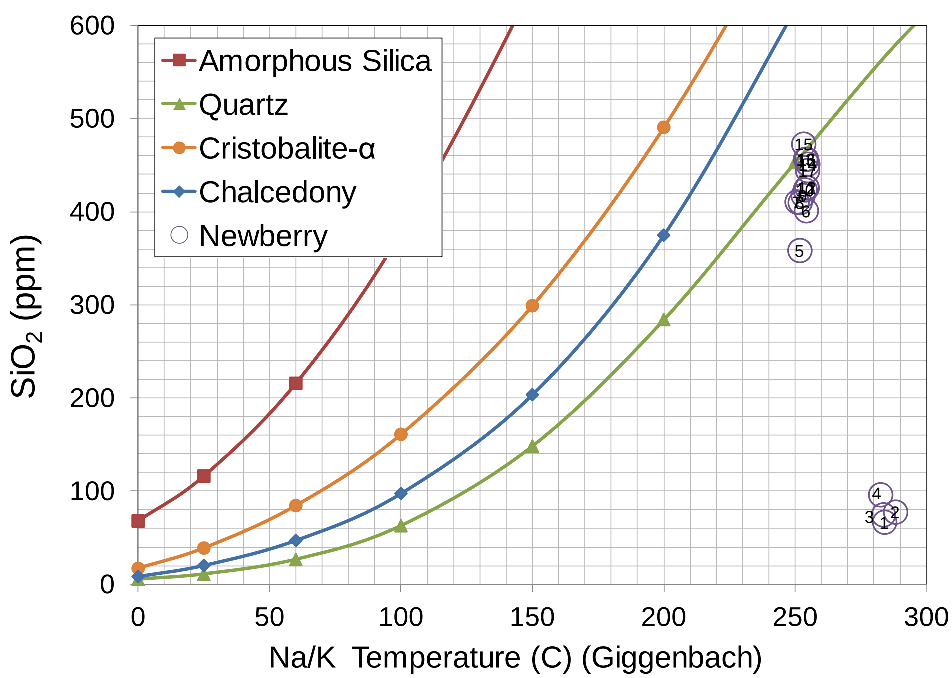

Figure 93. Well 55-29 flow back geochemistry relative to sodium/potassium-silica geothermometers

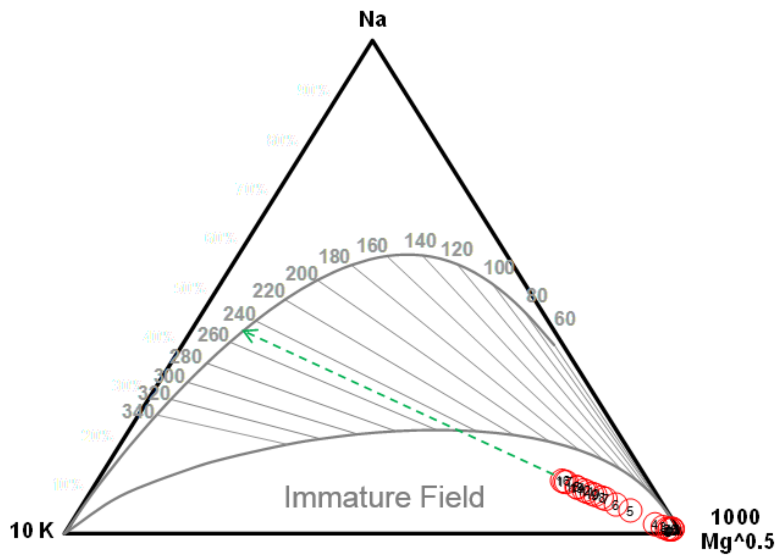

Figure 94. Well 55-29 flow back geochemistry relative to Na-K-Mg geothermometer shows "immature" waters evolving with time towards equilibrium temperature 250°C

Multicomponent geothermometry using GeoT (Spycher et al., 2011, 2014) were performed on the last water collected at the end of the flow back (Figure 95). Minerals are at equilibrium where the saturation curves log (Q/K) = 0.0. Above 0.0, the minerals are supersaturated, and below they are under-saturated. Although minerals may not be fully equilibrated, the combination of reacting (dissolving) primary minerals that are approaching equilibrium and precipitating secondary minerals yield a clustering around log (Q/K) = 0.0, which through statistical analyses can yield a "best fit" temperature. These temperatures are usually much more consistent than empirical geothermometers because they don't rely on equilibration of a single or pair of minerals and utilize a well-tested thermodynamic database.

Some recalculations and adjustments of the water compositions are usually necessary. Since HS^- was not analyzed, it was taken as the difference between total S and SO_4^{-2} (approximately 56 µm). A minor correction to HCO_3^- was made for charge balance (approximately 7.5 vs 7.2 mM). Al concentration was recalculated from equilibration with albite (approximately 15 vs 0.66 µm), since Al measurements are usually unreliable. Multicomponent geothermometry of this "original" slightly adjusted water is shown on the left in Figure 95. The calculated equilibration temperature is in the range of 240-250°C. However, calcite is clearly highly supersaturated likely as a result of boiling in the wellbore. Chlorite also hugely above saturation. Therefore in the second analysis, Ca was adjusted for calcite saturation (approximately 39 vs 20 µm) and HCO_3^- for charge balance (approximately 7.1 vs 7.2 mM). The calculated temperature of the fluid "equilibration" is still around 240-250°C. In both cases, pyrite saturates at about 230-240°C, which is consistent with the 230°C temperature determined independently from the oxygen isotope sulfate-water geothermometry results shown in the last section.

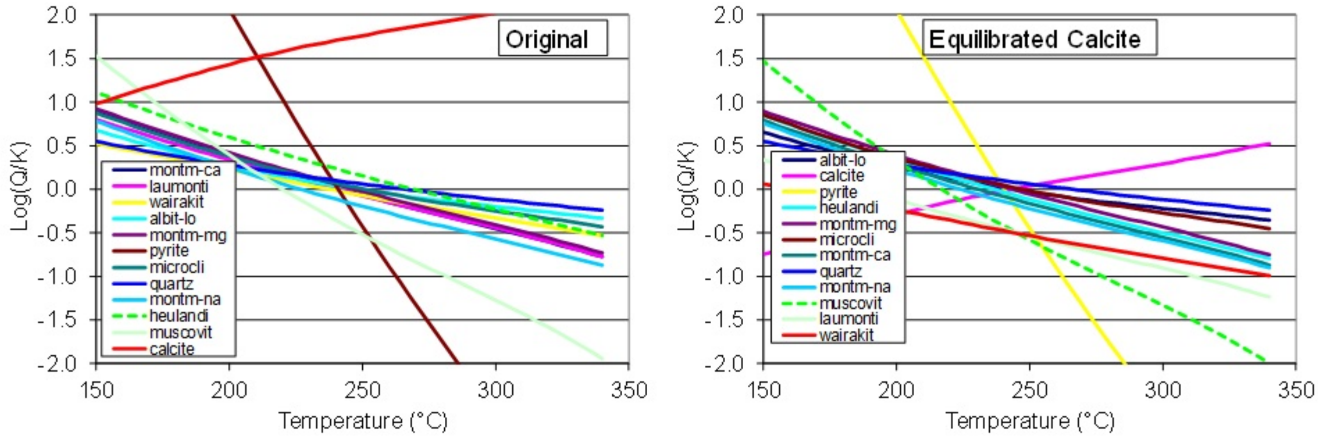

Figure 95. Reservoir geothermometry based on geochemical speciation and the multicomponent geothermometry method using the GeoT software program. Results indicate a reservoir temperature estimated around 240-250°C.

In summary, multicomponent geothermometry using GeoT, empirical, and sulfate-water isotope geothermometers yielded water-rock interaction temperatures of 230-250°C, indicating reactions with feldspars, pyrite, quartz, calcite, and Fe-Mg silicates in fractures outside the borehole. These temperatures are much higher that the temperatures in the borehole during the periods of maximum wellhead pressure (<200°C), indicating significant interaction with minerals in fractures in the deeper stimulated zones outside the borehole. Although groundwater has a Sr isotopic ratio close to the mean value in surface basalts, flow back waters show shifts toward more radiogenic pre-Newberry Miocene-Pliocene tuffs.

7.8 TH(M)C MODELS AND FUTURE MODELING EFFORTS

Typical EGS evaluations at other sites have been done primarily by separate analyses of injectivity, temperatures, tracer returns, microseismicity, geochemical data, and sometimes THM modelling, and in some cases THC modelling. However, the reactive chemistry in THMC models is commonly thought of as the extra factor affecting permeability over longer time scales, and most studies have therefore used simple systems looking at precipitation of one or two common minerals such as quartz or calcite. However, THMC models including more complex reactive geochemical and isotopic systems are much more powerful because they can provide independent constraints on usually poorly known and non-unique THM properties of the reservoir such as fracture porosity, surface area, fracture-matrix interaction, connectivity, elastic moduli, volume stimulated, mixing with geothermal water, boiling, in addition to changes directly due to mineral precipitation/dissolution (Sonnenthal et al., 2012, 2015 a,b; Wanner et al., 2014). Injection of groundwater with its unique chemistry provides a multitude of natural geochemical and isotopic systems that range from unreactive tracers to temperature-dependent and mineral surface area-specific reactive species. Through introduction of reactive chemistry, then the various THM models that may all match permeability and injectivity changes in the reservoir can be independently assessed. Including introduced tracers also adds another set of important constraints.

Developing a THMC model that can predict processes during EGS stimulation and over longer times (sustainability periods) requires parallel development of separate models so that understanding of the pertinent thermodynamic, kinetic, thermal, hydrological, and mechanical data and the important types and scales of processes can be assessed independently of the full THMC coupling. That is, one must have constrained the data to a reasonable range before integrating the system and avoiding errors. This involves models of the native-state system.

Predictive THC models of injection and production after stimulation were performed on refined horizontal 2-D models with initial heterogeneous permeability and injecting the Newberry groundwater composition (Figure 96). The permeability range was from 10^{-10} to 10^{-18} m^2. The injector and producer are 500m apart and injection and production were assumed to be equal and at 80 kg/s, with an initial reservoir temperature of 200°C. Simulations were performed using the new parallel TOUGHREACT V3-OMP code (Sonnenthal et al., 2014). Although production was to the NW of the injector, a high-permeability fracture zone trending S resulted in significant temperature drops after 2 years up to 200 m from the injector, although the initial modelled reservoir temperature is lower than the actual deep stimulated zone, which is likely closer to 300°C. Even still, temperature declines at the producer, which was not well connected to the injector, took over 20 years. A naphthalene sulfonate tracer showed arrival times of around 8 months to a year. Simulations show calcite precipitation adjacent to the wellbore, and dissolution in fractures away from the wellbore, consistent with the observed isotopic changes, and possibly consistent with the lack of significant increases in injectivity at later periods in the stimulation.

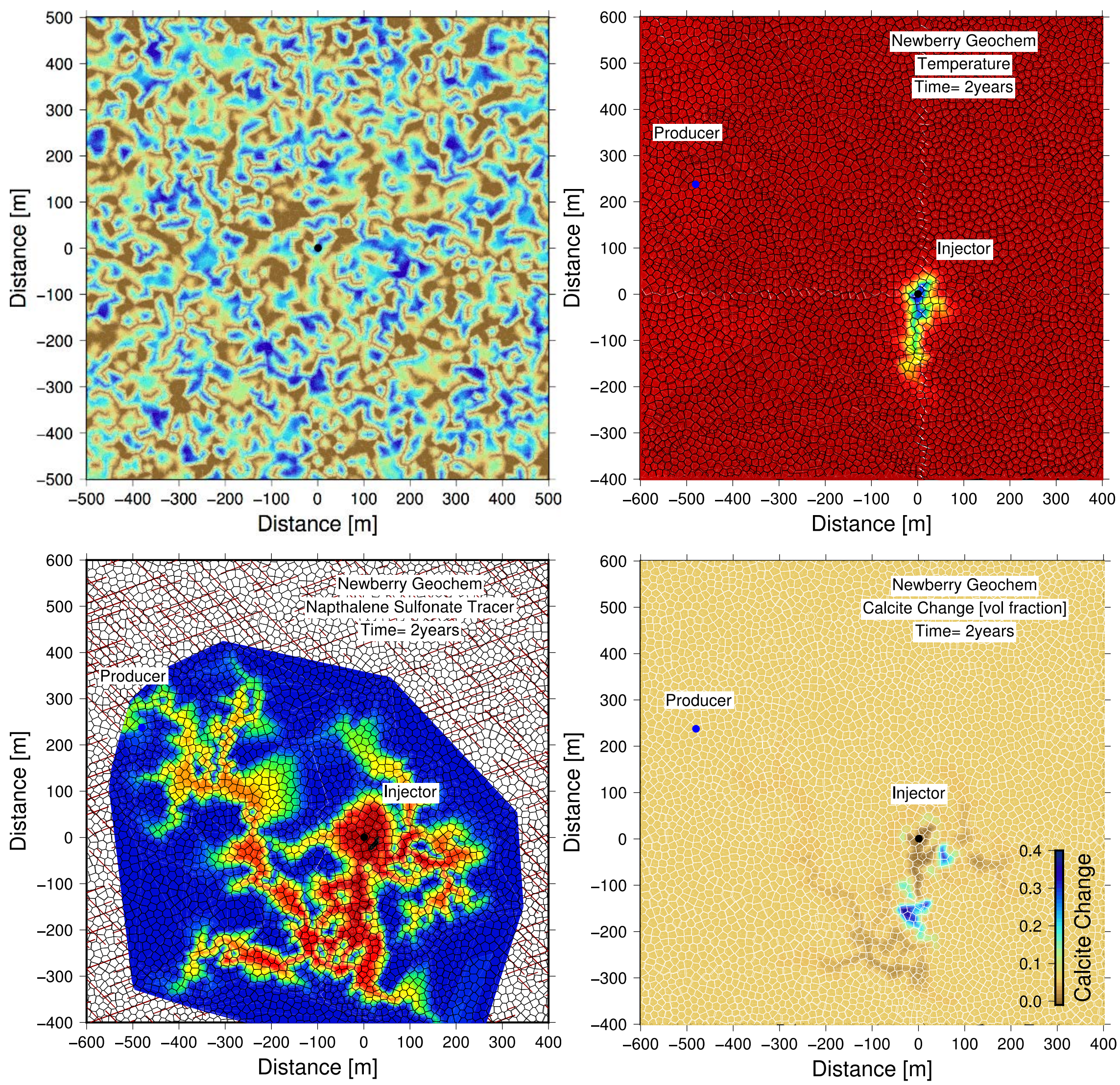

Figure 96. THC horizontal 2-D model simulation results for well NWG 55-29 and a producer 500m apart. Upper left - Initial permeability field. Upper right - Temperatures after 2 years injection and production at 80 kg/s. Lower left - Naphthalene sulfonate injected tracer distribution after 2 years of injection-production. Lower right - Calcite dissolution (blue) and precipitation (brown).

Now that THM models have been developed that include stimulated permeability fields and match injectivity increases as well as downhole temperatures, this model will be revised to include these distributions. Alternative models will also be done using seismic density maps as proxies for permeability changes in the reservoir.

Further THMC modelling will focus on the following tasks:

1. Wellbore temperature matches during the second stimulation (11/17/2014)
2. Tracer flow back model comparing measured and modeled tracer returns
3. Simulate heat-up of bottom of hole after fibrous TZIM.
4. The 2015 flow back geochemistry data and its GeoT analysis will be used to calibrate the native state coupled THMC model, an example of which is shown in Figure 96. The updated modeling results will improve decision making for stimulation strategies, production rates, and sustainability
5. Permeability away from well based on MEQs
    (ii) Compare R versus T and Diffusivity and pore pressure
    (iii) seismic density maps
    (iv) Anisotropy

1. Simulate production well – Use permeability-field based on MEQ density + Well permeability
2. Research in FY2015 will include the following, plus considerations for future work having the most impact on EGS goals:
3. Complete geochemical and isotopic analyses on all remaining flow back samples
4. XRD of filter papers to look at mineral precipitates
5. Future work should be aimed at doing flow-through experiments at reservoir temperatures on rock chips from potential stimulated zones to compare to sampled waters in order to pinpoint highest permeability zones and spatial extent of stimulation

8 SUMMARY

Overall, the 2014 stimulation effort went very smoothly. In particular, uncontrolled stimulation pump shutdowns and pump damages – problems that plagued the 2012 stimulation – were eliminated. Improvements were largely due to the preparation efforts of the Phase 2.1 Stage Gate report (AltaRock, 2014) which cataloged the lessons learned from 2012 and analyzed how to avoid those mistakes. In the same spirit, this section reviews lessons learned in 2014, our successes, and some of the challenges that remain.

8.1 SUCCESSES

8.1.1 GENERATOR, PUMP, AND INSTRUMENT RELIABILITY

The largest setback during the 2012 stimulation were issues surrounding the new stimulation pumps. Problems with the pumps included pump speed variability, decline in pump effectiveness, and total pump failure. The pump problems of 2012 were caused by issues with the Variable Frequency Drives (VFD), generator shutdowns, frozen instrumentation, and large debris getting drawn into the pumps. VFD problems were fixed by Baker Hughes, but other issues resulted from poor design and were successfully addressed in preparing the 2014 stimulation work.

During the 2012 stimulation three generators were installed each able to handle a one megawatt load. The system as a whole required just under two megawatts of power, meaning two generators needed to run at all times. The generators were designed to be able to be automatically switched in case any problems were detected with generator output. However, the switching mechanism was too slow, and the pump controller logic powered down the generators every time automatic switching occurred which caused a cascading effect that shut down the whole system. Thus any problems with the generators brought the whole system down, sometimes unexpectedly. Secondly, the switching systems with three generators required duplicate wiring and unneeded complexity requiring maintenance and repair to take longer and complicated troubleshooting. The goal for the 2014 stimulation was to have a system that was reliable, simple, and less susceptible to uncontrolled shut-downs. This was accomplished by using two 2 MW generators each of which could handle the entire load of the pad alone, wiring all of the equipment on the pad to both these generators, and using a simplified switching system. Changing the stimulation infrastructure in this way allowed for better maintenance, easier fueling, and a system less prone to errors. An electrical fail-over system was not used.

Freezing of instrumentation during the 2012 stimulation led to a total pump failure due low intake pressure on stimulation pump one. An unseasonal cold front hit Newberry on October 21st with temperatures well below freezing. Pump instrumentation had not been not insulated, was not designed for harsh climates, and froze the pressure readings on the pump in place. When a booster pumps failed it created a dangerous pressure low on the intake side of stimulation pump one which was not detected when the pressure gauge froze. The logic written into the Programmable Logic Controller (PLC) to prevent the pump from operating in this condition did not work because the pressure reading was incorrect. Field operators did not notice the low pressure on the manual gauge until after stimulation pump one had been damaged. For the 2014 stimulation heavy duty industrial grade instrumentation and transmitters were used for temperature and pressure monitoring of the stimulation system. These units were then insulated and wrapped in heating wire to prevent freezing. Despite freezing temperatures during the 2014 stimulation, good preparation for cold temperatures led to a stimulation without the significant issues encountered during the 2012 stimulation. Still, there were some problems with instruments, namely calibration issues, which highlighted the importance of having backup sensors on site.

In 2012, insufficient pressure on the intake to stimulation pump one caused problems associated with the intake booster pumps and water tank storage. The booster pumps used were unreliable and continually failing or underperforming. The water tank system design also did not provide enough head to the booster pumps during periods of high flow because the piping system connecting tanks to the pumps had too much head loss. This problem was solved by using the northern sump to hold water and two sump pumps which supplied sufficient head and flow to the stimulation pumps. For the 2014 stimulation, the sump pump configuration was implemented from the beginning. Additionally, two sump pumps were installed in the northern sump with automatic switches to insure one pump was always running. During operational episodes in which flow rates were expected to increase rapidly, such as when TZIM was injected through the DIVA both sump pumps were switched on insure sufficient inlet pressure and flow rate. Overall, in contrast to 2012, no problems with water supply were encountered in 2014.

During the 2012 stimulation the stimulation pumps wore down prematurely due to gravel and pieces of string that had been sucked into the pump chambers. Wearing down of the stages within the pump was responsible for the ever decreasing of output of the stimulation pumps, so a screen was installed in to the intake line of stimulation pump one. The screen insured that the inlet water was clean so that no materials could reach the pump innards, eliminating the degradation of pump performance. For the 2014, stimulation screens were installed on both the inlet to the sump pumps and the inlet of stimulation pump one, and no degradation of pump performance occurred.

8.1.2 DATA COLLECTION AND ANALYSIS

In both the 2012 and 2014 stimulations we planned for PTS logs to be run before and after diverter application. This was a prudent decision as the DTS failed during both stimulations. The data recovered from the PTS surveys showed the most conclusive evidence that the diverter material worked as intended. If only wellhead pressure and flow rate data were available, we would not have been able to conclude that the diverter had worked and the depth at which flow was blocked. Future stimulation work, despite the application of DTS, should plan to include PTS surveys because they are currently the most reliable logging technology available for environments such as Newberry.

Real time data visualization was an invaluable resource during stimulation. Real time visualization during the 2012 stimulation was responsible for helping to recognize and adapt to the problems that were encountered. For the 2014 stimulation, we expanded our real time data visualization abilities and created updated processing algorithms and software for visualization of seismic data, DTS data, and sensor data. These programs allowed us to better monitor the effects of stimulation downhole and the operations of the stimulation infrastructure.

8.2 REMAINING CHALLENGES

8.2.1 SEISMIC DATA COLLECTION AND ANALYSIS

The microseismic data has been critical to characterizing the stimulated reservoir volume, but there have been challenges related to the accuracy of the MEQ data set. The Newberry seismic velocity model is not well calibrated, resulting in significant event location uncertainty... The best solutions to improve the velocity model would be a down-hole calibration shot (i.e., an explosive charge set off deep within the well) large enough to be recorded on the majority of the sensors. The 790 gram perforation shots in the liner performed in November were detected on some borehole stations, but not well enough to improve the velocity model. Larger shows (i.e. 2 kg) in an unlined hole would likely provide sufficient arrivals to improve the velocity model, resulting is much less uncertainty in event locations and depths.

Another issue of accuracy of seismic locations is exemplified by the significantly different event locations by three different groups of seismologists (see Section 6.1.3). Because the groups used the same velocity model, location discrepancy was caused by the different codes used to interpret the seismic data, and difference between how seismologist choose arrival times. For this project the location discrepancies were handled by employing the seismic density plot methodology outlined in section 6.1.3. Code comparison exercises between different seismic software and seismologists could further explore this issue, but is outside the scope of a demonstration project. The DOE has initiated code comparisons of other types of software, such as recent efforts with reservoir models. A similar approach with seismic software might be warranted.

8.2.2 REAL TIME DOWN-HOLE MONITORING

In theory, distributed temperature sensing (DTS) systems can provide a valuable real-time indication of the evolution of fracture permeability within the wellbore. However, the practical use of DTS in geothermal settings has proven unreliable, not reaching its theoretical promise. The DTS has multiple failure modes (mechanical, thermal, chemical deterioration), which have made it unreliable in a field setting, and so using a DTS is both high risk and high reward. It is high risk because the DTS is expensive and requires additional engineering efforts to be deployed, and as evident form both stimulations it is prone to failure. However, the insight into fracture permeability behavior during stimulation provided from a continuous temperature dataset derived from the DTS cannot be emphasized enough. It is likely the best way to determine where in the wellbore stimulation is occurring and how much flow is going into each stimulated zone. Furthermore, providing high quality data in one minute time intervals allows for detailed assessment of the stimulation in real time. Possible solutions to the riskiness of DTS deployment could be better armoring, designing for higher temperature conditions, and reducing fiber embrittlement.

8.2.3 WELL BORE STRESS

There were significant variations between the design estimates of well head pressure (WHP) required for stimulation and what was actually needed due to a lack of initial data. Estimate of WHP requirements were based on fracture characteristics and borehole breakouts measured in the BHTV data and assumed rock properties of the varying lithology recorded in the wellbore. Direct measurement of the local stress conditions can best be obtained by conducting an extended leak-off test (for more information refer to Section 9.3.1). An extended leak off test will give a stress magnitude for the local region. Observation of the resultant fracture created from this process by the BHTV will give stress direction. Conducting such analysis will allow for much better predictions of WHP requirements and should also provide much needed information for directional drilling.

8.2.4 MODELING

The modeling efforts conducted by Eric Sonnenthal at LBNL helped AltaRock understand the processes occurring during stimulation. Given the knowledge gained from the modeling efforts in both 2012 and 2014 it may prove fruitful to use the model developed for Newberry to plan and test stimulation using the coupled model developed at LBNL. Designing a stimulation in this way would allow AltaRock to test multiple stimulation strategies and further verify the accuracy of the numerical model. Testing the numerical stimulation will help determine future stimulation infrastructure parameters such as wellhead rating, pump design and water supply requirements.

8.2.5 PUMPS

In both the 2012 and 2014, stimulations a bypass line was used to balance the pressure/flow requirements of the pumps and the injectivity of the well. The bypass line allowed for the pumps to operate within the defined pump curves given by Baker Hughes even when the well was taking only a very small amounts of flow. While necessary and practical, this system is inefficient and overly complex. Going forward it will be beneficial to design pumps that meet the characteristics of the well, namely ones that can pump at high pressures but at low flow rates to allow for greater system reliability and more latitude with regards to stimulation pressure.

8.2.6 WELL BORE PERMEABILITY

In 2014 it was discovered that much of the wellbore permeability enhancement occurred during the very beginning of stimulation and stopped roughly after 7 days. EGS reservoir growth did not stop at that time based on micro-seismic data indicating stimulation occurred in the far field the whole time, but it may indicate that other tools will be needed to increase permeability at the wellbore. While TZIM was not thoroughly tested with regard to wellbore permeability due to pressure constraints, it may be valuable to explore other options such as chemical stimulations, mechanical packers, and possibly stronger perforation shots than those tried in 2014.

9 PRELIMINARY PHASE 2.3 PLAN

9.1 PRODUCTION WELL TARGET

The primary objective of Phase 2.3 is the installation of production well 55A-29 that will be hydraulically connected to well NWG 55-29. The primary concerns are whether the two wells will be connected enough to provide economic flow and what will be the rate of thermal decline along the flow paths between the wells. The challenge in targeting 55A-29 is balancing these concerns to obtain maximum net power output for the life of the project. In targeting the new well it was decided to maximize connectivity in order to produce the best geothermal flow possible. Although the original project plan was a well spacing of planned 350-500 m, the spacing has been readjusted to 200-250 m to improve the probability of good connectivity between the wells. While the reduced spacing will increase the heat drawdown from the reservoir, better flow rates are key to making this project a successful demonstration of EGS technologies.

A production well path with an azimuth of N86°E has been designed based on the seismic density maps to intersect the western edge of the stimulated zone and below the existing well (Figure 97). The cased section of the hole will be drilled at a slight inclination and reach a depth of 2200 m (7200 ft) TVD. The open-hole interval will begin after completion of the well path's deviation from vertical.

A well path along the eastern edge of the seismic cloud would also intersect regions with high seismic density at approximately 200 meter (656 ft) away from the well and would terminated above the existing well. However, drilling above the existing well is more risky as it would require multiple deviations that could create unstable well conditions. Drilling below the well is simple in comparison, and far less risky.

To further ensure that the proposed well course intersects the stimulated reservoir, a 3D representation of the seismic density cloud with the proposed well path is shown in Figure 98 which uses the same data and weighting scheme as the 2D cross sections (Table 5). The 3D plot has been gridded with the same dimensions as the 2D plots, but the grid cells used 3D inverse distance weighting with a power of 2, and an iso-surface was placed at the weight value of 0.25. Two main stimulated volumes become apparent; 1) 2200-2400 m depth just to the north of the existing wellbore and 2) 3000-3200 m depth to the south of the bottom of the well – the stimulated volume being targeted by the proposed well path.

The well orientation is also designed to take advantage of the average T-axis orientation as calculated by Foulger Consulting's moment tensor interpretations (Section 6.1.2). The T-axis for an individual seismic event is the direction of maximum extensional strain. Thus, a well drilled in the direction of the average T-axis for a set of events will intersect fractures in the direction that the fracture set is most likely to open. The average T-Axis during the 2014 stimulation had a trend of N12°E and plunge of 57°. The planned azimuth of the production interval of 55A-29 is N86°E with a plunge of 74°, which is within the tensile quadrant of the 2014 seismic events and 32° from the average T-axis orientation (Figure 99).

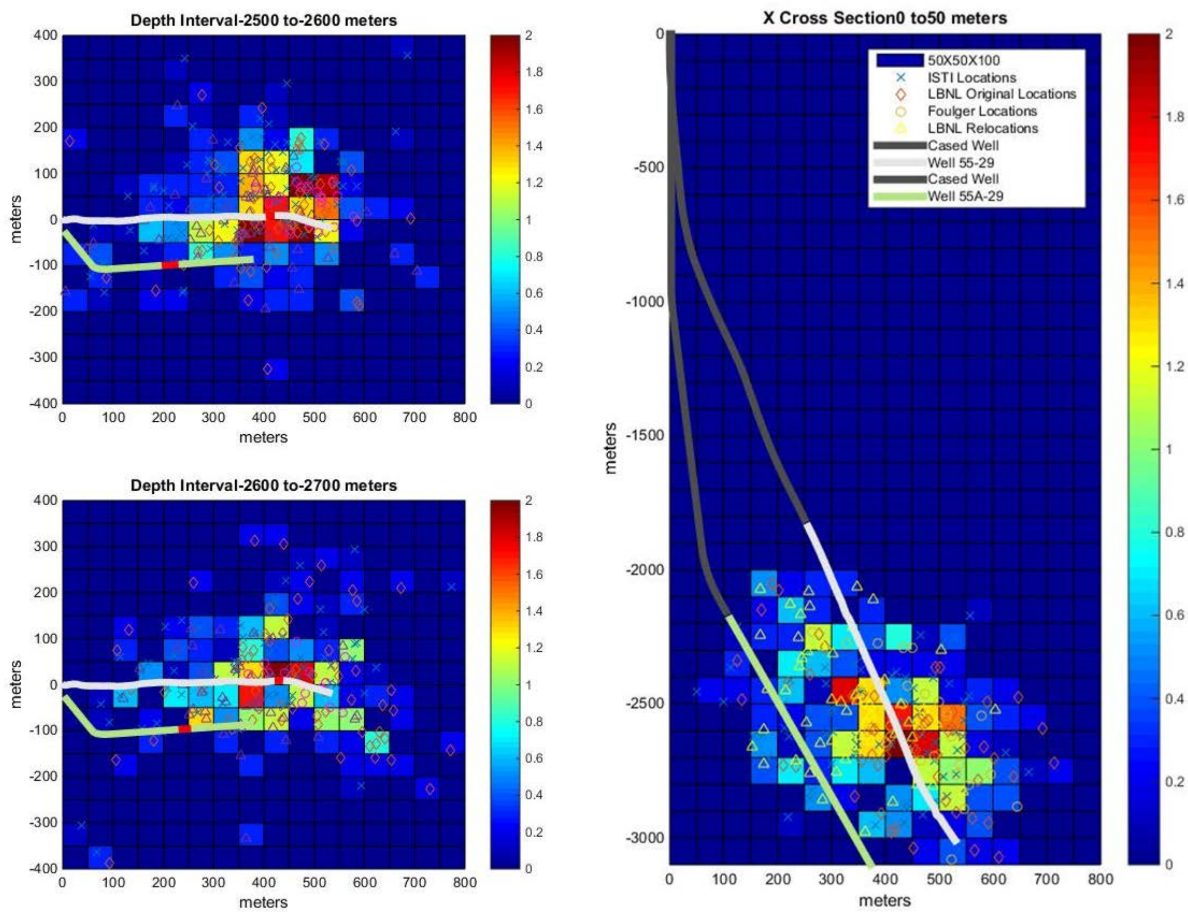

Figure 97. Seismic density plots for well 55-29. Map at depth slices of 2400-2500 m (top left) 2700-2800 m (bottom left). Red sections of the proposed well path are well intersections with the depth slices. Cross section at 0-50 m south of the well (right).

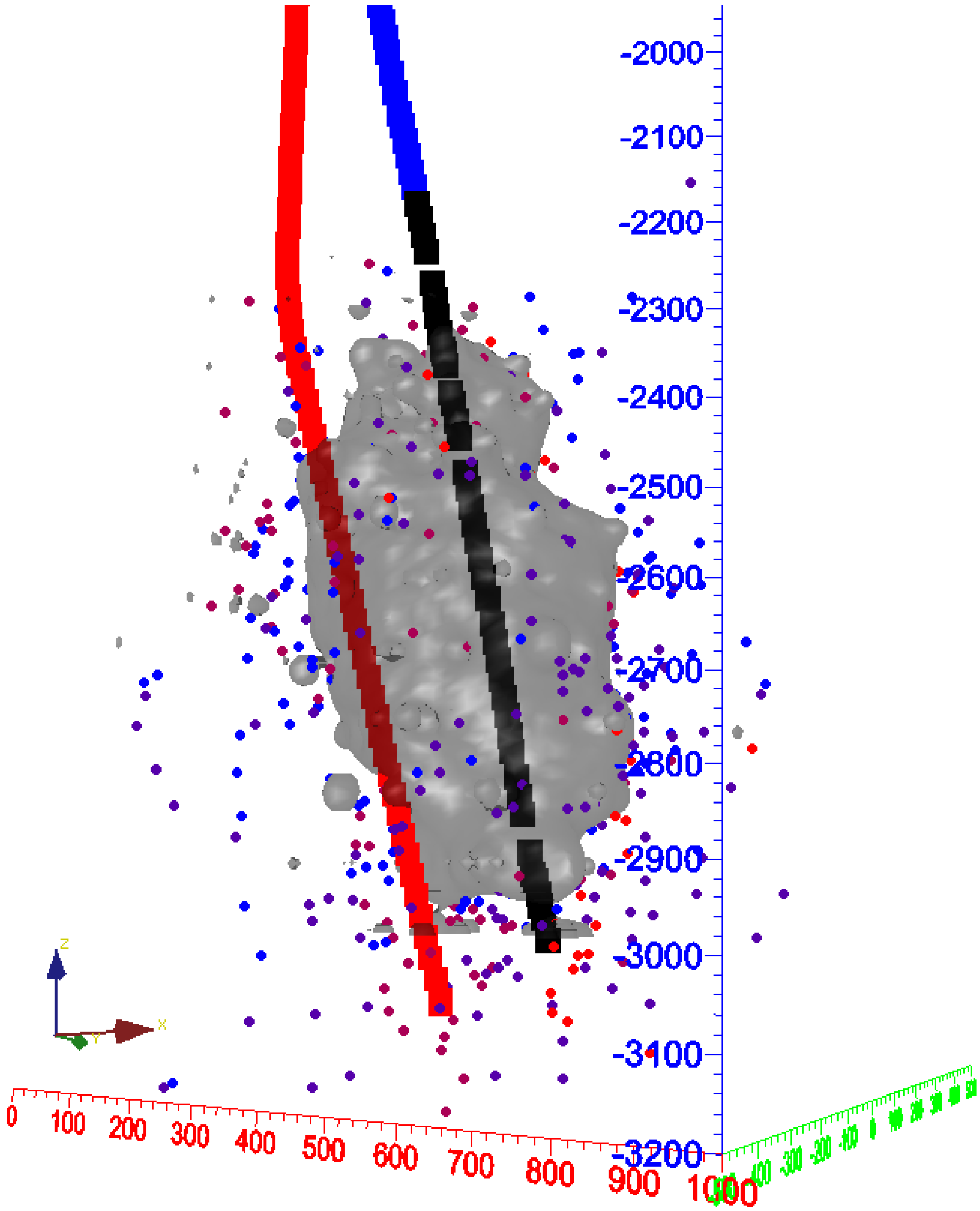

Figure 98. 3D representation of weighted seismic density data with the proposed well path in red, using inverse distance weighting with a power of 2 and contoured at 0.2. Bright red events have the highest weight of 0.4 and dark blue events have the lowest weight of 0.1.

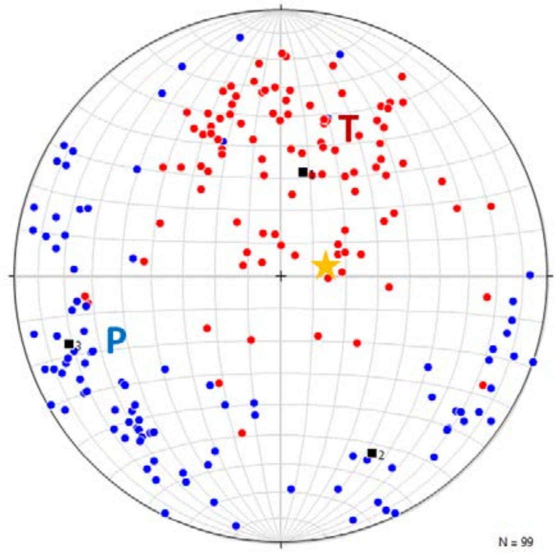

Figure 99. Lower hemisphere stereonet P (blue) and T (red) axes of moment tensors determined by Foulger Consulting. Black square is the average T-axis (N12°E, 57°). Gold star shows the azimuth and plunge (N86°E, 74°) of the production interval of 55-29.

The proposed well direction will increase the probability that the well will intersect pre-existing permeable fractures. For the proposed doublet system to work efficiently, the new well should be accessing the stimulated reservoir at multiple depths along the length of the wellbore. Having multiple permeable zones along the length of the wellbore will both improve the impedance and reduce the risk of short circuiting between the wells.

The choice of well path also attempts to mitigate potential thermal breakthrough by varying the distance between the wells. Rather than have the two wells parallel each other, the two wells will get closer with depth and temperature. The beginning of the open-hole section of well 55-29A is 250 meters (820 ft) away from well 55-29 and the bottom of the well is 200 meters (660 ft) from well 55-29. This wedge design accomplishes multiple objectives. It increases the probability that the two wells will connect in the deepest (hottest) part of the reservoir, it increases the probability of high fracture surface area between wells in the shallow part of the stimulated reservoir, and it increases connectivity between wells with depth. Having a shorter fracture pathway between the bottoms of both wells will result in an increased flow within the deeper part of the reservoir. This is primarily because there will be less frictional loss along these deeper shorter fracture pathways. This design creates a doublet system where extraction of heat from the reservoir will be gradational, with the most heat being mined from the deeper, highest heat recharge, section of the reservoir.

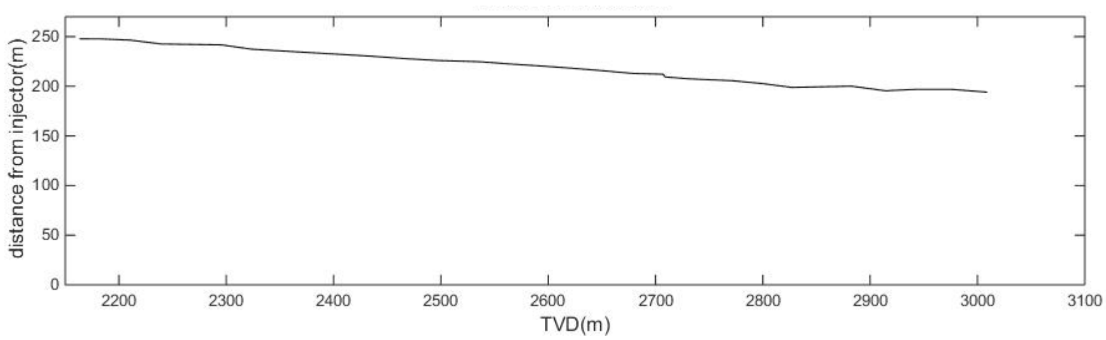

Figure 100. Distance between the two wells as a function of True Vertical Depth (TVD).

9.2 55A-29 PLANS

9.2.1 Permitting

Permits have already been discussed in Section 2.2 above. To reiterate, the following permits will be needed specifically for drilling NWG 55A-29.

DOGAMI Geothermal Well Permit

The Drilling Plan (Appendix H) has been submitted to DOGAMI for review and issuance of obtain a permit to drill the new production well to be drilled on the S-29 well pad.

BLM Geothermal Drilling Permit (GDP)

BLM will require a GDP for the drilling of the new production well, NWG 55A-29, to be drilled on the S-29 well pad. The Drilling Plan will be submitted for review once the DOGAMI permit is complete.

Oregon Department of Environmental Quality (DEQ) Air Control Discharge Permit (ACDP)

We currently have a Simple ACDP that we have put into suspension to cover the diesel generators needed to drill the production well. Depending on the size, type and duration of use of these generators, we may be exempt and can cancel the permit. Otherwise, we will modify this permit to allow the use of the specific generators needed to drill the production well. We will seek a determination from DEQ early in 2015 as to whether we should cancel or modify the permit.

9.2.2 Well Path Design

The current drilling plan for proposed production well NWG 55A-29 includes an initial vertical section of 13⅜ in cased borehole to 945 m (3,100 ft), where directional drilling will begin building to six degrees in the S37E direction, increasing distance between NWG 55-29 and NWG 55A-29. The six degree angle will hold to 1,920 m (6,300 ft) measured depth (MD) and then build to 16 degrees while turning orientation to N86E. Directional drilling will end at 2,129 m (6,983 ft) MD (2,121 m [6,956 ft]) TVD prior to proposed 9⅝ in casing depth at 2,159 m (7,083 ft) MD. The N86°E direction will be maintained to total depth at 3,119 m (10,232 ft) MD. Initial review of this plan indicates no major drilling challenges. Dogleg severity (DLS) will be kept at 2°/100 ft or less, maintaining manageable torque and drag at depth. While two directional turns is less than ideal, both turns will occur in 12¼ in borehole in the low temperature environment. This arrangement keeps the 55A-29 production well vertically below the 55-29 injection well, and allows for maximum interaction with the microseismic events indicating reservoir fractures and maximizes potential flow path distance between the wells while staying within the EGS reservoir. Figure 101, Figure 102 and Table 9 detail the production well path relative to 55-29 and cased and open hole intervals. Once the drilling plan is approved and permitted, there will be several long lead-time items to be purchased before drilling commences. These are outlined in the following section along with the drilling schedule.

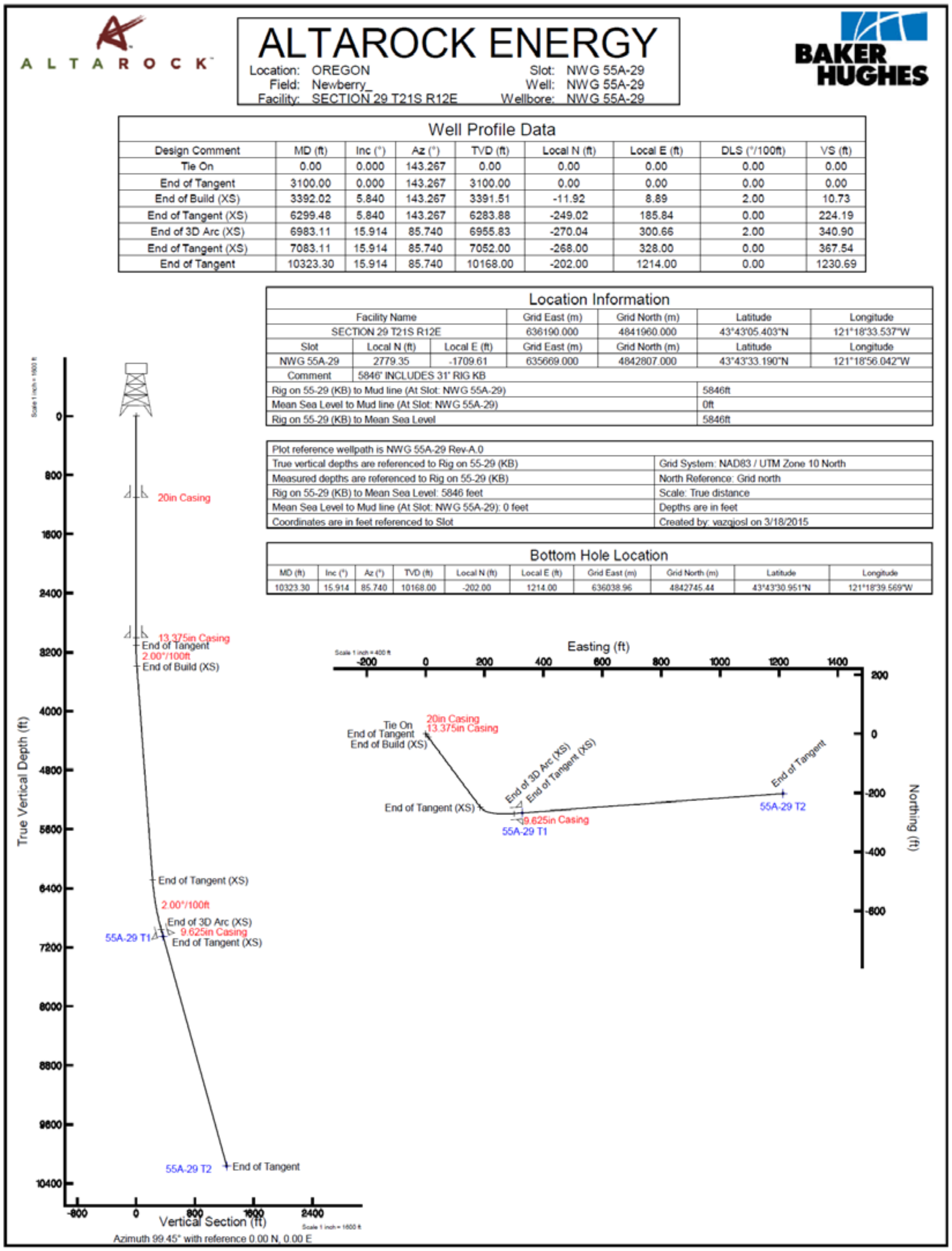

ALTAROCK ENERGY

Location: OREGON — Field: Newberry_ — Facility: SECTION 29 T21S R12E

Slot: NWG 55A-29 — Well: NWG 55A-29 — Wellbore: NWG 55A-29

Well Profile Data

Design Comment	MD (ft)	Inc (°)	Az (°)	TVD (ft)	Local N (ft)	Local E (ft)	DLS (°/100ft)	VS (ft)
Tie On	0.00	0.000	143.267	0.00	0.00	0.00	0.00	0.00
End of Tangent	3100.00	0.000	143.267	3100.00	0.00	0.00	0.00	0.00
End of Build (XS)	3392.02	5.840	143.267	3391.51	-11.92	8.89	2.00	10.73
End of Tangent (XS)	6299.48	5.840	143.267	6283.88	-249.02	185.84	0.00	224.19
End of 3D Arc (XS)	6983.11	15.914	85.740	6955.83	-270.04	300.66	2.00	340.90
End of Tangent (XS)	7083.11	15.914	85.740	7052.00	-268.00	328.00	0.00	367.54
End of Tangent	10323.30	15.914	85.740	10168.00	-202.00	1214.00	0.00	1230.69

Location Information

Facility Name			Grid East (m)	Grid North (m)	Latitude	Longitude
SECTION 29 T21S R12E			636190.000	4841960.000	43°43'05.403"N	121°18'33.537"W
Slot	Local N (ft)	Local E (ft)	Grid East (m)	Grid North (m)	Latitude	Longitude
NWG 55A-29	2779.35	-1709.61	635669.000	4842807.000	43°43'33.190"N	121°18'56.042"W
Comment	5846' INCLUDES 31' RIG KB					
Rig on 55-29 (KB) to Mud line (At Slot: NWG 55A-29)					5846ft	
Mean Sea Level to Mud line (At Slot: NWG 55A-29)					0ft	
Rig on 55-29 (KB) to Mean Sea Level					5846ft	

Plot reference wellpath is NWG 55A-29 Rev-A.0	
True vertical depths are referenced to Rig on 55-29 (KB)	Grid System: NAD83 / UTM Zone 10 North
Measured depths are referenced to Rig on 55-29 (KB)	North Reference: Grid north
Rig on 55-29 (KB) to Mean Sea Level: 5846 feet	Scale: True distance
Mean Sea Level to Mud line (At Slot: NWG 55A-29): 0 feet	Depths are in feet
Coordinates are in feet referenced to Slot	Created by: vazqjosl on 3/18/2015

Bottom Hole Location

MD (ft)	Inc (°)	Az (°)	TVD (ft)	Local N (ft)	Local E (ft)	Grid East (m)	Grid North (m)	Latitude	Longitude
10323.30	15.914	85.740	10168.00	-202.00	1214.00	636038.96	4842745.44	43°43'30.951"N	121°18'39.569"W

Figure 101. Cross-sectional, plan view and drilling location information for planned production well NWG 55A-29.

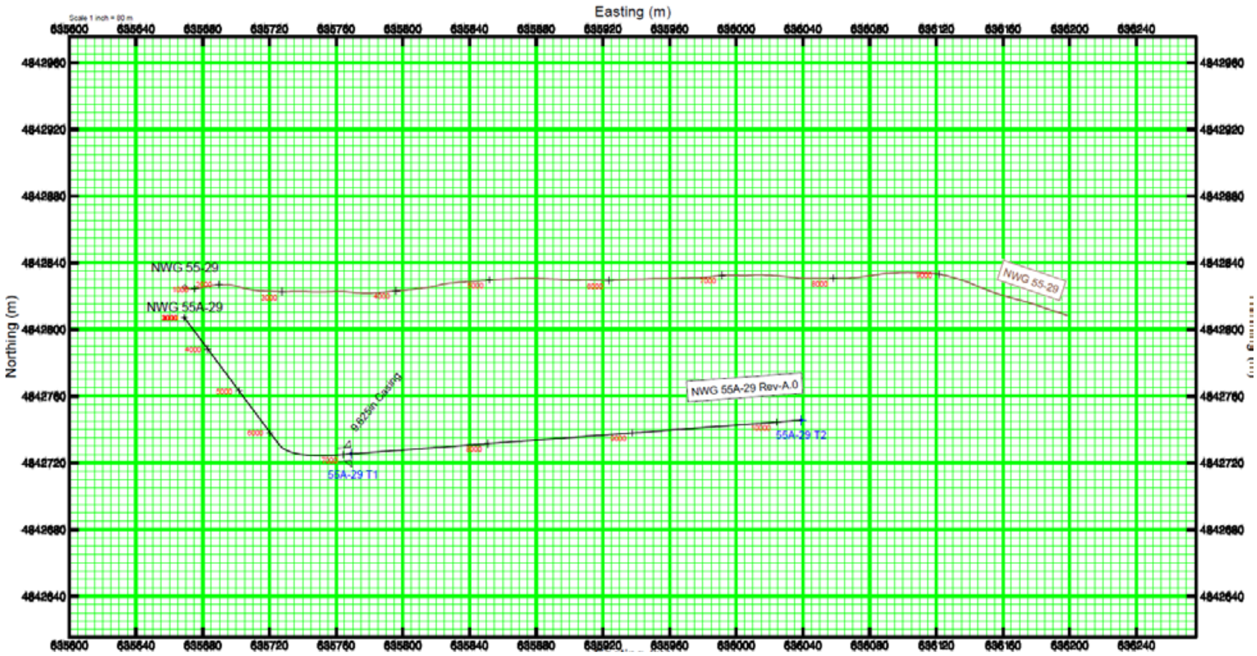

Figure 102. Map view of planned production well NWG 55A-20 drilling location relative to existing injection well NWG 55-29.

Table 9. Proposed open hole and cased sections for production well NWG 55A-29.

String / Bit Diameter	Start MD (ft)	End MD (ft)	Interval (ft)	Start TVD (ft)	End TVD (ft)	Start N/S (ft)	Start E/W (ft)	End N/S (ft)	End E/W (ft)
26 in drill bit	0	1100	1100	0	1100	0	0	0	0
20 in Casing	0	1100	1100	0	1100	0	0	0	0
17½ in drill bit	1100	3000	3000	0	3000	0	0	0	0
13⅜ in Casing	0	3000	3000	0	3000	0	0	0	0
12¼ in drill bit	3000	7083	4083	0	7052	0	0	-268	328
9⅝ in Casing	0	7083	7083	0	7052	0	0	-268	328
8½ in drill bit	7083	10323	3240	7052	10168	-268	328	-202	1214

9.2.3 Drilling Plan

This section is a summary of the drilling plan for the production well (Appendix H), the final details of which will evolve during discussions with the technical review teams and permitting authorities. The production well, 55A-29, will be drilled with a conventional drilling rig. The upper 3100 ft will be vertical, drilled with rotary bits with 20 in surface casing to approximately 1100 feet and 13⅜ in intermediate casing to 3000 ft. The surface section of 55-29 was excessively troublesome and took 39 days to drill. The extra time was related to stuck pipe, unstable formation and loss circulation zones, and enlarging out to 26 in hole size. Because this vertically drilled section to 3100 feet will be tracking only about 60 feet from the 55-29 well, much of the same geology and drilling conditions will be expected. However, with a revised hole size program along with some different drilling practices and proper maintenance of drilling fluid properties, it is anticipated that many of the former problems can be mitigated resulting in a significant reduction in rig days and expense.

After the 13⅜ in casing is set directional drilling equipment will be used to turn the well with an SE azimuth to establish separation from 55-29 well course. Once this directional drilling section is completed, the Hanjin D&B Water Hammer system will be deployed by our partner On Energy, Inc., the exclusive U.S. drilling services partner of Korean drilling equipment manufacturer Hanjin D&B. The water hammer system includes pumps, fluid systems, and filtration equipment for solids processing. The water hammer system is being cost-shared to the project by On Energy to demonstrate potential performance improvements that this new technology can achieve, which would result in significant cost and time savings. Based on our analysis of the data provide to AltaRock by Hanjin, the water hammer may be able to drill from 3400 ft to 6300 ft at a rate of 45 ft/hr. When compared to the drilling performance of 55-29, this would result in a savings of seven days of rig time. Single shot directional surveys will be made every 90-120 feet to determine whether the hammer bit system is maintaining the course set at 3400 ft. If deviations from the planned well course are minor while hammer drilling, course corrections may not be necessary in this section of the hole. This section of drilling will provide some insight into how effective the hammer assembly will be in maintaining directional objectives.

Starting at 6400 ft, another directional change becomes necessary and the water hammer system (which cannot make directional changes) will be temporarily removed. Steerable directional systems will be used to turn the well course to an azimuth of N85°E and inclination of 16°. Once this directional drilling section is completed, 9⅝ in production casing will be installed.

The well's production interval between 7083 ft and 10323 ft will be drilled with the Hanjin D&B water hammer system. Again the potential savings predicted by the use of this system is seven days compared to 55-29 performance. Single shots will be made every 90-120 feet to determine whether the hammer bit system is maintaining the desired well course objectives. If the well course deviates further than 300 m apart or closer than 200 m (see Figure 102 for ideal well spacing) from well 55-29, then a steerable directional system will be used as necessary to make directional corrections.

During drilling of the production interval, the down-hole pressure response in 55-29 will be continuously monitored. A pressure response in 55-29 will indicate that stimulated fractures have been intersected by 55A-29.

9.3 WELL LOGGING, TESTING AND COLLABORATORS

Testing and logging of the well will occur during drilling and after completion of the well. Two different tests will be performed during the drilling of this well. Upon the completion of the final casing string a stress test will be performed to determine the minimum principal stress magnitude. The other test to be run during drilling will be high resolution monitoring of the down hole pressure in 55-29. After the open hole is complete, a Bore-Hole Tele Viewer (BHTV) run will then be used to image natural fractures, bore hole breakouts, and possibly the tensile fracture created by the stress test. In addition to the BHTV, a full suite of geophysical logging tools will be run. Upon completion of the logging a seismic calibration shot will be fired within the well. This calibration shot will provide data for a more robust seismic velocity model.

9.3.1 IN SITU STRESS TEST

An *in situ* stress test is an extended leak-off test which creates a small tensile fracture and allows it to grow an incremental amount before shutting in the well. This test provides information about the mechanical rock properties, most importantly the formation breakdown pressure, or minimum principal stress. Knowing the formation breakdown pressure will allow the AltaRock team to put upper constraints on the stimulation pressure to ensure no large scale tensile fractures are formed during stimulation. On completion of the well a BHTV will capture the orientation of the induced fracture. This information will provide a direction for S_{hmin} around the well bore and help improve the stress model at Newberry Volcano.

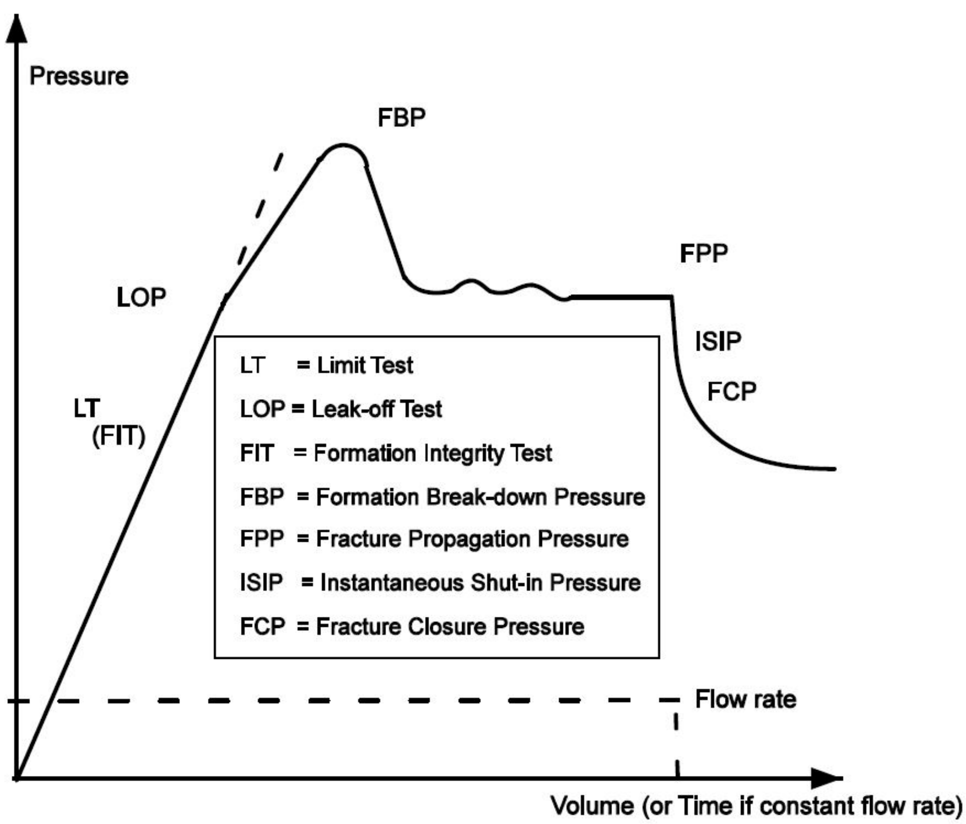

Figure 103. Schematic showing the different phases of a stress test (Zoback 2007).

9.3.2 PRESSURE MONITORING

During drilling of the EGS production well, 55A-29, the downhole pressure in the EGS injection well, 55-29, will be monitored at a high sample rate. This high precision monitoring will allow quantification of any pressure communication between the two wells during drilling. For instance, if the drill bit hits a fracture network that connects the wells, there will be a pressure response in well 55-29. The magnitude of such a response will provide constraints to inter-well connectivity and reservoir geometry parameters. Prior to drilling AltaRock will determine the necessary instrumentation needed to collect useful data and methods to analyze the data to characterize the hydraulic parameters useful for EGS. It is possible that we will find collaborators for this study.

9.3.3 LOGGING

Because of the relative importance of the data, the BHTV will be the first logging run after the well is drilled. The other logs will be run after the BHTV. The second logging suite includes an induction log to measure resistivity, a sonic log to measure interval transit time, lithodensity or spectral density logs to measure electron density, and natural gamma ray log to measure the presence of uranium, thorium and potassium in the rock formations. A static and injecting pressure-temperature-spinner survey will also be performed along with a caliper survey. The static PTS survey will be run immediately following the open-hole logging run. A second static pressure-temperature survey will be conducted approximately three to seven days after the first, so that a comparison between the two surveys can be made and the well heat-up rate can be determined. Table 10 summarizes the available high temperature logging tools and their temperature limitations. A review of the logging suite and their uses is described below:

- Natural GR measurements – The gamma ray tool measures the presence of naturally-occurring uranium, thorium and potassium in the formation. Typically, clays contain high amounts of these radioactive isotopes, so the GR is a great tool to identify clay-filled veins since typical granitic material like quartz will have a very low GR signature. Clay-filled veins, although we do not expect many of them at the demonstration site, are not ideal pathways to target for hydroshearing since they would close and seal after pumping pressure is removed. Our target fractures will be quartz-filled and open -since the fracture face asperities will prop the fractures open after pressure is removed. In addition, the GR log provides depth control and aids in well correlation. Potassium feldspar concentrations may provide depth control along with the casing shoe location.
- Neutron density measurements – The neutron density tool measures captured gamma rays (or the hydrogen index). The log will have to be “calibrated” for a granite matrix. The neutron tool helps to determine rock physical properties such as density and porosity and, combined with the sonic log, strength and static elastic moduli. In combination with the lithodensity tool, water-filled fractures may be distinguished from other fractures if a neutron density response is noted. The tool is not that useful in a massive granitic body since the only gamma rays will be emitted from clay-filled natural fractures, which will most likely not be seen by the tool because of poor vertical resolution. Plus, the natural GR tool provides the same information in an EGS well for less cost.
- Lithodensity – Emits gamma rays from a radioactive source and measures the electron density of a formation. Electron density is directly related to bulk density. The tool senses atomic mass and the relative spacing of those atoms in a rock mass. The lithodensity log will enhance our understanding of variations in rock strength. Vertical resolution is approximately 12 inches and the depth of investigation is less than 6 inches in low porosity rock. The lithodensity log will have to be calibrated for a granitic formation. The raw log data will be manipulated with the core analysis data to “calibrate” it to the Newberry site. Our petrophysical model will be developed from the raw logging data in combination with the core analysis data.

- Sonic logging measurements – A sonic log measures interval transit time. Assuming that the well bore is in good condition and that there is no other known problems with the logging environment, the sonic tool is capable of recording a very accurate interval transit time profile with depth. The sonic log is used in combination with other logs (e.g., density and neutron) in sedimentary rocks for porosity, shaliness, and interpretation of lithology. For EGS situations, it is used to help model the sonic travel time for locating microseismic events during hydroshearing. Additionally, the P-wave information aids in rock strength characterization and hydrothermal alteration. This is especially true in low porosity intrusive rocks, where P-wave velocity is the best proxy for rock strength. The rock strength information is vital in analyzing break-out information from the BHTV log to determine differential stress. The full-wave form is useful in examining known permeable fractures.
- Borehole Tele Viewer - Acoustic tele viewers provide a 360-degree image of the borehole wall. Tiger Energy Services claims a vertical resolution of 1 inch with its tool. In conjunction with temperature & spinner survey information as well as GR & neutron density measurements, open fractures can be identified. The borehole breakouts and tensile drilling-induced fractures are also captured by borehole tele viewers. The breakout data is the only way to reliably determine the principal horizontal stress directions which control fracture growth directions.
- Pressure-Temperature-Spinner surveys –The PTS surveys measure static and dynamic pressure, temperature & flow rate information down-hole. They can be used during injection, production or during times of build-up. Direct measurement of formation temperature and pressure is not only useful for immediate procedural designs (i.e. cementing and diversion systems), but also for reservoir modeling purposes.

Along with AltaRock staff, Dr. Hickman and Dr. Davatzes will analyze the log data to refine the geologic model, analyze the open-hole for open fractures and to further define the local stress regime.

Table 10: High temperature tool options for open hole logging and their temperature limitations.

High-Temperature Tool Options	Temperature Rating
Halliburton HEAT suite (GR, spectral density, sonic, induction, neutron density)	260°C / 500°F
Schlumberger Xtreme suite (GR, neutron density, full-wave sonic, induction, lithodensity)	260°C / 500°F
Baker Atlas Nautilus suite (GR, neutron density, sonic, induction, lithodensity)	260°C / 500°F
Tiger Energy Services' Acoustic Formation Imaging Technology tool	300°C / 572°F
USGS ALT acoustic tele viewer, non-commercial tool	268°C / 514°F
Welaco's PTS data-relay tool	260°C / 500°F
Pacific Process Systems' PT memory tool	316°C / 600°F

9.4 STIMULATION PLAN

Stimulation infrastructure will be installed after completion of the second well and demobilizing of the drill rig; installation took approximately 10 days during the 2014 stimulation. The specific details of the stimulation program is presented as Appendix I. Once completed the stimulation infrastructure will be tested to make sure there are no leaks or electrical control issues. This testing phase will be especially important because new pumps may be used during the stimulation of 55A-29. The first phase of stimulation will last seven days, after which it will be decided, based on acquired data, whether to move forward with a dual stimulation. If it is decided that a dual stimulation is necessary then the stimulation infrastructure will be changed accordingly and dual stimulation will commence. Dual stimulation will then last 10 to 14 days and will require two to four diverter stages. The option to divert in both wells will be available. If we do not decide to move forward with dual stimulation then there will be two diverting stages each lasting two days for well 55A-29.

9.4.1 CALIBRATION SHOT

A seismic calibration shot will either be run before logging commences or after. The real constraint with this tool is temperature. The tool cannot be set in part of the well that is above 400 °F. This means that if there is enough injectivity to cool the well the calibration shot can happen at any time. If the well proves to be fairly impermeable it might be prudent to conduct the shot right after drilling, while the well is still cool. To be effective the shot must contain greater than 2 kg of explosive. This number was arrived at by experience with the perforation shots as well as from advice from different seismologists. A Distributed Acoustic Sensor (DAS) may be installed in 55-29 before the shot to gather higher resolution data. Such data would provide unique insight into how seismic velocity changes with depth and allow for a well calibrated velocity model. If a DAS is deployed, then a vibroseis truck will be hired to occupy each of the MSA sites for sufficient time to record sufficient signals for stacking. This option was explored in 2014 and nearly executed. The effort was cancelled when it was determined that the single mode optic fiber deployed in 55-29 has a shallow break, thus was not usable.

9.4.2 STIMULATION PUMPS

As mentioned in section 6 of the report, during this round of stimulation we found that we were pressure limited with respect to stimulation. Initial seismicity began at 2400 psi (166 bar) and the seismic cloud effectively did not propagate past 200 meters (656 ft) once the max pressure of 2850 psi (197 bar) was reached. To propagate the seismic cloud further and have a more effective stimulation, AltaRock has asked Baker Hughes to redesign the pump barrels of the pumping system to accommodate conditions we encountered during this last round of stimulation. The design that Baker Hughes has come up will allow for a high pressure at low flow conditions (Figure 104). Changing the pumping system in this way will allow pump operation more consistently within the optimal pumping range of the equipment, less reliance on the bypass infrastructure, and the ability to reach pressures of up to 3500 psi (240 bar), which is the max well head pressure we can reach with the new well design. Currently Baker Hughes has priced this system at $284,000 for two new barrels. The two new pump barrels are longer than the currents pumps and therefore will require additional cost associated with infrastructure changes. These cost should not be substantial.

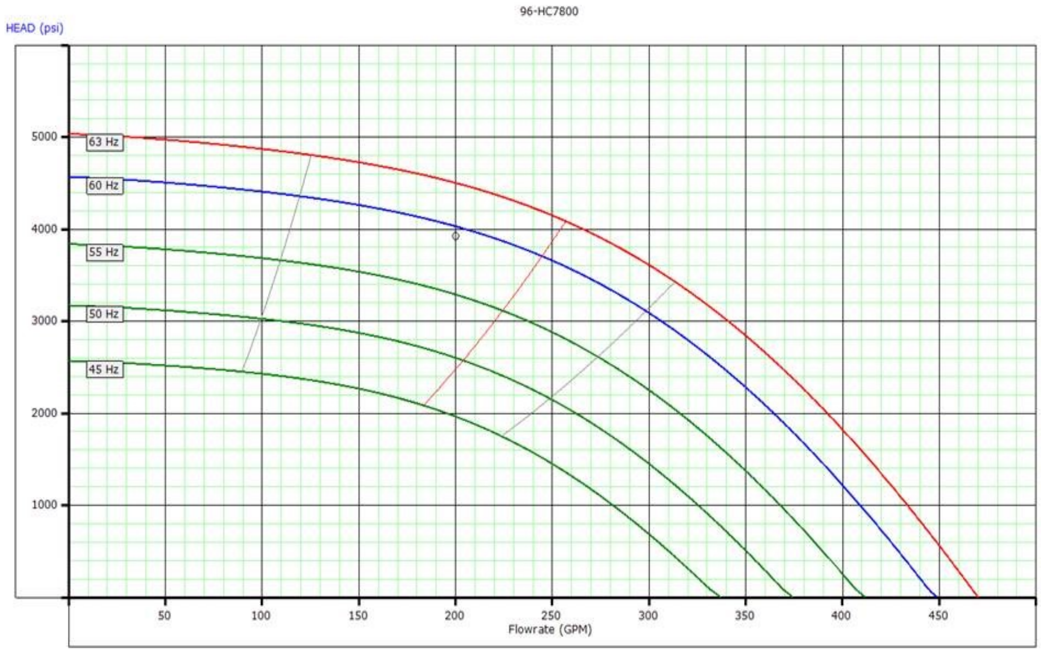

Figure 104. Pump curve for new pump barrels to be provided by Baker Hughes.

Buying a rig pump at auction is also being considered to achieve increased injection pressures. Rig pumps are effective at a range of pressures and flows and they can be considered reliable. Rig pumps are prone to break down but they can be considered reliable because there are many people who know how to operate them and there is a large supply infrastructure in place, thus maintenance and repair of this system will be faster and less costly. The lowest bid found by AltaRock is currently $330,000. The Baker Hughes option is the least expensive but rig pumps may allow for increased flexibility in the future.

9.4.3 SINGLE WELL STIMULATION

Stimulation of the new well will be similar to the 2014 stimulation operations with some key differences (Appendix I). In 2014, most of increase in injectivity occurred during the first seven days of stimulation, after which increases were generally flat. For this reason the first stage of stimulating the new well will be seven days followed by stimulating both wells simultaneously for 4 more days including two diverter stages. Some other differences are that no tracer will be injected during stimulation but will be saved for the circulation test. A working DTS will allow us to monitor and respond to stimulation down hole and provide better insight into the difference in applying fibrous and granular diverter.

9.4.4 DUAL STIMULATION

Dual stimulation has been proposed for this round to increase fracture complexity and transmissivity in the far field of the reservoir. Dual stimulation should dramatically increase the pressure between both wells, therefore increasing the likelihood that shear failure will occur along fractures between the two wells. While this technique has been tried before with only minor success at Soultz (Schindler et al. 2010), the pressures proposed for this stimulation are much greater.

Parameter sensitivity of the pore-pressure diffusion model was performed to determine the degree to which high pressure dual stimulation would create significantly higher pore-pressures between the wells. Two scenarios were modeled for a 190 bar (2,800 psi) WHP which was the maximum WHP for the single well stimulation, and for a 240 bar (3,500 psi) WHP which is the anticipated stimulation WHP for the dual stimulation. Both scenarios were modeled from 10-50 days of injection.

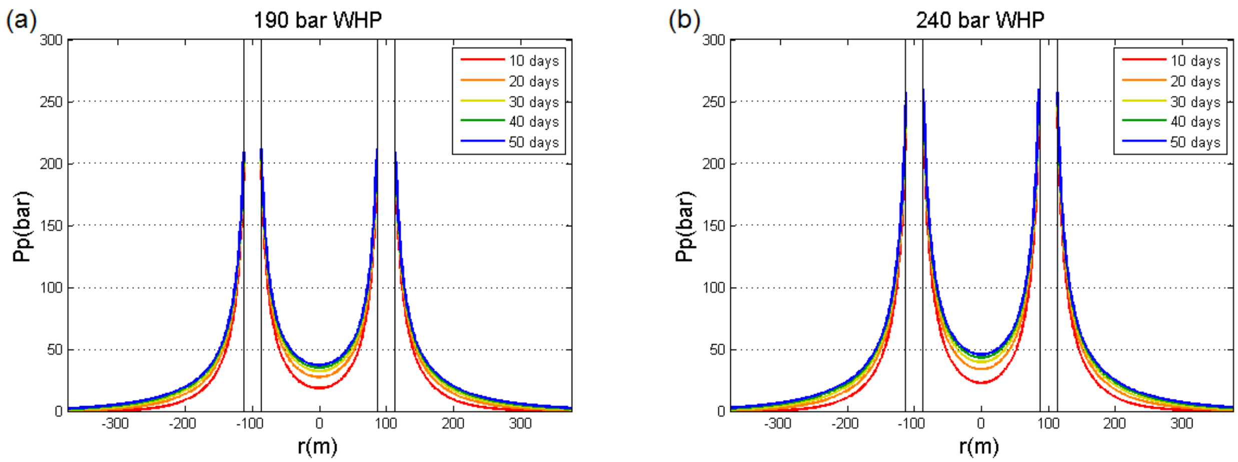

Figure 105. Pore pressure surrounding dual stimulation for 10-50 days of injection for (a) 190 bar WHP and (b) 240 bar WHP.

After 10 days of injection, the pore-pressure between the wells is 4.2 bars higher for 240 bar WHP than 190 WHP, but after 30 days of injection it is 7.3 bars higher. 20 days of injection causes nearly a 50% increase in pore-pressure between the wells from 10 days. 30 days of injection causes a 17% increase above 20 days, and 40 days of injection causes a 9% increase above 30 days. 50 days of injection causes a 6% increase above 40 days, and after that the change is less than 5% for any 10 day period. Figure 106 is a contoured map of pore pressure for the round 1 stimulation, and has the boundary for pore pressure 250 m away from the well contoured. Figure 106b is a contoured map of pore pressure for a dual well stimulation with the same boundary after a 14 day stimulation using a 240 bar WHP. The boundary does not extend as far away from the well, but covers a larger area.

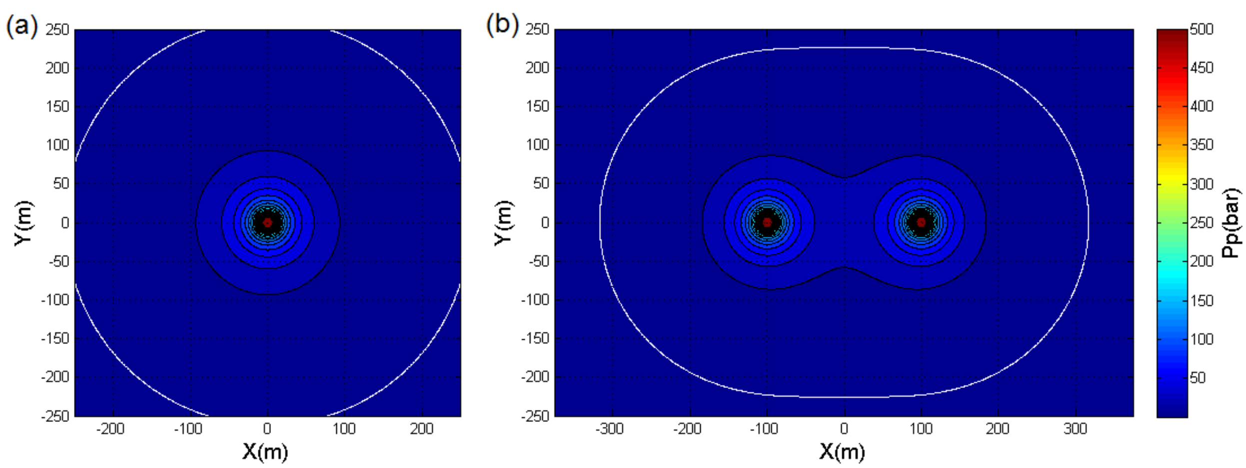

Figure 106. a) contoured map of pore-pressure of round 1 stimulation and b) contoured map of dual well stimulation after 14 days. The white line is the pressure threshold of induced seismicity.

9.5 WELL PAIR FLOW AND PRODUCTION ECONOMICS

Production from the proposed doublet system will produce near economic power and is within the lower range of MW production predicted in Phase 1.1. In Phase 1.1 AltaRock predicted that the stimulated doublet would produce between 1-10 MW of power. Using the transmissivity values from the fall off test and hall plot analysis, as well as other intrinsic properties of the reservoir, AltaRock has determined that the probable MW output to be approximately 3.9 MW (initial) net production. This finding has been independently been corroborated by analysis done by Mitchell Plummer from the Idaho National Laboratory Appendix J. Other economic parameters were also explored using GETEM to determine the levelized cost of electricity (LCOE) for different development scenarios. This analysis shows that economic production from a doublet system with 225 meter spacing is potentially economic given further reservoir improvement.

To accurately constrain the economics of the doublet system a sufficient estimate of permeability must be made. Table 6 in section 6 of this report summarizes the different transmissivity values obtained from different analysis techniques. The table shows both initial transmissivity, before stimulation, and final transmissivity, after stimulation. The most accurate of the transmissivity measurements is determined by Horner analysis of the pressure fall off curves. Fall off curve analysis shows a transmissivity of approximately 2.9×10^{-13} m^3. This measurement is within the range of other analysis techniques such as, numerical modeling, Hall plot analysis and R vs time diffusivity analysis. With a valid transmissivity value, flow between the proposed well can be estimated using a modified version of Darcy's Law (Li et al., 2014):

$$q = \frac{\Delta P_{res} T h \rho}{\mu D} \quad 8.1$$

Where $\Delta \boldsymbol{P_{res}}$ is the change in pressure between the injector and the producer, **T** is the transmissivity, **h** is fracture height, $\boldsymbol{\rho}$ is density of water at reservoir conditions, $\boldsymbol{\mu}$ is viscosity of water at reservoir conditions, **q** is flow, and **D** is distance between the two wells. Given the high pressure and temperature values found in the reservoir the fluid and fracture properties are shown in Table 11.

Table 11. Fluid and reservoir properties for calculation of flow.

Variable	Sym	Value	Unit
Change in Pressure	ΔP	3280	psi
Change in Pressure	ΔP	22.6	MPa
Transmissivity	T	2.90E-13	m^3
Fracture Height	h	150	m
Distance between wells	D	225	m
Density	ρ	750	kg/m^3
Viscosity	μ	1.37E-10	Mpa*s
Flow	q	24.8	kg/s

The change in pressure between the two wells is calculated assuming the injection well will have 1000 psi (6.9 MPa) of wellhead pressure during power operations. It is also assumed that the injected water will be 95 °C (203 °F), just under boiling, and that the water level in the producer will be roughly 1000 m (3280 ft) below the surface of the well. The pressure of steam coming out of the well will be between 100 and 200 psi (0.69 and 1.38 MPa). The fracture height, *h*, was assumed to be the width of the seismicity between the two wells. According to the seismic density plots the radius of high/connected seismicity is roughly 150 to 200 meters (492 to 656 ft). Therefore, a width of 150 meters represents a conservative estimate for the fracture height in this system. The distance, *D*, between the two wells is the average value of the open-hole section of the well, 225 meters (738 ft). Density and viscosity values for water were based off a water temperature of 290 °C and hydrostatic pressure, estimated average reservoir conditions. From the empirical data and constrained assumptions listed above, an estimated flow of 24.8 kg/s was obtained. Using a slightly lower transmissivity value, a different method of calculation and closer well spacing, Mitchell Plummer, a member of the Newberry Technical Monitoring

Team, obtained a flow of 16.7 kg/s. His work is shown in Appendix J. The result given by his analysis is close enough to corroborate the method outlined above.

Given a fairly well constrained estimate of flow between the wells, heat extraction as well as temperature decline from the resource can be estimated. To enable this analysis, AltaRock has chosen to use the heat recovery estimator within Geophires (©2012-2015), developed by Koenraad Beckers, to assess heat mining from the reservoir. The estimator uses the multiple parallel fracture model, based off of work done by (Gringarten, 1975), to estimate the heat extraction and temperature decline of the produced fluid with time. The Geophires model also uses Ramey's model (Ramey, 1962) for wellbore heat transmission; giving a more accurate estimate of produced fluid from the well. This model requires that one estimate the number of fractures connecting the two wells and it assumes that all fractures are evenly spaced and have the same transmissivity. These assumptions are clearly not representative of natural systems, but making these assumptions provide an analytical estimate of heat extraction using fracture flow, which is far less time consuming and computationally intensive than numerical methods. Information required by the model are shown in Table 12.

Table 12. Table outlines significant variable used by Geophires model.

Variable	Value	Unit
Thermal Conductivity of Rock	2.1	W/(m*K)
Heat Capacity of Rock	840	J/(kg*K)
Density of Rock	2900	kg/m^3
Geothermal Ggradient	103	°C/km
Number of Fractures	Variable	unitless
Fracture Spacing	Variable	m
Well Seperation	225	m
Flow	24.8	kg/s
Casing ID	8.5	inches
Injection Temperature	95	°C
Well Depth	3000	m

Table 13. Thermal Rock Properties derived from lab work conducted at SMU. Units for conductivity (K) are W/(m °K) (watts per meter degree Kelvin). Units for heat flow are in mW/m² (milli watts per square meter)

Top (ft)	Bottom (ft)	Final K	Log Temp (°C)	Corrected K	Average gradient	Heatflow	Corrected Heatflow
3750	4300	1.46	136.6	1.46	121.4	177.1	177.2
4850	5150	1.85	175.8	1.85	110.3	203.9	204.1
5150	5500	2.87	185.9	2.47	108.6	311.9	268.2
5650	6000	2.19	201.9	2.09	102	222.9	213.2
6050	6300	2.37	214.4	2.09	103.8	245.8	216.9
6300	6450	2.62	222.3	2.3	110.3	289.1	253.7
6500	7000	2.27	228.8	1.99	95.1	215.6	189.2
7000	7500	2.43	243.2	1.99	100.8	244.6	200.6
7550	7650	2.92	260	2.3	99.5	290.6	228.9
7800	8150	2.93	267.2	2.3	99.1	290.3	227.9
8400	8600	2.17	285	1.99	97.4	211	193.8
8650	8850	2.89	292.3	2.26	98.5	284.7	222.6
9250	9400	2.89	310.1	2.26	95	274.5	214.7
9750	10000	2.36	324.9	1.99	79.9	188.8	159

Thermal properties of the reservoir rock were derived from work completed by David Blackwell's group at SMU (Table 13). Other inputs were either known values or inferred from literature, like density values for basalts. In the analysis of possible heat extraction the number of fractures corresponds to the stimulated surface area of the reservoir. Assumed in the model is that the fractures connecting the wells are rectangular and roughly 225 meters long and 150 meter wide. We will also assume that the three major exit zones identified by PTS surveys during stimulation represent three separate fractures. With these assumptions two scenarios were run, one assuming reservoir surface area was contained entirely by flat parallel fractures and one which doubled the surface area by doubling the number of fractures to six. We also modeled these two scenarios with half the flow rate to get a better understanding of what the effect of a lower than predicted flow rate might mean on produced fluid temperature over time. Results of the Geophires model using these assumptions are shown in Figure 107.

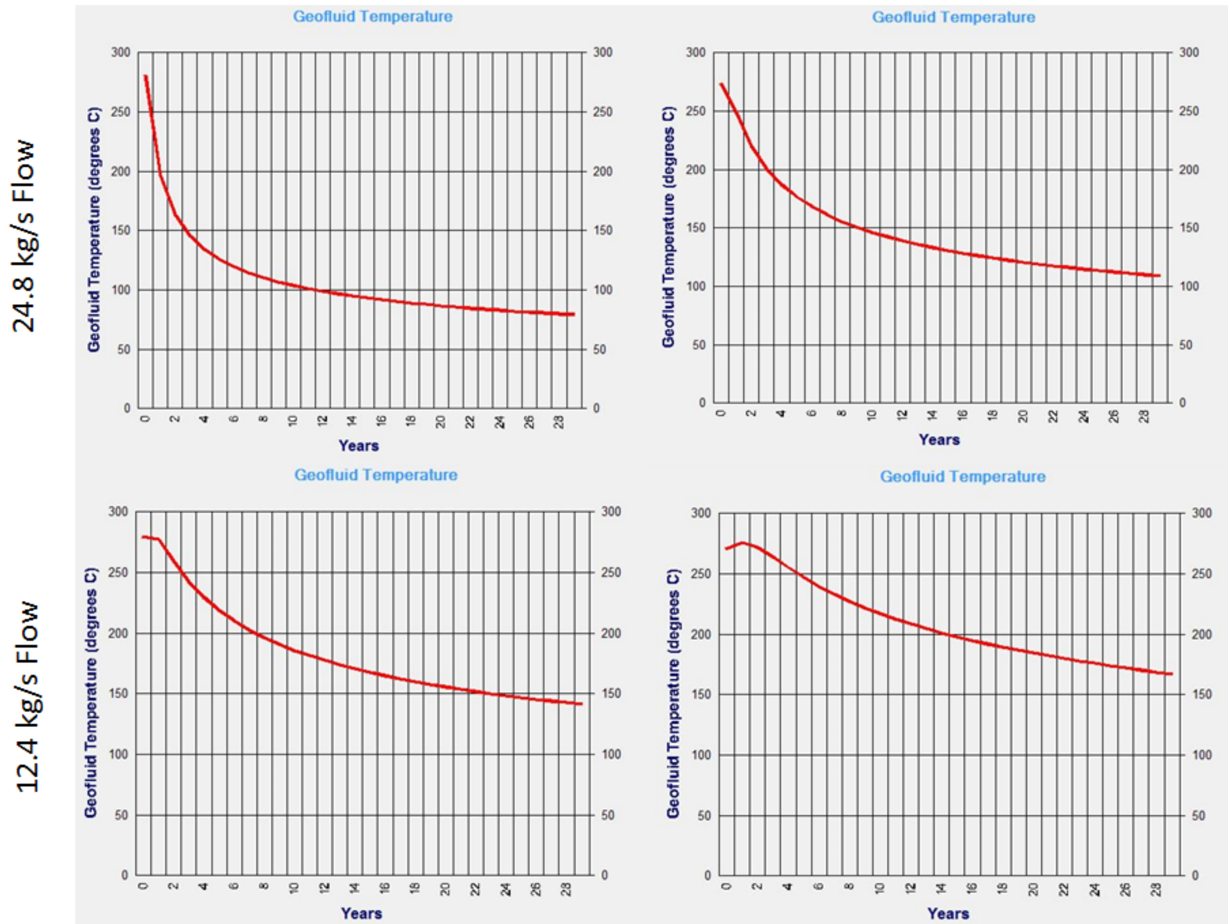

Figure 107. Graphs on the left shows produced fluid temperature decline for a three planar fracture system. Graphs on the right shows temperature decline for a six planar fracture system.

Initial MW production for both fracture scenarios and a flow rate of 24.8 kg/s is approximately 3.9 MW, but power production falls off rapidly. Power production for both scenarios in the 12.4 kg/s case is approximately 1.7 MW, and falls off much more gradually. The six planer fracture model is not necessarily supposed to represent six individual fractures between the two wells but rather a doubling of the surface area of the reservoir. This doubling of surface area could be the result of fracture pathway/network complexity.

Power production from a doublet system is determined by flow rate and the temperature of the produced fluid. Flow rate between to wells is most affected by the distance between the wells and the transmissivity of the reservoir, seen in equation 8.1. Produced fluid temperature is most effected by the ratio of flow through the reservoir to surface area of the reservoir. Simply stated, when wells are close together it is more important to have a reservoir with a high surface area than high transmissivity. Conversely, if the wells are far apart the transmissivity becomes far more important than the surface area of the reservoir. This suggests that for our proposed doublet, whose two wells are fairly close, stimulation efforts should be focused on enhancing fracture network complexity in the reservoir. Such enhanced complexity has the most likelihood of success in a dual stimulation scheme, this is simply because it raises the pressure in the far field of the reservoir to hydroshearing pressures.

Inputting the results obtained by Geophires, for a flow rate of 12.4 kg/s and 6 planar fractures, into the geothermal electricity technology evaluation model, GETEM, a levelized cost of electricity, LCOE, of 49.5 cents/Kwh was derived. This high cost of power is largely derived from the ratio of large infrastructure costs to power sold. As an example, this cost includes approximately $10,000,000 for transmission lines but the plant itself would only produce an average of 1.3 MW. This also does not consider re-drilling and expanding the reservoir. As more doublets come online and the stimulation process becomes more refined, cost will come down fairly quickly until about 20-30 MW capacity has been reached, this is the inflection point where incremental improvements in cost from scaling become reduced. Beyond just improvements in stimulation, cost can be reduced by drilling side tracks, employing new plant technologies and optimizing pumping and plant infrastructure needs. However, before accurate forecasts of cost can be made, the second well will have to be drilled and the doublet system tested. There are questions which need to be answered before accurate predictions can be made. These questions include:

1. Will the reservoir transmissivity increase with presence of another well?
2. Will transmissivity increase as the fracture systems cools, and what are the implications of this?
3. Will hydroshearing provide enough fracture path complexity to create a large surface area reservoir?
4. With a heterogeneous lithology, what will be the actual heat recharge into the reservoir?
5. Can potential thermal breakthrough be mitigated using diverters?
6. What will be the scaling issues associated with producing this fluid?

Until inter-well tests can be conducted within the stimulated reservoir, there will be many unknowns about how this process has worked and how it can be improved in the future.

9.6 SCHEDULE

The rough schedule for the proposed field work this year begins in July and extends to the middle of November. The field work during 2015 involves the siting and drilling of a new well called 55A-29 and the subsequent stimulation of both these wells. The schedule is subject to change.

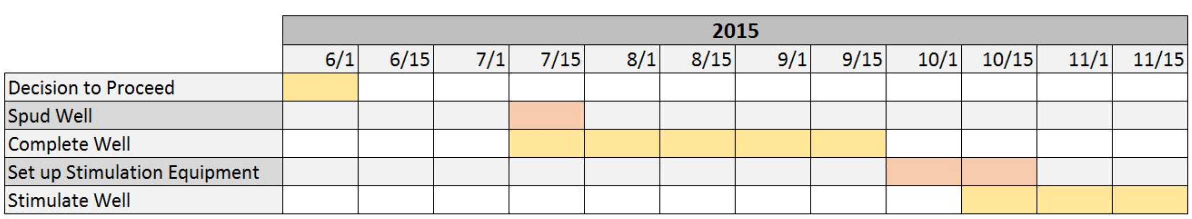

10 REFERENCES

AltaRock. 2014. Phase 2.1 Report, Newberry EGS Demonstration, DOE Award: DE-EE0002777. Prepared by AltaRock Energy, Inc., June 4.

AltaRock. 2011a. Phase I Report. Newberry EGS Demonstration, DOE Award: DE-EE0002777. Prepared by AltaRock Energy, Inc., August 26.

AltaRock. 2011b. Induced Seismicity Mitigation Plan. Newberry Enhanced Geothermal Systems Demonstration. Prepared by AltaRock Energy, Inc., August 3.

AltaRock. 2011c. Evaluation of Water Usage for the Newberry EGS Demonstration. Prepared by AltaRock Energy, Inc., February 9.

BLM. 2011. Environmental Assessment, Newberry Volcano Enhanced Geothermal System (EGS) Demonstration Project. United States Department of the Interior Bureau of Land Management (BLM). DOI-BLM-OR-P000-2011-0003-EA, DOE/EA-1897, December.

Baggeroer, A.B., Kuperman, W. A., and Mikhalevsky, P. N. 1993. An overview of matched field methods in ocean acoustics. IEEE Journal of Oceanic Engineering, 18, 401–424.

Bargar, K.E. and Keith, T.E.C. 1999. Hydrothermal Mineralogy of Core from Geothermal Drill Holes at Newberry Volcano, Oregon. USGS Professional Paper 1578.

Borja, R.I., Samma, K.M., and Sanz, P.F. 2003. On the numerical integration of three-invariant elastoplastic constitutive models. Computation Methods in Applied Mechanical Engineering, 192, 122.

Bucker, H.P. 1976. Use of calculated sound fields and matched-field detection to locate sound sources in shallow water. Journal of the Acoustical Society of America, 59, 368–373.

Century West. 1982. La Pine Aquifer Management Plan: Bend, OR. Prepared by Century West Engineering Corporation.

Charlaix, E., Guyon, E., Roux, S., 1987. Permeability of a random array of fractures of widely varying apertures. Transport in Porous Media, 2, 31–43.

Cladouhos, T.T., Swyer, M.W., Uddenberg, M. and Petty, S. 2015. Results from Newberry Volcano EGS Demonstration. Proceedings, fourtieth Workshop on Geothermal Reservoir Engineering, Stanford University, Stanford, CA.

Cladouhos, T.T., Petty, S., Callahan, O., Osborn, W., Hickman, S., and Davatzes, N. 2011a. The role of stress modeling in stimulation planning at the Newberry Volcano EGS Demonstration Project. Proceedings, Thirty-Sixth Workshop on Geothermal Reservoir Engineering, Stanford University, Stanford, California, February 11–13.

Cladouhos, T.T., Clyne, Matthew, C., Maisie, N. Petty, S. Osborn, W. L., Nofziger, L. 2011b. Newberry Volcano EGS demonstration stimulation modeling. Geothermal Resources Council Transactions, 35, 317–322.

Cladouhos, T.T., Petty, S., Nordin, Y., Moore, M., Grasso, K., Uddenberg, M., Swyer, M., Julian, B., Foulger, G. 2013. Microseismic monitoring of Newberry Volcano EGS Demonstration. Proceedings, Thirty-Seventh Workshop on Geothermal Reservoir Engineering Stanford University, Stanford, CA, February 11–13.

Dames and Moore. 1994. Revised Report Newberry Geothermal Project Hydrology Baseline Study Newberry Volcano, Oregon Force Exploration Company. Prepared by Dames and Moore, May 4.

Davatzes N.C., Hickman S.H. 2011. Preliminary analysis of stress in the Newberry EGS Well NWG 55-29, GRC Transactions, 35, 323–332.

Dorbath, L., Cuenot, N., Genter, A., Frogneux, M. 2009. Seismic response of the fractured and faulted granite of Soultz-sous-Forêts (France) to 5 km deep massive water injections. Geophysical Journal International, 177, 653–675.

Fetterman, J.A., 2011. Porosity evolution in the Newberry Volcano geothermal system, Oregon, USA: feedback between deformation and alteration. Geothermal Resources Council Transactions, 35, 339–346.

Fetterman, J.A., Davatzes, N.C. 2011. Fracture generated porosity evolution in the Newberry Volcano geothermal system, OR: feedback between deformation and alteration. Geothermal Resources Council National Meeting.

Foulger Consulting. 2010. Newberry Calibration Shot Project. Internal Report to AltaRock Energy, Inc., Prepared by Foulger Consulting, October 9.

Foulger, G.R., Julian, B.R. 2013a. Report to AltaRock Energy, Inc., Earthquake Seismicity associated with the Newberry EGS Demonstration. Draft Report, March 18.

Foulger, G.R., Julian, B.R. 2013b. Seismological software for geothermal monitoring. Proceedings, Thirty-Eighth Workshop on Geothermal Reservoir Engineering, Stanford University, Stanford, CA, February 11–13.

Fournier, R., and Truesdell, A.H. 1973. Empirical Na-K-Ca geothermometer for natural waters Geochimica et Cosmochimica Acta 37, (5), 1255-1275.

Gannett, M.W., Lite, K.E., Morgan, D.S., and Collins, C.A. 2001. Groundwater hydrology of the upper Deschutes Basin, OR. USGS Water-Resources Investigations Report 00–4162.

Goles, G., and Lambert, R. 1990. A strontium isotopic study of Newberry volcano, central Oregon: Structural and thermal implications. Journal Of Volcanology And Geothermal Research, 43(1-4), 159-174.

Gueguen, Y., Dienes, J. 1989. Transport properties of rocks from statistics and percolation. Journal of Mathematical Geology 21, 1–13.

Gringarten A.C., Witherspoon P. A., Yuzo Ohnishi, 1975. Theory of heat extracted from fractured hot dry rock. Journal of Geophysical Research. DOI:10.1029/JB080i008p01120.

Häring, M.O., Schanz, U., Ladner, F., Dyer, B. 2008. Characterization of the Basel-1 enhanced geothermal system. Geothermics, 37, 469–495.

Harris, D.B., and Kvaerna, T. 2010. Superresolution with seismic arrays using empirical matched field Processing. Geophysical Journal International, 182, 1455–1477.

Hudson, J.A., Pearce, R.G., Rogers, R.M. 1989. Source type plot for inversion of the moment tensor. Journal of Geophysical Research: Solid Earth, 94, 765–774.

James, R. 1970. Factors controlling borehole performance. Geothermics – Special Issue, 2, 2, Pt. 2.

Julian, B.R., Foulger, G.R. 1996. Earthquake mechanisms from linear-programming inversion of seismic-wave amplitude ratios. Bulletin of the Seismological Society of America, 86, 972–980.

Julian, B.R., Foulger, G.R. 2004. Microearthquake focal mechanisms – A tool for monitoring geothermal systems. Geothermal Research Council Bulletin, 33, 166–171.

Julian, B.R., Foulger, G.R., Monastero, F.C., Bjornstad, S. 2010. Imaging hydraulic fractures in a geothermal reservoir. Geophysical Research Letters, 37, L07305.

Julian, B.R., Miller, A.D., Foulger, G.R. 1997. Non-double-couple earthquakes at the Hengill-Grensdalur geothermal area, southeast Iceland. Geophysical Research Letters, 24, 743–746.

Julian, B.R., Miller, A.D., Foulger, G.R. 1997. Non-double-couple earthquakes at the Hengill-Grensdalur geothermal area, southeast Iceland. Geophysical Research Letters, 24, 743–746.

Julian, B.R., Miller, A.D., Foulger, G.R. 1998. Non-double-couple earthquakes 1. Theory. Reviews of Geophysics, 36, 525–549.

Kim, J., Sonnenthal, E., and Rutqvist, J. 2012. Formulation and Sequential Numerical Algorithms of Coupled Fluid/Heat Flow and Geomechanics for Multiple Porosity Materials. International Journal of Numerical Methods in Engineering, doi: 10.1002/nme.4340.

Kim J., Sonnenthal E., and Rutqvist J. 2015. A sequential implicit algorithm of chemo-thermo-poro-mechanics for fractured geothermal reservoirs. Computers & Geosciences, 76, 59–71.

King, G. 1991. Technical Reconnaissance Report, Survey of Groundwater Resources, Upper Deschutes River Basin, OR. U.S. Bureau of Reclamation, In-house Report.

LBNL. 2013. Interactive Map of Earthquakes at the Newberry Caldera. Maintained by Lawrence Berkeley National Laboratory (LBNL), Earth Sciences Division. Available at: http://esd.lbl.gov/research/projects/induced_seismicity/egs/newberry.html.

Li, Y., Wang, J., Jung, W., Ghassemi, A. 2012. Mechanical properties of intact rock and fractures in welded tuff from Newberry Volcano. Proceedings, Thirty-Seventh Workshop on Geothermal Reservoir Engineering Stanford University, Stanford, CA, January 30–February 1.

Majer, E., Baria, R., Stark, M. 2008. Protocol for induced seismicity associated with enhanced geothermal systems. Report produced in Task D Annex I (9 April 2008), International Energy Agency – Geothermal Implementing Agreement (Incorporating comments by: C. Bromley, W. Cumming, A. Jelacic and L. Rybach). Available at: http://iea-gia.org/wp-content/uploads/2014/01/Protocol-for-Induced-Seismicity-EGS_GIA-Doc-25Feb09-ed9Mar10.pdf.

Majer, E. J., Robertson-Tait, N.A., Savy, J., Wong, I. 2011. Protocol for Addressing Induced Seismicity Associated with Enhanced Geothermal Systems (EGS). Available at: http://esd.lbl.gov/files/research/projects/induced_seismicity/egs/EGS-IS-Protocol-Final-Draft-20110531.pdf.

Matzel, E., Templeton, D., Peterson, A., Goebel, M. 2014. Imaging the Newberry EGS Site using Seismic Interferometry, Proceedings, Thirty-Ninth Workshop on Geothermal Reservoir Engineering Stanford University, Stanford, CA, February 24–26.

McGarr, A. 1976. Seismic moments and volume changes. Journal of Geophysical Research, 81, 8, 1487–1494.

McGarr, A. 2014. Maximum magnitude earthquakes induced by fluid injection. Journal of Geophysical Research: Solid Earth, 119.

Miller, A.D., Foulger, G. R., Julian, B.R. 1998. Non-double-couple earthquakes 2. Observations. Reviews of Geophysics, 36, 551–568.

Morgan, D.S., Tanner, D.Q., Crumrine, M.D. 1997. Hydrologic, Water Quality, and Meteorological Data for Newberry Volcano and Vicinity, Deschutes County, OR, 1991–1995. USGS Open-File Report 97-4088.

Osborn, W.L., Petty, S., Cladouhos, T.T., Iovenitti, J., Nofziger, L., Callahan, O., Perry, D.S., Stern P.L. 2011. Newberry Volcano EGS Demonstration, Phase I results. GRC Transactions, 35, 499–505.

Parotidis, M., Shapiro, S.A., Rothert, E. 2004. Back front of seismicity induced after termination of borehole fluid injection. Geophysical Research Letters, 31, L02612.

Petty, S., Nordin, Y., Glassley, W., Cladouhos, T., Swyer, M. 2013. Improving geothermal project economics with multi-zone stimulation: results from the Newberry Volcano EGS Demonstration. Proceedings, Thirty-Eighth Workshop on Geothermal Reservoir Engineering, Stanford University, Stanford, California, February 11–13, 2013.

PNSN. 2013. Volcano Seismicity – Newberry. Pacific Northwest Seismic Network (PNSN). Available at: http://www.pnsn.org/volcanoes/newberry.

Ramey, H.J., Jr. 1962. Wellbore Heat Transmission. JPT 6 (2) 427–435; Trans., AIME, 225.

Reed, M., Palandri, J. L. 2006. SOLTHERM.H06, a database of equilibrium constants for minerals and aqueous species. Available from the authors, University of Oregon, Eugene, Oregon.

Reed, M, Spycher, N. 1984. Calculation of pH and mineral equilibria in hydrothermal waters with application to geothermometry and studies of boiling and dilution Geochimica Cosmochimica et Acta, 48, (7), 1479-1492.

Rinaldi, A.P., J. Rutqvist, E.L. Sonnenthal, and T.T. Cladouhos. 2012. TOUGH-FLAC coupled THM modeling of proposed stimulation at the Newberry Volcano EGS Demonstration. Proceedings, TOUGH Symposium 2012, Lawrence Berkeley National Laboratory, Berkeley, CA.

Roeloffs, E. 1996. Advances in Geophysics. Academic Press, San Diego, CA. v. 37.

Sammel, E.A., and Craig, R.W. 1983. Hydrology of the Newberry Volcano Caldera, Oregon. U.S. Geological Survey Water Resources Investigations Report 83-4091.

Sammel, E.A., Ingebritsen, S.E., and R.H. Mariner. 1988. The hydrothermal system at Newberry Volcano, Oregon. Journal of Geophysical Research, 93(B9), 10149–10162.

Schindler M., Baumgartner, J., Gandy, T., Hauffe, P., Hettkam, T., Menzel, H., Penzkofer, P., Teza, D., Tischner, T., Whal, G. 2010. Successful Hydraulic Stimulation Techniques for electric power Production in the upper Rhine Graben, Central Europe. World Geothermal Congress, Bali, Indonesia.

Shapiro, S., Krüger, O., Langenbruch, C., Dinske, C. 2010. Geometric control of earthquake magnitudes by fluid injections in rocks. Society of Exploration Geophysicists, Expanded Abstracts, 30, 1539–1543.

Sherrod, D.R., Taylor, E.M., Ferns, M.L., Scott, W.E., Conrey, R.M., and Smith, G.A. 2004. Geologic Map of the Bend 30x60-Minute Quadrangle, Central Oregon. USGS Geologic Investigations Series 1-2683.

Shiozawa, S. and McClure, M., 2014. EGS Designs with Horizontal Wells, Multiple Stages, and Proppant. Proceedings, Thirty-Ninth Workshop on Geothermal Reservoir Engineering, Stanford University, Stanford, California.

Smith, J. T., Sonnenthal, E., Cladouhos, T. 2015. Thermal-Hydrological-Mechanical Modelling of Shear Stimulation at Newberry Volcano, Oregon. 49th US Rock Mechanics / Geomechanics Symposium, San Francisco, CA, USA, 28 June- 1 July 2015.

Sonnenthal, E.L., Nakagawa, S., Christensen, J., Wanner, C., and Nakashima, S. 2015a. Geochemical and Isotopic Constraints on Fracture Surface Area: Experiments and Reactive Transport Modeling. PROCEEDINGS, Fortieth Workshop on Geothermal Reservoir Engineering Stanford University, Stanford, California, January 26-28, SGP-TR-204.

Sonnenthal, E. L., Smith, J.T., Cladouhos, T., Kim, J., and Yang, L. 2014. Thermal-Hydrological-Mechanical-Chemical Modeling of the 2014 EGS Stimulation Experiment at Newberry Volcano, Oregon. Proceedings, Fortieth Workshop on Geothermal Reservoir Engineering, Stanford University, Stanford, California, January 26-28, 2015. SGP-TR-204.

Sonnenthal, E.L., Smith, J.T., Cladouhos, T., Kim, J., and Yang, L. 2015b. Thermal-Hydrological-Mechanical-Chemical Modeling of the 2014 EGS Stimulation Experiment at Newberry Volcano, Oregon. PROCEEDINGS, Fortieth Workshop on Geothermal Reservoir Engineering Stanford University, Stanford, California, January 26-28, SGP-TR-204.

Sonnenthal, E. L., Spycher, N., Callahan, O., Cladouhos, T., Petty, S. 2012. A thermal-hydrological-chemical model for the enhanced geothermal system demonstration project at Newberry Volcano, Oregon. Proceedings, Thirty-Seventh Workshop on Geothermal Reservoir Engineering, Stanford University, Stanford, CA, January 30–February 1. SGP-TR-194.

Sonnenthal, E. L., Spycher, N., Xu, T., Zheng, L., Miller, N., Pruess, K. 2014. TOUGHREACT V3.0-OMP, http://esd.lbl.gov/research/projects/tough/software/toughreact.html.

Spycher, N., Sonnenthal, E.L., Kennedy, B.M. 2011. Integrating multicomponent chemical geothermometry with parameter estimation computations for geothermal exploration. Geothermal Resource Council Transactions, 35, 663-666.

Spycher, N., Peiffer, L., Sonnenthal, E.L., Saldi, G., Reed, M.H., and Kennedy, B.M. 2014. Integrated solute multicomponent geothermometry. Geothermics, 51:113-123.

Tarasovs, S., Ghassemi, A. 2012. On The Role of Thermal Stress in Reservoir Stimulation. Proceedings, Thirty-Seventh Workshop on Geothermal Reservoir Engineering. Stanford University, Stanford, California, January 30 - February 1.

URS. 2010. Evaluations of Induced Seismicity/Seismic Hazards and Risk for the Newberry Volcano EGS Demonstration. Prepared by URS Corporation, November 22.

Waldhauser, F. and W.L. Ellsworth. 2000. A double-difference earthquake location algorithm: Method and Application to the Northern Hayward Fault. Bulletin of the Seismological Society of America, 90, 1353–1368.

Wang, J., Templeton, D., Harris, D. 2011. Mapping Diffuse Seismicity Using Empirical Matched Field Processing Techniques. Proceedings, Thirty-Sixth Workshop on Geothermal Reservoir Engineering, Stanford University, Stanford, California, January 31–February 2.

Wanner, C., Peiffer, L., Sonnenthal, E.L., Spycher, N., Iovenitti, J., and Kennedy, B.M. 2014. Reactive transport modeling of the Dixie Valley geothermal area: Insights on flow and geothermometry. Geothermics, 51:130-141.

Xu, T., Sonnenthal, E., Spycher, N., and Pruess, K. 2006. TOUGHREACT: A simulation program for non-isothermal multiphase reactive geochemical transport in variably saturated geologic media: Applications to geothermal injectivity and CO2 geological sequestration. Computers & Geosciences. 32:145-156.

Xu, T., Spycher, N., Sonnenthal, E. L., Zhang, G., Zheng, L., Pruess, K. 2011. TOUGHREACT Version 2.0: A simulator for subsurface reactive transport under non-isothermal multiphase flow conditions. Computers and Geosciences, 37, 763–774.

Wessel, P., and Smith, W. H. F. 1998. New, improved version of Generic Mapping Tools released, EOS Transactions American Geophysical Union, 79, 47

Zoback M. 2007. Reservoir Geomechanics. Cambridge University Press, New York. P. 210.